

63-42

409 922

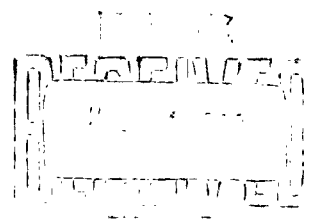
CATALOGED BY DDC 409922



Noise Transport in the Crossed-Field Diode

by

M. A. Pollack



Series No. 60, Issue No. 485

DA 36-039 SC-85278

October 22, 1962

ELECTRONICS RESEARCH LABORATORY

**UNIVERSITY OF CALIFORNIA
BERKELEY, CALIFORNIA**

Electronics Research Laboratory
University of California
Berkeley, California

NOISE TRANSPORT IN THE CROSSED-FIELD DIODE

by

M. A. Pollack

Institute of Engineering Research
Series No. 60, Issue No. 485

U. S. Army Signal Research and Development Laboratory
Fort Monmouth, New Jersey
Signal Corps Contract No. DA 36-039 SC-85278

October 22, 1962

ACKNOWLEDGMENT

The author wishes to express his appreciation to Professor J. R. Whinnery for his guidance of this research. His suggestions and advice lent direction to the work, yet permitted the author to discover for himself and to surmount many of the obstacles along the way.

Special appreciation is also due Professor T. Van Duzer for the many stimulating discussions on all phases of this research, and for his constant interest and assistance.

The author wishes to thank Professor C. K. Birdsall and Dr. W. B. Bridges for their suggestions and the often heated discussions about many parts of this work, and Dr. D. L. Judd for his criticism of the manuscript. The constant interchange of ideas with the students of the Microwave Tube Laboratory at the University of California is greatly appreciated. To Messrs. J. Meade and G. Becker, the author is grateful for the skillful design and construction of the experimental tube.

This research was supported by the U. S. Army Signal Corps under Contract No. DA 36-039 SC-85278.

ABSTRACT

The problem of excess noise in electron streams moving in mutually perpendicular electric and magnetic fields has been studied by many workers over the years. The present work treats the transport of noise, originating at a thermionic cathode, across a planar diode model of an accelerating crossed-field stream. Both rf open- and short-circuited diodes are studied. A single-velocity electronic theory and a multi-velocity Monte Carlo study are used to predict the growth of noise for magnetic fields up to a critical field, at which the stream has turned so as to graze the anode. The single-velocity theory is Van Duzer's extension of the familiar Llewellyn-Peterson equations to the crossed-field case. The Monte Carlo analysis essentially simulates actual thermionic emission by using random numbers to generate electron emission times and velocities. Trajectories for many charges are followed through the diode space, requiring the use of a high speed digital computer.

Low frequency measurements were performed on a planar, rf short-circuited, triode model for the crossed-field diode. They show that the normal component of anode noise current grows slowly with increasing magnetic field at first, then increases rapidly near the critical field. Both theories agree with these experimental findings. Measurements by other workers have shown the existence of large electron velocity spreads at the anodes of crossed-field diodes. The single-velocity theory predicts a corresponding growth of velocity fluctuations under certain operating conditions. The Monte Carlo study predicts the increase of both the normal anode velocity fluctuations and the spread of the velocity distribution with magnetic field. A simple dc model predicts the same magnitude of spread, which is then seen to be caused more by the "geometrical" spreading of the initial velocity distribution than by rf effects. This phenomenon explains in part some of the high equivalent temperatures and corresponding slow decrease of anode currents with increasing magnetic field found in crossed-field diodes.

The crossed-field potential minimum is found to be very similar to the ordinary minimum in this planar model. No instabilities were found. The normal and transverse velocity distributions and spectra maintain their initial form from the cathode to the minimum. The noise current smoothing at low frequencies found at the potential minimum in ordinary streams is predicted for moderate magnetic fields; it disappears for fields near the cutoff value.

Whinnery's approximate treatment of noise phenomena at the minimum of a short-circuited diode without crossed-magnetic field is extended to a wider range of velocity classes. The peak of noise current near the electron plasma frequency at the minimum is again found to be dependent on the transit time from cathode to minimum. This peak, and a dip in the noise current predicted by Tien and Moshman, are found in the Monte Carlo results for both the open- and short-circuited diodes. A discrepancy exists between the results for the open-circuited diode and those found by Dayem.

The range of validity of the single velocity theory is studied. Under certain operating conditions, input velocity fluctuations are found to produce trajectory crossovers which invalidate the single-velocity assumption. Use of the space charge parameter ξ in the transformation equations is extended to the crossed-field case. Although the common $\xi = 1$ assumption leads to erroneous coefficients in the low frequency limit, its use gives good results at slightly higher frequencies in many cases.

TABLE OF CONTENTS

	<u>Page</u>
Chapter I.	INTRODUCTION 1
Chapter II.	THE POTENTIAL MINIMUM AT HIGH FREQUENCIES 5
II. 1	The Physical Picture 5
II. 2	Model and Method 6
II. 3	The Crossed-Field Minimum 9
II. 4	Normalization and Transformation 12
II. 5	The Diode of Finite Spacing 15
II. 6	Computation and Results 18
II. 7	Discussion 21
Chapter III.	SINGLE VELOCITY MODEL OF THE ACCELERATING REGION. 26
III. 1	The Single Velocity Approach to Electron Beams 26
III. 2	The Single Velocity Approach to Crossed-Field Beams 28
III. 3	The Fluctuation Transformation Equations . . 29
III. 4	D. C. Conditions in the Diode 31
III. 5	The Effect of ξ in the Space-Charge-Limited Diode. 35
III. 6	Fluctuations in the Crossed-Field Diode . . . 44
Chapter IV.	MULTIVELOCITY MODEL OF THE CROSSED- FIELD DIODE-THEORY. 57
IV. 1	The Monte Carlo Method 57
IV. 2	Model, Assumptions and Methods. 58
IV. 3	Electric Field and Potential. 59
IV. 4	The Equations of Motion 65
IV. 5	Emission. 67
IV. 6	Theoretical Average Values. 72
IV. 7	Fluctuations in the Stream 76

TABLE OF CONTENTS

		<u>Page</u>
IV. 8	Spectral Theory	81
Chapter V..	MULTI-VELOCITY MODEL OF THE CROSSED- FIELD DIODE: RESULTS	88
V. 1	The Computer Calculation	88
V. 2	A Check on the Emission Process	92
V. 3	Noise Current at the Minimum with Zero Magnetic Field	95
V. 4	Dependence of the Average Beam Quantities on B/B_c	103
V. 5	Dependence of the Fluctuations on B/B_c . .	116
V. 6	Examination into the Validity of the Calculation	129
Chapter VI.	EXPERIMENTAL VERIFICATION OF THE THEORIES	134
VI. 1	Design of the Experimental Apparatus . . .	134
VI. 2	Space-Charge Limited Triode Behavior . .	143
VI. 3	Effects of the Crossed Magnetic Field . . .	145
VI. 4	Related Experiments	152
Chapter VII.	CONCLUSIONS AND SUGGESTIONS FOR FURTHER WORK	154
VII. 1	Conclusions	154
VII. 2	Suggestions for Further Work	157
APPENDIX A	DETAILS OF THE TIME DOMAIN ANALYSIS.	160
APPENDIX B	DETAILS OF THE FREQUENCY DOMAIN POTENTIAL MINIMUM ANALYSIS.	164
APPENDIX C	NUMERICAL APPROXIMATIONS FOR THE POTENTIAL MINIMUM ANALYSIS.	167
APPENDIX D	THE FLUCTUATION TRANSFORMATION COEFFICIENTS.	173
APPENDIX E	THE VALIDITY OF THE SINGLE-VELOCITY THEORY IN TERMS OF CROSSOVERS. . .	178
APPENDIX F	ESTIMATION OF η_1 FROM THE MONTE CARLO ANALYSIS	181

TABLE OF CONTENTS

	<u>Page</u>
APPENDIX G DISTRIBUTION OF THE NORMAL COMPONENT OF ANODE VELOCITY— EXCLUDING AC EFFECTS.	184
REFERENCES.	192

LIST OF FIGURES

<u>Figure</u>		<u>Page</u>
I-1	The crossed-field diode.	1
II. 3-1	Electron trajectories in the crossed-field potential minimum. Curves on the left are for $v_{ze} = 0.78(10^5)$ m/sec; curves on the right are for $v_{ze} = +0.78(10^5)$ m/sec.	10
II. 4-1	Typical curves of $\xi_c(\tau)$	14
II. 6-1	Variation of R^2 with η_1	20
II. 6-2	Variation of $ r ^2$ with τ_d	22
II. 6-3	Effect of more accurate finite spacing factor on $ r ^2$	23
II. 7-1	Comparison of weighted R^2 with the Tien- Moshman result	25
III. 2-1	The coordinate system for the model.	28
III. 4-1	Variations of θ and J_d with B/B_c	36
III. 5-1	Variations of $ a_{22} ^2$ and $ b_{22} ^2$ with $ \beta $, $\theta = 0$	38
III. 5-2	Variation of $ a_{23} ^2$ and $ b_{23} ^2$ with $ \beta $, $\theta = 0$	39
III. 5-3	Variation of $ a_{32} ^2$ and $ b_{32} ^2$ with $ \beta $, $\theta = 0$	40
III. 5-4	Variation of $ a_{33} ^2$ and $ b_{33} ^2$ with $ \beta $, $\theta = 0$	41
III. 5-5	Dependence of $ b_{22} ^2$ and $ b_{23} ^2$ on ξ near $ \beta = 0$	43
III. 6-1	The low frequency crossed-field noise function $G(\theta)$	45
III. 6-2	Variation of $ a_{22} ^2$ and $ b_{22} ^2$ with $ \beta $ and θ	47
III. 6-3	Variation of $ a'_{23} ^2$ and $ b'_{23} ^2$ with $ \beta $ and θ	48

LIST OF FIGURES

Figure		Page
III. 6-4	Variation of $ a'_{24} ^2$ and $ b'_{24} ^2$ with $ \beta $ and θ	49
III. 6-5	Variation of $ a'_{32} ^2$ and $ b'_{32} ^2$ with $ \beta $ and θ	50
III. 6-6	Variation of $ a_{33} ^2$ and $ b_{33} ^2$ with $ \beta $ and θ	51
III. 6-7	Variation of $ a_{34} ^2$ and $ b_{34} ^2$ with $ \beta $ and θ	52
III. 6-8	Variation of noise current with $ \beta $ and θ in the open-circuited diode.	54
III. 6-9	Variation of noise current with $ \beta $ and θ in the short-circuited diode	54
III. 6-10	Variation of noise velocity with $ \beta $ and θ in the open-circuited diode.	55
III. 6-11	Variation of noise velocity with $ \beta $ and θ in the short-circuited diode	55
IV. 3-1	Potential distribution for a single charge in the short-circuited diode.	63
IV. 3-2	Potential distribution for a single charge in the open-circuited diode	65
IV. 5-1	Mapping of R onto $\text{Cum } P(s)$	68
IV. 5-2	Emission probability distributions and their cumulative distribution functions	71
IV. 8-1	Aliasing of $P_w(f)$	82
V. 2-1	x-directed spectra at the cathode	94
V. 2-2	z-directed spectra at the cathode	96
V. 2-3	Cross-correlation spectra at the cathode	97
V. 3-1	R^2 for short- and open-circuited diodes.	99
V. 3-2	Comparison of R^2 with the results of other theories for the short-circuited diode	100
V. 3-3	Comparison of R^2 with the results of other theories for the open-circuited diode	102
V. 4-1	The dependence of the normal velocity distribution at $X = 0.05$ on B/B_c	109

LIST OF FIGURES

<u>Figure</u>		<u>Page</u>
V. 4-2	The dependence of the transverse velocity distribution at $X = 0.05$ on B/B_c	110
V. 4-3	The dependence of the normal velocity distribution at the anode on B/B_c in the short-circuited diode	111
V. 4-4	The dependence of the normal velocity distribution at the anode on B/B_c in the open-circuited diode	112
V. 4-5	The dependence of the transverse velocity distribution at the anode on B/B_c in the short-circuited diode	113
V. 4-6	The dependence of the transverse velocity distribution at the anode on B/B_c in the open-circuited diode	114
V. 5-1	x-directed current spectra at $X = 0.05$ in the short-circuited diode	117
V. 5-2	x-directed current spectra at $X = 0.05$ in the open-circuited diode	118
V. 5-3	x-directed velocity spectra at $X = 0.05$ in the short-circuited diode	120
V. 5-4	x-directed velocity spectra at $X = 0.05$ in the open-circuited diode	121
V. 5-5	z-directed velocity spectra at $X = 0.05$ in the short-circuited diode	122
V. 5-6	z-directed velocity spectra at $X = 0.05$ in the open-circuited diode	123
V. 5-7	x-directed current spectra at the anode in the short-circuited diode	125
V. 5-8	x-directed current spectra at the anode in the open-circuited diode	126
V. 5-9	x-directed velocity spectra at the anode in the short-circuited diode	127

LIST OF FIGURES

<u>Figure</u>		<u>Page</u>
V. 5-10	x-directed velocity spectra at the anode in the open-circuited diode	128
V. 5-11	z-directed velocity spectra at the anode in the short-circuited diode	130
V. 5-12	z-directed velocity spectra at the anode in the open-circuited diode	131
V. 6-1	Effect of N_s (or n_{s0}) on the spectra at the anode of the short-circuited diode.	133
VI. 1-1	Detail of the gun region	136
VI. 1-2	The a) Kino gun geometry and b) the Pierce gun geometry	137
VI. 1-3	Experimental crossed-field triode	139
VI. 1-4	Schematic of noise measurement circuit	141
VI. 1-5	DC characteristics of temperature-limited reference diode	142
VI. 2-1	DC characteristics of the experimental triode	144
VI. 2-2	a) Effect of cathode temperature on noise current with $B = 0$; b) Triode heater characteristics	146
VI. 3-1	Variation of average current with magnetic field	148
VI. 3-2	Variation of anode noise current with magnetic field for the short-circuited diode at small transit angles	149
VI. 3-3	Observations of the beam made by the introduction of H_2 gas into the tube	150
A. 1	a) Trajectories for $\eta_0 > \eta_1$; b) Trajectories for $\eta_1 < \eta_0$	161
B. 1	Curve of $\tau_1 - \tau_0^*$ for $\eta_0 > \eta_1$ and $\eta_1 > \eta_0$	166
C. 1	Form of crossover function and critical charge trajectory	168
C. 2	Crossover function for α electrons	170
E. 1	The criterion for crossovers	178
F. 1	Spectra of \tilde{V}_m for estimation of η_1	183

LIST OF FIGURES

<u>Figure</u>		<u>Page</u>
G. 1	Normal velocity distributions at cathode and anode in an ordinary electron stream.	186
G. 2	Conditions on the potential distribution to determine trajectories.	187
G. 3	The dependence of the normal anode velocity distribution on B/B_c	190
G. 4	Distribution of u_x^2 as a function of U_e	191

LIST OF TABLES

<u>Table</u>		<u>Page</u>
II. 6-1	Classes of η_0 and weights	19
III. 5-1	Low frequency limits of L-P coefficients. . .	42
IV. 8-1	Variability table	85
V. 1-1	Comparison of parameters for the Monte Carlo calculation	91
V. 2-1	Emission parameters	93
V. 4-1	Comparison of average values with theory for $B/B_c = 0$	105
V. 4-2	Average minimum potential and position, anode current, potential, and electric field, and number of charges in the diode space	106
V. 4-3	Average x-directed velocities and numbers in the crossed-field diode.	107
V. 4-4	Average z-directed velocities and numbers in the crossed-field diode.	107
C. 1	β -electron trajectory parameters	171
C. 2	β -electron crossover parameters	171
C. 3	α -electron crossover parameters	172
D. 1	The a_{ij} coefficients.	175

GLOSSARY

Notes on Subscripting

Symbol

x	x-directed quantity
z	z-directed quantity
$\bar{}$	average value, except as noted; omitted where not ambiguous
a	at "a" plane
b	at "b" plane
d	at anode
k	at cathode
∞	for infinite diode

Other Symbols

Symbol

\sim	ac part
—	average value
Δ, d, δ	increment

GLOSSARY, Cont'd.

<u>Symbol</u>	<u>Quantity</u>
a	normalized frequency
a	acceleration
"a"	input plane
a_o	integral function
a_{ij}	open-circuit electronic coefficients
A	fictitious area
A	constant for approximate trajectories
A	cross-correlation function (current, velocity)
\bar{A}	normalized cross-correlation function (current, velocity)
"b"	output plane
b_o	integral function
b_3	integral factor
b_{ij}	short-circuit electronic coefficients
B	magnetic field (constant)
B	cross-correlation function (current, velocity)
B	constant for approximate trajectories
\bar{B}	normalized cross-correlation function (current, velocity)
B_c	critical magnetic field, $\sqrt{2 V_d / \eta d^2}$
c_3	integral factor
C	auto-correlation function (general)
C	auto-correlation function (current)
C	constant for approximate trajectory
\bar{C}	normalized auto-correlation function (current)
CDF	cumulative distribution function

GLOSSARY, Cont'd.

<u>Symbol</u>	<u>Quantity</u>
d	diode spacing
d_{ga}	grid-anode spacing
d_3	integral factor
d_{cg}	cathode-grid spacing
D	constant for approximate trajectories
\bar{D}	auto-correlation function (velocity)
\bar{D}	normalized auto-correlation function (velocity)
$D(\tau)$	lag window, modified
$D_o(\tau)$	lag window, rectangular
e	magnitude of electronic charge
E	normalized electric field
\mathcal{E}	electric field
\mathcal{E}_{sc}	electric field, space charge component
f	frequency
f	function of integral factors
f_o	$1 / \Delta t$
$f_o(\tau)$	Fourier transform of $\ln(a)$
f_{max}	maximum usable frequency of spectral analysis
F	normalized frequency, ft_d
F_{pm}	normalized plasma frequency at potential minimum ($B = 0$)
$F(a \tau_d)$	finite spacing correction factor
$g(t)$	arbitrary time function
$g(a)$	transform of $j(\tau)$
$g_{o \infty}(a)$	transform of $\xi_c(\tau)$
$g_{l \infty}(a)$	transform of $-\xi_l(\tau / 2)$
$g_p(a)$	transform of $j_p(\tau)$
$G(\theta)$	noise current function
G_l	integral function
$G(f)$	Fourier transform of $g(t)$

GLOSSARY, Cont'd.

<u>Symbol</u>	<u>Quantity</u>
h_o	crossover function for finite diode
h_1	compensation function for finite diode
$h(t)$	arbitrary time function
$H(f)$	Fourier transform of $h(t)$
H_s	Heaviside step function
\mathcal{H}	magnetic field intensity
i	integer index, step index
i	current, convection*
i_r	compensation current
i_o	perturbation current
I_H	heater current
I_o	average current
I_n	integral function
I_d	total diode average current
\tilde{I}_d	total diode alternating current
j	integer index; charge index counting from anode
j	$\sqrt{-1}$
$j(\tau)$	normalized current
$j(t)$	instantaneous current density
J_d	total diode average current density*
J_{eo}	emission current density, average
J_{cl}	Child-Langmuir current density
k	equivalent number of degrees of freedom
k	integer index
k	Boltzmann's constant
k_1	proportionality constant, $e / \Delta t$

*Unless specifically noted, i is taken positive and j negative for electrons.

GLOSSARY, Cont'd.

<u>Symbol</u>	<u>Quantity</u>
l	integer index; lag number
m	electronic mass
m_{Δ}	steps per unit time, $t_d / \Delta t$
M	maximum number of lags
n	number of steps charges per step
n_{eo}	number of charges emitted per step, average
N	total number of steps
N_s	number of charges in diode space
"O"	electron stream with rf field parallel to focussing B field
p	dummy variable
p	shape factor of approximate trajectory
P	distribution function
P	power density spectrum
P_g	true power density spectrum
P_w	true power density spectrum of averages over step
\tilde{P}_w	aliased power density spectrum
\bar{P}_w	aliased, finite data, power density spectrum
q	trajectory shape factor
\tilde{q}	fluctuating part of convection current density (negative for electrons)
$Q_o(f)$	Fourier transform of $D_o(t)$
r	noise current reduction factor, single velocity class
$R(\eta_1)$	noise current reduction factor, all perturbing classes
R	noise current reduction factor, entire beam
R	random number
s	dummy variable
S	normalized ac charge flowing past anode

GLOSSARY, Cont'd.

<u>Symbol</u>	<u>Quantity</u>
t	time
t_a	electron entrance time (Appendix E)
t_d	unit time, d/v_d
$t_o(x)$	time along x_o trajectory
t_n	total time for N steps
$t_l(x)$	time along x_l trajectory
T	normalized time, t/t_d
T_c	cathode temperature
u	normalized velocity, v/v_d
U	normalized potential, V/V_d
U_e	normalized equivalent thermal potential, kT_c/eV_d
v	velocity, usually average
\tilde{v}	ac velocity
$v_o(x)$	velocity along x_o trajectory
$v_l(x)$	velocity along x_l trajectory
v_o	emission velocity of perturbing charge
v_l	emission velocity of critical charge
v_e	emission velocity
v_d	velocity equivalent of V_d , $\sqrt{2\eta V_d}$
$\langle \tilde{v}_R^2 \rangle$	Rack velocity fluctuation
V	potential
V_d	anode potential, average
\tilde{V}_d	anode potential, fluctuating part
V_e	thermal equivalent potential, kT_c/e
V_{BFE}	beam forming electrode potential
$V_o(x)$	average diode potential distribution
V_g	triode grid potential
V_g^i	triode grid plane equivalent potential

GLOSSARY, Cont'd.

<u>Symbol</u>	<u>Quantity</u>
W	weighting factor
W	stored electric energy
w	velocity class
w(t)	weighted-over-step time function
x	spatial coordinate, along electric field
x_m	position of potential minimum
x_c	crossover position
x'_c	crossover function
x_o	trajectory of perturbing charge
x₁	trajectory of critical charge and compensating charge, potential minimum to cathode
x₂	trajectory of compensating charge, beyond potential minimum
X	normalized position, x/d
y	spatial coordinate, along magnetic field
Y	normalized position, y/d
Y_e	external diode admittance per unit area
z	spatial coordinate
Z	normalized position, z/d
α	ratio of average emission to Child-Langmuir current density, J_{eo}/J_{cl}
α	class of returning electrons
α	constant for trajectory calculations
β	ratio of average emission to anode current density, J_{eo}/J_{do}
β	class of transmitted electrons
β	constant for trajectory calculations
β	transit angle $j\omega\tau$

GLOSSARY, Cont'd.

<u>Symbol</u>	<u>Quantity</u>
γ	spectral constant
Γ	zero magnetic field, low frequency noise current reduction factor
ΔV_1	energy added by compensating charge pair
ΔV_p	energy added by perturbing charge
Δq	surface charge density
Δq_p	surface charge density, perturbing charge
Δt	time interval
ΔT	normalized time interval
Δt	ac transit time
$\Delta \tau$	lag time interval
Δf	frequency interval
ΔF	normalized frequency interval
ϵ_0	dielectric constant, diode space and electron beam
ξ	normalized distance function
ξ	space charge factor
η	electronic charge to mass ratio, e/m
$\eta(\xi)$	Fry-Langmuir normalized potential
η_0	normalized equivalent of u_0 , initial energy
η_1	normalized equivalent of u_1 , initial energy
η_2	normalized equivalent of u_2 , initial energy
θ	cyclotron transit angle, $\omega_c \tau$
ξ	Fry-Langmuir's normalized distance
ξ_0	normalized trajectory x_0
ξ_1	normalized trajectory x_1
ξ_2	normalized trajectory x_2
ξ_c	normalized crossover distance
π	3.14159 +

GLOSSARY, Cont'd.

<u>Symbol</u>	<u>Quantity</u>
ρ	volume charge density
ρ_s	surface charge density
τ	lag time
τ	transit time between "a" and "b" planes
τ	normalized time, $2\omega_{pm} t$
τ_{10}	$ \tau_{1m} - \tau_{0m} $
$\tau_{\alpha 2}, \tau_{\alpha 3}$	constants for approximate trajectory
τ_d	minimum-anode normalized transit time
τ_o	normalized time along x_o trajectory
τ_o^*	modified form of τ_o
τ_1	normalized time along x_1 trajectory
τ_2	normalized time along x_2 trajectory
τ_{om}	normalized time, minimum cathode, perturbing charge
τ_{om}'	function of τ_{om} and τ_{1m}
τ_{1m}	normalized time, minimum-cathode, critical charge
τ_m	maximum lag time
$\phi(\theta)$	function in single velocity analysis
θ_d	cyclotron transit angle for unit time, $\omega_c t_d$
ω	radian frequency, $2\pi f$
ω_c	cyclotron radian frequency, ηB
ω_{pm}	plasma radian frequency at potential minimum

I. INTRODUCTION

Much progress has been made over the last three decades on the noise problem in crossed-field devices. However, the sources of the excess noise found in devices employing electron streams moving in orthogonal electric and magnetic fields are still not completely understood. The present investigation is not intended as a complete study of the causes of crossed-field stream noise. Rather its aim is the investigation of noise transport in a simple configuration, the crossed-field diode (Figure I-1). This configuration can be considered a model for the gun region of a typical crossed-field tube. It is hoped that the knowledge gained here will add to the understanding of the noise processes in more complex crossed-field configurations.

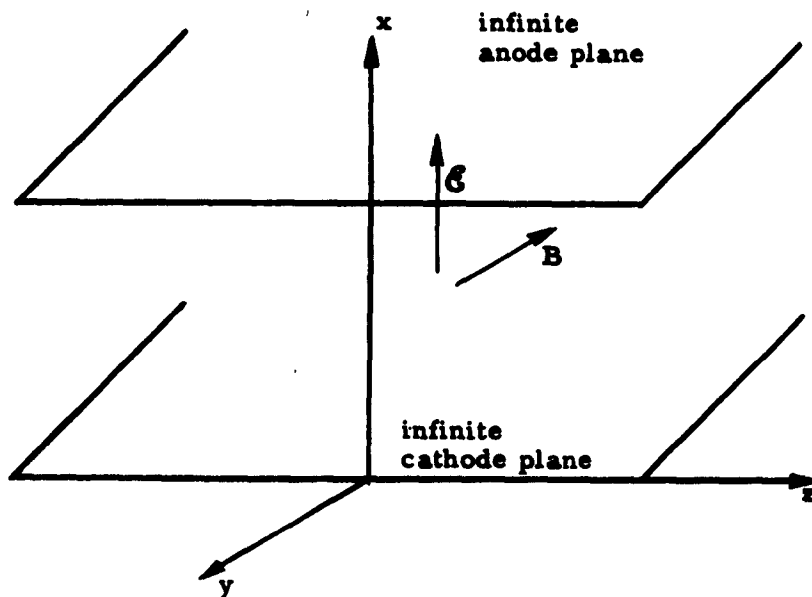


Figure I-1. --The crossed-field diode

The excess noise manifests itself in a number of ways. Crossed-field oscillators and amplifiers sometimes generate large quantities of output noise power over a wide range of the rf spectrum. This is accompanied by high noise measured in the current collected by many of the electrodes. The noise is many times larger than would be estimated solely on the basis of the diocotron amplification of shot noise in the circuit region (Doehler, 1958). An additional amplification mechanism is required to explain the magnitude of the noise.

Another manifestation of the excess noise is the collection of electrons by electrodes that could not be reached on the basis of static fields alone. Highly negative electrodes collect a significant portion of the stream current. In the planar crossed-field diode, or in the cylindrical magnetron configuration, the anode current should decrease toward zero as the magnetic field is increased toward a critical value,* B_c . If the effects of initial normal and transverse velocities at the cathode are neglected, the current should cut off sharply to zero at B_c (Hull, 1921). With the inclusion of initial velocities, the anode current should decrease at calculated rate with increasing magnetic field (Fulop, 1958). However, measurements by Fulop and others have shown that the anode current falls off more slowly than the rate calculated for normal cathode operating temperatures. Cathode temperatures on the order of $10^4 - 10^5$ degrees Kelvin are necessary to account for this. On the other hand, a gain mechanism could be postulated to explain this discrepancy.

Energy distributions have been obtained from the measurement of the current collected by negative electrodes. The equivalent temperatures (obtained from the slope of a logarithmic current-voltage plot) have also been reported to be in the range of 10^5 degrees Kelvin.

*The critical magnetic field is defined by $B_c = \sqrt{2 V_d / \eta d^2}$, where V_d is the cathode-anode voltage, d is the cathode-anode spacing, and η is the magnitude of the electronic charge to mass ratio.

Other measurements have indicated that the noise and current to negative electrodes are higher for space-charge-limited operation than for temperature-limited operation (Little, Ruppel and Smith, 1958). This has been found true even for beams with the same average current. Measurements by Anderson (1960) and Rando (1961) on a backward wave amplifier with a Kino type (Kino, 1960) convergent gun have resulted in noise figures around 25 decibels. This is on the same order as the noise figure of "O"-type (parallel electric and magnetic fields) tubes before the addition of noise-reducing electrodes. It is many orders of magnitude lower than noise figures measured on tubes having less well focused crossed-field beams. The Kino gun is designed to have zero average transverse electric field, and this might play some role in the noise problem.

Although the particular configuration of the crossed-field device seems to have an effect on the noise characteristics, excess noise has been found to some degree in almost all of them. For this reason, one of the simplest configurations, the planar diode, was chosen for study. The steady state characteristics of this device have been treated numerically by Lindsay (1960) for some operating conditions (however, not for space-charge-limited flow). Van Duzer and Whinnery (1961) have treated the potential minimum region for this model by an approximate method. By means of an extension of the single-velocity Llewellyn-Peterson equations (1941, 1944), Van Duzer (1961) developed the fluctuation transformation equations for the planar accelerating crossed-field stream. Others have treated this problem using similar methods but more complex two-dimensional models (Wadhwa, 1962).

Van Duzer's results for the planar model have shown the possibility of noise growth in the accelerated stream. However, no appreciable change could be attributed to the addition of the crossed magnetic field to the potential minimum region of an ordinary stream in the approximate analysis of Van Duzer and Whinnery.

Measurements across the body of a crossed-field stream by Van Duzer and Whinnery (1961b) have shown that the equivalent temperature at the inner edge is much higher than the temperature in the main part of the stream. This has led them to postulate a mechanism for the growth of crossed-field noise. They suggested that some form of turbulence or instability in the crossed-field potential minimum acts to drive waves growing along the stream boundary. The potential minimum region is implicated as a noise source because its formation in the transition from temperature-limited to space-charge-limited flow is accompanied by a large increase in noise. One aim of this work is the investigation of the Van Duzer-Whinnery hypothesis.

Both theoretical and experimental studies of the noise transport in the crossed-field diode are presented in the following chapters. The theoretical model is the one-dimensional diode. That is, no variations of any quantities are permitted in the plane parallel to the cathode. The usefulness of such a model is discussed in more detail later. However, it is clear that the dc model is the same one obtained by use of the Kino gun. The stream has no edges, so that there can be no growth of the type postulated by Van Duzer and Whinnery. Therefore any growth that results from the analyses must be a body effect in the electron stream.

At first the diode is separated into two regions, the cathode-minimum space and the accelerating stream. Then an analysis of the entire diode as a unit is presented. Chapter II presents the theory and methods of an approximate analysis of the effects of the potential minimum on noise at high frequencies. The results that are presented are an extension of Whinnery's (1960) results, obtained over a wider range of parameters for the diode with zero magnetic field. The reasons for not continuing with an extension of the Van Duzer-Whinnery crossed-field potential minimum analysis are given.

The accelerating stream is treated by means of the Van Duzer transformation theory in Chapter III. Both open- and short-circuited diodes are considered. The use of a well-known space-charge parameter to obtain approximate noise results is discussed

and extended to the crossed-field case. The effects of the magnetic field on the transport of noise quantities from the potential minimum region to the anode are evaluated. The range of transit angles for which the theory is invalid is obtained.

Treatment of the complete diode by the multi-velocity, nonlinear Monte Carlo theory is discussed in Chapters IV and V. The theoretical development of the model, formulation, and spectral analysis in Chapter IV is followed by the results of the analysis in Chapter V. Comparison of these results with those obtained for the individual regions is studied. Chapter VI presents the experimental verification of the theoretical results, obtained by measurements on a planar crossed-field triode.

II. THE POTENTIAL MINIMUM AT HIGH FREQUENCIES

II.1. The Physical Picture

Although we desire to describe completely the noise processes in the crossed-field electron stream, certain simplifications must generally be made to obtain even an approximate solution. This is certainly true in the case of noise propagation from a thermionic cathode in a space-charge-limited diode, where multi-velocity streams flow in opposite directions in the region up to the potential minimum. The Monte Carlo technique, applied to the crossed-field diode in a later section, is one possible improvement over an analysis that fails to treat the inherent nonlinearity of the problem. But it in turn fails to give a simple, concise analytic representation of the noise propagation, though its results are considerably more accurate than those to be described here. The intent of this section, then, is to examine an approximate treatment, which physically and analytically describes the phenomena considered to be important. By eliminating certain "refinements," we may be losing only the fine details of the solution, or we may be eliminating the very mechanism we desire to find. With this danger in mind we describe an approximate analysis of the potential minimum.

In the space-charge-limited diode with no magnetic field, the potential minimum acts to gate the flow of electrons between their thermionic source and the accelerating region beyond. Electrons with insufficient initial normal velocity, the " α " class, turn before the potential minimum and return to the cathode. Those with higher initial velocities form the " β " class and travel on into the transmitted stream. Electrons with initial normal velocities in the range to permit them to just reach the potential minimum in the unperturbed state are "critical" electrons. Perturbations to the steady flow will cause these critical electrons to be either accelerated or decelerated, changing their ultimate destinations.

An emitted electron, part of the cathode shot current, represents a perturbation to the steady flow and acts to decelerate following electrons. Hence fewer critical electrons will reach the anode. The electron holes traveling toward the anode and the returning critical electrons set up fields which continue to perturb other critical electrons. At low frequencies, this leads to a reduction in the noise currents, as described by Thompson and North (1940), Rack (1938), and others, due to the compensatory nature of the feedback produced. Whinnery (1954, 1960), Siegman and Watkins (1957b), Tien and Moshman (1956), Vivian (1960), and Dayem (1960), have found that this compensation fails at higher frequencies, and in some cases the feedback may result in oscillatory behavior.

II. 2. Model and Method

The model and technique of analysis are those used by Whinnery; the analysis is essentially a high-frequency extension of the Thompson-North approach. The ac short-circuited diode is assumed to be infinite in extent, with fields computed for infinite sheet charges at positions corresponding to those of point charge trajectories. Full shot noise perturbs the steady state flow, which originates at the thermionic cathode with a Maxwellian

distribution of initial velocities. Trajectories are assumed to be independent of the perturbations, implying a linearized theory. A difficulty arises because of the nature of the static potential distribution in the vicinity of the critical, or zero acceleration plane (the potential minimum in the ordinary diode). Here the potential distribution is quadratic with distance, and electrons arriving with zero velocity at the critical plane would never leave it. This is only a fault of the model, for normal fluctuations would cause such a difficulty to disappear. To avoid this inconsistency, Whinnery and Siegman and Watkins have assigned a small velocity to critical charges at the critical plane. The value of this velocity, although arbitrary, affects the results of the analysis, and will be discussed later.

The fluctuating current flowing into the accelerated stream is desired as the result of the analysis. The perturbing and compensating fields add an energy $e\Delta V$ to the charges arriving at the minimum, and due to the nature of the emitted Maxwellian velocity distribution, the change in current going to the anode is

$$\Delta I = \frac{\partial I}{\partial V} \Delta V = \frac{I}{V_e} \Delta V, \quad (1)$$

where V_e , the potential equivalent of thermal energy, is kT_c/e . The quantity, k , is Boltzmann's constant, e is the magnitude of the electronic charge, and T_c is the cathode temperature. For the ordinary diode (with spatial coordinate x measured from the cathode), the added energy, or integrated potential ΔV , must be evaluated up to the potential minimum.

First, consider the anode to be removed to infinity. Then the field lines all terminate on the cathode. If Δq is the charge per unit area of each sheet charge, the field due to the perturbing charge is $-\Delta q_p/\epsilon_0$. All charges and currents in this analysis are considered for a unit diode area. As long as the critical charge is between the perturbing charge and the cathode, this field must

be integrated to give ΔV_p . For the simple case of perturbing charge velocity v_o equal to critical charge velocity v_1 , the integrating distance is x_m , the position of the minimum, and

$$\Delta V_p(x_m) = \frac{\Delta q_p}{\epsilon_o} x_m \quad (2)$$

When v_o is not equal to v_1 , the trajectories cross, and

$$\Delta V_p(x_m) = \frac{\Delta q_p x'_c}{\epsilon_o} \quad (3)$$

In general, then,

$$\begin{aligned} x'_c &= x_m - x_c & v_o &> v_1 \\ &= x_c & v_1 &> v_o \\ &= x_m & v_1 &= v_o \end{aligned} \quad (4)$$

where x_c is the position of crossover.

The effects of the compensation charge pairs leaving the minimum at all times t' prior to t , the time the critical charge arrives at the minimum, must be taken into account. A positive compensation current ΔI (of increased electron flow) produces a charge $-\Delta I(t')dt'$ at $x_2(t-t')$ and a hole charge $-\Delta I(t')\Delta t'$ at $x_1(t-t')$. The quantities $x_2(t)$ and $x_1(t)$ represent the distance-time functions for compensating charges beyond and before x_m , respectively. The quantity $x_1(t)$ is also the trajectory of the critical charge moving to the potential minimum.

Because of the symmetry of critical and compensation charge trajectories, their crossover plane is

$$x_1\left(t - \frac{[t+t']}{2}\right) = x_1\left(\frac{t-t'}{2}\right) \quad (5)$$

The field between the compensating charge pair can then be integrated to give the potential

$$\Delta V_1(x_m) = \frac{-\Delta I(t')dt'}{\epsilon_o} \left[x_m - x_1\left(\frac{t-t'}{2}\right) \right] \quad (6)$$

Combining (1), (3), and (6),

$$V_e \Delta I = \Delta V_p + \Delta V_1 = \frac{\Delta q x_c'}{\epsilon_0} - \int_0^t \frac{\Delta I(t') dt'}{\epsilon_0} \left[x_m - x_1 \left(\frac{t-t'}{2} \right) \right]. \quad (7)$$

This integral equation can be solved for $\Delta I(t)$ and the corresponding frequency spectrum added to the spectrum of the perturbing charge, to obtain the total noise spectrum at the potential minimum.

II. 3. The Crossed-Field Minimum

The effect of the potential minimum on noise currents in the crossed-field diode can also be described in terms of perturbing and compensating charges. However, the initial transverse velocities can no longer be ignored, and a whole range of transverse as well as normal initial velocities must be taken into account. To better understand the effect of the magnetic field on the crossed-field potential minimum, an analog model was first set up on an EASE analog computer. Electron trajectories were obtained directly in graphical form as solutions to the equations of motion. The magnetic field was assumed uniform, while the electric field was given by a parabolic approximation to the actual static potential obtained by Yankina (1959),

$$\mathcal{E} = \mathcal{E}(x) = - \frac{2V_m}{x_m} \left(1 - \frac{x}{x_m} \right) \text{ volts/meter} \quad (1)$$

The potential of the minimum, V_m , is -0.18 volts and the cathode-minimum spacing, x_m , is $1.5(10^{-5})$ meters, for a diode with a magnetic flux density of 100 gauss in the minus y direction.

Trajectories are shown in Figure II.3-1 for several different values of v_{xe} , the initial x -directed velocity. Electrons leave the cathode with an initial z velocity, v_{ze} , equal to plus or minus the average velocity of the stream moving in that direction. Here the effect of the magnetic field on electrons with equal v_{xe} but opposite v_{ze} can be clearly seen.

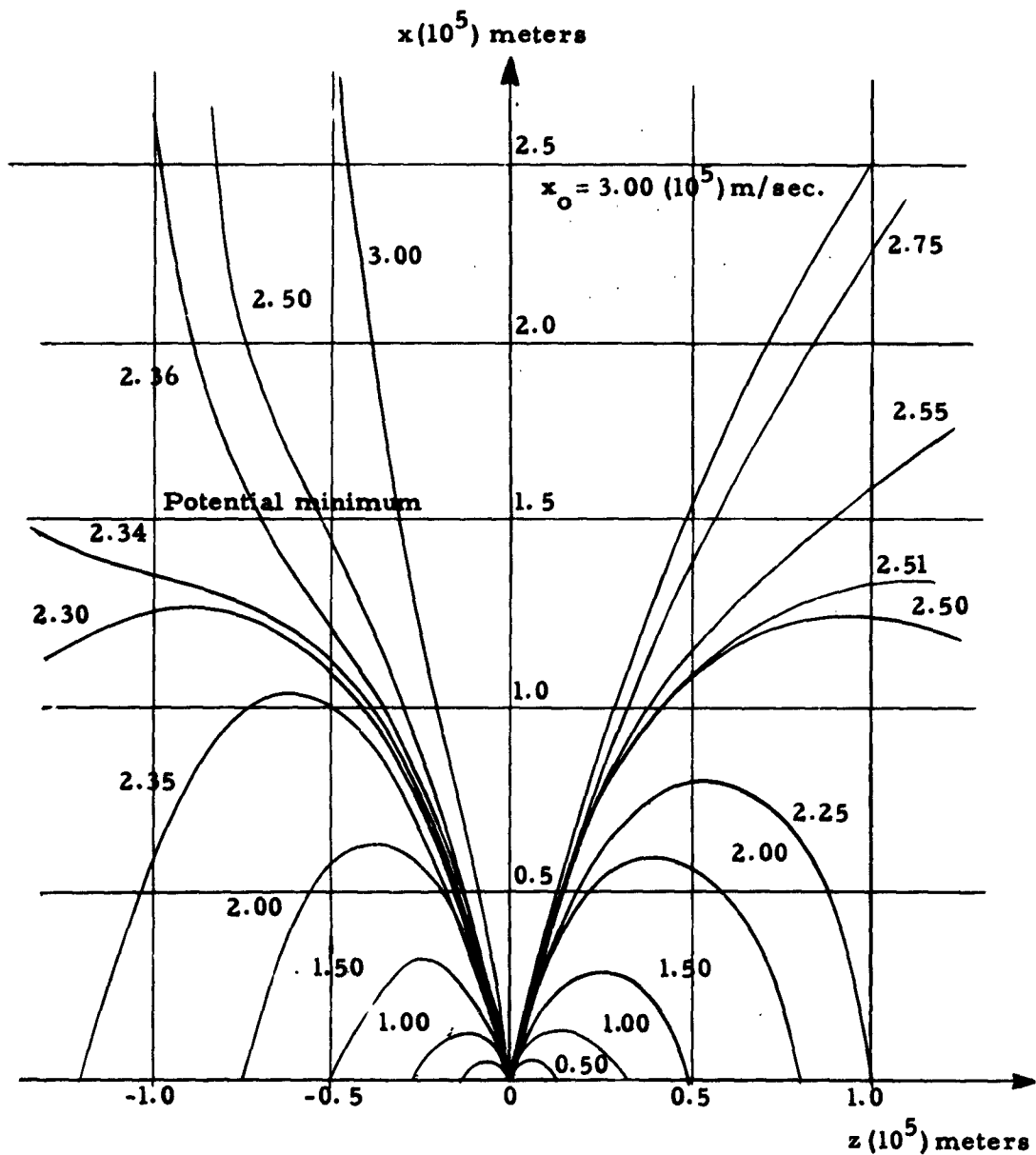


Figure II. 3-1. Electron trajectories in the crossed-field potential minimum. Curves on the left are for $v_{ze} = -0.78(10^5)$ m/sec; curves on the right are for $v_{ze} = +0.78(10^5)$ m/sec.

This complicates the physical picture, since the plane at which electrons separate into α and β classes is now removed from the potential minimum, and depends in fact on the initial transverse velocity of each electron. The normal component of velocity that alone specified whether or not the electron would be transmitted into the stream in the ordinary diode becomes a function of the initial transverse velocity in the crossed-field diode.

Therefore, instead of one integral equation to solve, there is an infinite number of simultaneous integral equations, each integral term representing the effect of a class of compensating charge, on one transverse velocity class of critical charge. Van Duzer and Whinnery (1961) have set up these equations and evaluated the coefficients and integral kernels for the case of the infinitely spaced diode, with no portion of the beam re-entering the cathode-critical plane space. They further assumed the parabolic approximation to the potential distribution given in (1).

To reduce the infinite set of coupled integral equations to a tractable number, Van Duzer and Whinnery considered first two transverse velocity classes, each with plus or minus the average velocity of electrons traveling in one transverse direction, and then four transverse classes. They treated the crossed-field case as a perturbation on the ordinary diode solution. For a magnetic field of 100 gauss, approximately $0.75 B_c$, (B_c is the field necessary to just cause electrons to graze the anode of the diode), they found very little change in $\Delta I(t)$ due to the crossed magnetic field.

Although the original intention of the present study was to extend the Van Duzer-Whinnery work to higher magnetic fields and to remove some of the other limiting approximations, it was felt that the problem could best be treated in other ways. Extending this approximate analysis for the crossed-field diode would lead to more involved numerical calculations, and the simplicity of the

physical picture would be sacrificed. Instead, further treatment of the crossed-field problem was handled using the Monte Carlo method and fluctuation transformation equations. These will be discussed in following sections. However, in the process of investigating the approximate analysis of the ordinary potential minimum, additions were made to Whinnery's theory, and noise spectra were computed over a wider range of parameters than had been possible previously using hand calculations alone. The remaining part of this chapter will discuss the extension of Whinnery's analysis of the ordinary potential minimum at high frequencies.

II. 4. Normalization and Transformation

At this point it is convenient to introduce the normalizations used by Whinnery (1954). The $V_o(x)$ potential distribution is replaced by the $\eta(\xi)$ function of Langmuir (1923), and this well-known function is used to calculate the charge trajectories. Thus:

$$\eta(\xi) = \frac{V_o(x) - V_o(x_m)}{V_e},$$

$$\xi = \frac{2\omega_{pm}}{(2\eta V_e)^{1/2}} (x - x_m), \quad (1)$$

and

$$\tau = 2\omega_{pm} t,$$

where

$$V_e = kT_c/e,$$

$$\omega_{pm}^2 = \left[\frac{\pi \eta}{2V_e} \right]^{1/2} \frac{|J_o|}{\epsilon_o},$$

and

e = electronic charge magnitude

m = electronic mass

k = Boltzmann's constant

J_o = anode current density

$V_o(x)$ = diode potential as a function of position, x

x_m = position of static potential minimum

ω_{pm} = plasma radian frequency at x_m

If v_0 and v_1 are the emission velocities of the perturbing and critical charges, respectively, we can define the normalized distance-time functions as

$$\begin{aligned}\tau_0 &= \int_{\xi_k}^{\xi} [\eta(\xi) + \eta_0]^{-1/2} d\xi, \quad \xi_k < \xi < 0; \quad \eta_0 = \frac{v_0^2/2\eta + V_0(x_m)}{V_e} \\ \tau_2 &= \int_0^{\xi} [\eta(\xi) + \eta_1]^{-1/2} d\xi, \quad \xi > 0; \quad \eta_1 = \frac{v_1^2/2\eta + V_0(x_m)}{V_e} \\ \tau_1 &= \int_{\xi}^0 [\eta(\xi) + \eta_1]^{-1/2} d\xi, \quad \xi_k < \xi < 0\end{aligned}\quad (2)$$

where $\xi_k = \xi$ at $x = 0$.

Using the definition of x'_c ,

$$\begin{aligned}\xi_c(\tau) &= -\xi_c(\tau), \quad \eta_0 > \eta_1 \\ &= \xi_c(\tau) - \xi_k, \quad \eta_1 > \eta_0\end{aligned}\quad (3)$$

Figure II.4-1 shows typical curves of the crossover function. These are derived from trajectories like those shown in Figure B.1 of Appendix B. Note that the time τ is measured from the time the first critical electron arrives at the potential minimum, i. e., the first flow of compensation current, and that the perturbing charge may arrive at the minimum at some later time for $\eta_1 > \eta_0$ or it may be returned to the cathode if $\eta_0 < 0$.

With $j(\tau) = \frac{\Delta I}{2\omega_{pm}\Delta q}$, Equation II.2(7) becomes

$$j(\tau) = \frac{1}{2\sqrt{\pi}} \left[\xi_c(\tau) + \int_0^{\tau} j(\tau') \xi_1 \left(\frac{\tau - \tau'}{2} \right) d\tau' \right] \quad (4)$$

for the infinite spaced diode.

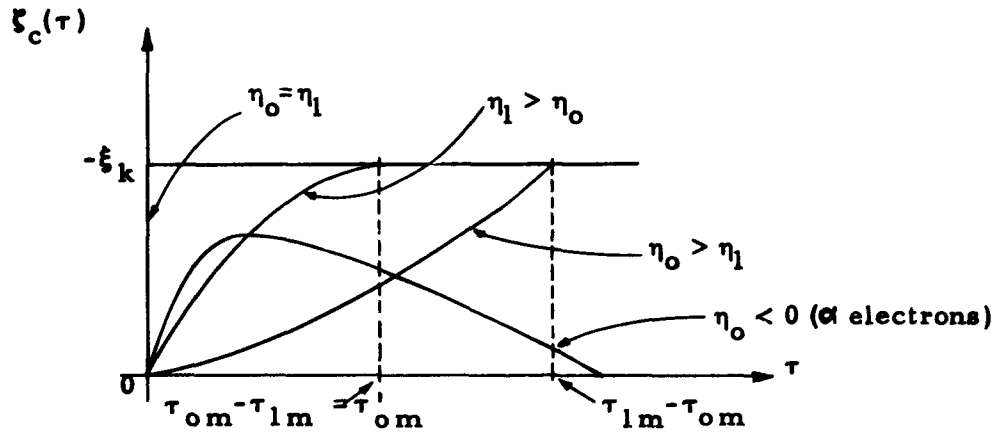


Figure II.4-1. Typical curves of $\xi_c(\tau)$

This expression can be readily transformed to the frequency domain:

$$g_{\infty}(a) = \frac{1}{2\sqrt{\pi}} [g_{0\infty}(a) - 2\pi g_{\infty}(a) g_{1\infty}(a)] \quad (5)$$

or

$$g_{\infty}(a) = \frac{1}{2\pi} \left[\frac{\sqrt{\pi} g_{0\infty}(a)}{1 + \sqrt{\pi} g_{1\infty}(a)} \right], \quad (6)$$

with

$$g_{\infty}(a) = \frac{1}{2\pi} \int_0^{\infty} j(\tau) e^{-ja\tau} d\tau, \quad (7)$$

$$g_{0\infty}(a) = \frac{1}{2\pi} \int_0^{\infty} \xi_c(\tau) e^{-ja\tau} d\tau, \quad (8)$$

$$g_{1\infty}(a) = \frac{1}{2\pi} \int_0^{\infty} -\xi_1\left(\frac{\tau}{2}\right) e^{-ja\tau} d\tau, \quad (9)$$

and $a = \omega/2\omega_{pm}$, the normalized frequency.

II. 5. The Diode of Finite Spacing

With an anode located at a finite distance from the potential minimum the analysis must be modified to consider the fields now existing between charges and the anode. A charge Δq at position x' in a diode of spacing d produces a field at x ,

$$\begin{aligned}\Delta \mathcal{E}(x) &= - \frac{\Delta q}{\epsilon_0} \left(1 - \frac{x'}{d}\right), \quad 0 < x < x' \\ &= \frac{\Delta q x'}{\epsilon_0 d}, \quad x' < x < d.\end{aligned}\tag{1}$$

The field of the perturbing charge is evaluated with $x' = x_0(t)$, the perturbing charge trajectory. The compensating fields are found using $x' = x_1(t)$ and $x' = x_2(t)$, where $x_1(t)$ and $x_2(t)$ have the same meaning as before.

We must now add the terms of $\Delta \mathcal{E}(x)$ that became zero when d was infinite. By integrating II. 5(1) between the proper limits, the potential change due to the perturbing and compensating charges can be found. Under the assumption that $x_m < d$, the normalized integral equation for current for the finite spaced diode can be evaluated as before, yielding

$$j(\tau) = \frac{1}{2\sqrt{\pi}} \left[h_0(\tau) - \int_0^\tau j(\tau') h_1(\tau - \tau') d\tau' \right] \tag{2}$$

$$h_0(\tau) = \xi_c(\tau) - \int_{\xi_k}^0 \frac{\xi_0[\tau - \tau_1(\xi)]}{\xi_d} d\xi \tag{3}$$

$$h_1(\tau) = -\xi_1\left(\frac{\tau}{2}\right) + \frac{1}{\xi_d} \int_0^{\xi_1(\tau)} \{ \xi_2[\tau - \tau_1(\xi)] - \xi_1[\tau - \tau_1(\xi)] \} d\xi \tag{4}$$

The quantities ξ_0 , ξ_1 , and ξ_2 are the inverse functions of τ_0 , τ_1 , and τ_2 . The reader may find additional details in Whinnery's original analysis.

The integral equation II. 5(2) can be readily Fourier-transformed. It can be written in a form containing $g_{0\infty}(a)$ and $g_{1\infty}(a)$, the transforms of $h_0(\tau)$ and $h_1(\tau)$ for the infinite diode case (where the integrals in II. 5(3) and II. 5(4) vanish). Adding $g_p(a)$, the spectrum of the perturbing current, to $g(a)$ and normalizing to $g_p(a)$, the resulting expression for the noise power reduction factor for perturbing electrons flowing past the minimum ($\eta_0 > 0$) is

$$|\tau_\beta|^2 = \left| \frac{1 + \sqrt{\pi} [g_{1\infty} - g_{0\infty} e^{+ja\tau_{0'm}}]}{1 + \sqrt{\pi} [g_{1\infty} - F(a\tau_d)]} \right|^2. \quad (5)$$

The intermediate steps are presented in Appendix A.

Here $\tau_{0'm}$ is the difference between the perturbing and critical charge transit times to the minimum for $\eta_1 > \eta_0$ and is zero for $\eta_0 \geq \eta_1$, and

$$F(a\tau_d) = -\frac{1}{2\pi} \int_0^{\tau_d} e^{-ja\tau} [\xi_k \left(\frac{\tau}{\tau_d}\right)^3 + b_3 \left(\frac{\tau}{\tau_d}\right)^2 - c_3 \left(\frac{\tau}{\tau_d}\right) + d_3] d\tau - (\xi_k/2\pi ja) e^{-ja\tau_d}. \quad (6)$$

The terms b_3 , c_3 , and d_3 are integrals defined in Appendix A, and τ_d is the transit time from the minimum to the anode.

For the case of " α " electrons, those returned to the cathode, we obtain the same expressions for $j(\tau)$ and $h_1(\tau)$ as in II. 5(2) and II. 5(4), but the integral in II. 5(3) for $h_0(\tau)$ is now negligible, since $x_0 < x_m < d$. Therefore, there is no correction to $g_0(a)$ with this approximation, and no contribution from the perturbing charge itself. It is still convenient to refer to the same base as for β electrons, so

$$|r_{\alpha}|^2 = \pi \left| \frac{g_{00}(a)}{1 + \sqrt{\pi} [g_{10}(a) - F(a\tau_d)]} \right|^2 \quad (7)$$

For comparison, the reduction factor can be developed directly in the frequency domain. If we define $i_0(0)$ as the perturbing current (per unit area) leaving the cathode, and $-i_r(x_m)$ as the compensation current flowing from the minimum, the charge density on the anode and cathode sides of the minimum can be evaluated in terms of these currents as

$$\Delta q = \frac{i_0(0)}{v_0(x')} e^{-j\omega t_0(x')} - \frac{i_r(x_m)}{v_2(x')} e^{-j\omega t_2(x')}, \quad x_m < x' < d \quad (8)$$

$$\Delta q = \frac{i_0(0)}{v_0(x')} e^{-j\omega t_0(x')} + \frac{i_r(x_m)}{v_1(x')} e^{-j\omega t_1(x')}, \quad 0 < x' < x_m.$$

The electric field can be evaluated from the charge density using II.5(1), and this can be integrated as before to obtain an "integrated potential" on the critical electrons. Relating this to the compensation current through the slope of the Maxwellian distribution, and defining

$$r_{\beta} = \frac{-i_r(x_m) + i_0(0) e^{-j\omega t_0(x_m)}}{i_0(0) e^{-j\omega t_0(x_m)}}, \quad (9)$$

we finally obtain in normalized form (see Appendix B and Whinnery's analysis for further details):

$$|r_{\beta}|^2 = \left| \frac{1 + \sqrt{\pi} [g_{10} - g_{00} e^{ja\tau'_{om}}]}{1 + \sqrt{\pi} [g_{10} - F(a\tau_d)]} \right|^2 \quad (10)$$

where now

$$F(a\tau_d) = e^{-ja\tau_d} \left[\frac{3j}{a\tau_d} + \frac{6}{(a\tau_d)^2} \right] \left[\frac{1}{2\pi ja} \int_{\xi_k}^0 e^{-ja\tau_1} d\xi \right]. \quad (11)$$

Expanding $\exp [-ja\tau_1]$ in a power series and retaining terms up to second order in $1/a\tau_d$, it can be shown that this last expression for F is exactly the same as the one obtained by evaluating II. 5(6) in the time-domain analysis. Thus the complete equivalence of the two expressions for the reduction factor is proven. The corresponding expressions in Whinnery's work are equivalent only for $\eta_0 > \eta_1$, because of the incomplete treatment of the τ'_{om} terms.

II. 6. Computation and Results

The expressions II. 5(5), (7), and (11) were numerically evaluated with the help of a Bendix G-15 and an IBM 704 computer. A combination of linear and exponential approximations to the trajectories (calculated from the dc potential distribution) and the crossover curves derived from them were used to obtain simplified expressions for $g_{1\infty}$, $g_{0\infty}$, and $F(a\tau_d)$. Appendix C gives the approximations and numerical values used. The approximations are the same ones used by Whinnery, except that additional ones for $\eta_1 \neq \eta_0$ have been developed.

The numerical values of the constants were chosen for comparison with the Tien-Moshman (1956) Monte Carlo analysis, as this appeared to be the most complete analysis available for the short-circuited diode at the time. A ratio of saturation to anode current density of 5 was used, for which the normalized energy at the cathode, η_k , equals 1.609. Computation was carried out for five values of η_1 . Because of the agreement with the Tien-Moshman work that Whinnery found using $\eta_1=1$, this value was chosen. In the analysis of the open-circuited diode by Siegman and Watkins (1957b) this value was also found to give the same general agreement. An estimate, using the Monte Carlo results, of the energy added to a critical electron by the fluctuations of the potential minimum is

described in Appendix F. This estimate suggests that a value of η_1 between 0.001 and 0.125 would be more suitable. Therefore, for the present calculation, values for η_1 of 0.01, 0.125, and 1.00 were used, as well as intermediate values of 0.25 and 0.50.

Values for η_0 were chosen to cover the complete range of emitted energies. In addition to the same five values used for η_1 , eight negative values were used to cover the "α" electrons, with η_0 between zero and $-\eta_k$. Table II. 6-1 shows the values used, as well as the fraction of emitted current represented by each value for use in obtaining a weighted reduction factor,

$$R^2(a, \eta_1) = \int_{-\eta_k}^{\infty} e^{-\eta_0} |r(a, \eta_1, \eta_0)|^2 d\eta_0$$

$$\approx \sum_{i=1}^{13} W(\eta_{0i}) |r(a, \eta_1, \eta_{0i})|^2. \quad (1)$$

η_{0i}	$W(\eta_{0i})$	
-1.50	0.945	} $\sum W_i = 4.0$
-1.30	0.735	
-1.10	0.602	
-0.90	0.492	
-0.70	0.404	
-0.50	0.330	
-0.30	0.271	
-0.10	0.221	
0.01	0.049	} $\sum W_i = 1.0$
0.125	0.133	
0.25	0.148	
0.50	0.264	
1.00	0.407	

(These classes also represent η_1)

Table II. 6-1. Classes of η_0 and weights

Figure II. 6-1 compares the Tien-Moshman results with R^2 computed for the representative values of η_1 equal to 0.01, 0.125 and 1.00. The quantity, τ_d was made equal to 11.5, the value corresponding to the average transit time from the minimum to the anode found by Tien and Moshman. The plasma frequency at

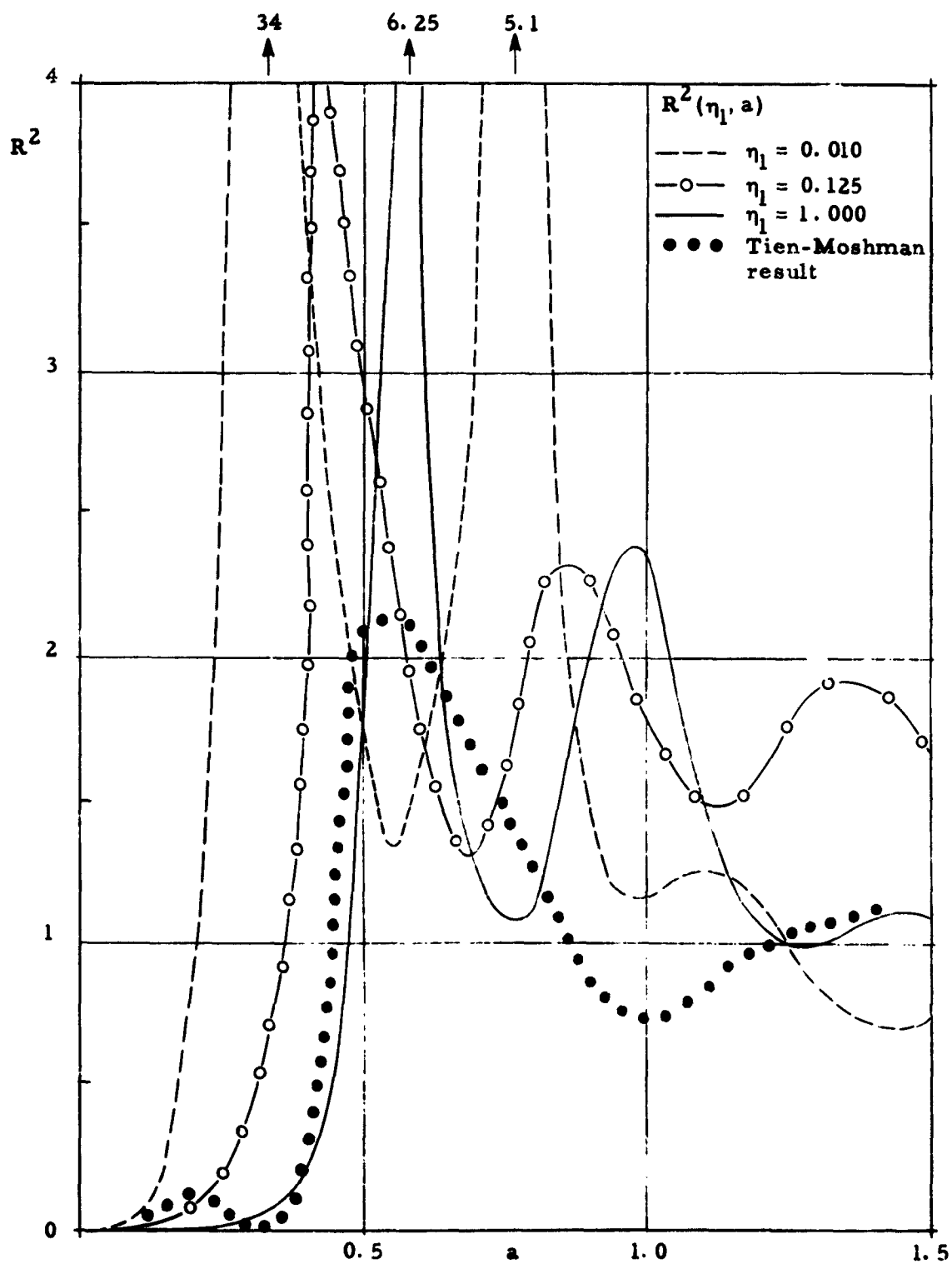


Figure II.6-1. Variation of R^2 with η_1

the minimum is located at $a = 0.5$. The location and amplitude of each maximum and minimum are clearly dependent on the value given to η_1 .

The effect of τ_d on the spectrum was investigated by computing the reduction factor for a single η_0, η_1 class ($\eta_0 = \eta_1 = 0.125$) for τ_d equal to 7.0, 10.0, and 11.5. The results, shown in Figure II. 6-2, indicate that the first, or main noise peak, is not drastically affected by τ_d , but is mainly a function of τ_{lm} . The other peaks and dips depend more on τ_d , and are nearly the zeros and poles of the denominator of II. 5(5) and (6), as the numerators are more slowly varying functions of a .

The strong dependence of the reduction factor on τ_d led to speculation that the approximations leading to II. 5(11) might not yield sufficiently accurate results. Therefore, the questionable terms were integrated numerically (see B-2) and (B-3) for these terms) with the values of $\xi(\tau)$ again obtained from the dc potential distribution, including the effect of the initial velocity at the minimum.

Figure II. 6-3 shows the effect of this more accurately computed $F(a\tau_d)$ and compares the resulting spectrum with that obtained from the approximate expression. Both cases have $\eta_0 = \eta_1 = 1.0$ and $\tau_d = 11.5$. Except for the difference at large values of a , the spectra are nearly identical. It therefore appears that the approximate form of $F(a\tau_d)$ is adequate.

II. 7. Discussion

The extension of Whinnery's formulation to include both α and β classes of electrons, and the many more values of η_1 and η_0 used in the calculations permit a more complete picture of the potential minimum behavior than was possible before. However, it is still difficult to choose parameters for the computations that allow close agreement with previous theories, if this is deemed desirable. The following conclusions and comparisons with the Tien-Moshman results may be drawn:

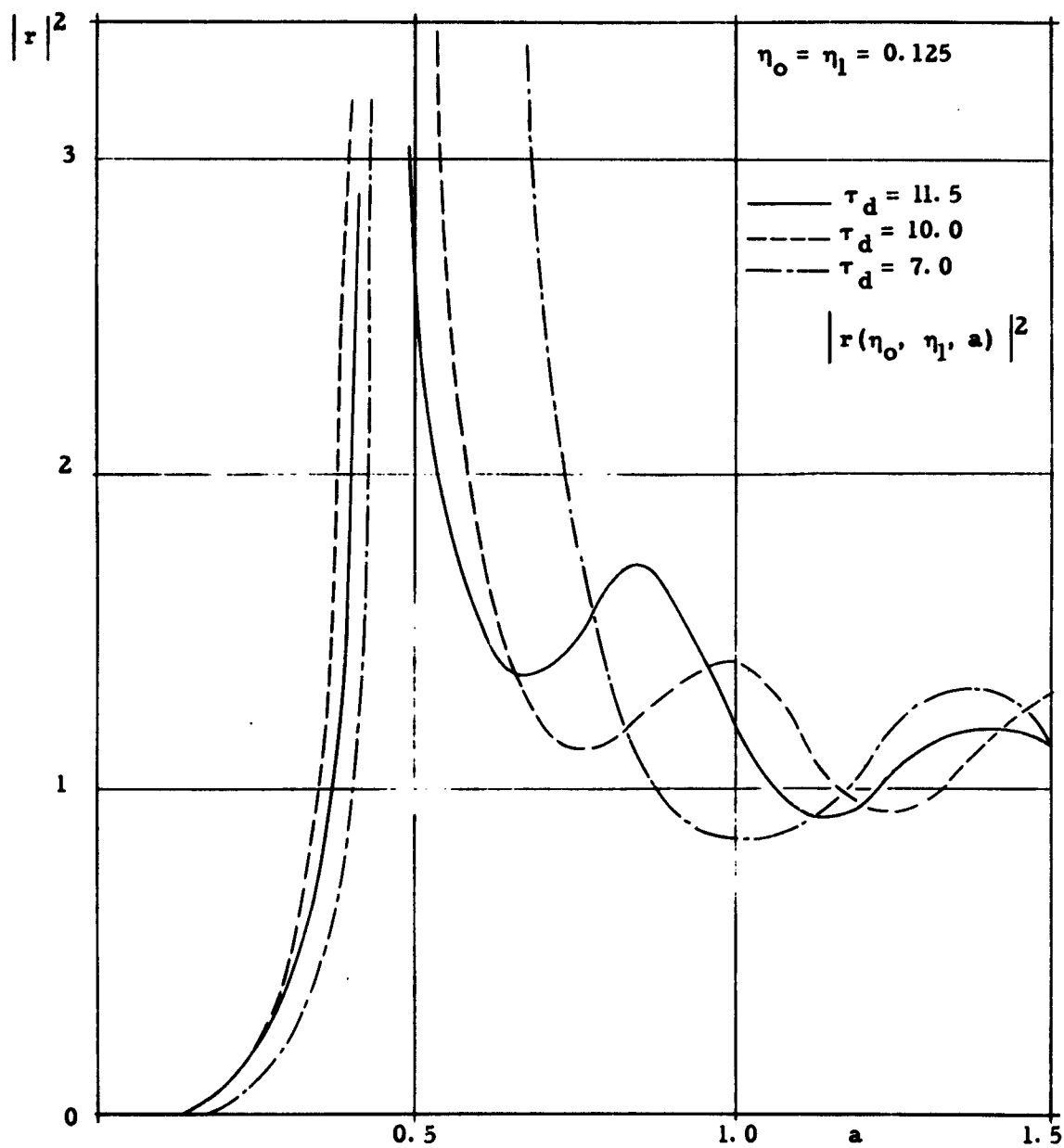


Figure II. 6-2. Variation of $|r|^2$ with τ_d

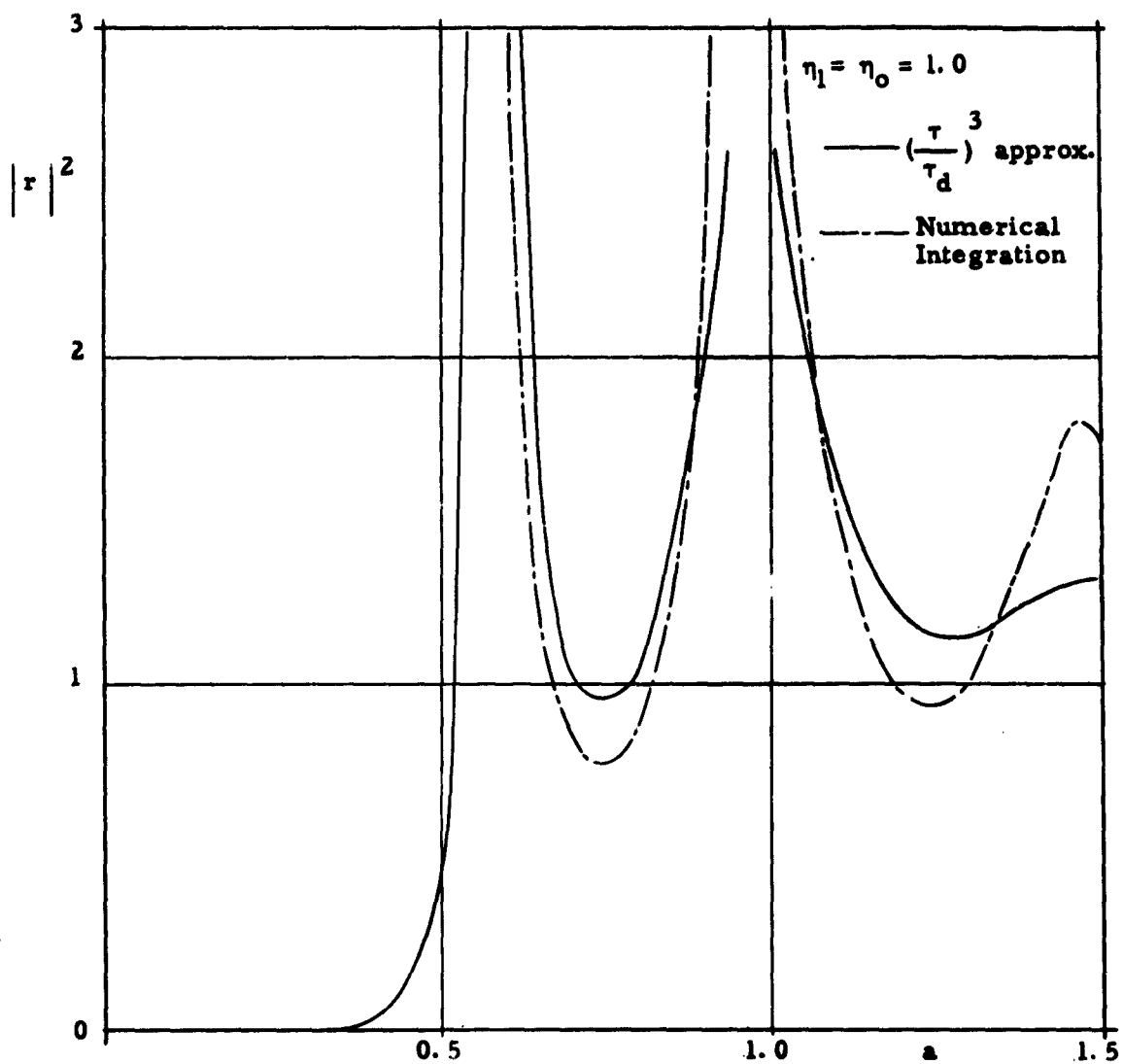


Figure II. 6-3. Effect of more accurate finite spacing factor on $|r|^2$

a. The large peak of noise current predicted by the Tien-Moshman study to occur near the plasma frequency at the potential minimum is present in this analysis. Its location is strictly dependent on the transit time of charges from the cathode to the minimum. It can be shown that the predicted feedback period is on the order of the plasma period at the minimum (Whinnery, 1955). However, the plasma period has less physical significance than the transit time, as is clearly seen in the analysis.

b. None of the reduction factor curves show a "Tien dip" below $a = 0.5$, where the Tien-Moshman study shows a first dip in the noise current spectrum, although the noise power is small there as it should be at low frequencies. The dip reported in Whinnery's paper was due to an inaccuracy in hand computation. The existence of the dip will be considered in a later section.

c. The peaks and dips calculated by Tien and Moshman above $a = 0.5$ are also found in this analysis. They are attributed to the location of an anode at a finite distance from the cathode, short-circuited to it for ac fields. The detailed behavior of the spectrum is dependent on the potential minimum-anode transit time.

d. The inclusion in the problem of the class of electrons returned to the cathode modifies the results only in a limited way for the parameters chosen. It mainly modifies the amplitude of the main noise peak, as the locations of the peaks and dips depend almost entirely on η_1 , and little on η_0 . Their inclusion in the analysis is generally desirable, as is the weighting over a wide range of η_0 , as was done here.

Comparison of any of the curves of $R^2(a, \eta_1)$ with the Tien-Moshman result shows general agreement in order of magnitude only. An average of $R^2(a, \eta_1)$ over the five chosen classes of η_1 weighted according to the Maxwellian distribution was used to obtain Figure II. 7-1. There still does not appear to be any close agreement with the Tien-Moshman result. However, had more classes of η_1 been used, the resulting weighted average curve would lose much of its peaked nature, and better agreement could no doubt be obtained.

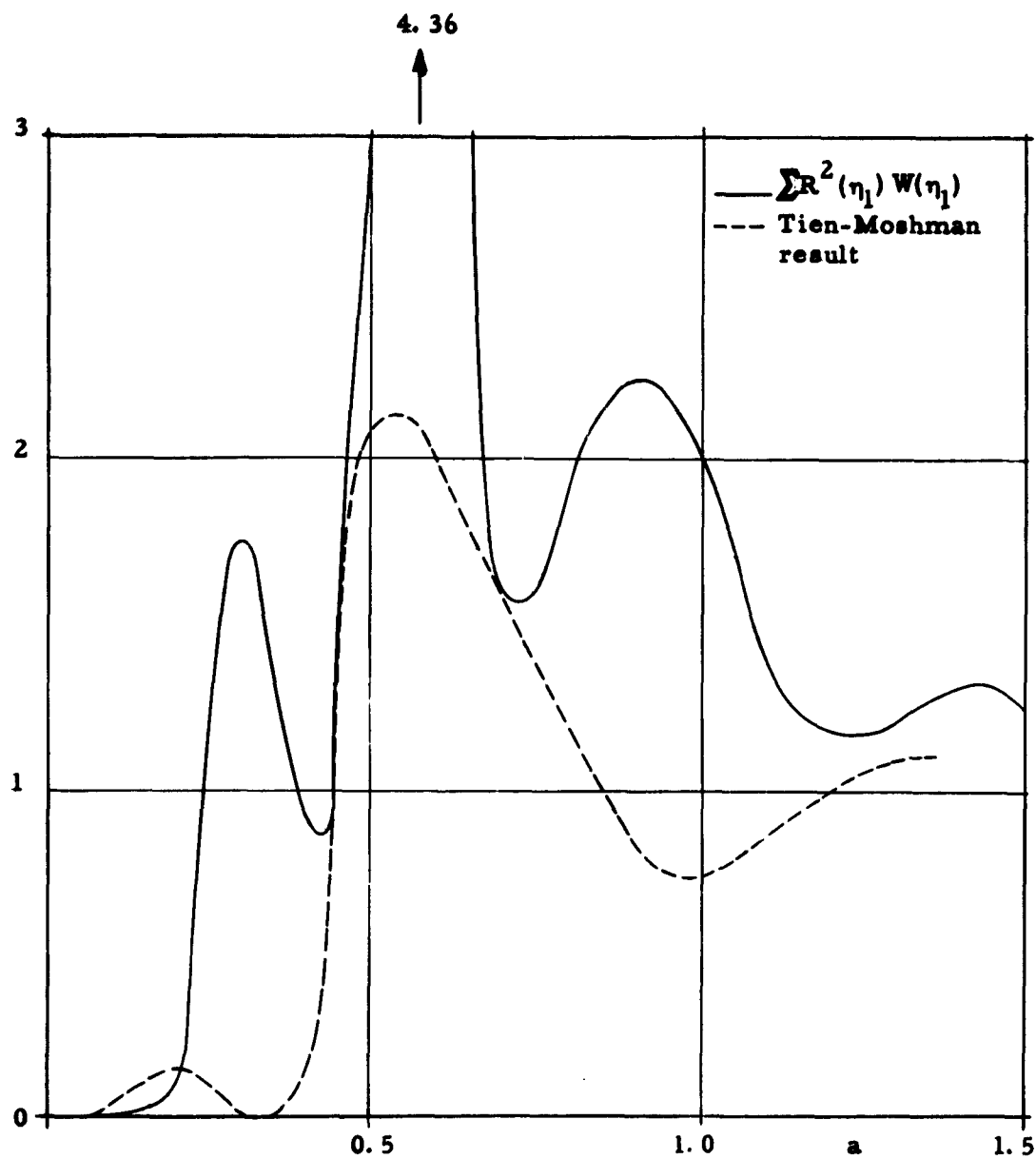


Figure II. 7-1. Comparison of weighted R^2 with the Tien-Moshman result

After describing the Monte Carlo study of the crossed-field diode, we will return to the question of the noise current at the potential minimum. Additional conclusions can then be drawn for the "O" type beam and comparisons made with the Monte Carlo results and the results of other studies.

III. SINGLE VELOCITY MODEL OF THE ACCELERATING REGION

III. 1. The Single Velocity Approach to Electron Beams

Noise propagation in the low velocity region should be described by a thorough analysis taking into account the multi-velocity nature of the electron flow. Such an analysis has not been particularly amenable to closed form analytic solutions. The Monte Carlo technique, described in succeeding chapters, is a more exact theory of the low velocity region, but its results cannot be described in a form in which the effect of each parameter is immediately evident. It is of considerable value to develop a satisfactory, if more approximate theory, that can be described by a system of transformation equations.

By eliminating the multivelocitv aspect of the problem, a relatively simple closed-form solution can be found. In place of the velocity distribution in the stream at every point, a single velocity is chosen. The well-known Llewellyn-Peterson (1941, 1944) system of equations is an example of the single velocity approach to the propagation of fluctuations in the one-dimensional "O"-type stream. These equations, derived using the small-signal assumption, relate fluctuations in convection current and velocity at an entrance plane to the corresponding quantities at an exit plane. The total current in the enclosed region, the potential difference between the planes, and the dc beam quantities also enter into the transformation.

The Llewellyn-Peterson (L-P) analysis assumes uniform, planar flow between the entrance and exit planes. By differentiating the force equation, a relation between the rate of change of the acceleration and the total current is obtained. This is possible

because of the one-dimensional nature of the electric field. By integrating between an entrance time and a general time t , relations for acceleration and velocity can be found. If these are now split into dc and ac parts, the ac transit time Δt can be determined from the requirement that the distance between entrance and exit planes does not fluctuate. The ac fluctuations of the other quantities are obtained using Δt .

Rack (1938) made use of the L-P equations to evaluate the effect of transit time on shot noise in the space-charge-limited diode. By using the potential minimum as the input plane, Rack arrived at the same low frequency limit for the space-charge smoothing of shot noise as was derived by North, et al, (1940) in the limit of large anode voltages, using a more rigorous and detailed analysis of the cathode-potential minimum region. Others have predicted the behavior of multi-electrode and beam type tubes by means of these equations. Cutler and Quate (1950), by measuring the noise in an electron beam with a moving cavity, showed the validity of the L-P transformation from the potential minimum input plane to an exit plane located a large transit angle away. Yadavalli (1953) verified the medium transit angle validity of the current coefficients in the L-P approach to the space-charge-limited diode. Thus the L-P transformation equations have gained wide acceptance for the treatment of noise problems in the "O" type electron beams.

The use of the potential minimum as an input plane has been shown to be a good approximation in many cases, despite the still multi-velocity nature of the flow there. However, the use of the L-P equations in this region should not be indiscriminate, as large errors can result under certain conditions. In a later section, the range of validity of the single velocity theory will be discussed. The effects of neglecting the initial velocities will also be seen to produce certain irregularities in the transformation coefficients. This is not a new result, but has often been ignored by others in their use of these equations.

III. 2. The Single Velocity Approach to Crossed-Field Beams

Van Duzer (1961) analyzed the one-dimensional crossed-field diode by means of the single-velocity assumption. He obtained a transformation similar to the smaller set of L-P equations, but included the effects of the dc transverse magnetic field.

The diode, Van Duzer assumed, is infinite in the transverse plane (y, z) and has an anode spaced a finite distance normal to the cathode in the x direction. Figure III.2-1 shows the coordinate system of the diode. No spatial variations are permitted in the y, z plane. Although this one-dimensional model is quite common in the study of "O"-type beams, its use in crossed-field beams is limited. In a crossed-field gun of simple geometry, static transverse space charge forces, dependent on transverse position, act in addition to the magnetic forces on the electrons. However, by a suitable arrangement of electrode shapes and potentials, as derived analytically by Kino (1960), guns can be designed to produce beams with zero dc electric field in the z direction. Thus the dc model has some physical significance.

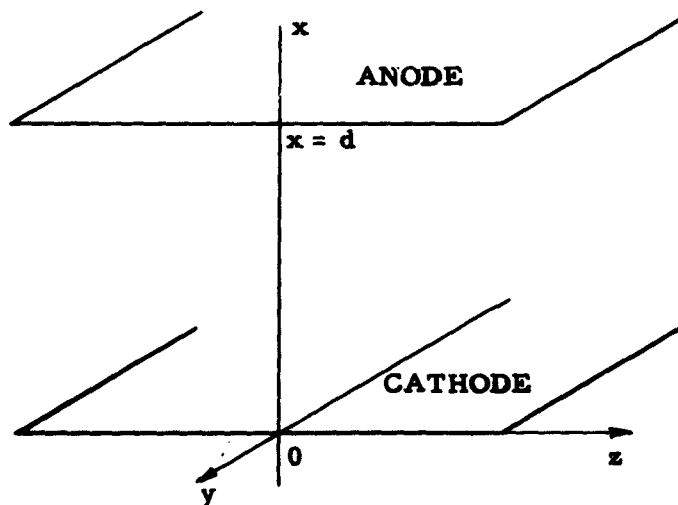


Figure III.2-1. The coordinate system for the model

Van Duzer (1960) has shown that the ac z-directed force for a typical diode is predominantly due to the x-directed velocity fluctuations coupling with the dc magnetic field. The forces due to the ac z-directed current and electric field are of lesser importance. Thus, by retaining motion in the x and z directions and ac x- and z-directed forces due to both components of velocity, the planar model may be used to closely approximate the true ac behavior of the diode. Even if the exact conditions for the neglect of all the z-directed forces except the $\bar{\mathbf{v}} \times \bar{\mathbf{B}}$ force are not satisfied, this assumption may still give a good approximation at the interior of the beam, where little transverse change in the quantities can be expected.

The Van Duzer analysis further assumes that the magnetic field is constant and uniform and that the frequency of interest is low enough to permit the use of Poisson's equation for the electric field (zero ac magnetic field). The system is assumed linear and the fluctuating quantities small compared with the average values. Although it is possible to treat the case of a diode with a general external impedance by means of the transformation equations, choice of a diode either short- or open-circuited to ac fields permits a major simplification of the problem. The exact load impedance for an electron beam is rarely known, so it seems satisfactory to consider these two extreme cases. Although a short-circuit model appears less difficult to produce in practice, both models will be used for the crossed-field diode. For diodes of large transit angle, the transformation equations should predict the same results for either assumption.

III. 3. The Fluctuation Transformation Equations

The single velocity electronic transformation equations relate fluctuations at two planes arbitrarily placed across the electron stream. If \tilde{q}_{xa} , \tilde{v}_{xa} and \tilde{v}_{za} are the complex amplitudes at a frequency ω of the ac x-directed convection current density and the ac x- and z-directed velocity at the input plane, then the corresponding quantities

at the exit plane, \tilde{q}_{xb} , \tilde{v}_{xb} , and \tilde{v}_{zb} , can be obtained in general by a system of equations of the form

$$\begin{bmatrix} \tilde{V}_d \\ \tilde{q}_{xb} \\ \tilde{v}_{xb} \\ \tilde{v}_{zb} \end{bmatrix} = \begin{bmatrix} a_{11} & a_{12} & a_{13} & a_{14} \\ a_{21} & a_{22} & a_{23} & a_{24} \\ a_{31} & a_{32} & a_{33} & a_{34} \\ a_{41} & a_{42} & a_{43} & a_{44} \end{bmatrix} \begin{bmatrix} \tilde{J}_{xd} \\ \tilde{q}_{xa} \\ \tilde{v}_{xa} \\ \tilde{v}_{za} \end{bmatrix} \quad (1)$$

\tilde{V}_d is the fluctuating voltage between planes "a" and "b," while \tilde{J}_d is the ac total x-directed current density, convection plus displacement. The coefficients a_{ij} are functions of the average beam quantities and the frequency ω . The z-directed current is not included in this transformation, as it can be obtained from the other quantities.

The Llewellyn-Peterson equations can be described by (1), with $a_{14} = a_{4j} = 0$. The coupling of z-directed velocity to the other beam quantities is clearly absent for a beam with no magnetic field component in the transverse plane. The Van Duzer analysis of the one-dimensional crossed-field beam takes into account the entire array (1), although the elements a_{42} , a_{43} , and a_{44} are zero, and a_{41} has a unit magnitude. It is this complete array that will be used in the single velocity model of the accelerating region. Wadhwa (1960) has developed another system of transformation equations for the crossed-field beam. He has considered a two-dimensional model and has thus obtained a larger array of matrix elements.

The equations (1) may be used with any arbitrary external impedance. The relation between \tilde{J}_d and \tilde{V}_d is then used to obtain five equations for the five unknowns (\tilde{J}_d and the unknown quantities on the left of (1)). However, (1) is particularly simple to solve when $\tilde{J}_d = 0$. When \tilde{J}_d is precisely zero, the diode formed between planes "a" and "b" is said to be open-circuited.

Another particularly simple case occurs when \tilde{V}_d is set to zero. The current \tilde{J}_d can then be expressed in terms of the input quantities and used to obtain a reduced set of equations for the output fluctuations. In general, \tilde{V}_d could be made a dependent variable, and the equations could be rewritten in the form

$$\begin{bmatrix} \tilde{J}_{xd} \\ \tilde{q}_{xb} \\ \tilde{v}_{xb} \\ \tilde{v}_{zb} \end{bmatrix} = \begin{bmatrix} b_{11} & b_{12} & b_{13} & b_{14} \\ b_{21} & b_{22} & b_{23} & b_{24} \\ b_{31} & b_{32} & b_{33} & b_{34} \\ b_{41} & b_{42} & b_{43} & b_{44} \end{bmatrix} \begin{bmatrix} \tilde{V}_d \\ \tilde{q}_{xa} \\ \tilde{v}_{xa} \\ \tilde{v}_{zb} \end{bmatrix} \quad (2)$$

The b_{ij} coefficients are readily written in terms of the a_{ij} coefficients, and the relations between the two sets are given in Appendix D. Appendix D also contains the complete set of coefficients a_{ij} for the general crossed-field case and the simplified set of Llewellyn-Peterson coefficients, to which the first set reduces as the magnetic field is decreased to zero.

III. 4. D. C. Conditions in the Diode

Many of the important average quantities in the stream can be determined from the average position and velocity at an arbitrary plane. When the arbitrary plane is coincidental with the exit, or "b" plane, the position and velocity become

$$x_b = v_{xa} \tau \frac{\sin \theta}{\theta} + a_{xa} \tau^2 \left(\frac{1 - \cos \theta}{\theta^2} \right) + \frac{\eta J_{xd} \tau^3}{\theta_0} \left(\frac{\theta - \sin \theta}{\theta^3} \right) \quad (1)$$

and

$$v_{xb} = v_{xa} \cos \theta + a_{xa} \tau \frac{\sin \theta}{\theta} + \frac{\eta J_{xd}}{\epsilon_0} \left(\frac{1 - \cos \theta}{\theta^2} \right) \quad (2)$$

θ is the cyclotron transit angle, a convenient measure of the magnetic field B . It equals $\omega_c \tau$, where τ is the transit time between planes $x_a = 0$ and x_b . The quantity ω_c is the cyclotron radian frequency, ηB . The average diode current density J_{xd} ,

taken only in the x direction, also appears in these equations.

Historically, the dc relations and the coefficients a_{ij} and b_{ij} have been simplified by the introduction of a space charge parameter,

$$\xi = \frac{\eta J_d \tau^2}{2 \epsilon_0 (v_a + v_b)} \quad (3)$$

into the Llewellyn-Peterson equations. For a temperature limited diode, or a space with relatively small current, ξ is taken to be very small, and is often set equal to zero as an approximation. For a space-charge-limited diode, the space between the potential minimum and anode can be approximated by an equivalent diode with a value of ξ close to unity, and often taken as that value. Rewriting the equation for v_{xb} ,

$$a_{xa} \tau = v_{xb} - v_{xa} - \frac{\eta J_d \tau^2}{2 \epsilon_0} \quad (4)$$

or

$$a_{xa} \tau = (v_{xb} - v_{xa}) - \xi (v_{xb} + v_{xa})$$

For ξ identically zero, velocity is a linear function of time, as expected. For ξ identically unity, however, (4) becomes a relation between a_{xa} and v_{xa} that is not generally true, except when a_{xa} and v_{xa} are both zero. Thus ξ may never be precisely unity. With the usual assumption that a_{xa} is zero for the space charge limited diode,

$$\xi = \frac{v_{xb} - v_{xa}}{v_{xb} + v_{xa}} \quad (5)$$

With typical emission velocities, v_{xa} is usually quite small compared with v_{xb} , and $\xi = 1$ is a good approximation. However, it can give erroneous results for many of the transformation coefficients when v_{xb} is comparable with v_{xa} , as will be shown in the following section. The quantity $\xi = 1$ then implies that v_{xa} is much smaller than v_{xb} , and it is often convenient to take v_{xa} to be exactly zero. The dc relations and the transformation coefficients then become considerably more simple.

The Van Duzer coefficients may be put into a form similar to the L-P coefficients by the introduction of a suitable ξ factor. By analogy with the $\theta = 0$ case,

$$\xi = \frac{\eta J_d \tau^2}{2\epsilon_0 (v_{xa} + v_{xb})} \frac{2(1 - \cos \theta)}{\theta^2} \quad (6)$$

For a region with zero initial acceleration, a simplifying assumption in the crossed-field case,

$$\xi = \frac{v_{xb} - \cos \theta v_{xa}}{v_{xb} + v_{xa}} \quad (7)$$

Since v_{xb} is now a function of θ , ξ is no longer constant. However, ξ may be approximated by unity if the average anode velocity with no magnetic field is much greater than v_{xa} and θ is not in the vicinity of 2π .

By assuming that a_{xa} and v_{xa} are both zero ($\xi = 1$), several interesting expressions can be found for the dc beam quantities. The expression for the dc potential across the diode is given by Van Duzer as

$$\begin{aligned} V_d = & \frac{a_{xa}^2 \tau^2}{\eta} \frac{(1 - \cos \theta)}{\theta^2} + \frac{\eta J_d^2 \tau^4}{\epsilon_0^2 \theta^4} (1 - \cos \theta + \frac{\theta^2}{2} - \theta \sin \theta) \\ & + \frac{v_{xa} a_{xa} \tau}{\eta} \frac{\sin \theta}{\theta} + \frac{J_d a_{xa} \tau^3}{\epsilon_0} \frac{(1 - \cos \theta)}{\theta^2} \\ & + \frac{J_d v_{xa} \tau^2}{\epsilon_0 \theta^2} (\cos -1 + \theta \sin \theta) + \frac{v_{za} x \theta}{\eta \tau} \end{aligned} \quad (8)$$

With a_{xa} , v_{xa} , and v_{za} set to zero, equations (1), (2), and (8) can be written (for the "b" plane a distance d from the "a" plane) as

$$v_{xb} = \frac{\eta J_d \tau}{2 \epsilon_o} \frac{2(1 - \cos \theta)}{\theta^2} \quad (9)$$

$$d = \frac{\eta J_d \tau^3}{6 \epsilon_o} \frac{6(\theta - \sin \theta)}{\theta^3} \quad (10)$$

$$V_d = \frac{\eta J_d^2 \tau^4}{\epsilon_o^2} \frac{\phi(\theta)}{\theta^4} \quad (11)$$

where $\phi(\theta) = (1 - \cos \theta + \frac{\theta^2}{2} - \theta \sin \theta)$. (12)

Combining (10) and (11), noting that $\theta = \eta B \tau$, and defining

$$B_c^2 = \frac{2 V_d}{\eta d^2}, \quad (13)$$

we obtain a relation between B and θ :

$$\left(\frac{B}{B_c}\right)^2 = \frac{(\theta - \sin \theta)^2}{2 \phi(\theta)}. \quad (14)$$

The quantity, B_c , is the field required to cause a zero initial velocity charge to just graze the "b" plane. With no magnetic field, it is well known that

$$\tau(0) = \frac{3d}{v_{xb}} \quad (15)$$

$$J_d(0) = \frac{4}{9} \frac{\epsilon_o \sqrt{2\eta} V_d^{3/2}}{d^2} \quad (16)$$

and $v_{xb}(0) = \sqrt{2\eta V_d}$. (17)

Then, by means of (9), (10), and (11),

$$\frac{\tau(\theta)}{\tau(0)} = \frac{\sqrt{2\eta} \theta \phi(\theta)^{1/2}}{3(\theta - \sin \theta)} \quad (18)$$

$$\frac{J_d(\theta)}{J_d(0)} = \frac{9}{4\sqrt{2}} \frac{(\theta - \sin \theta)^2}{\phi(\theta)^{3/2}} \quad (19)$$

and

$$\frac{v_{xb}(\theta)}{v_{xb}(0)} = \frac{1 - \cos \theta}{\sqrt{2} \phi(\theta)^{1/2}} \quad (20)$$

As a check, substitution of these values into (6) shows that ξ is independent of θ as long as v_{xa} can be neglected.

More accurate evaluation of these parameters can be made if v_{xa} is included. Figures III. 4-1a and b show θ and $J_d(\theta)/J_d(0)$ a) for the $\xi = 1$ approximation, and b) for v_{xa} included. The initial transverse velocity v_{xa} has again been assumed to be zero.

III. 5. The Effect of ξ in the Space-Charge-Limited Diode

There is a certain difficulty in interpreting the coefficients when ξ is precisely unity. This can be seen in both the L-P and Van Duzer coefficients. The L-P coefficients will be used in this discussion to eliminate the additional confusion of a variable magnetic field. Figures III. 5-1 through -4 compare the open and short circuited L-P coefficients, plotted as magnitude-squared, against the transit angle, $|\beta| = \omega\tau$, for $\xi = 1$ and

$$\xi = \frac{v_b - v_a}{v_b + v_a} = 0.84.$$

The latter value is obtained by assuming an anode potential of 10 volts and a thermal equivalent potential, kT_c/e , of 0.1 volts at the input plane. The velocity ratio can then be found from the ratio of voltages.

The open circuit coefficient $|a_{22}|^2$ has the same value for either value of ξ , as can be seen in Figure III. 5-1. At large values of $|\beta|$, $|b_{22}|^2$ approaches $|a_{22}|^2$. However, for $|\beta|$ less than 3π , there is a fundamental difference in the coefficients $|b_{22}|^2$ for the two values of ξ . For small $|\beta|$, $\xi = 1$ predicts

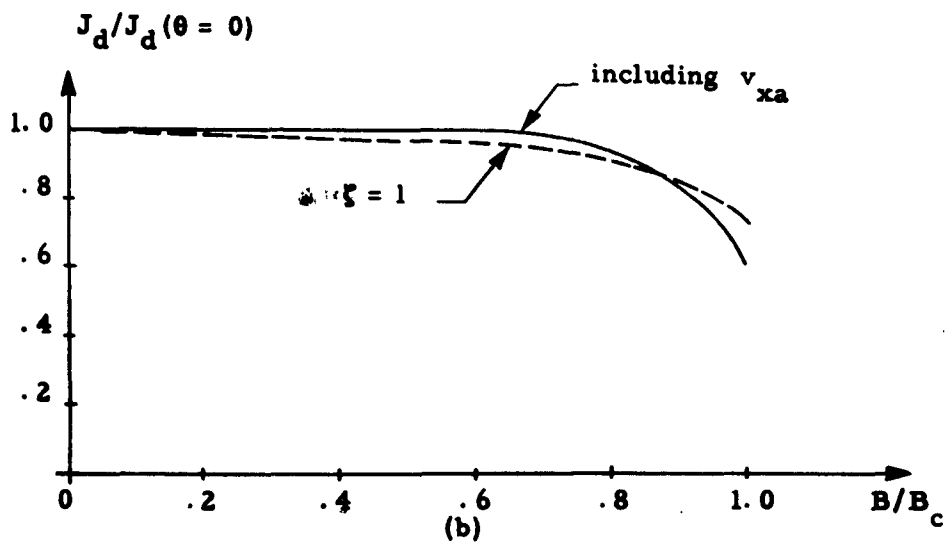
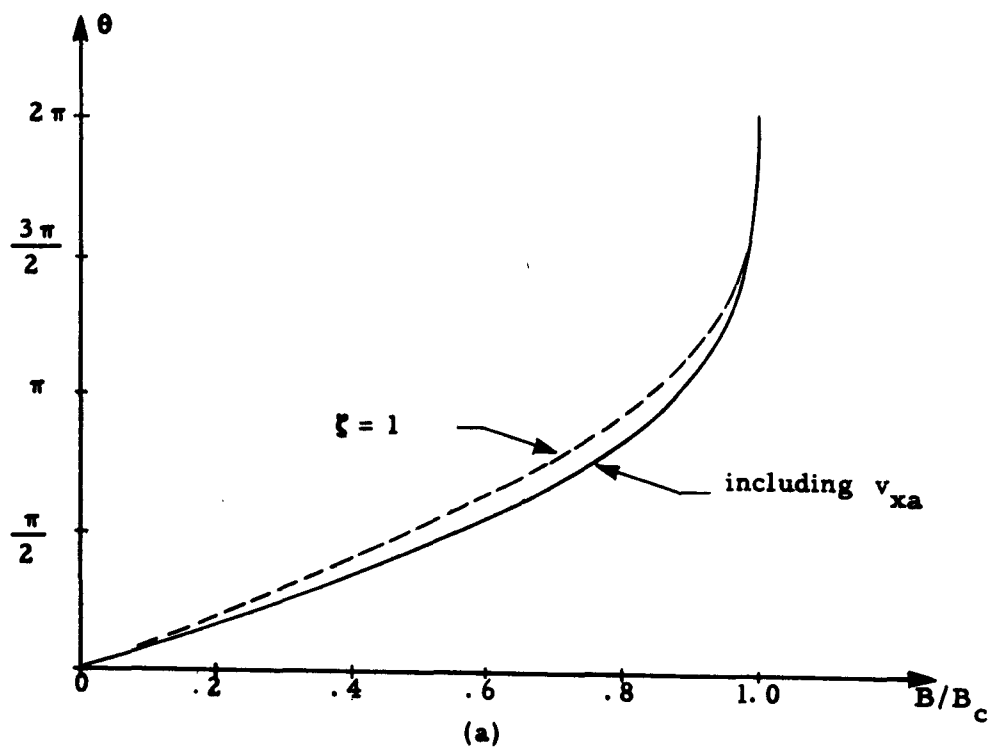


Figure III.4-1. Variation of θ and J_d with B/B_c

that the current fluctuations at the "b" plane are not at all dependent on the current fluctuations at the "a" plane. This contradicts the requirements that the ac convection current be continuous at low frequencies. For any value of ξ other than unity, however, $|b_{22}|^2$ approaches unity at low frequencies, as it should.

For $\xi = 1$, Figure III. 5-2 shows an instantaneous conversion of velocity to current fluctuations at low values of $|\beta|$. This non-physical result is again modified when ξ is given its more exact value, so that the conversion occurs gradually with increasing transit angle. The difference between the open- and short-circuit coefficients is minor for $\xi = 0.84$.

Velocity fluctuations in the open-circuited diode are independent of input current fluctuations when $\xi = 1$. In Figure III. 5-3 it is clear that these current fluctuations cause a considerable effect at small transit angles when $\xi \neq 1$. The short-circuit coefficients $|b_{32}|^2$ also differ considerably when ξ is given a more realistic value.

The transmission of velocity fluctuations $|b_{33}|^2$ for the short-circuited diode is smoothed at small $|\beta|$ (Figure III. 5-4). At larger values, an asymptotic level, equal to the coefficient for the open-circuited diode is reached. This level is lower for smaller values of ξ . As $|\beta|$ approaches zero, $|b_{33}|^2$ becomes zero, when the $\xi = 1$ model is used. When $\xi \neq 1$, $|b_{33}|^2$ approaches $(v_a/v_b)^2$, the value one obtains from simple energy considerations in the short-circuited diode.

The low frequency limits of the various coefficients are summarized in Table III. 5-1 for the two values of ξ .

Chapter II presented a theory for the fluctuations of currents at the potential minimum of a short-circuited diode. There is full shot noise at high frequencies, but smoothed shot noise currents at low frequencies. At short transit angles, the convection current fluctuations should be continuous from the potential minimum, the "a" plane, to the anode, the "b" plane. The exact L-P equations applied to the accelerating stream for $|\beta| \rightarrow 0$ only show this continuity of current, $|b_{22}|^2 = 1$.

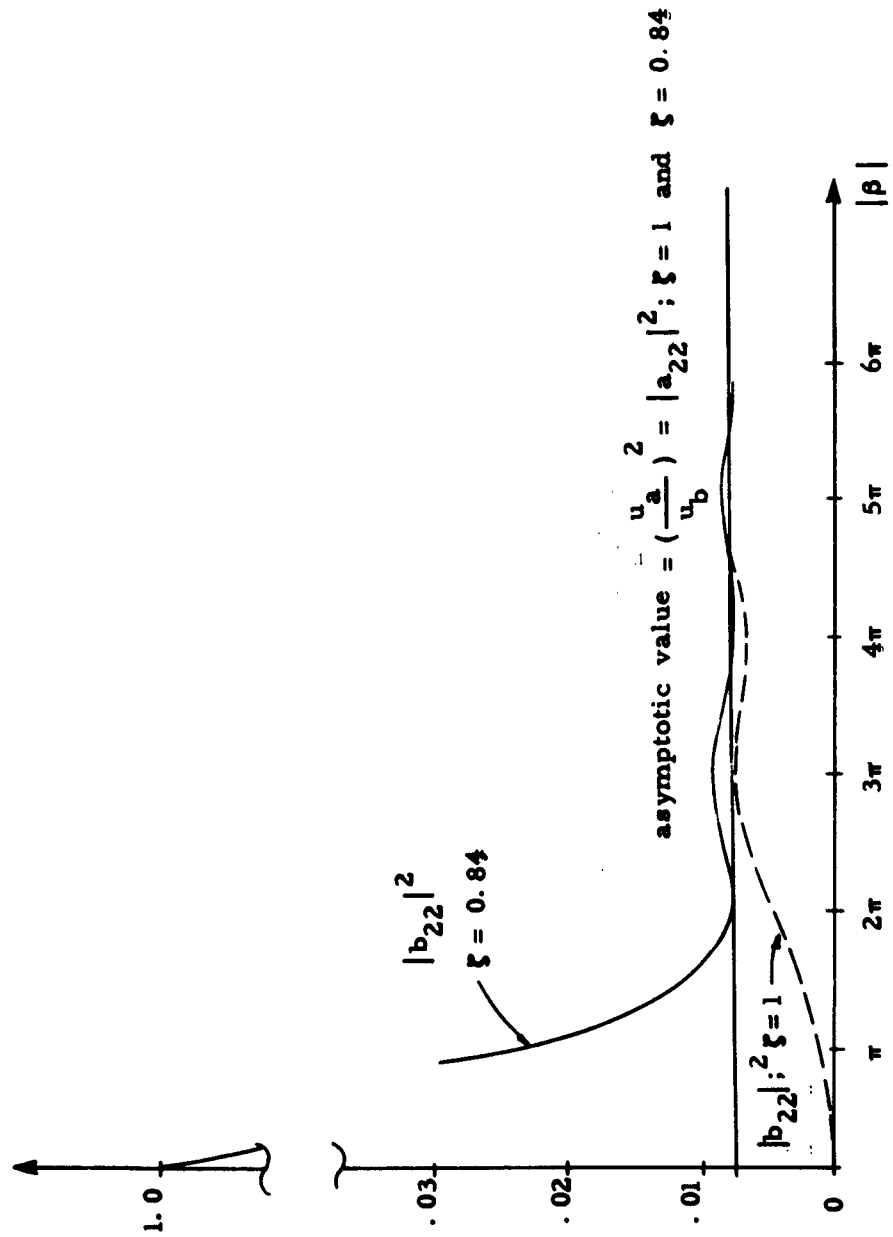


Figure III.5-1. Variation of $|a_{22}|^2$ and $|b_{22}|^2$ with $|\beta|$, $\theta = 0$

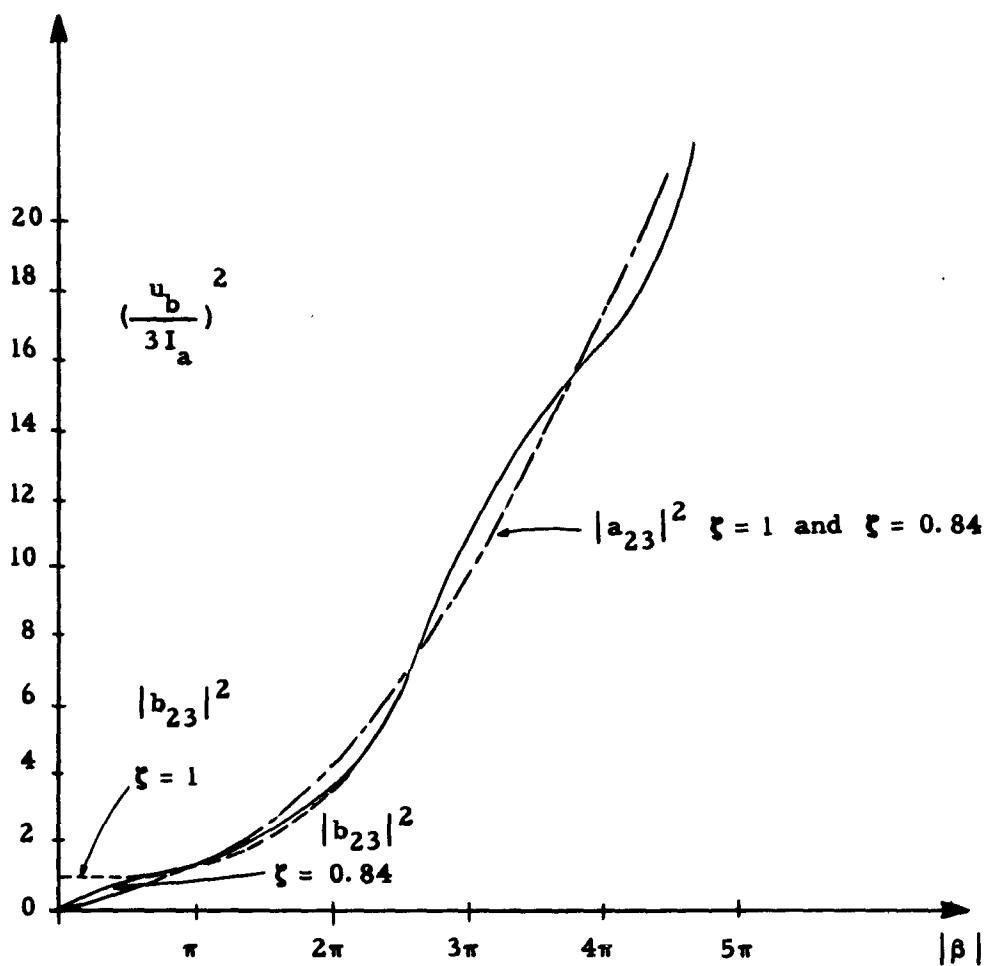


Figure III. 5-2. Variation of $|a_{23}|^2$ and $|b_{23}|^2$ with $|\beta|$, $\theta = 0$

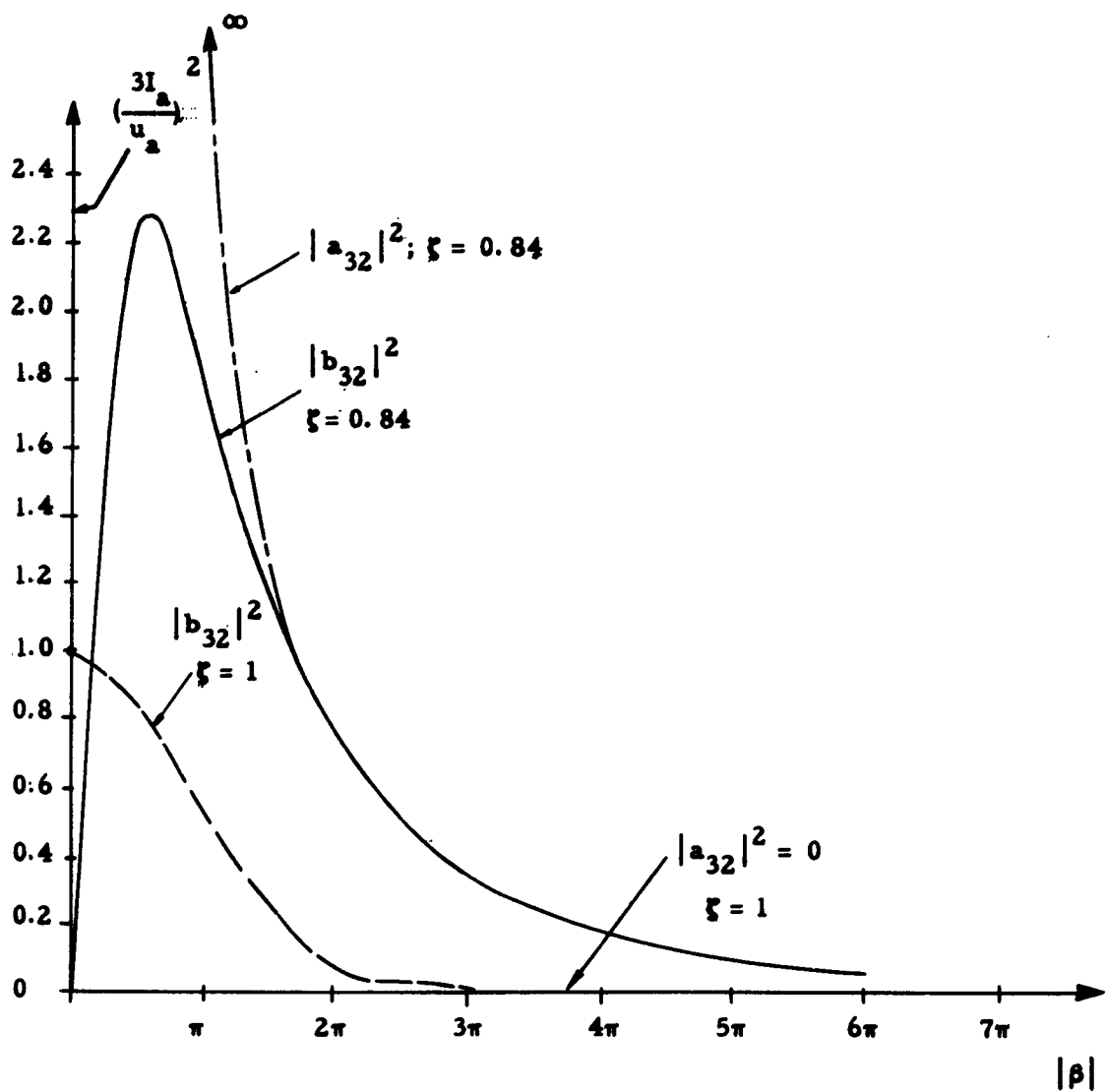
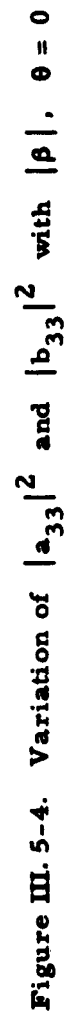


Figure III. 5-3. Variation of $|a_{32}|^2$ and $|b_{32}|^2$ with $|\beta|$, $\theta = 0$



	$\xi = 1$	$\xi = \frac{v_b - v_a}{v_b + v_a}$
$ a_{22} ^2$	$(\frac{v_a}{v_b})^2$	$(\frac{v_a}{v_b})^2$
$ a_{23} ^2$	0	0
$ a_{32} ^2$	0	$\rightarrow \infty$
$ a_{33} ^2$	1	$(\frac{2v_a - v_b}{v_b})^2$
$ b_{22} ^2$	0	1
$ b_{23} ^2$	$(\frac{v_b}{3J_d})^2$	0
$ b_{32} ^2$	$(\frac{3J_d}{v_a})^2$	0
$ b_{33} ^2$	0	$(\frac{v_a}{v_b})^2$

Table III. 5-1. Low frequency limits of L-P coefficients

Velocity fluctuations, from a quasi-static energy argument (Watkins, 1955), can be shown to remain constant at their value at the cathode, as the beam moves toward the potential minimum. This value, discussed in Section IV. 8, and first presented by Rack (1938), is

$$|\tilde{v}_R|^2 = \frac{(4 - \pi) \eta k T_c \Delta f}{I_d} \quad (1)$$

I_d is the average current in the stream.

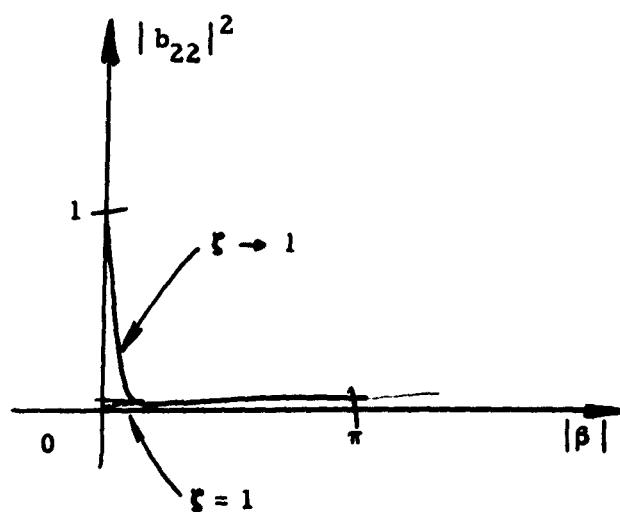
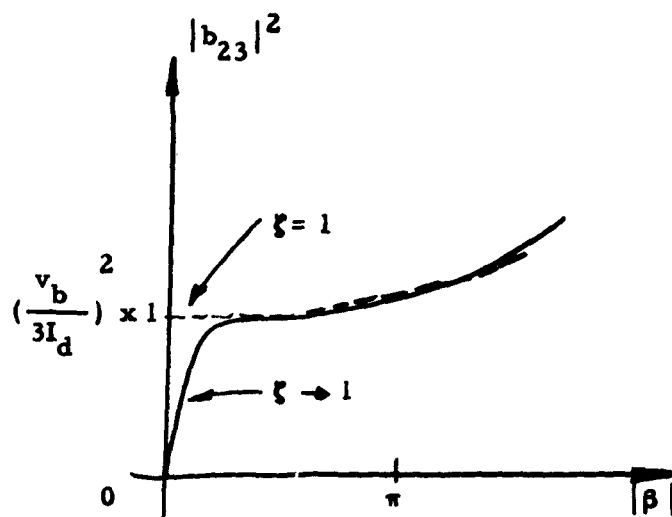


Figure III. 5-5. Dependence of $|b_{22}|^2$ and $|b_{23}|^2$ on ξ near $|\beta| = 0$

When the $\xi = 1$ coefficients are used instead of the exact coefficients,

$$|\tilde{q}_b|^2 = |b_{23}|^2 |v_R|^2 \quad (2)$$

$$= \Gamma^2 2 e I_d \Delta f \quad (3)$$

where

$$\Gamma^2 = \frac{9}{4} \frac{(4-\pi)(kT_c/e)}{(v_b + v_a)^2 / 2 \eta} \approx \frac{1.925 k T_c}{e V_d} \quad (4)$$

Since current is continuous, this is also the value of $|\tilde{q}_a|^2$, the smoothed current fluctuation at the potential minimum. The value of Γ^2 is exactly that obtained by North, et al., in their rigorous analysis, for large anode voltages. Note that we may use (2) as $|\beta| \rightarrow 0$ because the coefficients $|b_{22}|^2$ and $|b_{23}|^2$ attain their $\xi = 1$ asymptotic values at very small transit angles when v_a/v_b is small (see Figure III. 5- 7). Therefore, for small v_a/v_b , the same result can be obtained by using the $|\beta| = 0$ limit of the $\xi = 1$ coefficients as with the $|\beta|$ near zero values of the exact coefficients.

III. 6. Fluctuations in the Crossed-Field Diode

The $\xi = 1$ approximation is useful also in the crossed-field diode for the prediction of noise behavior in the small transit angle limit. When this assumption is made, the current fluctuations become dependent only on the input velocity fluctuations, as in the ordinary diode. In the crossed-field diode, however, transverse velocity fluctuations play an important role in the noise process. In analogy with III. 5(2),

$$|\tilde{q}_{xb}|^2 = |b_{23}|^2 |\tilde{v}_{xa}|^2 + |b_{24}|^2 |\tilde{v}_{za}|^2 \quad (1)$$

where $|\tilde{v}_R|^2$ is given in III. 5(1) and (Van Duzer, 1961b),

$$|\tilde{v}_{za}|^2 = \left(\frac{2}{4-\pi}\right) |\tilde{v}_R|^2 = \frac{2 \eta k T_c \Delta f}{I_d} \quad (2)$$

Using the simplified $\xi = 1$ coefficients from Appendix D and assuming a variation of v_{xb} as in III.4(18),

$$|\tilde{q}_{xb}|^2 = \Gamma^2 G(\theta) 2 e I_d \Delta f \quad (3)$$

where

$$G(\theta) = \frac{[(1 - \cos \theta)^2 + \left(\frac{2}{4-\pi}\right) (\theta - \sin \theta)^2] \phi(\theta)}{9 [2(1 - \cos \theta) - \theta \sin \theta]^2} \quad (4)$$

and Γ^2 has its $\theta = 0$ value given in III.5(4). $G(\theta)$ is plotted in Figure III.6-1. This calculation of current fluctuations at small

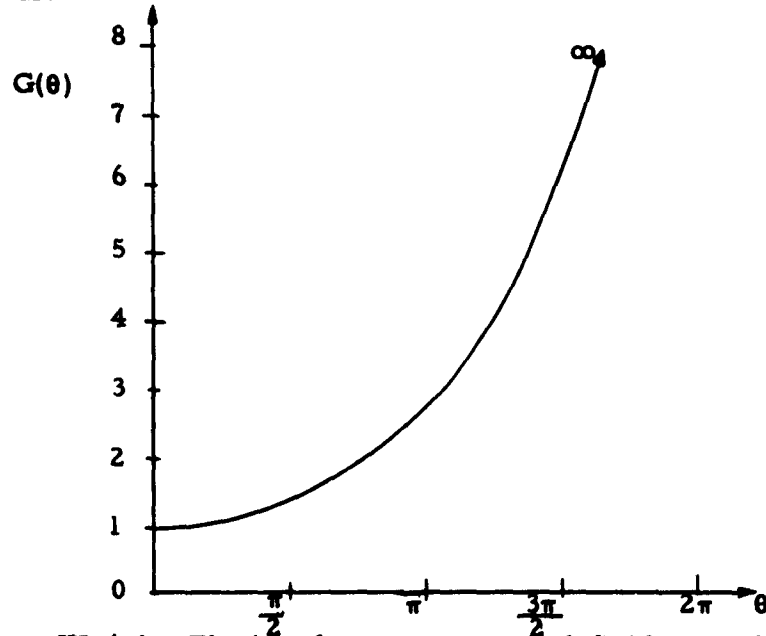


Figure III.6-1. The low frequency crossed-field noise function $G(\theta)$

transit angles will be compared with measured values in a later chapter. It is also useful in providing an assumption about the input quantities for the general evaluation of noise transport in the crossed-field diode.

Because of the complexity of the transformation coefficients, they were evaluated for only three values of θ , as functions of $|\beta|$. Figures III. 6-2 through -7 show the open- and short-circuit coefficients for $\theta = 0, 3\pi/4$, and 2π . These correspond to values of $B/B_c = 0, 0.75$, and 1.00 . The exact values of v_{xb} , including initial velocities were used, and ξ was taken from III. 4(5). The coefficients a_{22} , a_{33} , and a_{34} are plotted directly. The current-velocity coefficients have been normalized so that:

$$a_{23} = \left(\frac{3 I_d}{v_{xb}} \right) a'_{23},$$

$$a_{24} = \left(\frac{3 I_d}{v_{xb}} \right) a'_{24},$$

and

$$a_{32} = \left(\frac{v_{xa}}{3 I_d} \right) a'_{32},$$

with the same normalization for the corresponding b_{ij} coefficients. As stated previously, $a_{42} = a_{43} = a_{44} = 0$ and $a_{41} = \exp(-\beta)$.

From the form of the coefficients a_{23} and a_{24} in Appendix D, it is evident that the current fluctuations must increase as $|\beta|^2$ for the open-circuited diode. At the potential minimum it is reasonable to assume behavior similar to that found in the ordinary diode. Thus

$$|\tilde{q}_{xa}|^2 = R^2 2 e I_d \Delta f = \Gamma^2 \left(1 + \frac{|\beta|^2}{9} \right) G(\theta) 2 e I_d \Delta f \quad (6)$$

for the short circuited diode, and

$$|\tilde{q}_{xa}|^2 = R^2 2 e I_d \Delta f = \Gamma^2 \frac{|\beta|^2}{9} G(\theta) 2 e I_d \Delta f \quad (7)$$

for the open-circuited diode, both at small values of $|\beta|$.

For $|\beta|$ greater than 2π , $|\tilde{q}_{xa}|^2$ is assumed to be full shot noise ($R^2 = 1$, rather than $G(\theta) \rightarrow \infty$) while it is assumed to be 1/4 full shot noise at $|\beta| = \pi$. The results of the approximate

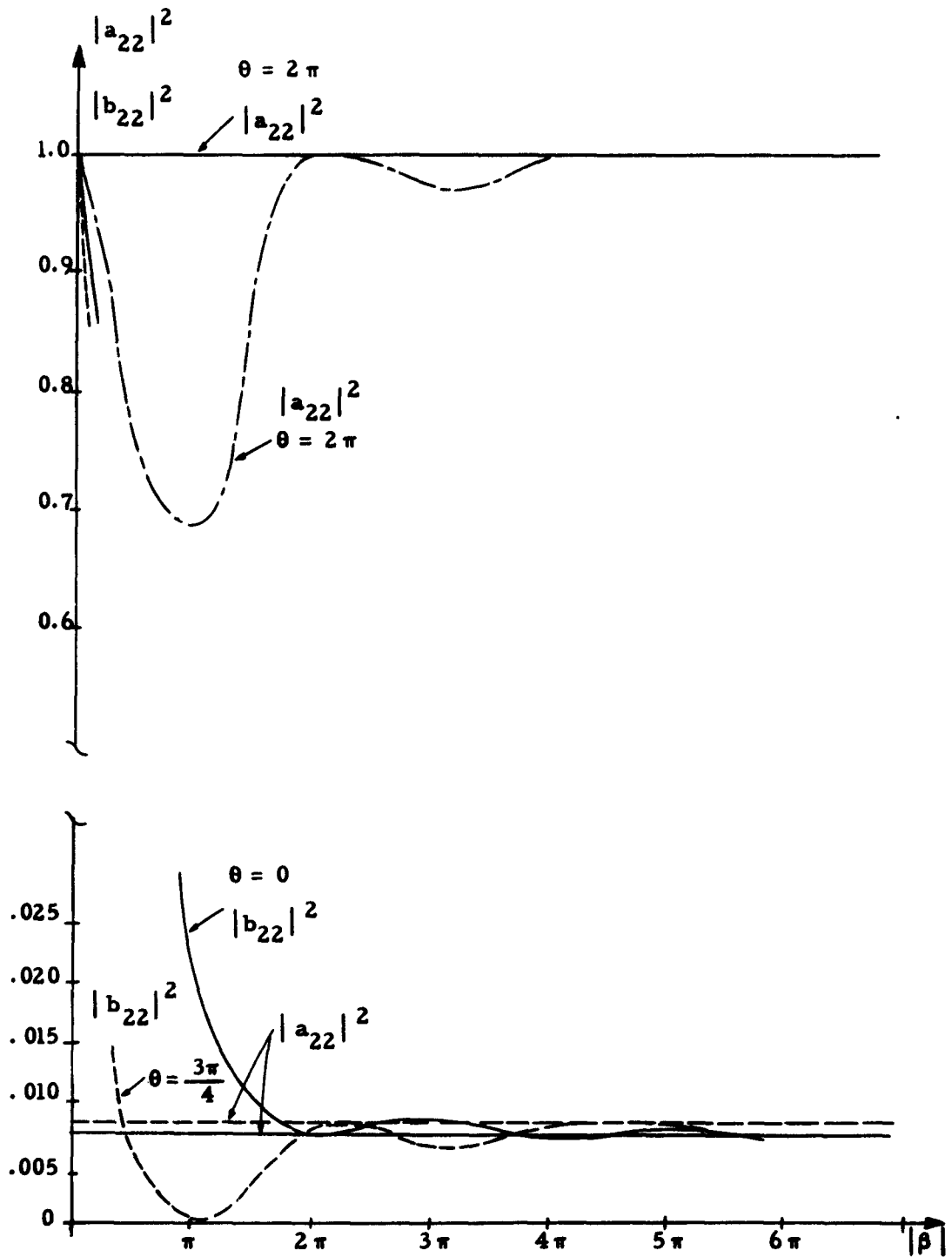


Figure III.6-2. Variation of $|a_{22}|^2$ and $|b_{22}|^2$ with $|\beta|$ and θ

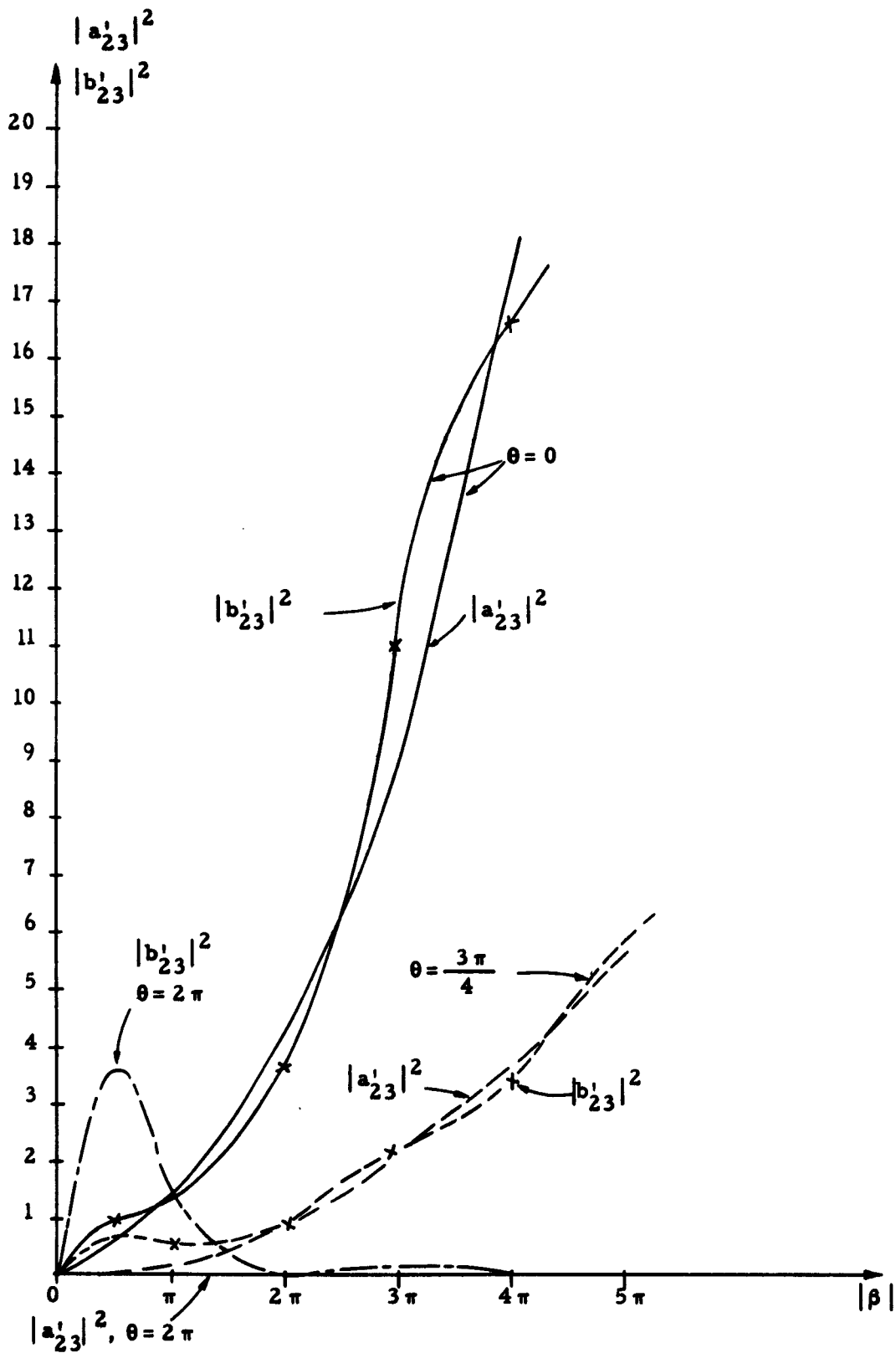


Figure III. 6-3. Variation of $|a'_{23}|^2$ and $|b'_{23}|^2$ with $|\beta|$ and θ

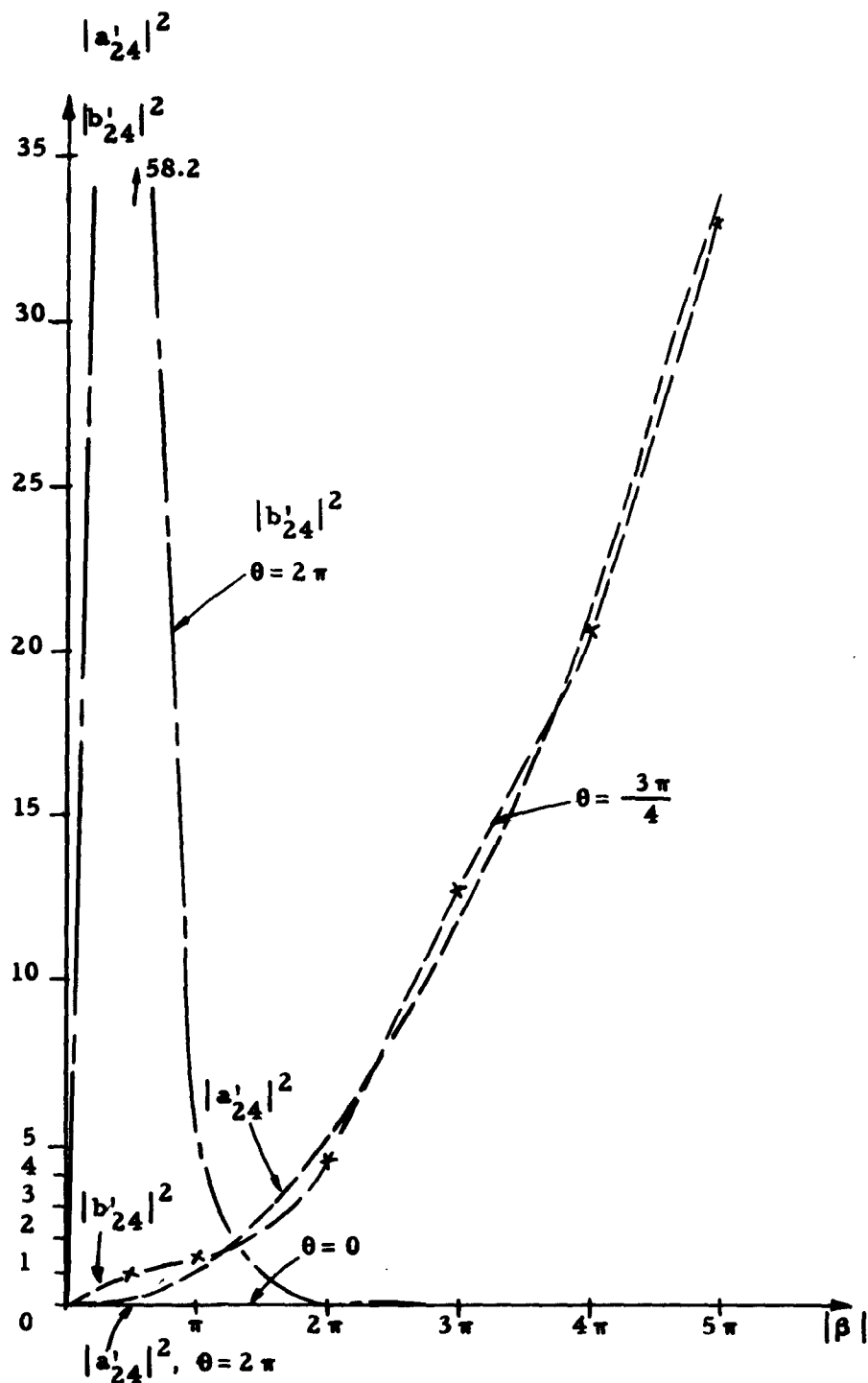


Figure III.6-4. Variation of $|a'_{24}|^2$ and $|b'_{24}|^2$ with $|\beta|$ and θ

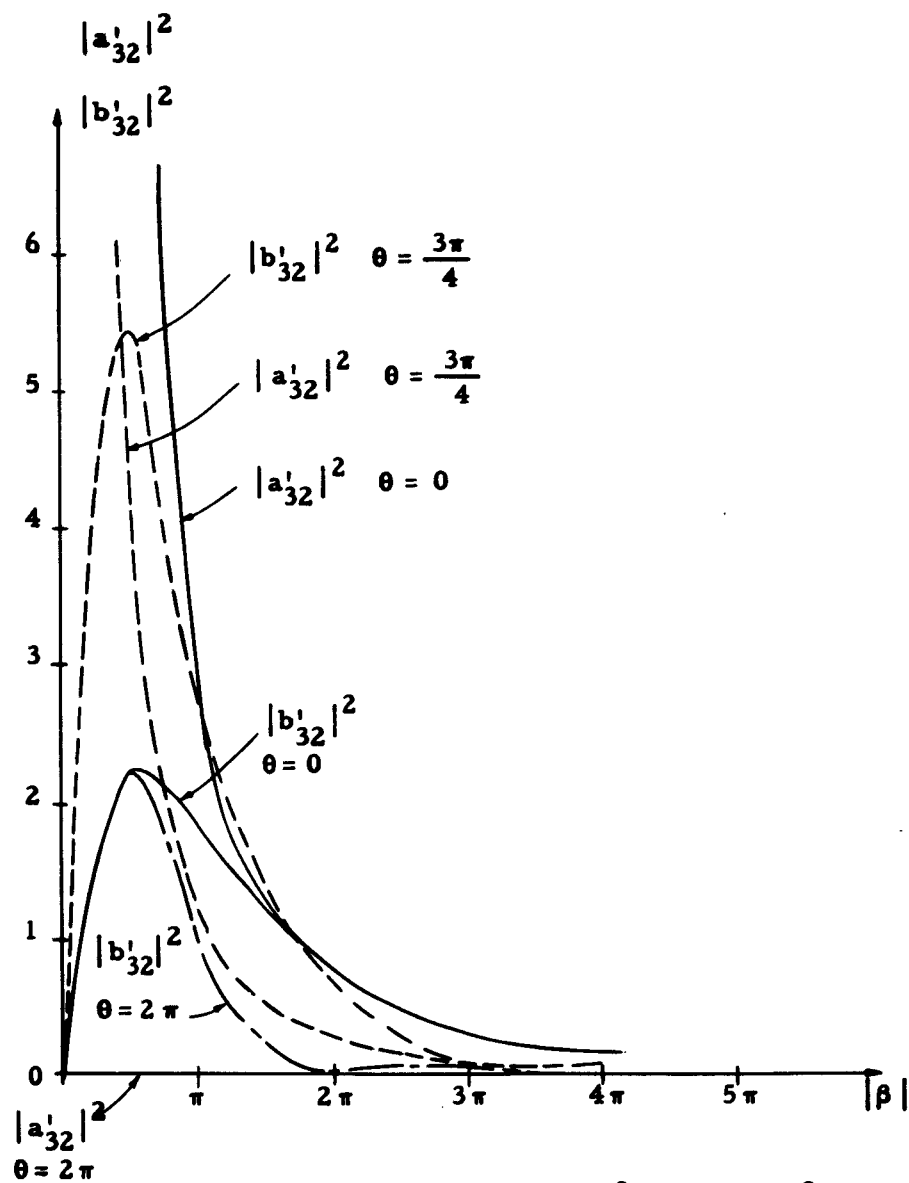


Figure III. 6-5. Variation of $|a'_{32}|^2$ and $|b'_{32}|^2$ with $|\beta|$ and θ

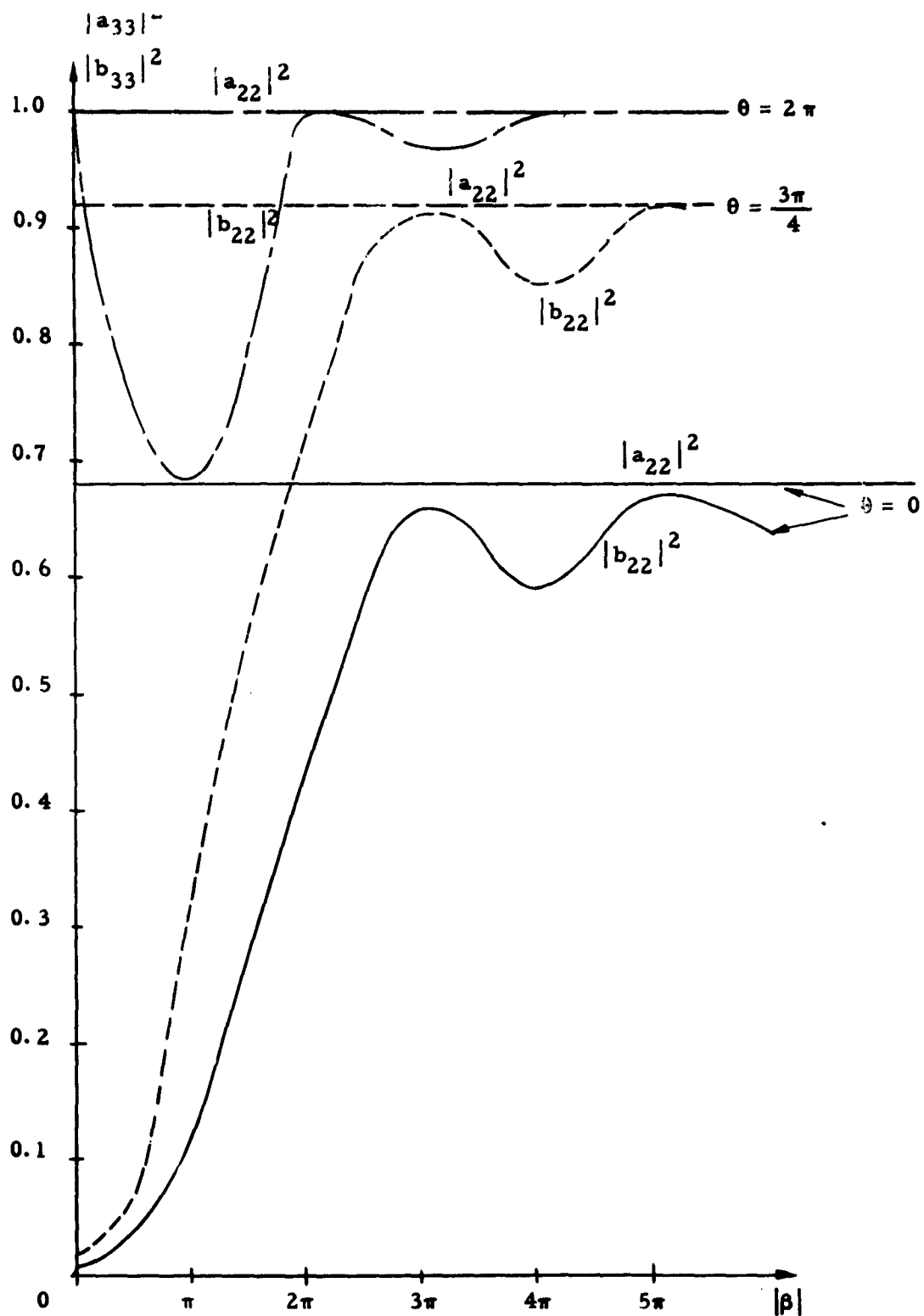


Figure III. 6-6. Variation of $|a_{33}|^2$ and $|b_{33}|^2$ with $|\beta|$ and θ

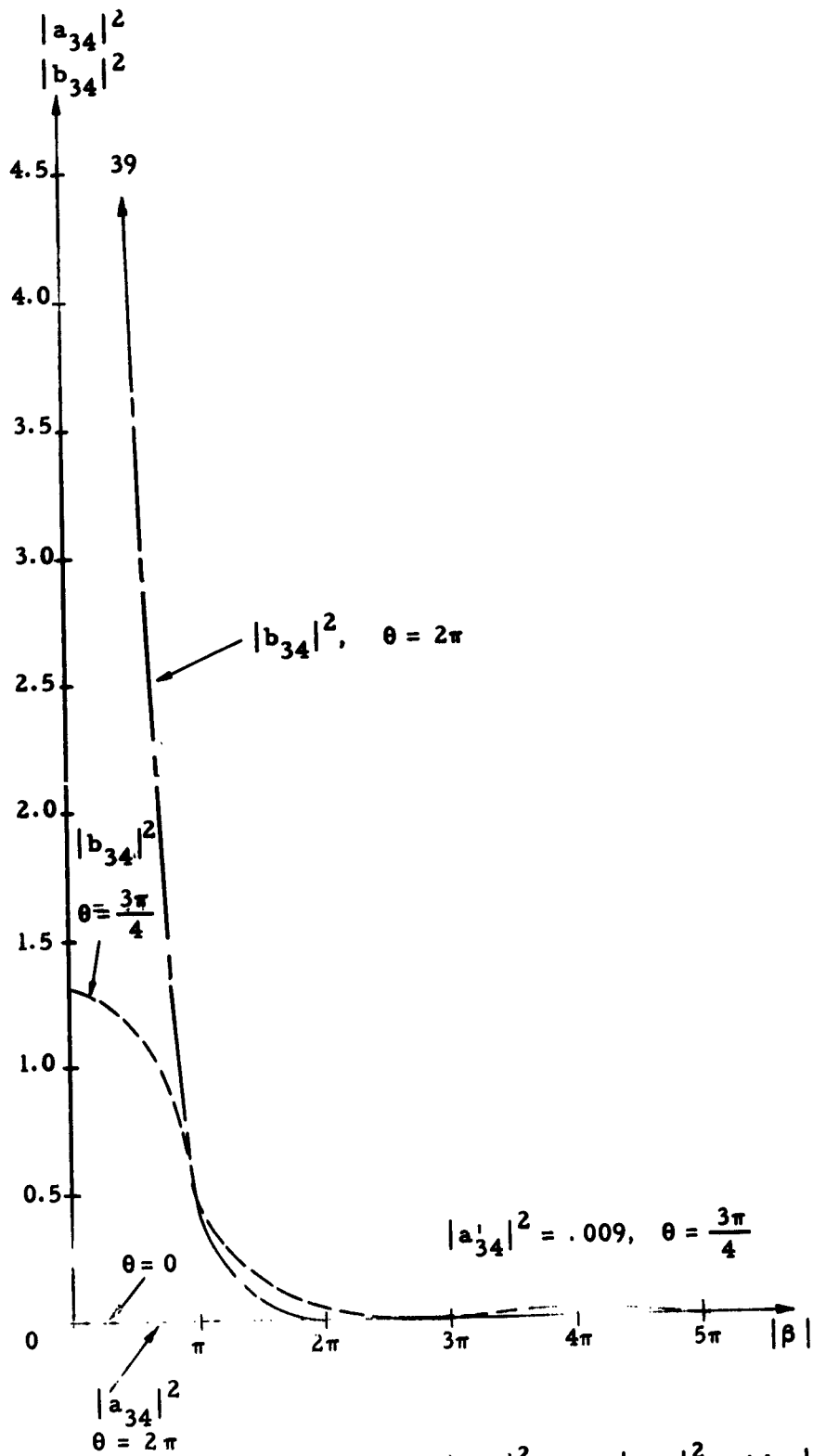


Figure III. 6-7. Variation of $|a_{34}|^2$ and $|b_{34}|^2$ with $|\beta|$ and θ

analyses of the potential minimum suggest that these are reasonable assumptions. Also, the effects of the input velocity fluctuations, given in III. 5(1) and III. 6(2) are more important numerically than the effects of the input current fluctuations, so the exact values of $|q_{xa}|^2$ are not critical.

Normalizing the fluctuations of current to full shot noise and of velocity to the Rack value:

$$\frac{|\tilde{q}_{xb}|^2}{2eI_d\Delta f} = |a_{22}|^2 R^2 + \left(\frac{v_{xb}(0)}{v_{xb}(\theta)}\right)^2 \Gamma^2 \left[|a'_{23}|^2 + \left(\frac{2}{4-\pi}\right) |a'_{24}|^2 \right] \quad (8)$$

and

$$\frac{|\tilde{v}_{xb}|^2}{|\tilde{v}_R|^2} = |a'_{32}|^2 \left(\frac{v_{xa}}{v_{xb}(0)}\right)^2 \frac{R^2}{\Gamma^2} + |a_{33}|^2 + \left(\frac{2}{4-\pi}\right) |a_{34}|^2 \quad (9)$$

The z-directed velocity fluctuations remain unchanged in this one-dimensional model. Substituting the values of R^2 and the coefficients a_{ij} (and b_{ij} alternately) into (8) and (9), the resulting anode current and velocity spectra are obtained. They are shown in Figures III. 6-8 and III. 6-10 for the open-circuited diode and in III. 6-9 and III. 6-11 for the short-circuited diode. θ has the same values as before.

The current fluctuations (Figures III. 6-8 and -9) grow with magnetic field. The spectra for $\theta = 2\pi$ are perhaps the most doubtful, for here the multivelocity nature of the true flow is most important. For the smaller values of θ , the current spectra grow as $|\beta|^2$. In the short-circuited diode, a large peak of noise is predicted near $|\beta| = \pi/2$ for $\theta = 2\pi$.

The velocity fluctuations remain fairly constant with transit angle at their initial value in the open-circuited diode. In the short-circuited diode, this is true at large transit angles. At smaller transit angles, however, there is a velocity smoothing with no magnetic field but an enhancement of the velocity fluctuations with increased field.

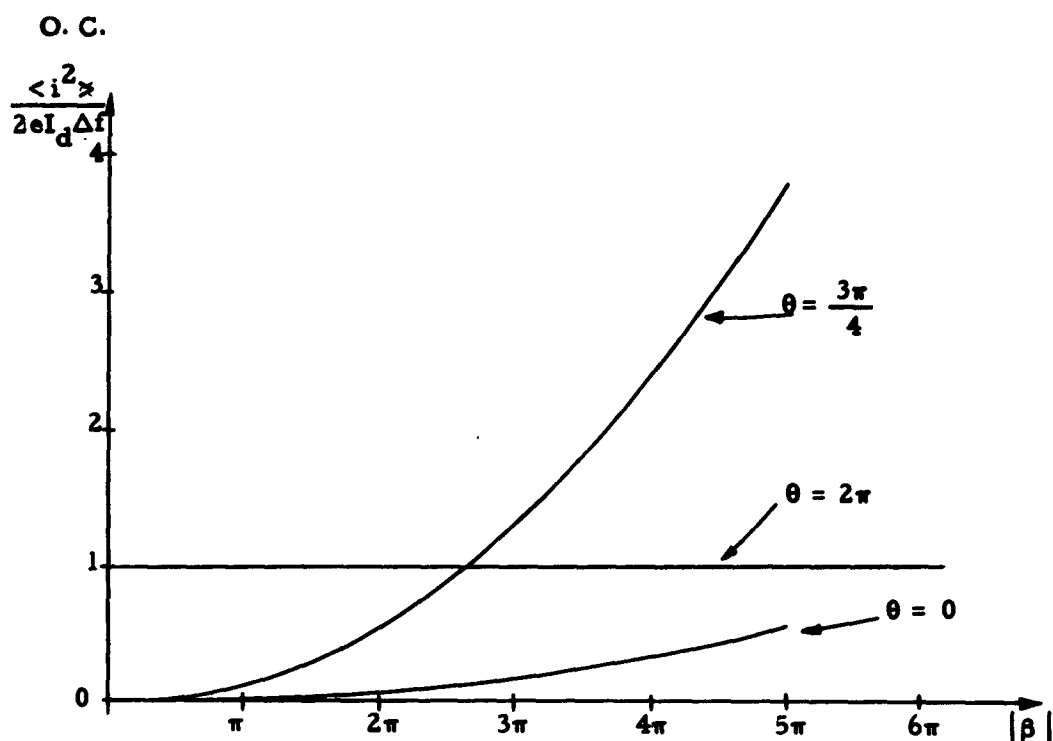


Figure III. 6-8. Variation of noise current with $|\beta|$ and θ in the open-circuited diode

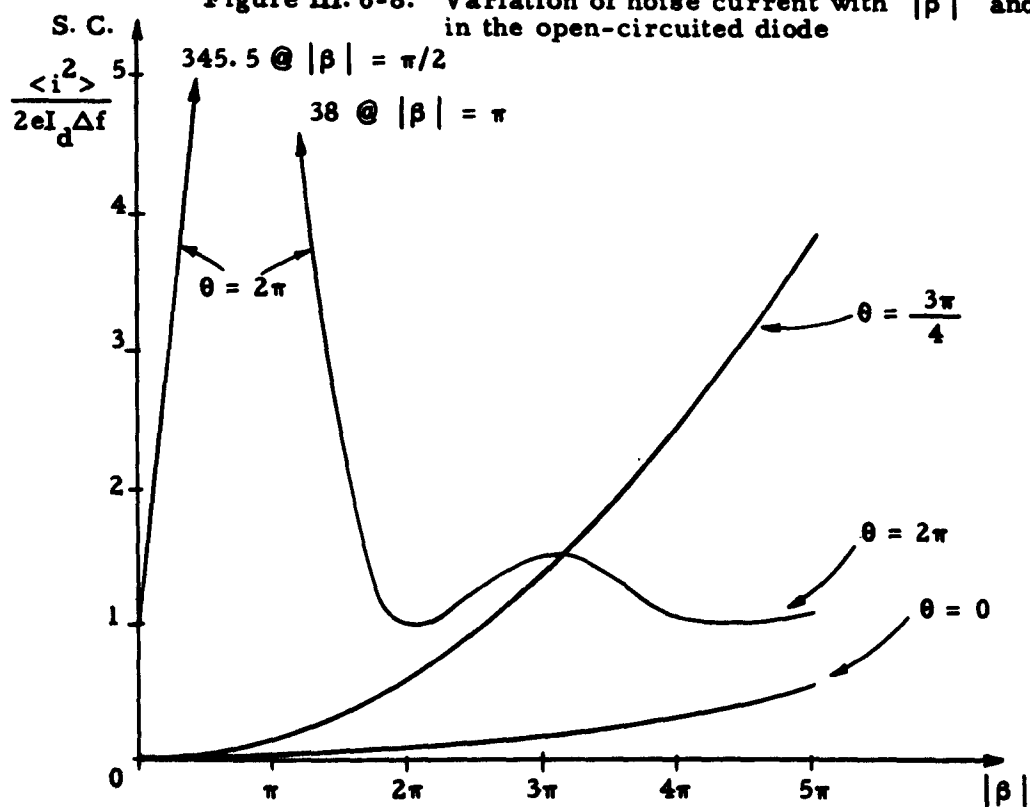


Figure III. 6-9. Variation of noise current with $|\beta|$ and θ in the short-circuited diode

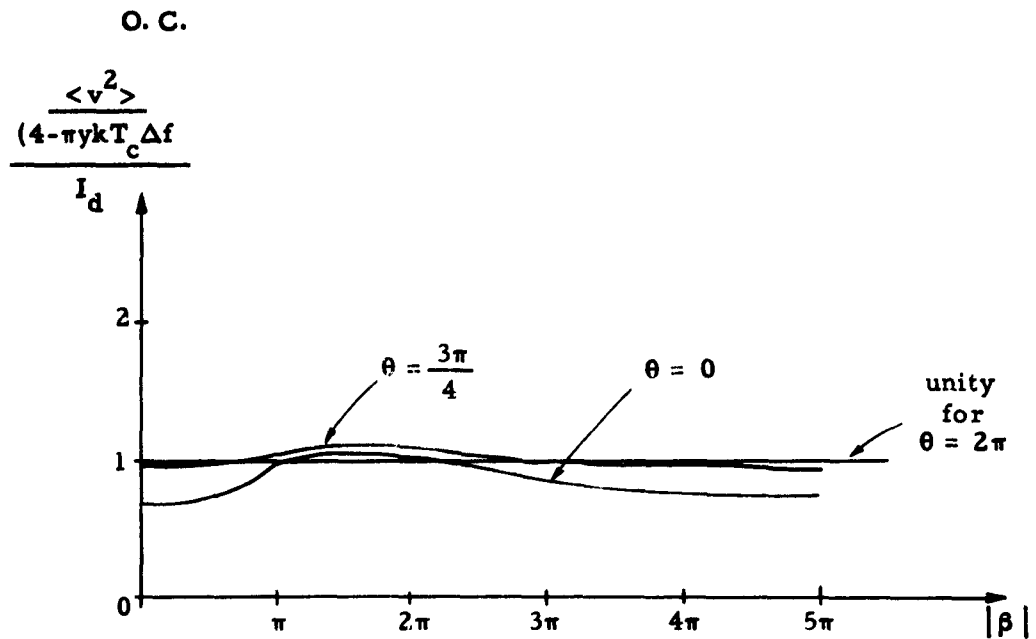


Figure III. 6-10. Variation of noise velocity with $|\beta|$ and θ in the open-circuited diode

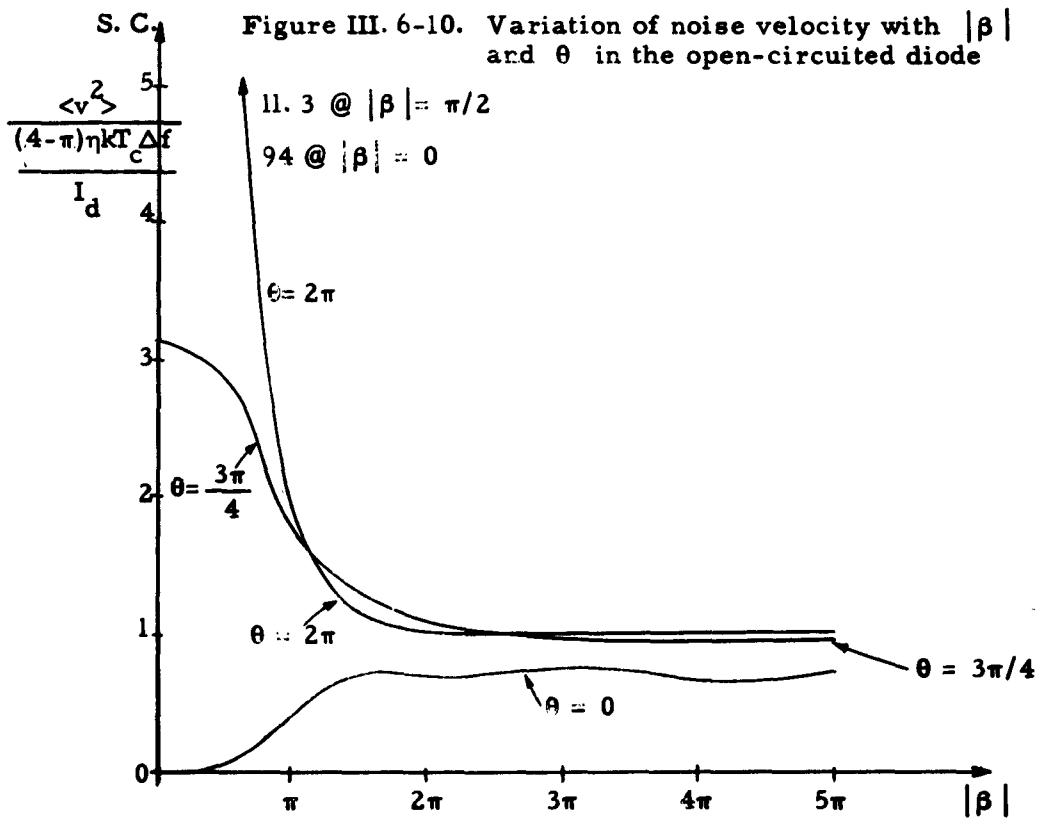


Figure III. 6-11. Variation of noise velocity with $|\beta|$ and θ in the short-circuited diode

The single-velocity theory remains valid only as long as the fluctuations are small compared with the average values of all quantities. In terms of the velocity fluctuations, we can require that they be small enough so that charges do not cross over one another. In the space-charge-limited diode, by assuming that initial current fluctuations can be neglected and that there exist at the initial plane independent velocity fluctuations with potential equivalent V_e , the condition for the prevention of crossovers reduces to

$$|\beta|^2 < \frac{\theta^2 (1 - \cos \theta)}{4 \phi(\theta)} \frac{V_d}{V_e} \quad (10)$$

This is shown in Appendix E.

For the values used here ($V_d/V_e = 100$) this means that crossovers occur at $|\beta| = 3.18\pi$ for $\theta = 0$ and at $|\beta| = 2.9\pi$ for $\theta = 3\pi/4$. When $\theta = 2\pi$, (10) is not valid, and there never appear to be crossovers for this value of V_d/V_e . For $\theta = 3\pi/4$, the single-velocity theory is invalid when the noise current reaches the vicinity of full shot noise. The theory is invalidated at even smaller noise currents for $\theta = 0$. Because ac energies greater than V_e are found at the "a" plane, the theory may be invalidated at still smaller transit angles. In Chapter IV, the results of the Monte Carlo analysis will show what behavior exists at transit angles above which the single velocity analysis is invalid.

It is interesting that for any ratio V_d/V_e , the theory becomes invalid at the same fraction of full shot noise in the magnetic field-free diode. From the coefficients, at large transit angles in either the short- or open-circuited diodes,

$$|\tilde{\alpha}_b|^2 \approx \frac{\Gamma^2 |\beta|^2}{9} (2 e I_d \Delta f) = \frac{1.925 V_e}{V_d} \frac{|\beta|^2}{9} (2 e I_d \Delta f). \quad (11)$$

Putting in (10) with $\theta = 0$,

$$\frac{|\tilde{\alpha}_b|^2}{2 e I_d \Delta f} \approx \frac{1.9 V_e}{V_d} \frac{V_d}{9 V_e} = 0.21 \quad (12)$$

when crossovers occur. It seems unlikely that the increase of noise current as $|\beta|^2$ continues beyond the point where the assumptions are violated.

IV. MULTIVELOCITY MODEL OF THE CROSSED-FIELD DIODE-THEORY

IV.1. The Monte Carlo Method

The low velocity region immediately in front of a thermionic cathode can not be accurately described or analyzed unless account is taken of the multiveLOCITY nature of the electron flow. The spread of electron velocity is of the same order of magnitude as the average velocity of the beam, indicating the necessity for a large signal theory. In this region, electrons cross one another's trajectories as they travel from the cathode, through the potential minimum and on into the accelerating stream. Although the average thermionic emission characteristics of a cathode are known, there is no knowledge of individual electrons, which are emitted at random times and with random velocities.

These factors combine to make a problem that is quite suitable for treatment by the Monte Carlo technique, which involves the use of random numbers to generate the random variables of the emission process. It is a numerical approximation to the rather complex physical phenomena under study. The emission and subsequent motion of the electrons must be followed carefully. To do this, a high-speed digital computer is required. An IBM 704 computer was used in this study, which in reality is the digital simulation of the electronic flow in a diode.

Fundamentally, the computer was programmed to follow simultaneously the trajectories of many charges in the cathode-anode space of a thermionic diode. Random emission times and velocities simulated the thermionic emission. The total "observation" time was divided into a number of small intervals, at the end of

which the equations of motion were approximately integrated, charges advanced or retarded, and checks made for crossovers and anode or cathode plane crossings. The details of the actual computation will be covered in later sections.

While it may be difficult to look experimentally into the real diode with our crude probes and instruments, the simulated diode is completely open for investigation. Observation may be readily made of the dc characteristics, the trajectories of individual charges, and the propagation of fluctuations from the cathode on into the stream--all without perturbing the physical processes.

On the other hand, the Monte Carlo approach to this problem is not free of drawbacks. A purely analytic solution, with which the effect of each parameter could readily be determined, would be most desirable. On the computer, however, the problem must be rerun, or a new diode simulated, for each change of parameters. The accuracy of the results depend on the time allowed for each run. This may become a time-consuming and expensive approach, but the alternative, until a satisfactory analytic solution can be found, is a much more approximate analysis, with more doubtful assumptions. The Monte Carlo approach seems to be the best choice.

IV. 2. Model, Assumptions and Methods

The same configuration used in the single-velocity analysis of the preceding chapter will be used here. Both the open- and short-circuited diodes will be investigated. The major difference is the inclusion of the nonlinear, multivelocity nature of the electron flow.

The model for this analysis is the planar diode, with electrons replaced by infinite sheets of constant charge density. The charges move under the influence of an average anode-cathode potential V_d , a constant transverse magnetic field B and the space charge fields due to the sheets themselves. Sheets are allowed to cross over or pass one another, according to their individual trajectories.

The entire elapsed time t_n is divided into N time intervals of length Δt . The choice of the size of Δt depends on several factors, and will be discussed later. The equations of motion are integrated numerically and the sheets moved accordingly at the end of each time interval, at $t = i \Delta t$, where i here is a running index. Sheets which cross the anode plane at $x = d$, or return and cross the cathode plane at $x = 0$, are removed from the computer memory, hence from the computation.

Initially, the diode space is filled with a suitable number of charges. Their positions and velocities are obtained by allowing an arbitrarily filled diode (sheets usually uniformly spaced in x position) to reach equilibrium, permitting any initial transients to decay. This procedure takes a rather short time relative to t_n . Tien and Moshman (1956) and Dayem (1960) used the Fry-Langmuir (1921, 1923) steady state potential distribution to establish the initial conditions. As the corresponding potential for the crossed-field diode has not been evaluated in such detail, and the decaying transient method seemed perfectly satisfactory, it was used in these calculations.

IV. 3. Electric Field and Potential

A. Short-Circuited Diode

In the short-circuited diode, the electric field and potential at any point are uniquely determined by the positions of the charges within the diode. The electric field \mathcal{E} is the sum of the applied field, V_d/d , and \mathcal{E}_{sc} , the space charge field. Consider a single sheet, with constant, uniform surface charge density ρ_s (negative for electrons) located at x' . From Gauss' law, the fields on both sides of the charge can be obtained as

$$\begin{aligned} \mathcal{E}(x) &= \frac{\rho_s x'}{\epsilon_0 d}; \quad x' < x \leq d \\ \mathcal{E}(x) &= \frac{\rho_s}{\epsilon_0 d} (x' - d); \quad 0 \leq x < x'. \end{aligned} \tag{1}$$

At the position of the charge, the average of these two values is

$$\mathcal{E}(x') = \frac{\rho_s}{\epsilon_0 d} \left(x' - \frac{d}{2} \right). \quad (2)$$

That this is the field acting on the charge can be shown by first calculating the stored electric energy in the diode,

$$W = \frac{1}{2} \epsilon_0 \int_0^d \mathcal{E}^2(x) dx = \frac{\rho_s^2}{2 \epsilon_0 d} \left[\frac{d^2}{3} - x'^2 + x'd \right]. \quad (3)$$

Then

$$\mathcal{E}(x') = \frac{\text{Force}}{\rho_s} = - \frac{\partial W}{\partial x'} = \frac{\rho_s}{\epsilon_0 d} \left(x' - \frac{d}{2} \right). \quad (4)$$

This self-electric field term is made necessary by the limited number of sheets used to represent the electron stream. As the total number of sheets increases, the contribution from this term to the total field should become negligible.

Considering all the charges in the diode space,

$$\mathcal{E}(x) = \sum_{x' > x} \frac{\rho_s}{\epsilon_0 d} (x' - d) + \sum_{x > x'} \frac{\rho_s x'}{\epsilon_0 d} + \frac{\rho_s}{\epsilon_0 d} \left(x - \frac{d}{2} \right). \quad (5)$$

It is convenient to index the charges by numbering them, starting at the anode, from one to N_s , the number of charges in the space. Then, combining terms, (5) becomes

$$\mathcal{E}(x^j) = \frac{\rho_s}{\epsilon_0} \left[\sum_{\text{all } x'} \frac{x'}{d} - j + \frac{1}{2} \right] \quad (6)$$

where the index j is the number of charges, including the one at x , between x and the anode.

Adding the constant applied field, $-V_d/d$,

$$\mathcal{E}(x^j) = -\frac{V_d}{d} + \frac{\rho_s}{\epsilon_0} \left[\sum_{\text{all } x'} \frac{x'}{d} - j + \frac{1}{2} \right] \quad (7)$$

Since average emitted current density, J_{eo} is a more useful parameter than the charge density of each sheet, ρ_s is written as

$$\rho_s = \frac{J_{eo} \Delta t}{n_{eo}}, \quad (8)$$

where n_{eo} is the average number of sheets emitted per Δt .

It is convenient to make certain normalizations to reduce the number of independent parameters. All distances and potentials will be normalized to the diode spacing and applied dc potential. Velocities will be normalized to the equivalent of the anode potential. The normalizing time unit can then be chosen as unit distance per unit velocity. The accelerating field on the negative sheet charges is normalized to the applied dc accelerating field. Thus:

$$X = \frac{x}{d}, \quad Z = \frac{z}{d}$$

$$U = \frac{V}{V_d}$$

$$u_x = \frac{\frac{v_x}{V_d}}{\sqrt{2\eta V_d}} = \frac{v_x}{V_d} \quad (9)$$

$$u_z = \frac{\frac{v_z}{V_d}}{\sqrt{2\eta V_d}} = \frac{v_z}{V_d}$$

$$T = \frac{t}{t_d} = \frac{t}{(d/v_d)}$$

$$E = -\frac{\mathcal{E}}{(V_d/d)}.$$

By choosing $m_{\Delta} = t_d/\Delta t$, the number of intervals per unit time, the normalized electric field can be written as:

$$E(X^j) = 1 + \frac{J_{eo} \eta d^2}{m_{\Delta} \eta_{eo} \epsilon_o (2\eta)^{3/2} V_d^{3/2}} \left[\sum_{\text{all } k} X^k - j + \frac{1}{2} \right]. \quad (10)$$

The Child-Langmuir current density, which is approximately equal to the anode current density in a space-charge-limited diode with no magnetic field, is given by

$$J_{cl} = -\frac{4}{9} \epsilon_o \frac{\sqrt{2\eta}}{d^2} V_d^{3/2} \quad (11)$$

Defining $\alpha = J_{eo}/J_{cl}$, the emitted current density parameter, and rearranging the terms,

$$E(X^j) = 1 - \frac{4/9 \alpha}{m_{\Delta} \eta_{eo}} \left[j - \frac{1}{2} - \sum_k X^k \right]. \quad (12)$$

The potential at any point within the short-circuited diode can be calculated by summing the potentials arising from each charge. Integrating (1), for one charge at X' ,

$$U(X) = \frac{\rho_s d}{\epsilon_o V_d} X' (1-X); \quad X' \leq X \leq 1, \quad (13)$$

$$U(X) = \frac{\rho_s d}{\epsilon_o V_d} X (1-X'); \quad 0 \leq X \leq X'.$$

This potential distribution is shown in Figure IV. 3-1 for negative ρ_s .

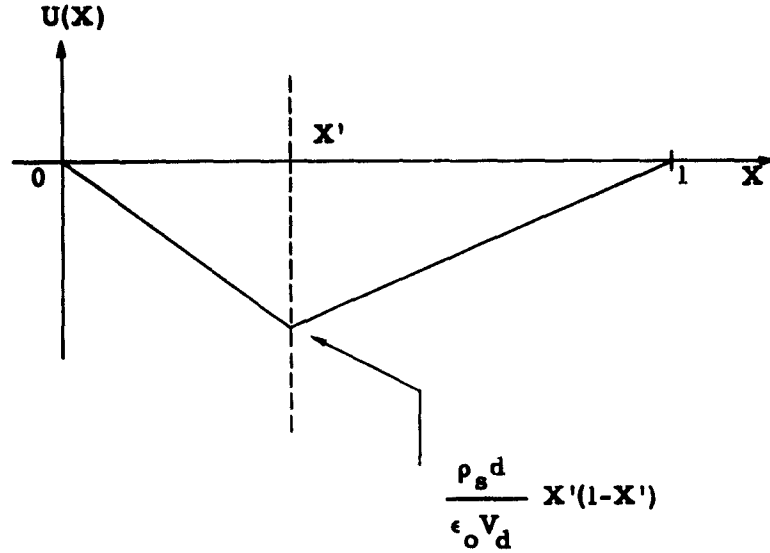


Figure IV. 3-1. Potential distribution for a single charge in the short-circuited diode

For many charges in the space, the potential at the j^{th} charge, due to the other charges, is

$$U(X^j) = \frac{\rho_s^d}{\epsilon_o V_d} \left[\sum_{k=1}^{j-1} x^j(1-x^k) + \sum_{k=j}^{N_s} x^k(1-x^j) \right]. \quad (14)$$

Using the same normalization as in the electric field equation, rearranging the summations, and adding the dc potential $X^j V_d$,

$$U(X^j) = X^j - \frac{4/9\alpha}{m_{\Delta}^n \epsilon_o} \left[X^j(j - \sum_{k=1}^s X^k) + \sum_{k=j+1}^s X^k \right]. \quad (15)$$

B. Open-Circuited Diode

Unlike the electric field of the short-circuited diode, which is uniquely determined by the positions of the various charges, the electric field of the open-circuited diode must be adjusted to cause the total diode current to be zero. In the planar model, this can be stated as

$$(\nabla_x \vec{\mathcal{H}})_x = j_x + \epsilon_o \frac{\partial \mathcal{C}_x}{\partial t} = 0. \quad (16)$$

Integration with respect to time then gives the electric field,

$$\mathcal{E}_x = \mathcal{E}(t) = \mathcal{E}(0) - \frac{1}{\epsilon_0} \int_0^t j_x dt. \quad (17)$$

Replacing the current density by $\rho_s n / \Delta t$, and evaluating the integral at the anode by means of a summation over the finite time intervals,

$$\mathcal{E}_d = \mathcal{E}_d(0) - \frac{\rho_s}{\epsilon_0} \sum_{l=1}^i (n_{de} - n_{do}), \quad (18)$$

where n_{do} is the average value of n_{di} , the number of sheets crossing the anode per Δt . Since all electric field lines terminate on the cathode in the open-circuited diode, the field at any point x in the diode can be expressed in terms of the number of charges between x and the anode, from Gauss' law. The field on the j^{th} charge from the anode is the average of the fields on either side, as in the short-circuited diode:

$$\mathcal{E}(x_j) = \mathcal{E}_d(0) - \frac{\rho_s}{\epsilon_0} \left[\left(j - \frac{1}{2} \right) + S \right] \quad (19)$$

where

$$S = \sum_{l=1}^i (n_{de} - n_{do}). \quad (20)$$

In terms of the normalized parameters,

$$E(X_j) = E_d(0) - \frac{4/9 \alpha}{n_{eo} m \Delta} \left[j - \frac{1}{2} + S \right]. \quad (21)$$

The instantaneous potential at x for a single charge at x' is

$$V(x) = x \frac{\rho_s}{\epsilon_0} ; x' \leq x$$

$$V(x) = x' \frac{\rho_s}{\epsilon_0} ; x > x'.$$

Figure IV. 3-2 shows this potential distribution for negative ρ_s .

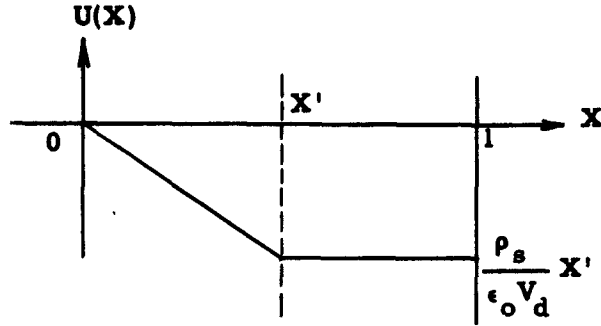


Figure IV. 3-2. Potential distribution for a single charge in the open-circuited diode

Considering all the charges in the diode, and the potential arising from the anode field, the potential at x^j is

$$V(x^j) = - \mathcal{E}_d x^j + \frac{\rho_s}{\epsilon_0} \left[\sum_{k=1}^j x^j + \sum_{k=j}^{N_s} x^k \right] \quad (22)$$

Substituting for \mathcal{E}_d and normalizing,

$$U(X^j) = X^j E_d(0) - \frac{4/9\alpha}{m_{\Delta}^n \epsilon_0} \left[X^j (j+S) + \sum_{k=j+1}^{N_s} X^k \right]. \quad (23)$$

The similarity between the equations for potential and electric field in the open- and short-circuited diodes simplifies the computer formulation considerably.

IV. 4. The Equations of Motion

The equations of motion, under the assumptions given above, are

$$\frac{dv_x}{dt} = \frac{dx^2}{dt^2} = - \eta \mathcal{E} - \eta B v_z \quad (1)$$

and

$$\frac{dv_z}{dt} = \frac{d^2 z}{dt^2} = \eta B v_x \quad (2)$$

where $\eta = \left| \frac{e}{m} \right|$, the magnitude of the electronic charge-to-mass ratio, B is the dc magnetic field in the negative y direction and \mathcal{E} is the total x -directed electric field. Equation (2) can be integrated directly, to give

$$v_z = \omega_c x + v_{ze} \quad (3)$$

where $\omega_c = \eta B$ and v_{ze} is the initial z velocity of a charge.

By defining $\omega_c t_d = \phi_d$, and using the normalizations of the last section, the x -directed acceleration can be written as:

$$\frac{d u_x}{d \tau} (X^j) = \frac{E(X^j)}{2} - \phi_d u_z. \quad (4)$$

$E(X^j)$ for the short- or open-circuited diode can be taken from the last section.

The normalized z -directed velocity becomes:

$$u_z = \phi_d X + u_z(0) \quad (5)$$

The parameter ϕ_d has a more physical interpretation than is implied by its definition. By substituting $\omega_c = \eta B$ and $t_d = d/v_d$,

$$\phi_d = B/B_c, \quad (6)$$

where B_c is the critical field defined previously.

The x -directed velocity of the j^{th} particle at the $(i+1)$ st time step, u_{i+1}^j , can be expanded about the velocity at the i^{th} step. With $\Delta T = 1/m_\Delta$,

$$u_{x, i+1}^j = u_{x, i}^j + \frac{\partial u_{x, i}^j}{\partial T} \Delta T + \frac{\partial^2 u_{x, i}^j}{\partial T^2} (\Delta T)^2 + \dots \quad (7)$$

or

$$u_{x,i+1}^j \approx u_{x,i}^j + a_{x,i}^j \Delta T + \frac{(a_{x,i}^j - a_{x,i-1}^j)}{\Delta T} (\Delta T)^2 = u_{x,i}^j + (3a_{x,i}^j - a_{x,i-1}^j) \frac{\Delta T}{2}$$

where $a_i^j = \partial u_{x,i}^j / \partial T$ is calculated at the $(i+1)$ st step on the basis of positions at the i^{th} step. This formula, suggested by the work of Hess (1961), gives more accurate trajectories than the formula used by Tien-Moshman, which assumed the acceleration constant over the time interval.

The new position X_{i+1}^j is found from the average velocity over the interval,

$$X_{i+1}^j = X_i^j + \frac{(u_{x,i}^j + u_{x,i+1}^j)}{2} \Delta T. \quad (8)$$

The Z velocity, $u_{z,i+1}^j$, is next obtained using (5) directly, with $X = X_{i+1}^j$, and from it,

$$Z_{i+1}^j = Z_i^j + \frac{(u_{z,i}^j + u_{z,i+1}^j)}{2} \Delta T. \quad (9)$$

IV. 5. Emission

The Monte Carlo nature of the analysis is introduced in the emission process. Here charges are emitted randomly to simulate true thermionic emission. Thermionic emission is characterized by the random emission times of the electrons, with the velocity of each electron being independent of the velocities of all the others. The random numbers of electrons emitted per interval are distributed according to a Poisson distribution, while their velocities form a Maxwellian distribution.

If n_{eo} is the average number of charges emitted per time interval, then the probability that s charges will be emitted in any given interval is

$$P(s) = \frac{e^{-n_{eo}} n_{eo}^s}{s!}. \quad (1)$$

The cumulative distribution function, expressing the probability that s or fewer charges will be emitted, is

$$\text{Cum } P(s) = \sum_{p=0}^s P(p). \quad (2)$$

If random numbers R , distributed uniformly between 0 and 1, are mapped onto $\text{Cum } P(s)$, such that

$$\text{Cum } P(s-1) < R \leq \text{Cum } P(s), \quad (3)$$

then s charges are to be emitted. For a large number of random numbers, s will then obey the Poisson distribution. Figure IV. 5-1 sketches this relationship graphically.

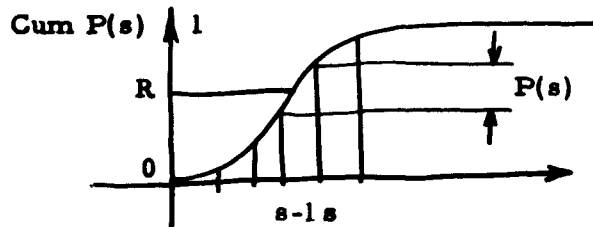


Figure IV. 5-1. Mapping of R onto $\text{Cum } P(s)$

The requirement for many random numbers is satisfied by generating them within the computer as needed. This is done by operating on a 35 bit binary number in the computer storage (Caughran, 1961). An initial 35 bit number, equivalent to R , is entered into the computer. A new random number is obtained by multiplying this by $(2^9 + 1)$, and retaining the 35 bits of highest place value from the resulting 70 bit number. From this number, R is obtained by conversion to a decimal fraction. The series of random numbers obtained in this manner will provide several orders

of magnitude more numbers than the problem requires before the series repeats itself.

The exact emission times of the individual charges within the interval are obtained from s more random numbers. If R is now used to represent a new random number each time it appears, the exact emission time, t'_1 , is

$$t'_1 = t_1 + R\Delta t \quad (4)$$

or in normalized form,

$$T'_1 = T_1 + R\Delta T. \quad (5)$$

The probability of emitting an electron with a normal component of velocity between v_{xe} and $v_{xe} + dv_{xe}$ is approximated by the half-Maxwellian distribution

$$P(v_{xe})dv_{xe} = \frac{mv_{xe}}{kT_c} \exp\left(-\frac{mv_{xe}^2}{2kT_c}\right) dv_{xe} \quad (6)$$

where k is Boltzmann's constant and T_c is the cathode temperature.

The probability of emitting an electron with transverse component of velocity between v_{ze} and $v_{ze} + dv_{ze}$, however, is the "normal" distribution.

$$P(v_{ze})dv_{ze} = \sqrt{\frac{m}{2\pi kT_c}} \exp\left(-\frac{mv_{ze}^2}{2kT_c}\right) dv_{ze}. \quad (7)$$

Defining $U_e = kT_c/eV_d$, the normalized equivalent thermal energy,

$$P\left(\frac{u_{xe}}{U_e^{1/2}}\right) d\left(\frac{u_{xe}}{U_e^{1/2}}\right) = \frac{u_{xe}}{U_e^{1/2}} \exp\left(-u_{xe}^2/U_e\right) d\left(\frac{u_{xe}}{U_e^{1/2}}\right) \quad (8)$$

and

$$P\left(\frac{u_{ze}}{U_e^{1/2}}\right) d\left(\frac{u_{ze}}{U_e^{1/2}}\right) = \frac{1}{\sqrt{\pi}} \exp\left(-u_{ze}^2/U_e\right) d\left(\frac{u_{ze}}{U_e^{1/2}}\right). \quad (9)$$

The theoretical mean and mean square values of emission velocity can readily be computed from these probabilities, and are

$$\begin{aligned}\overline{v_{xe}} &= \left(\frac{\pi k T_c}{2m} \right)^{1/2}, \quad \overline{v_{ze}} = 0 \\ \overline{v_{xe}^2} &= \frac{2k T_c}{m}, \quad \overline{v_{ze}^2} = \frac{k T_c}{m}.\end{aligned}\tag{10}$$

With the normalization to v_d ,

$$\begin{aligned}\overline{u_{xe}} &= \left(\frac{\pi}{4} \right)^{1/2} U_e^{1/2}, \quad \overline{u_{ze}} = 0 \\ \overline{u_{xe}^2} &= U_e, \quad \overline{u_{ze}^2} = U_e/2.\end{aligned}\tag{11}$$

The cumulative distribution functions (CDF) are

$$\text{CDF} \left(\frac{u_{xe}}{U_e^{1/2}} \right) = \int_0^{u_{xe}/U_e^{1/2}} p e^{-p^2} dp = 1 - \exp \left(-\frac{u_{xe}^2}{U_e} \right)\tag{12}$$

and

$$\text{CDF} \left(\frac{u_{ze}}{U_e^{1/2}} \right) = \frac{1}{\sqrt{\pi}} \int_{-\infty}^{u_{ze}/U_e^{1/2}} e^{-p^2} dp.\tag{13}$$

Figure IV.5-2 shows the probabilities as well as their CDF's. The CDF's are uniformly distributed between 0 and 1, so the exact emission velocity can be obtained from a random number R by finding $u_{xe}/U_e^{1/2}$ or $u_{ze}/U_e^{1/2}$ such that $\text{CDF}(u_{xe}/U_e^{1/2})$ or $\text{CDF}(u_{ze}/U_e^{1/2})$ equals R .

For the normal component of velocity, the CDF can be expressed analytically. If R is a random number between 0 and 1, then $(1-R)$ is also, so that

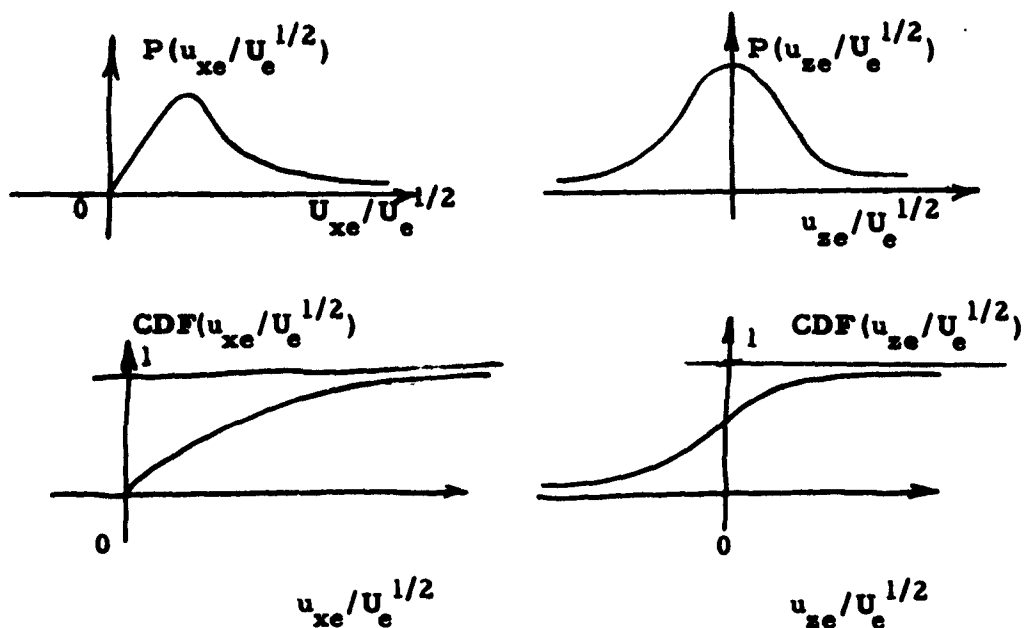


Figure IV.5-2. Emission probability distributions and their cumulative distribution functions

$$1 - R = 1 - \exp(-u_{xe}^2 / U_e) \quad (14)$$

or

$$u_{xe} = U_e^{1/2} [-\ln R]^{1/2} \quad (15)$$

is the formula for X emission velocity.

The CDF for the normal distribution with unity mean square value is readily available in tabular form. Therefore, a routine was set up (Caughran, 1961) to interpolate linearly or quadratically between table entries to find s such that

$$R = \text{CDF}(s). \quad (16)$$

Accuracy is maintained to $\pm 4(10^{-4})$ in the interpolation and by means of a series expansion for s when R is close to zero or unity.

Since $\overline{u_{ze}^2} = U_e/2$, the normally distributed random number so obtained must be multiplied by $(U_e/2)^{1/2}$ to obtain u_{ze} .

The new charges are added to the diode and then all the charges are moved according to their computed trajectories, sorted to maintain ordering in X position counting from the anode, and checked for anode or cathode plane crossings. To eliminate the added complication of the random emission times, all charges are advanced initially to positions

$$\begin{aligned} X_e &= u_{xe} R \Delta T \\ Z_e &= u_{ze} R \Delta T, \end{aligned} \tag{17}$$

where R is that random number used to determine emission time. Little error results from the neglect of the acceleration terms and the effect of the magnetic field if ΔT is small. Thus all charges emitted between the i^{th} and $(i+1)^{\text{st}}$ steps are added to the diode in advanced positions at the $(i+1)^{\text{st}}$ step. These then become part of the computation at the $(i+2)^{\text{nd}}$ step, and the cycle is repeated.

IV. 6. Theoretical Average Values

The theory and equations of the preceding sections are complete for the calculation of trajectories, potentials, currents, and velocities. However, both as a check on the operation of the computer programs and a means of estimating the statistical errors of the method, it is convenient to form the theoretical average values of several quantities in terms of the parameters of the problem. The emission number and velocity averages have already been evaluated. Since, as discussed previously, the exact steady state solution for the crossed-field diode is not available, other comparisons can only be made for the "O"-type diode.

The X -acceleration on each charge is normally calculated as part of the forward integration. However, as can be seen from equation IV. 4(5), the acceleration at the i^{th} step must be known to calculate the velocity at the $(i+1)^{\text{st}}$ step. This presents no

difficulty, (for this value can be stored in the computer memory) except for a charge newly emitted at the i th step. As an approximation, these charges are given the theoretical average acceleration evaluated at the cathode for the zero magnetic field case, which is obtained from the dc potential profile. It was more convenient for the computer program to use this acceleration than the exact one, and little error was introduced.

The Fry-Langmuir potential profile is used to describe the magnetic-field-free diode. The reduced variables, rewritten from II. 4(1) in modified form, are:

$$\xi = 4 \left(\frac{\pi}{2kT_c} \right)^{3/4} m^{1/2} \left(\frac{eJ_{do}}{4\pi\epsilon_0} \right)^{1/2} (x - x_m) \quad (1)$$

and

$$\eta(\xi) = \frac{V(x) - V(x_m)}{U_e} \quad (2)$$

where J_{do} is the dc anode current and x_m and $V(x_m)$ are the average values of the position and potential of the minimum.* If ξ_k and η_k are the values of ξ and η at the cathode, and

$$\beta = \frac{J_{eo}}{J_{do}} = \exp \eta_k, \quad (3)$$

then, in terms of the normalized parameters,

$$\xi - \xi_k = \frac{1.25(\alpha/\beta)^{1/2}}{U_e^{3/4}} x \quad (4)$$

and

$$\eta - \eta_k = \frac{U(X)}{U_e}. \quad (5)$$

*The normalized potential should not be confused with $\eta = \left| \frac{e}{m} \right|$.

From (4) and (5),

$$\frac{dU}{dx} = 1.25 U_e^{1/4} \left(\frac{\alpha}{\beta}\right)^{1/2} \frac{d\eta}{d\xi} \quad (6)$$

Tables of the normalized electric field $d\eta/d\xi$ exist, but it is more convenient to compute it directly. For $\beta \gg 3$

$$\left(\frac{d\eta}{d\xi}\right)_{\xi=\xi_k}^2 = 2\beta - \frac{2}{\sqrt{\pi}} \eta_k^{1/2} - 1 - \frac{1}{\sqrt{\pi} \eta_k^{1/2}} \left[1 - \frac{1}{2\eta_k} + \frac{3}{4\eta_k^2} - \frac{15}{8\eta_k^3}\right] \quad (7)$$

and

$$\left(\frac{d\eta}{d\xi}\right)_{\xi=\xi_d}^2 = \frac{2}{\sqrt{\pi}} \eta_d^{1/2} \left[1 + \frac{1}{2\eta_d} - \frac{1}{4\eta_d^2} + \frac{3}{8\eta_d^3} - \frac{15}{16\eta_d^4} + \dots\right] \quad (8)$$

η_d and ξ_d are values at the anode, and (6) and (8) may be used to find the anode electric field.

In the absence of a magnetic field, the x acceleration equals

$$\frac{d^2x}{dt^2} = \eta \frac{dV}{dx} \quad (9)$$

or

$$\frac{d^2X}{dT^2} = \frac{1}{2} \frac{dU}{dX}$$

Then, for use as the approximate acceleration for each newly emitted charge,

$$\left.\frac{d^2X}{dT^2}\right|_{X=0} = .625 U_e^{1/4} \left(\frac{\alpha}{\beta}\right)^{1/2} \left(\frac{d\eta}{d\xi}\right)_{\xi=\xi_k} \quad (10)$$

The theoretical average values of the minimum potential and its position can also be calculated from (4) and (5). Noting that $\xi = \eta = 0$ when $x = x_m$ and $U = U_m$,

$$\begin{aligned} U_m &= -U_e \eta_k \quad \text{and} \\ X_m &= -0.8 \xi_k \left(\frac{\beta}{\alpha}\right)^{1/2} U_e^{3/4}. \end{aligned} \quad (11)$$

The total charge contained in the diode space can be computed from Poisson's equation,

$$\frac{d^2 V}{dx^2} = -\frac{\rho}{\epsilon_0}. \quad (12)$$

Integrating with respect to distance, and recognizing that for the model under consideration,

$$\int_0^d \rho dx = N_s \rho_s, \quad (13)$$

we obtain

$$N_s = -\frac{\epsilon_0}{\rho_s} \left(\frac{dV}{dx}\right) \bigg|_0^d. \quad (14)$$

After normalization, the average number of sheets in the space, in terms of the potential profile, is

$$N_s = \frac{2.81 n_{eo} m \Delta U_e^{1/4}}{(\alpha \beta)^{1/2}} \frac{d\eta}{d\xi} \bigg|_k^d \quad (15)$$

The plasma radian frequency at the potential minimum, from II.4(1) can be given by

$$\omega_{pm}^2 = \frac{\pi^{1/2} \eta |J_{do}|}{\epsilon_0 \sqrt{2\eta U_e}}. \quad (16)$$

Using the relation for J_{cl} , the plasma frequency, normalized to the unit frequency, $1/t_d$, is then

$$F_{pm} = f_{pm} t_d = \frac{0.1 (\alpha/\beta)^{1/2}}{U_e^{1/4}}, \quad (17)$$

or the plasma period at the potential minimum is

$$T_{pm} = \frac{t_{pm}}{t_d} = 10 U_e^{1/4} (\beta/\alpha)^{1/2}. \quad (18)$$

IV. 7. Fluctuations in the Stream

Noise in the electron stream originates in the thermionic emission process at the cathode. The mean square ac current and normal velocity corresponding to full shot noise at the cathode in a frequency band Δf are well known to be

$$\overline{i_{ox}^2(f)} = 2 e I_{eo} \Delta f \quad (1)$$

and

$$\overline{v_{ex}^2(f)} = \frac{(4-\pi) \eta k T_c}{I_{eo}} \Delta f, \quad (2)$$

where I_{eo} is the average emission current, taken positive here for electrons (Rack, 1938).

The current fluctuations transverse to the cathode plane are identical to the normal current fluctuations,

$$\overline{i_{ex}^2(f)} = 2 e I_{eo} \Delta f. \quad (3)$$

The transverse velocity fluctuations, as suggested by Van Duzer (1961) are not the same, however, and are found to be

$$\overline{v_{ex}^2(f)} = \frac{2 \eta k T_c \Delta f}{I_{eo}}. \quad (4)$$

The corresponding spectral densities, taken for positive and negative frequencies, are then

$$P_{i\text{ ex}}(f) = P_{i\text{ ez}}(f) = e I_{e0} \quad (5)$$

$$P_{v\text{ ex}}(f) = \left(\frac{4-\pi}{2}\right) \frac{\eta k T_c}{I_{e0}} \quad (6)$$

$$P_{v\text{ ez}}(f) = \frac{\eta k T_c}{I_{e0}} \quad (7)$$

As the electron stream flows away from the cathode, these spectral densities generally change. It is natural to normalize the spectral densities at any other plane to those corresponding to (5), (6), and (7) at the same average current to observe the relative variation. However, the current and electron charge required for the noise formulae are not part of the model, which only contains current and charge densities. This makes it necessary to develop the connection between the model and a physical electron stream that will give the correct noise quantities.

The basis for shot noise lies in the randomness of electron emission and the discrete nature of the electronic charge. The important quantity in shot noise is the number of independent events, i. e., the emission of an electron, occurring during a given period. In the model, the equivalent of the independent events is the emission of n sheet charges per time interval. In order for this process to have the correct amount of "shot noise" for comparison with the physical diode, the normalizing spectra (5), (6), and (7) must use the current I_0 that arises from the passage of n electrons per time interval. This relation gives the same result that one obtains by normalizing the noise spectrum due to the sequence of discrete sheets past any plane to the "shot noise" spectrum for the same average sheet "current". The relation that results,

$$n_o = \frac{J_o \Delta t}{\rho_s} = \frac{I_o \Delta t}{e}, \quad (8)$$

is the same one implied by Tien and Moshman, and Dayem by their use of an artificial area A such that $\rho_s A = e$ and $J_o A = I_o$.

We can define $k_1 = e/\Delta t$ for convenience. Then from (8),

$$I_o = k_1 n_o \quad (9)$$

and

$$i = k_1 n. \quad (10)$$

Note that e , i , and I_o are positive, while ρ_s and J_o are negative for electrons. The subscript e has been omitted to show that these relations apply at any plane.

The ac x-directed current at any plane is then

$$\tilde{i}_x = i - I_o = k_1 (n - n_o) = k_1 \tilde{n}_x. \quad (11)$$

In the planar, sheet charge model, the z -directed current cannot be meaningfully defined. For the purpose of checking the randomness of the cathode emission we can investigate the quantity

$$(n_z - n_{zo}) = \tilde{n}_z, \quad (12)$$

where n_z is the number of sheets moving in the positive z direction minus the number of sheets moving in the negative z direction.

The definition of ac velocity is more complex, since it must be completely equivalent to that definition used to obtain the velocity spectrum associated with thermionic emission. Consider the beam to be divided into many velocity classes, each with instantaneous current di , average current dI_o , and ac current $d\tilde{i}$.

The time average velocity over the whole beam is then

$$\bar{v} = \frac{\int v dI_o}{\int dI_o} = \frac{\int v dI_o}{I_o}. \quad (13)$$

Shot fluctuations in each class change the average velocity of the beam from instant to instant. For a change $d\tilde{I}_w$ in velocity class w_i the average beam velocity changes to

$$\bar{v} + \delta\bar{v}_w = \frac{\int (v dI_o + w d\tilde{I}_w)}{\int (dI_o + d\tilde{I}_w)}. \quad (14)$$

Then, if $\int d\tilde{I}_w = \delta\tilde{I}_w$,

$$\delta\bar{v}_w = \frac{(w - \bar{v}) \delta\tilde{I}_w}{I_o + \delta\tilde{I}_w}. \quad (15)$$

The current fluctuations are usually negligible compared to the average current, so summing over all velocity classes,

$$\delta\bar{v} = \sum_w \frac{(w - \bar{v}) \delta\tilde{I}_w}{I_o} \quad (16)$$

This form is equivalent to that derived by Siegman (1957a) using the density function method. The normal and transverse mean square velocity fluctuations can be computed from this by adding mean square fluctuations in each class. If each class has pure shot noise,

$$\overline{(\delta\tilde{I}_w)^2} = 2e dI_o \Delta f, \quad (17)$$

and the sum is replaced by appropriate integrals over v_x and v_y , the formulae (1) and (2) are obtained.

By adding

$$\sum_w \frac{(w - \bar{v}) dI_o}{I_o} = 0 \quad (18)$$

to $\delta\bar{v}$, a form more suitable for the Monte Carlo calculation is obtained,

$$\delta \bar{v} = \sum_w \frac{(w - \bar{v}) di_w}{I_o} . \quad (19)$$

Each velocity class in the analysis is a single sheet, carrying a current (positive for electrons) k_1 . Thus

$$\sum \bar{v} di_w = k_1 n_i \bar{v} ,$$

$$I_o = k_1 n_o , \quad (20)$$

$$\sum w di_w = k_1 \sum_{j=1}^{n_i} v_i^j ,$$

and

$$\delta \bar{v} = \tilde{v} = \frac{\sum_{j=1}^{n_i} v_i^j - n_i \bar{v}}{n_o} . \quad (21)$$

This is the same formula for ac velocity used by Tien and Moshman, and holds for z-directed velocities as well, by replacing $v = v_x$ by v_z and retaining n_i and n_o as total number of sheets per interval.

The average beam velocity, \bar{v} , is defined in an ensemble sense. Then

$$\sum_{i=1}^N n_i = n_o N ,$$

the total number of charges passing the reference plane over the entire duration of N time intervals can be thought of as a single simultaneous observation of $n_o N$ individual systems, and

$$\bar{v} = \frac{\sum_{i=1}^N \sum_{j=1}^{n_i} v_i^j}{n_o N} . \quad (22)$$

For the emission process to be ergodic, the ensemble and time averages must be equal. The time average of the total velocity is

$$\sum_{i=1}^N \left[\frac{\sum_{j=1}^{n_i} v_i^j - (n_i - n_0) \bar{v}}{n_0 N} \right] = \bar{v}, \quad (23)$$

and the ergodic hypothesis is satisfied.

After a discussion of spectral theory in general, the spectra of the fluctuating quantities just developed will be normalized to the values corresponding to cathode emission at the same average current.

IV. 8. Spectral Theory

Considerable information about the physical processes taking place in the diode can be obtained from a spectral analysis of the fluctuating currents and velocities. However, there are several problems to be considered in going from the theoretical calculation, with an infinite amount of continuous data, to the practical one, involving limited discrete data. The following brief treatment is based on the work of Blackman and Tukey (1958), and is similar to the work of Dayem.

A random time function $g(t)$, continuously defined and finite over all time, has a true self-power density spectrum $P_g(f)$, and a true autocorrelation function $C(\tau)$ related by

$$C(\tau) = \lim_{T \rightarrow \infty} \frac{1}{2T} \int_{-T}^T g(t) g(t + \tau) dt, \quad (1)$$

$$P_g(f) = \int_{-\infty}^{\infty} C(\tau) e^{-j\omega\tau} d\tau = 2 \int_0^{\infty} C(\tau) \cos \omega\tau dt \quad (2)$$

where $\omega = 2\pi f$, and τ may be termed a "lag" time.

The Monte Carlo calculation yields a finite collection of discrete values for $g(t)$, each one an average of the actual $g(t)$ over a time interval Δt . Thus, if

$$w(t) = \frac{1}{\Delta t} \int_{s=t-\Delta t}^t g(s) ds, \quad (3)$$

then

$$P_w(f) = \left(\frac{\sin \pi f \Delta t}{\pi f \Delta t} \right)^2 P_g(f) \quad (4)$$

can be obtained. For $f\Delta t \ll 1$, $P_w(f)$ is a close approximation to the true spectrum. However, for $f\Delta t \sim 1$, $P_w(f)$ is attenuated considerably.

With data available only at discrete intervals spaced Δt apart, the true spectrum is imaged about $f_0 = 1/\Delta t$. This process, called aliasing, produces a spectrum

$$\tilde{P}_w(f) = P_w(f) + \sum_{l=1}^{\infty} \left[P_w(f - l f_0) + P_w(f + l f_0) \right] \quad (5)$$

Figure IV. 8-1 shows how $P_w(f)$ might be aliased.

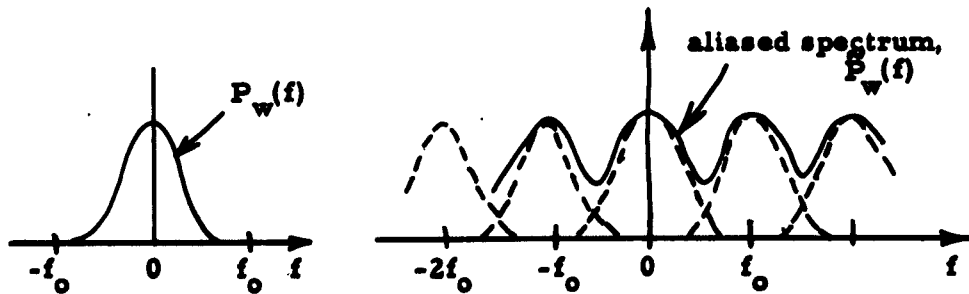


Figure IV. 8-1. Aliasing of $P_w(f)$

Aliasing would normally produce an erroneous result, unless the true spectrum were limited so that $P_w(f)$ vanished for $|f| < f_0/2$. Fortunately, the averaging process produces a spectrum that is attenuated in this region, and the problems caused by averaging and aliasing can be ignored if the frequency range of interest is restricted to $f_{\max} \lesssim f_0/10$.

The limited period of time, t_n , for which data is available, provides the most serious problem. If the correlation function is computed for all lags up to the maximum lag τ_m , an equivalent correlation function is produced, that is the product of $C(\tau)$ with a "lag window,"

$$\begin{aligned} D_0(\tau) &= 1, \quad |\tau| \leq \tau_m \\ &= 0, \quad |\tau| > \tau_m. \end{aligned} \quad (6)$$

The resulting spectrum, $\bar{P}_w(f)$, is a convolution of $\tilde{P}_w(f)$ with $Q_0(f)$, the Fourier transform of $D_0(\tau)$. $\bar{P}_w(f)$, given by

$$\bar{P}_w(f) = \int_{-\infty}^{\infty} Q_0(f - \nu) \tilde{P}_w(\nu) d\nu \quad (7)$$

where

$$Q_0(f) = 2\tau_m \left(\frac{\sin 2\pi f \tau_m}{2\pi f \tau_m} \right) \quad (8)$$

is a weighted-over-frequency spectrum. The weighting factor $Q_0(f)$ has undesirable sidebands which cause $\bar{P}_w(f)$ to depend not only on f , but also on adjacent frequencies. As τ_m approaches infinity, the sidebands of $Q_0(f)$ are reduced, until finally, as the time interval becomes infinite, $Q_0(f)$ becomes the delta function $\delta(f)$ and $\tilde{P}_w(f) = \bar{P}_w(f)$.

The modified lag window,

$$D(\tau) = 1/2 \left(1 - \frac{\cos \pi \tau}{\tau_m}\right); \quad |\tau| < \tau_m$$

$$= 0 \quad ; \quad |\tau| > \tau_m,$$
(9)

has a spectrum with smaller side lobes and greater concentration of "power" near zero frequency. Multiplication of $C(\tau)$ by $D(\tau)$ is equivalent to producing a smoothed spectrum

$$P(f) = \frac{\bar{P}_w(f)}{2} + \frac{\bar{P}_w(f+1/2\tau_m) + \bar{P}_w(f-1/2\tau_m)}{4}.$$
(10)

Although the resulting spectrum $P(f)$ is more nearly equal to $P_g(f)$ than $\bar{P}_w(f)$ would be, there is still considerable overlap for frequencies separated by $1/2\tau_m$. Frequencies separated by $1/\tau_m$ or more are nearly independent, and $1/\tau_m$ is called the resolution. It is pointless to calculate spectral estimates spaced closer than $1/2\tau_m$, although estimates spaced $1/2\tau_m$ are needed for IV. 8(10).

The finite period of data t_n also causes a spectral "variability." Economic considerations will lead to a limit on the size of t_n . Although τ_m can theoretically approach and equal t_n , producing the most resolved spectrum, this produces an error in $C(\tau)$ for intervals where $\tau_m < \tau < t_n$. The accuracy of the spectral estimate depends on t_n/τ_m , and can be expressed in terms of

$$k = 2 \left(\frac{t_n}{t_m} - \frac{1}{3} \right) \approx 2 \frac{t_n}{\tau_m},$$
(11)

the equivalent number of degrees of freedom in a chi-square distribution.

For 80% of all spectral estimates for a given frequency to fall within a given range about the true spectrum, Table IV. 8-1 gives the corresponding value of k .

VARIABILITY TABLE IV. 8-1

k	Range
10	. 49 - 1. 60
30	. 69 - 1. 39
50	. 75 - 1. 26
100	. 82 - 1. 18
200	. 873 - 1. 139

If one spectral estimate P is considered, there is an 80% confidence that the true spectrum lies within $P/.75$ and $P/1.26$ for $t_n/\tau_m = 30$. For a given t_n , τ_m must be made small enough to provide a minimum variability, but large enough to produce a usable frequency resolution.

If $g(t)$ and $h(t)$ are any arbitrary finite time functions defined continuously over the same interval, then the cross-power density spectrum can be defined in terms of the cross-correlation functions as follows. If $A(\tau)$ and $P_{g,h}(f)$ are Fourier transform pairs, such that

$$A(\tau) = \int_{-\infty}^{\infty} P_{g,h}(f) e^{j\omega\tau} df \equiv \lim_{T \rightarrow \infty} \frac{1}{2T} \int_{-\infty}^{\infty} H(f) G^*(f) e^{j\omega\tau} df, \quad (12)$$

where $H(f)$ and $G(f)$ are the Fourier transforms of $h(t)$ and $g(t)$, then it can be shown that

$$A(\tau) = \lim_{T \rightarrow \infty} \frac{1}{2T} \int_{-T}^T g(t) h(t+\tau) dt. \quad (13)$$

If

$$B(\tau) = \lim_{T \rightarrow \infty} \frac{1}{2T} \int_{-T}^T h(t) g(t+\tau) dt, \quad (14)$$

$$\text{then } A(\tau) = B(-\tau) \quad (15)$$

and

$$B(\tau) = \int_{-\infty}^{\infty} P_{g,h}^*(f) e^{j\omega\tau} df. \quad (16)$$

The real part of $P_{g,h}(f)$, written $\text{Re}[P_{g,h}(f)]$, can be obtained from

$$\text{Re}[P_{g,h}(f)] = \frac{1}{2} \int_{-\infty}^{\infty} [A(\tau) + B(\tau)] e^{-j\omega\tau} d\tau = \int_0^{\infty} [A(\tau) + B(\tau)] \cos \omega\tau d\tau \quad (17)$$

and the imaginary part from

$$\text{Im}[P_{g,h}(f)] = \frac{1}{2} \int_{-\infty}^{\infty} [A(\tau) - B(\tau)] e^{j\omega\tau} d\tau = \int_0^{\infty} [B(\tau) - A(\tau)] \sin \omega\tau d\tau. \quad (18)$$

The correlation coefficients and spectral densities for the discrete data case can be obtained by dividing t_n and τ_m into N and M intervals of size Δt . Then any particular correlation coefficient $C(\tau)$ becomes

$$C(l \Delta\tau) = C_l = \frac{1}{N-l} \sum_{k=1}^{N-l} g^k g^{k+l}, \quad (19)$$

where τ is replaced by $l \Delta\tau = l \Delta t$.

If l is allowed to vary from zero to m , and f is replaced by $r \Delta f$,

$$\text{where} \quad \Delta f = \frac{1}{2\tau_m} = \frac{1}{2M \Delta t} \quad (20)$$

then

$$P(r \Delta f) = \Delta t \left[C_0 + 2 \sum_{l=1}^{M-1} C_l \cos \frac{\pi r l}{M} + C_m \cos r \pi \right]. \quad (21)$$

The formulas for digital computation can now be developed in normalised form from the fluctuation relations, the general spectral theory, and the proportionality between current and numbers of sheet charges.

The true correlation coefficients can be written in terms of the normalized velocity u and number of sheets n as

$$A_l = k_1 v_d \sum_{i=1}^{N-l} \tilde{u}_i \tilde{u}_{i+l} / N-l = k_1 v_d \bar{A}_l \quad (22)$$

$$B_l = k_1 v_d \sum_{i=1}^{N-l} \tilde{n}_i \tilde{u}_i / N-l = k_1 v_d \bar{B}_l \quad (23)$$

$$C_l = k_1^2 \sum_{i=1}^{N-l} \tilde{n}_i \tilde{n}_{i+l} / N-l = k_1^2 \bar{C}_l \quad (24)$$

$$D_l = v_d^2 \sum_{i=1}^{N-l} \tilde{u}_i \tilde{u}_{i+l} / N-l = v_d^2 \bar{D}_l \quad (25)$$

Here \tilde{n} and \tilde{u} stand for the ac values of either x - or z -directed fluctuations, and the barred coefficients are normalized.

Normalization of the current spectrum is made to the pure shot noise spectrum for the same average current.

Since eI_0 is equivalent to $k_1^2 n_0 \Delta t$,

$$P_i(r) = \frac{\Delta t k_1^2 [\bar{C}_0 + 2 \sum \bar{C}_l \cos \frac{\pi r l}{M} + \bar{C}_m \cos r \pi]}{k_1^2 n_0 \Delta t} \quad (26)$$

or

$$P_i(r) = \frac{[\bar{C}_0 + 2 \sum \bar{C}_l \cos \frac{\pi r l}{M} + \bar{C}_m \cos r \pi]}{n_0} \quad (27)$$

Normalization of the velocity spectrum is made to the cathode velocity fluctuation spectrum for the same I_0 . If γ represents the constant $(4-\pi)/4$ for the x fluctuations and $1/2$ for the z fluctuations,

$$\bar{P}_v(r) = \frac{\Delta t v_o^2 [\bar{D}_o + 2 \sum \bar{D}_l \cos \frac{\pi r l}{M} + \bar{C}_m \cos r \pi]}{2 \gamma \eta k T_c \Delta t / e n_o} \quad (28)$$

or

$$P_v(r) = \frac{n_o [\bar{D}_o + 2 \sum \bar{D}_l \cos \frac{\pi r l}{M} + \bar{C}_m \cos r \pi]}{\gamma U_e} \quad (29)$$

Use has been made of the equivalence between I_o and $n_o e / \Delta t$.

In a similar manner, the cross-power spectral densities can be normalized to their values at the cathode for the same I_o . The resulting relations are:

$$\text{Re} [\bar{P}_{i, v(r)}] = \frac{[\bar{A}_o + \sum (A_l + B_l) \cos \frac{\pi r l}{M} + \frac{(\bar{A}_m + \bar{B}_m)}{2} \cos r \pi]}{[\gamma U_e]^{1/2}} \quad (30)$$

and

$$\text{Im} [\bar{P}_{i, v(r)}] = \frac{[\sum (\bar{B}_l - \bar{A}_l) \sin \frac{\pi r l}{M}]}{[\gamma U_e]^{1/2}} \quad (31)$$

The frequency increment for the spectral estimate is

$$\Delta F = \frac{t_d}{2 M \Delta t} = \frac{m \Delta}{2 M} \quad (32)$$

in normalized form, since the time samples are taken every $1/m \Delta$ of the unit time t_d .

V. MULTI-VELOCITY MODEL OF THE CROSSED-FIELD DIODE: RESULTS

V.1. The Computer Calculation

The bulk of the calculations, along with much testing of the programs, was carried out on an IBM 704 high speed digital computer. The economics of computer usage necessarily placed

an upper limit on the real time available for each run, and the number of runs that could be made altogether. Some trial runs were made to determine adequate balance between computer time and obtainable information and accuracy. The final choice of parameters was somewhat flexible, but was, of course, guided by these and the many theoretical considerations.

The computation was divided into two parts: a) the Monte Carlo simulation itself and b) the spectral analysis of the fluctuating quantities. In addition to printed output prepared from the information recorded at each step, i. e., emission velocity and current, position and potential at the minimum, total current, number of charges in the space, etc., a magnetic tape containing the necessary input quantities for the spectral analysis was "written." For each run this tape contained all the velocities and currents at the cathode, anode, and potential minimum reference plane and the potential and position of the minimum.

The currents were represented by the number of charges, n_i , crossing the particular plane during the time interval, while the velocities were stored as the sum of velocities of the n_i charges. This was convenient for use in the spectral analysis program, although it caused difficulties in obtaining the velocity distributions to be described in a following section. The savings obtained by preparing the tape in this manner outweighed the disadvantage of slightly inaccurate distributions.

Both normal and transverse number and velocity were recorded. The spectral analysis program, using the theory of Chapter IV, read the prepared magnetic tape and computed correlation functions and spectral densities from the temporal data.

Several parameters could be prescribed independently of computer running time considerations. One of these is U_e , the ratio of thermal equivalent potential at the cathode to anode average potential. The choice of $U_e = 0.01$ agrees with the values $kT_c/e = 0.1$ volts and $V_d = 10$ volts used by Tien and Moshman (1956) and Dayem (1960) in their studies. The ratio of saturated emission

current to anode current β could, of course, not be prescribed in this dynamic analysis. However, by choosing α , the ratio of emission current to Child-Langmuir current, to equal 7, the equivalent for the parameters of the Tien-Moshman and Dayem diodes, β is found to equal 5 when the magnetic field is zero, according to the dc theory of the space-charge-limited diode.

For the $B = 0$ case, these parameters lead to a normalized plasma frequency $F_{pm} = 0.375$ or period $T_{pm} = 2.667$ at the potential minimum (from IV. 6(17) and (18)). For accurate trajectories, there should be many time intervals per plasma period. Also, from the definition of t_d , a zero initial velocity charge should cross the potential minimum-anode space in three time units. Then a typical transit time across the diode for a charge with initial velocity should also be around $3t_d$, a time on the order of the plasma period in this case. By setting m_Δ , the number of steps per t_d , equal to 25, there is an adequate number of steps per plasma period or transit time for all values of B/B_c , and accurate trajectories can be expected.

We wish to be able to investigate the phenomena near the potential minimum plasma frequency discussed in Chapter II. There should then be several frequency intervals ΔF between zero and F_{pm} . Since $\Delta F = m_\Delta / 2M$, a choice of M , the number of lags used in the spectral analysis, of 100 gives $\Delta F = 0.125$. The computer time for both the synthesis and the spectral analysis depends on the total number of time intervals N . As $k = 2N/M$ increases, the variability of the estimates decreases. However, an increase in k from 30 to 50 only decreases the spread from 70% to 51% of the mean spectral estimate. Choosing N equal to 1500 ($k = 30$) gives a rather wide spread, but it is adequate for most results, as the following sections will show.

A somewhat separate choice is the number of charges in the diode, N_g , which in the ordinary diode is proportional through IV. 6(15) to n_{eo} , the average number of charges emitted per step.

Although the spectral considerations do not require this to be a large number, for accurate representation of an actual beam, N_s should be large enough to make the self electric field of a charge small compared with the total electric field at some point in the diode. In lieu of a more detailed formulation of this requirement, the anode electric field was chosen for comparison with the self electric field. A choice of $n_{eo} = 5$ was found to give between 100 and 150 charges in the diode for the various values of B/B_c used. In section V.6, the requirement on N_s is discussed in more detail, and it is shown that the values of N_s obtained here are sufficiently large for good results.

The magnetic field parameter was varied between zero and a value slightly greater than unity, where the one-dimensional model can no longer adequately represent a typical "short" crossed-field gun. Larger values of B/B_c might represent the so-called "long" gun, which contains many cycloids of electron motion. For comparison with the Van Duzer-Whinnery (1961) approximate analysis of the crossed-field potential minimum, an intermediate value for B/B_c of 0.75 was used. Table V.1-1 summarizes the parameters and compares them with the equivalent values obtained from the data of Tien-Moshman, Dayem, and Van Duzer-Whinnery.

Table V.1-1. Comparison of parameters for the Monte Carlo calculation

	This Study	Tien-Moshman	Dayem	Van Duzer-Whinnery Approximate Theory
α	7	7	7	6.9
β	5	5	5	7.3
U_c	0.01	0.01	0.01	_____
B/B_c	0, 0.75, 1.05	0	0	0.75
m_Δ	25	50	50	_____
n_{eo}	5	8.182	8.182	_____
N	1500	1920	7000	_____
M	100	*192	125-500	_____
ΔF	0.125	*0.13	0.2-0.05	_____

*Tien and Moshman used a smoothed, extended correlation function.

V.2. A Check on the Emission Process

The emission formulae of Section IV.5 are the heart of the Monte Carlo method. Using them, the random nature of thermionic emission is simulated in the calculation. The emission current and velocity averages and frequency spectra are a check on the total emission process. All of the computer runs used the same initial random number* and the sequence of random numbers, obtained as described in Section IV.6, was then the same for each run. Therefore identical emission velocities and numbers were used from run to run.

For a sufficiently long Monte Carlo run, the results should be independent of the particular emission characteristics used. However, for limited data we will see that the spectra of the emission quantities are not perfect. Differences arising from the use of different random numbers do exist in the spectra. The use of identical emission characteristics from run to run makes interpretation of other effects in the diode less difficult, and eliminates the need to compute and display the additional cathode spectra. In Section V.6, we will see that the spectra at the anode for runs with different spectra at the cathode are quite similar. Therefore the use of one set of random numbers for all runs does not appear to introduce any major statistical errors.

Table V.2-1 compares the calculated average values of the emitted quantities with the theoretical values obtained from IV.5(10) with $U_0 = 0.01$.

Emission current is represented by the number of sheets moving in the positive coordinate direction past the reference plane. Velocity has been normalized to v_d , the velocity equivalent of the anode potential.

As described previously, the current spectra were normalized to full shot noise at the same average current. Only the x-directed

*This initial number had the octal representation $R_0 = 042226310600$.

	Theoretical	Calculated	% Error
\bar{n}_{xe}	5.00000	5.02533	0.507 %
\bar{n}_{ze}	0.00000	0.04933	0.980 % \bar{n}_{xe}
\bar{u}_{xe}	0.08862	0.08932	0.790 %
\bar{u}_{ze}	0.00000	0.00131	1.480 % \bar{u}_{xe}
$\overline{u^2_{xe}}$	0.01000	0.01015	1.500 %
$\overline{u^2_{ze}}$	0.00500	0.00481	3.800 %

Table V.2-1. Emission parameters

current spectra have been computed, since the z-directed current cannot be meaningfully defined for this model. The x-directed velocity spectra were normalized to the Rack velocity spectrum, while the z-directed velocity spectra were normalized to their cathode value, $(2/4-\pi)$ times the Rack value, both for the average current in the beam at that plane.

These normalized spectra at the cathode would have a value of unity for an infinite length of computer data. However, with the equivalent number of degrees of freedom equal to 30, we expect 80% of all spectral estimates for a given frequency to fall within a range from 0.69 to 1.39 of the true spectral density, unity. Since values at each frequency are independent, we can expect 80% of all values from a single run to lie within this range.

Figure V.2-1 shows the computed x-directed fluctuations, weighted over frequency according to IV.8(10). Unless specially noted, all spectra presented here have been weighted in the same manner. The x-directed current and velocity spectra fall within the limits of the 80% range far more than 80% of the frequency band. The large variations with frequency are a result of the limited quantity of data available. They preclude obtaining much precise information on exact spectral values, but are not so large as to mask out many important phenomena.

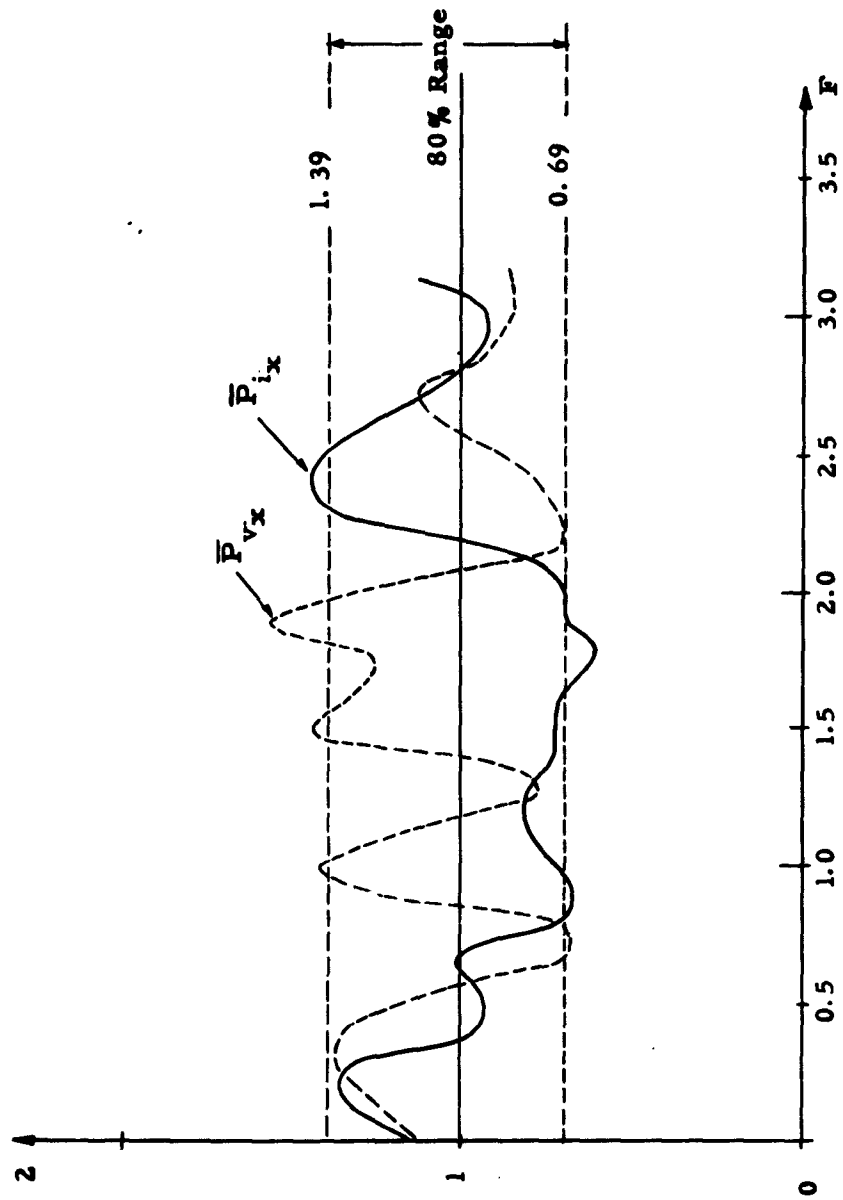


Figure V.2-1. x-directed spectra at the cathode

The z-directed fluctuations (Figure V.2-2) show much the same result. The velocity spectrum seems to have a somewhat low value, yet it easily falls within the 80% range. The spectrum of n_z (see Section IV. 7) is included to show that the selection of positive or negative transverse emission direction (Eqn. IV. 5(16)) is random. Normalization has been made to "shot noise" for an average sheet current \bar{I} .

The cross-power density spectra have been normalized to the square root of the product of the full shot noise spectrum and the Rack velocity spectrum. The real and imaginary parts of the cross-power spectrum at the cathode are shown in Figure V.2-3. They vary near zero and do not attain values greater than 0.2. The fact that the spectra are not zero does not necessarily mean that there exists correlation between the velocity and current fluctuations at the cathode. Rather, the finite length of available data tends to produce non-zero spectra. The spectra are within the range of variability, and no further detailed information is obtainable in this range.

V. 3. Noise Current at the Minimum with Zero Magnetic Field

The approximate analysis of Chapter II describes the effects of the potential minimum on the noise currents in the space-charge-limited diode with no magnetic field. The purpose of this section is to compare the results of Chapter II with those obtained using the more detailed Monte Carlo method as well as other theories.

Both the short- and open-circuited diodes have been treated. The resulting current spectra were normalized to full shot noise, so that they are equivalent to the reduction factor curves of the approximate analysis. The spectra were evaluated at $x/d = 0.05$, which is 1.2 times the theoretical average position of the potential minimum (Table V.4-1). This is the same point used in the Tien-Moshman and Dayem analyses, and has been chosen here for comparative purposes. Additional runs could be made for other nearby reference planes to determine the dependence of the resulting spectra on the particular plane. However, this would be very time

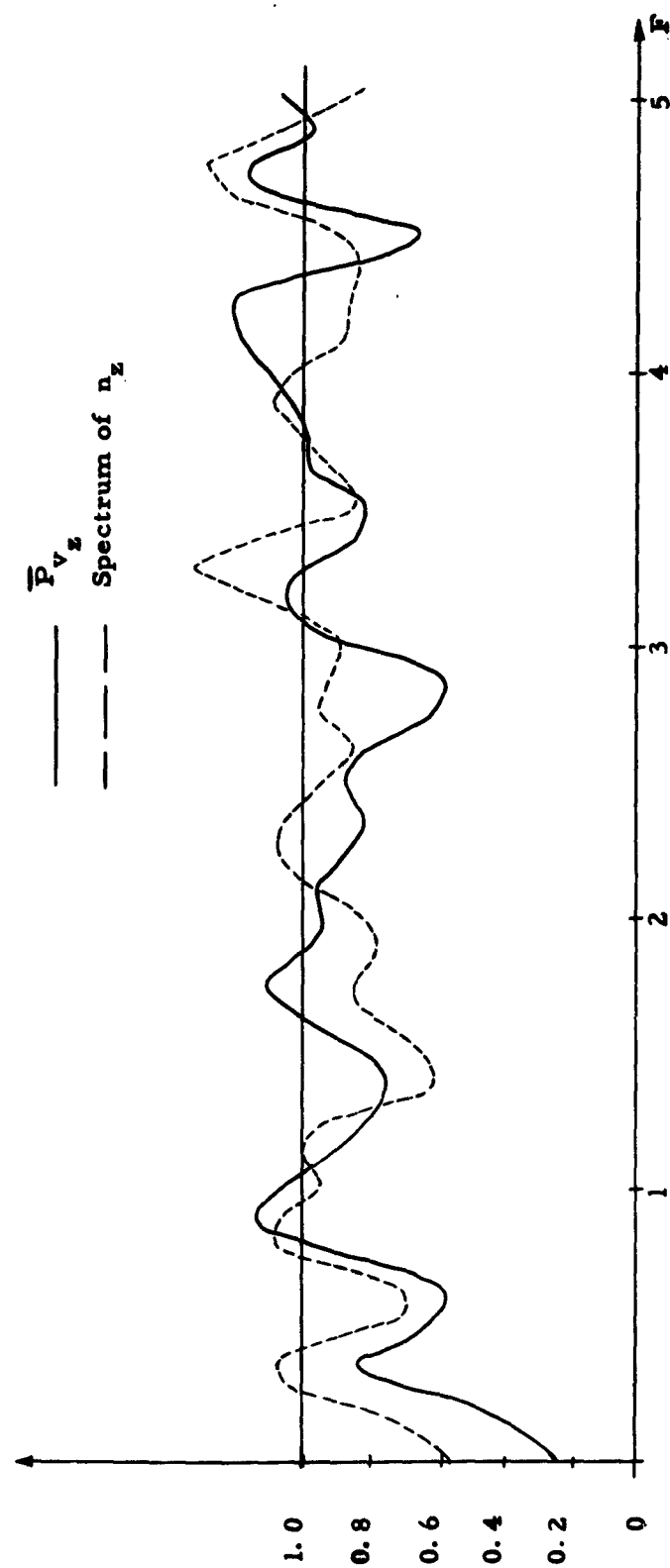


Figure V.2-2. z-directed spectra at the cathode

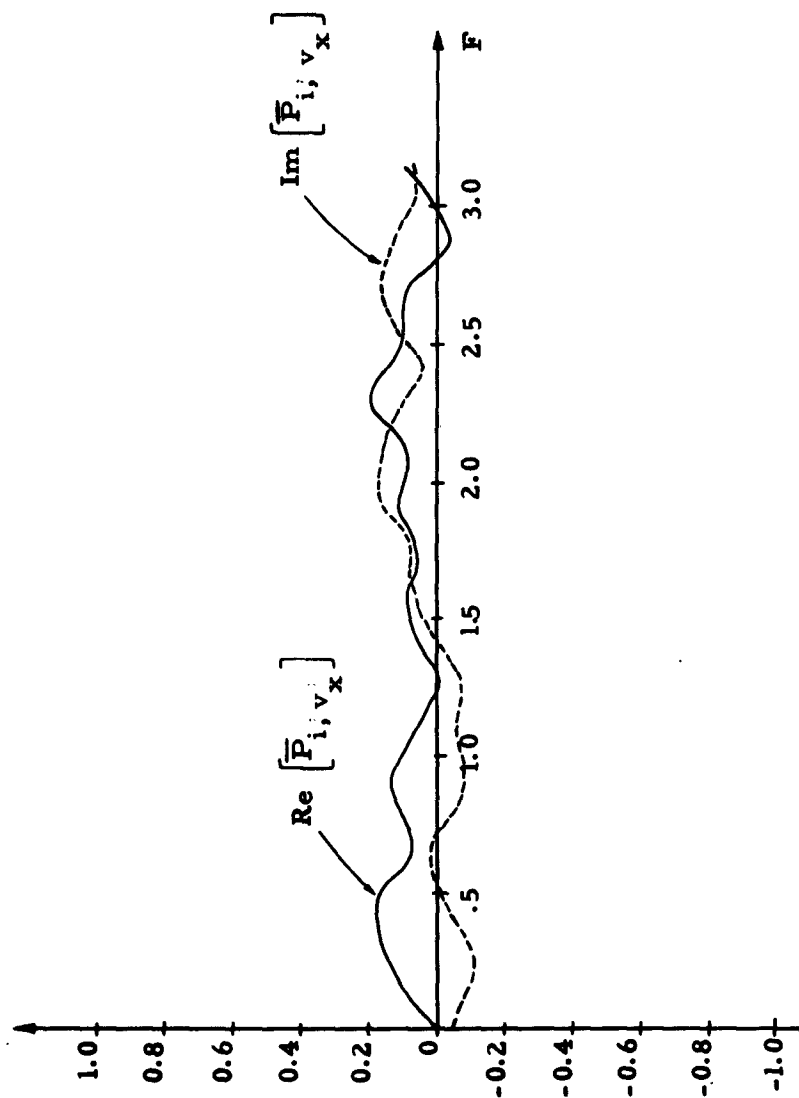


Figure V.2-3. Cross-correlation spectra at the cathode

consuming, and it was felt that the results would be relatively independent of the exact plane chosen.

Figure V. 3-1 shows the reduction factors obtained from the short- and open-circuit runs. These curves have been weighted over frequency, which has the effect of smoothing out any peaks or dips. The weighting procedure is generally useful in obtaining more accurate spectral estimates, but when ΔF is large, weighting can easily remove the existing fine structure of a particular spectrum. The most interesting observation is that there is little difference between the reduction factors for the two cases. At small values of F , there is smoothing of the current fluctuations, while at higher frequencies, R^2 varies around unity. The spectral estimates are connected with straight lines in this case, to underline the fact that information about the spectrum between the estimates is unavailable. Thus there might be a much larger current peak just below $F = 0.5$, but the curves show only a small one at $F = 0.5$ that could be entirely a result of the variability of the estimates.

Figure V. 3-2 is a comparison of the results for the short-circuited diode with other theories. The spectrum from Figure V. 3-1 is repeated in its unweighted form, for comparison with the Tien-Moshman result, which was also an unweighted spectrum. Included too is the weighted average R^2 from Chapter II. As described in Section V.1, the same physical parameters were used for this Monte Carlo study as for the Tien-Moshman calculation. However, since the number of steps and charges emitted per step were different statistically, different spectra could be expected.

The agreement between the two calculations is then quite good, even to the presence of a dip in R^2 near $F = 0.25$. It is unlikely that this is purely coincidental. Although the individual curves of $|r(a, \eta_1, \eta_0)|^2$ from the approximate theory do not show this dip, the weighted curve shown suggests that such a dip might be found if many more critical charge classes were included in the calculation. The conclusion about the "Tien dip" is still not

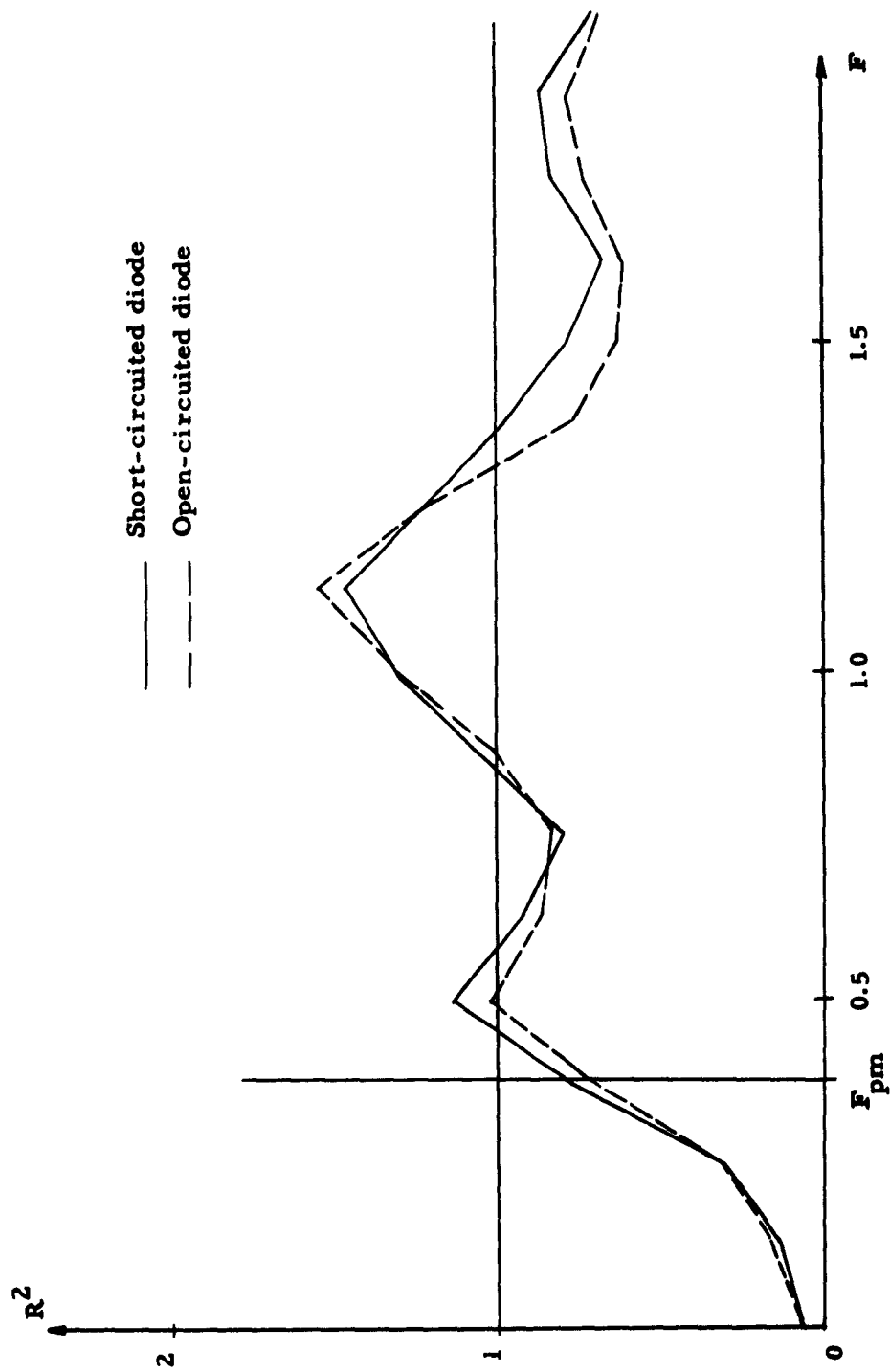


Figure V. 3-1. R^2 for short- and open-circuited diodes

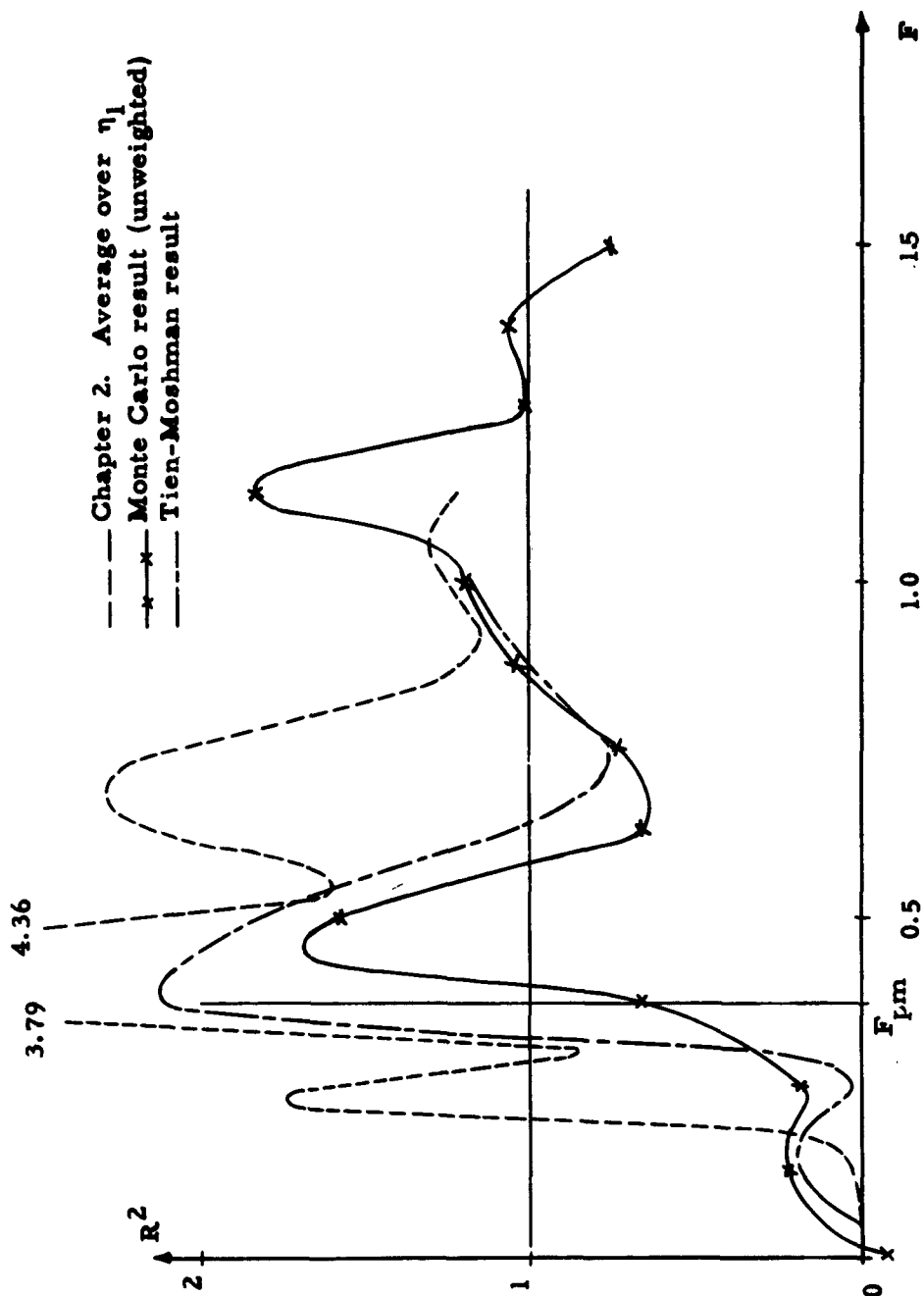


Figure V.3-2. Comparison of R^2 with the results of other theories for the short-circuited diode

clear, but it does seem likely that such a dip in R^2 exists in this model. A choice of beam parameters in a tube such that this dip fell in the operating band would significantly lower the tube's noise figure.

The agreement between the two Monte Carlo studies extends to the locations of the main peak near $F = 0.4$ and the dip near $F = 0.7$. Tien and Moshman used a pre-smoothed auto-correlation function that had been extended artificially to infinity to evaluate their spectrum. This is probably the cause of the higher amplitude of the peak they found. Also, the exact location of the peak found here could lie within the frequency interval ΔF , and its exact height could then not be determined by this method. The agreement between the two Monte Carlo results adds to the argument that weighting can easily smear out important features of the spectra.

The results for the open-circuited diode are compared in Figure V.3-3 with other theories. The weighted spectrum from Figure V.3-1 has been graphically smoothed, and is compared with Dayem's Monte Carlo result. Again, as in the short-circuited diode, the same physical parameters were used. However, Dayem's spectral result was obtained for a run nearly five times as long as this one, and should have been more accurate. Despite the same parameters, there is an obvious disagreement between the two results. Dayem's spectrum does not show the peaks and dips predicted here. The variability of the estimates is not large enough to explain this discrepancy, which would appear to be even larger had the unweighted data been compared. These results have been carefully checked, and no errors could be detected. Aside from an irregularity* in his emission process, Dayem's

*Dayem used $\text{Cum } P(s-1/2) < R \leq \text{Cum } P(s+1/2)$ in place of IV.5(3) and had some anomalous results in comparing theoretical and computed values for N_s .

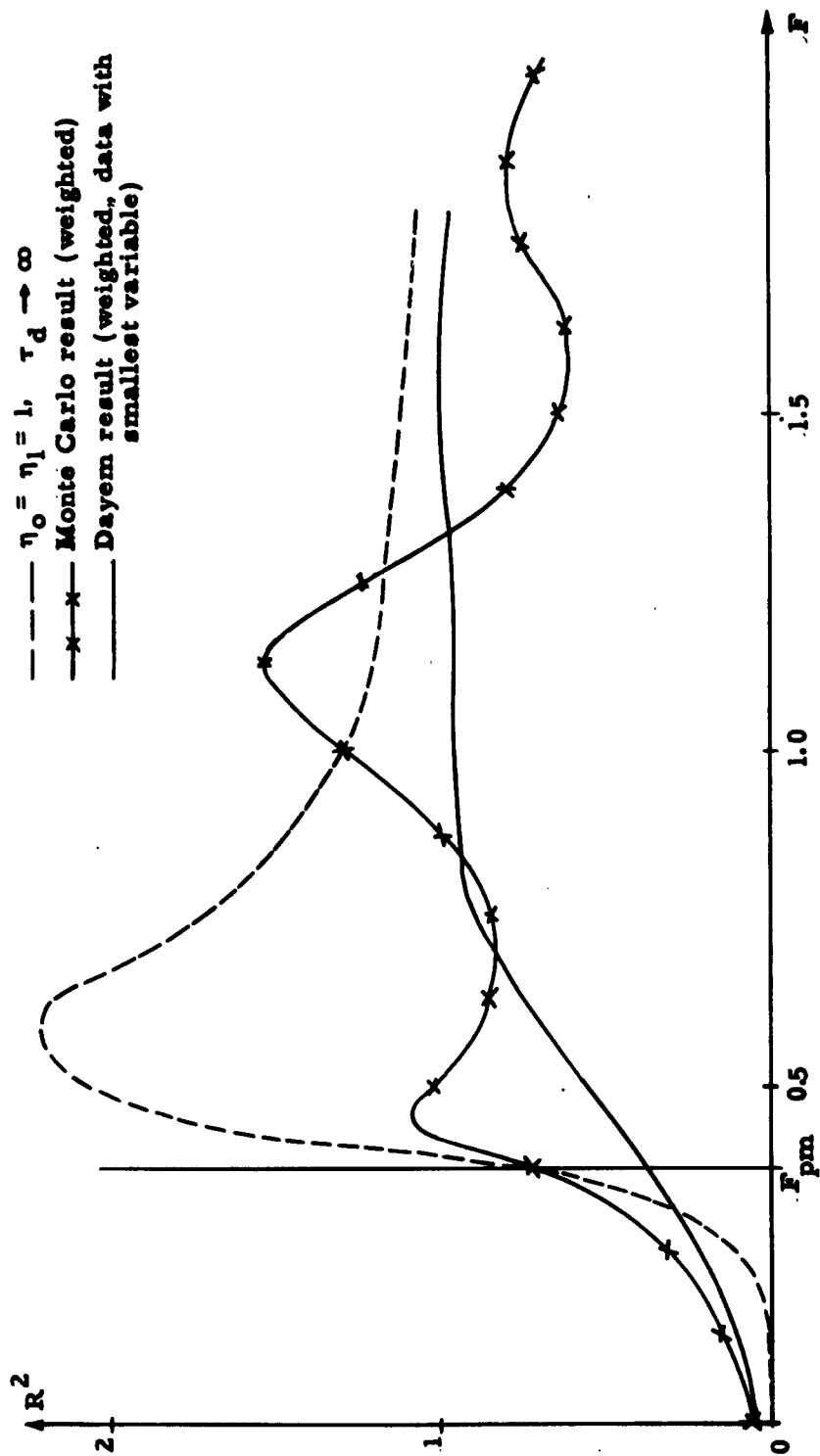


Figure V.3-3. Comparison of R^2 with the results of other theories for the open-circuited diode

formulation is identical to that described in Chapter IV. No conclusion can be drawn at present as to the reason for the difference between the two results.

Also included in Figure V. 3-3 is Whinnery's (1960) result for the infinite diode with $I_e/I_d = 5$, the same value used here, and $\eta_0 = \eta_1 = 1$. This curve is very similar to that obtained by Siegman and Watkins (1957) for $I_e/I_d = 6$, $\eta_1 = 1$ for the open-circuited diode, where the reduction factor had been averaged over η_0 . The fact that a peak near $F = 0.5$ appears in Whinnery's result seems reasonable from the physical picture of Chapter II. There the peak is not dependent on the particular choice of open- or short-circuit model, but is due to the compensating mechanism involving critical charges. Dayem's spectrum is in general agreement with the detailed analysis of Vivian (1960) and to the result of Watkins' (1955) approximate analysis, which ignored the transit time of charges to the minimum. The result of this Monte Carlo study, however, is closer in form to the approximate analysis of Whinnery and Siegman-Watkins, which included the effects of this transit time. Until further evidence is available, nothing further can be concluded about the exact nature of R^2 at the potential minimum for the open-circuited diode. Additional computation is evidently required to settle the question.

V. 4. Dependence of the Average Beam Quantities on B/B_c

A number of runs were made with the same basic parameters to study the effect of the magnetic field on noise transport. For this purpose, B/B_c was set equal to 0, 0.75, and 1.05 for both the short- and open-circuited diodes. In addition, after it had been found that the self-force term had been left out of the electric field equations for the short-circuited diode, a rerun for $B/B_c = 1.05$ was made to check the effect of the error. This is reported in Section V. 6. An additional short-circuited diode run with $B/B_c = 1.10$ was intended to check the extension to higher magnetic fields, but the spectra were not significantly different from the $B/B_c = 1.05$ run. The rf behavior for these runs will be discussed in the following sections.

Here we wish to compare the average beam quantities only. For the sake of comparison, the runs will be labeled in the following manner. O C - 0.75 represents the open-circuited diode with B/B_c equal to 0.75. The corresponding short-circuited diode run is designated SC - 0.75. The subscript "ns" designates the runs that included no self-force terms.

The S C runs were started after an arbitrary diode filling was allowed to reach equilibrium (see Section IV. 2). This usually took 50 to 100 time intervals. Incomplete attainment of equilibrium is believed to be the cause of some peculiarities in the spectra. The O C runs, which require an initial electric field and average anode current for IV. 3(21), were started after 50 to 200 steps of operation following the corresponding S C run. The initial field and number of anode-crossing charges per time interval were obtained as average values from the S C runs. Although the initial charges were different from run to run, the same emission characteristics were used for all runs.

From Section IV. 6 several average quantities can be evaluated for comparison with the zero magnetic field runs. This theoretical information is not readily available for the crossed-field cases.

For J_{eo}/J_{do} equal to 5,

$$\eta_k = 1.609 \quad (1)$$

$$\text{and } \xi_k = 1.8845.$$

From IV. 6(5),

$$\eta_d - \eta_k = 1/U_e \quad (2)$$

Then using $\eta_d = 98.391$ and the other parameters of the analysis in the equations of Section IV. 6, Table V. 4-1 can be constructed. It compares the theoretical quantities with the corresponding values obtained from the runs O C-0.00 and SC-0.00.

	SC-0.00	% Error	Theoretical Value	OC-0.00	% Error
U_m	-0.0191	18.6 %	-0.0161	-0.0197	23.6 %
X_m	0.0440	9.2 %	0.0403	0.0467	13.4 %
I_a/I_s	0.2000	0 %	0.2000	0.2001	0.05 %
N_s	115.430	3.99 %	111.0	115.492	4.04 %
E_d	1.5140	1.2 %	1.496	1.5109	1.0 %
V_d	1.0000	0 %	1.0000	0.9879	1.21 %

Table V.4-1. Comparison of average values with theory for $B/B_c = 0$

The average values for the open- and short-circuited diodes are quite close, and the differences from the theoretical values are small in most cases. The only exceptions are the position and potential of the minimum. The average minimum is deeper and further from the cathode than the dc theory predicts. No suitable explanation for this could be found.

Table V.4-2 compares the average minimum potential and position for each run, as well as average values of the total current, number of charges in the space N_s , anode electric field E_d and anode voltage V_d .

The currents in run OC-1.05 are lower than the corresponding currents in SC-1.05 because n_{d0} was inadvertently set at 0.1553, the value from SC-1.10, instead of 0.2787. Run OC-1.05 is, in a sense, then, a hybrid run.

The electric fields were not computed at first for the "ns" runs. A rerun of SC-0.00 with n_{e0} equal to unity was used to obtain the value in the table. The corresponding spectra for this rerun will be discussed in a following section. The electric field to

start OC-0.75 was taken from a 200 step test run.

Table V. 4-3 shows the x-directed average numbers and velocities at the reference planes within the diode. The z-directed quantities are tabulated in Table V. 4-4. In addition to the anode reference plane, the reference plane at $X = 0.05$ was chosen for each run. This plane was near the potential minimum for all magnetic fields, although sometimes on the cathode side of the minimum. This could not be known in advance, due to the nature of the analysis. Only the transmitted stream, moving in the positive x direction, was taken into account for evaluation of velocities and currents.

Run	V_m	X_m	I_a/I_s	N_s	E_a	V_a
SC _{ns} -0.00	-0.0191	0.0440	0.2000	115.430	(1.5140)	1.0000
SC _{ns} -0.75	-0.0201	0.0461	0.1709	118.302	---	1.0000
SC _{ns} -1.05	-0.0266	0.0652	0.0565	133.280	---	1.0000
SC-1.05	-0.0274	0.0678	0.0576	135.112	1.8808	1.0000
SC-1.10	-0.0295	0.0748	0.0316	134.262	1.8374	1.0000
OC-0.0	-0.0197	0.0467	0.2001	115.492	1.5109	0.9879
OC-0.75	-0.0206	0.0469	0.1709	118.183	1.5586	0.9839
OC-1.05	-0.0309	0.0801	0.0314	131.352	1.7555	0.9173

Table V. 4-2. Average minimum potential and position, anode current, potential, and electric field, and number of charges in the diode space.

	$x/d = .05$		$x/d = 1.0$	
Run	\bar{u}_x	\bar{n}	\bar{u}_x	\bar{n}
SC _{ns} -0.00	0.0946	0.9986	1.0094	0.9980
SC _{ns} -0.75	0.0950	0.8813	0.7066	0.8540
SC _{ns} -1.05	0.0939	0.5253	0.3135	0.2787
SC-1.05	0.0946	0.5220	0.3145	0.2880
SC-1.10	0.0927	0.4700	0.2636	0.1553
OC-0.00	0.0942	1.0020	1.0093	1.0000
OC 0.75	0.0953	0.8853	0.7045	0.8533
OC 1.05	0.0923	0.4413	0.2675	0.1560

Table V. 4-3. Average x-directed velocities and numbers in the crossed-field diode

	$x/d = .05$		$x/d = 1.0$	
Run	\bar{u}_z	\bar{n}_z	\bar{u}_z	\bar{n}_z
SC _{ns} -0.00	0.0013	0.0253	0.0004	0.0153
SC _{ns} -0.75	0.0104	0.1000	0.7188	0.8540
SC-1.05	0.0104	0.0647	0.9610	0.2880
OC-0.00	0.0010	0.0207	-0.0001	0.0053
OC-0.75	0.0102	0.0973	0.7181	0.8533
OC-1.05	0.0076	0.0333	0.9362	0.1560

Table V. 4-4. Average z-directed velocities and numbers in the crossed-field diode

In addition to the average velocities at the reference planes, the velocity distributions can be obtained approximately from the Monte Carlo data. However, the velocity data, stored as the sum of velocities over a single step, can only be used to obtain the average velocity for each step. This leads to gross inaccuracies in the distributions at the cathode, where an average of five charges are emitted per step. At $X = 0.05$ and at the anode the distributions are fairly good, because there are relatively few intervals with more than one charge in them.

The distributions that follow have been normalized so that the enclosed area is equal to the ratio of the average x-directed current to its zero magnetic field value. Although the calculated distributions are rather rough, it is not difficult to picture the smoothing that would occur if more charges were taken into account.

The theoretical distributions at the $X = 0.05$ reference plane for zero magnetic field should be the same ones established at the cathode: the normal distribution for z-directed velocities and the half-Maxwellian distribution for the x-directed velocities. The calculated distributions agree quite well with the theoretical expectations. Figure V.4-1 shows the distribution of x-directed velocities at $X = 0.05$ for both the short- and open-circuited diodes. There is not much difference between the results for the two cases. The curves show that the shape of the distribution does not change appreciably for the three values of magnetic field. The areas are equal to the values of \bar{n} from Table V.4-3 (Run SC-1.05 was used in obtaining the distributions for $B/B_c = 1.05$ and the corresponding spectra in the next section). The distribution of z-directed velocity also maintains its shape with increased magnetic field (Figure V.4-2). These results indicate that at least for $B \leq 1.05 B_c$, the velocity distributions remain unchanged in shape when moving from the cathode to $X = 0.05$.

The distribution of x-directed velocity at the anode is shown for the short- and open-circuited diodes in Figures V.4-3 and -4. The corresponding distributions of z-directed anode velocity are given in Figures V.4-5 and -6. As expected, with no magnetic

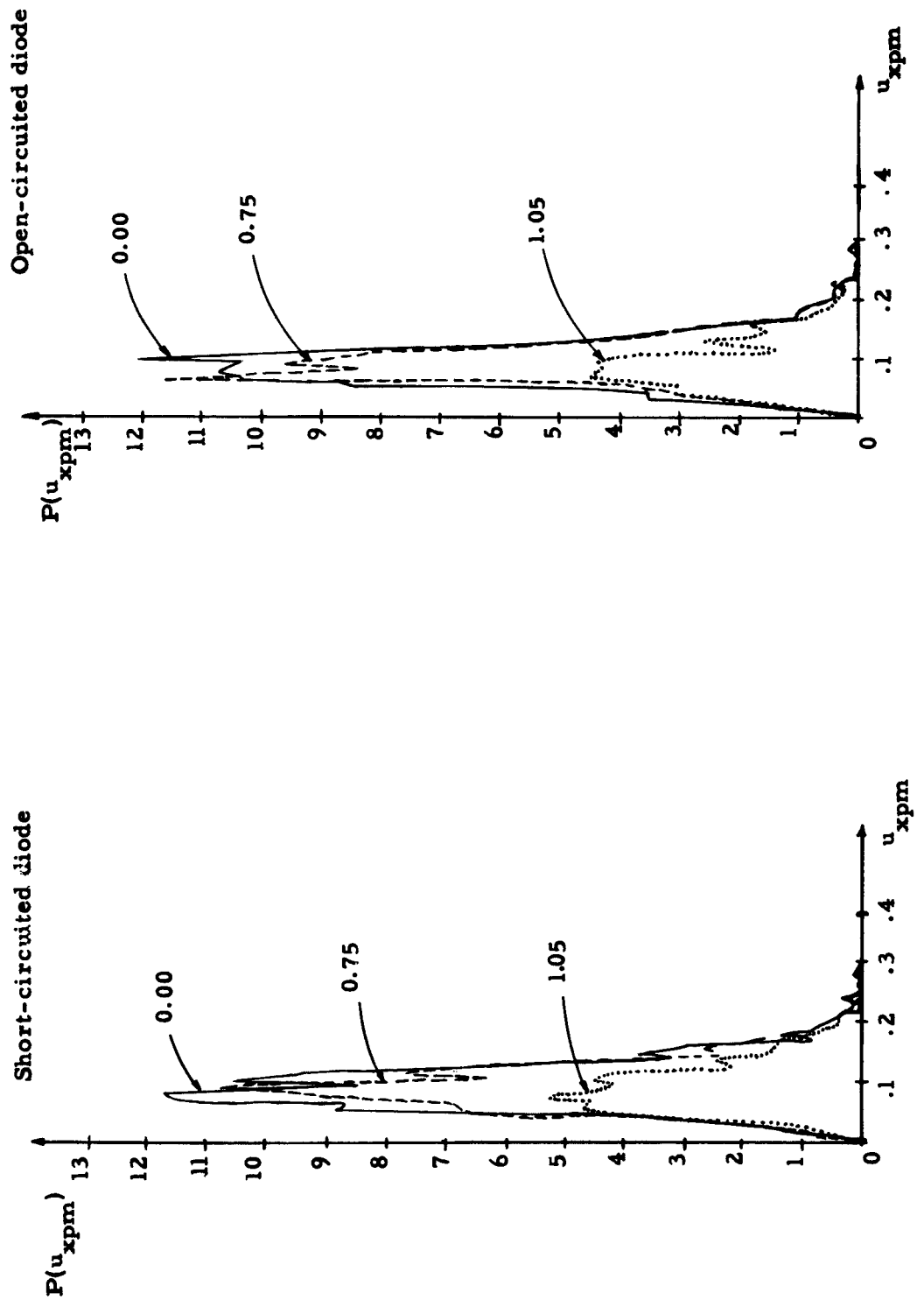


Figure V.4-1. The dependence of the normal velocity distribution at $X = 0.05$ on B/B_c

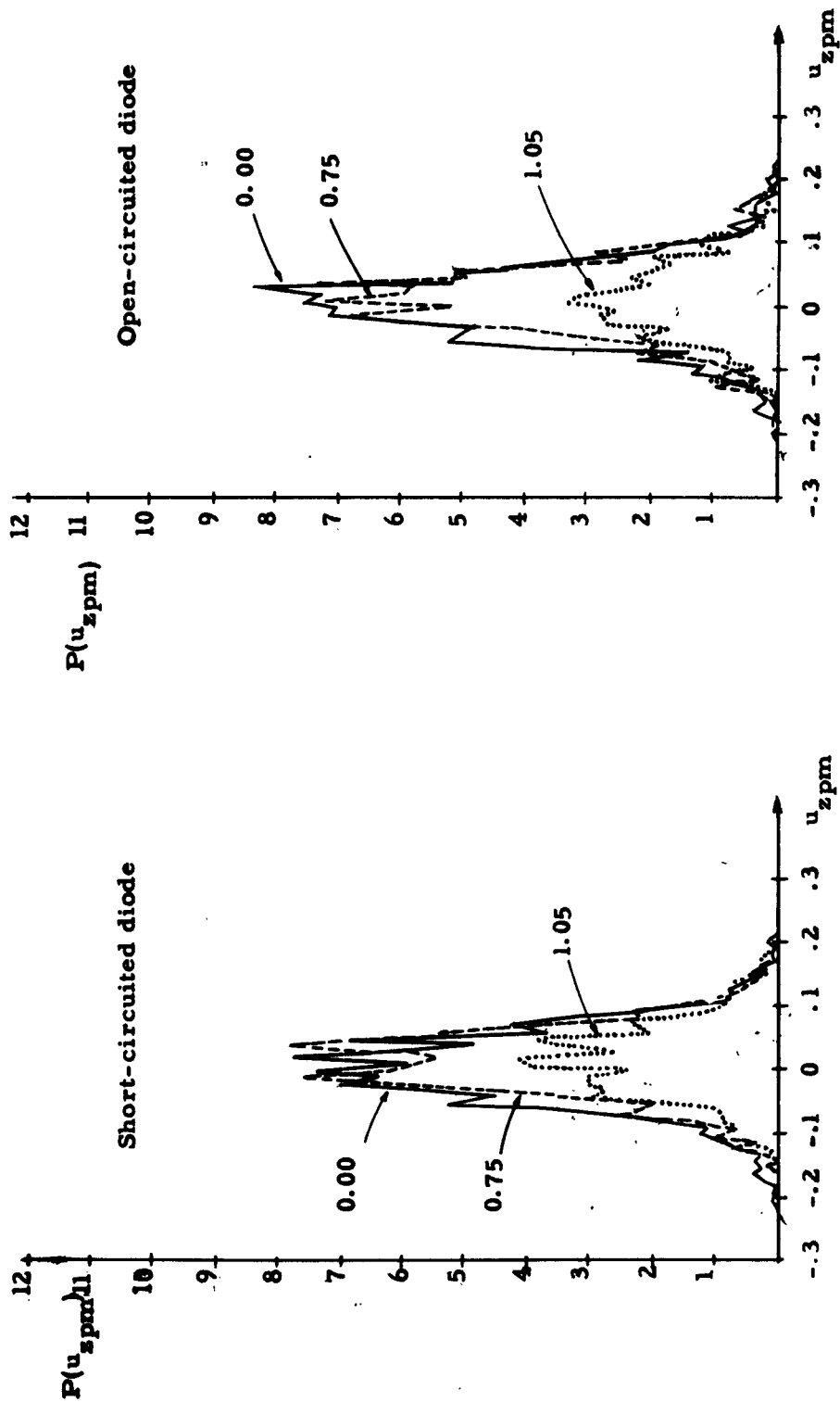


Figure V.4-2. The dependence of the transverse velocity distribution at $X = 0.05$ on B/B_c

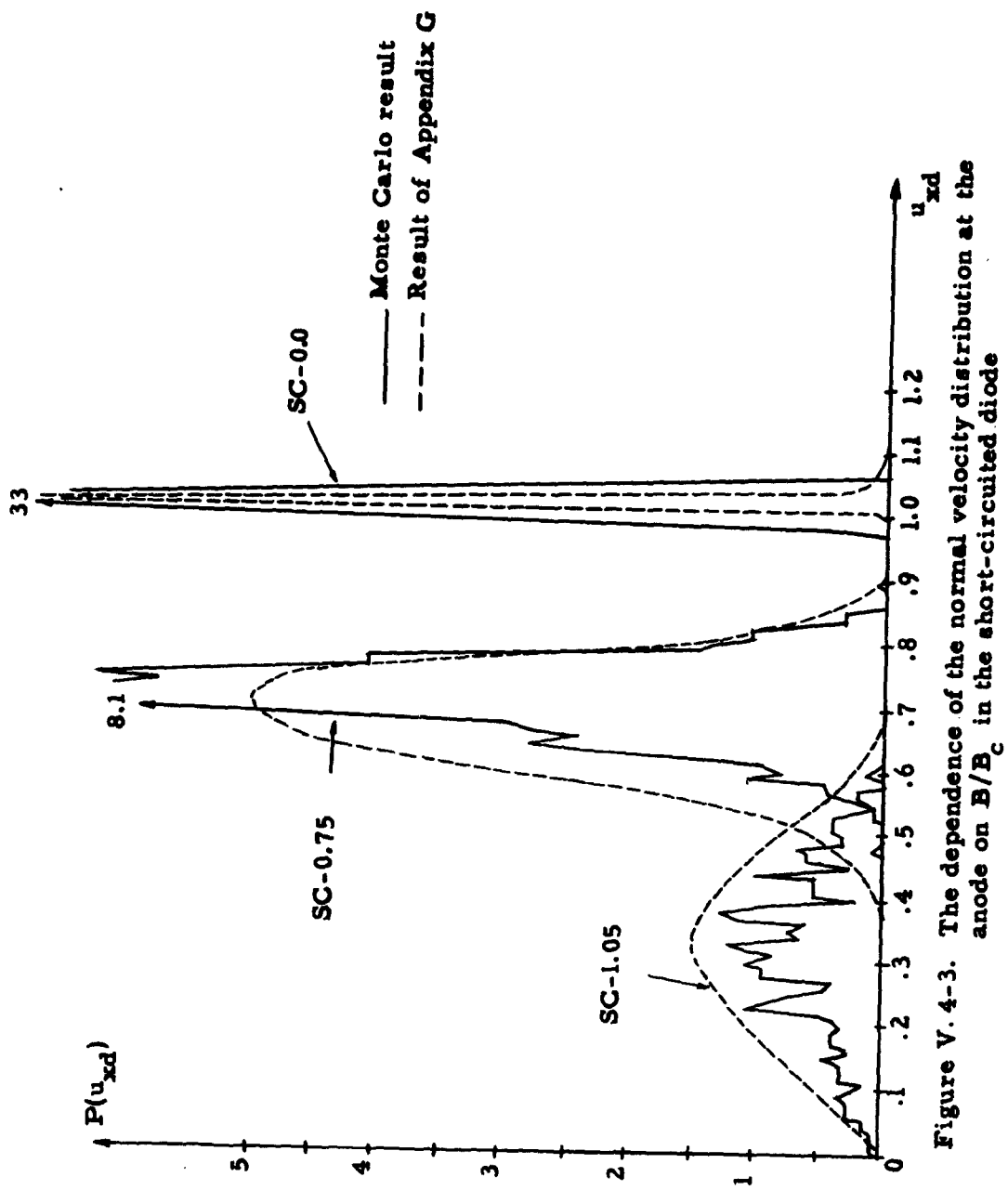


Figure V.4-3. The dependence of the normal velocity distribution at the anode on B/B_c in the short-circuited diode

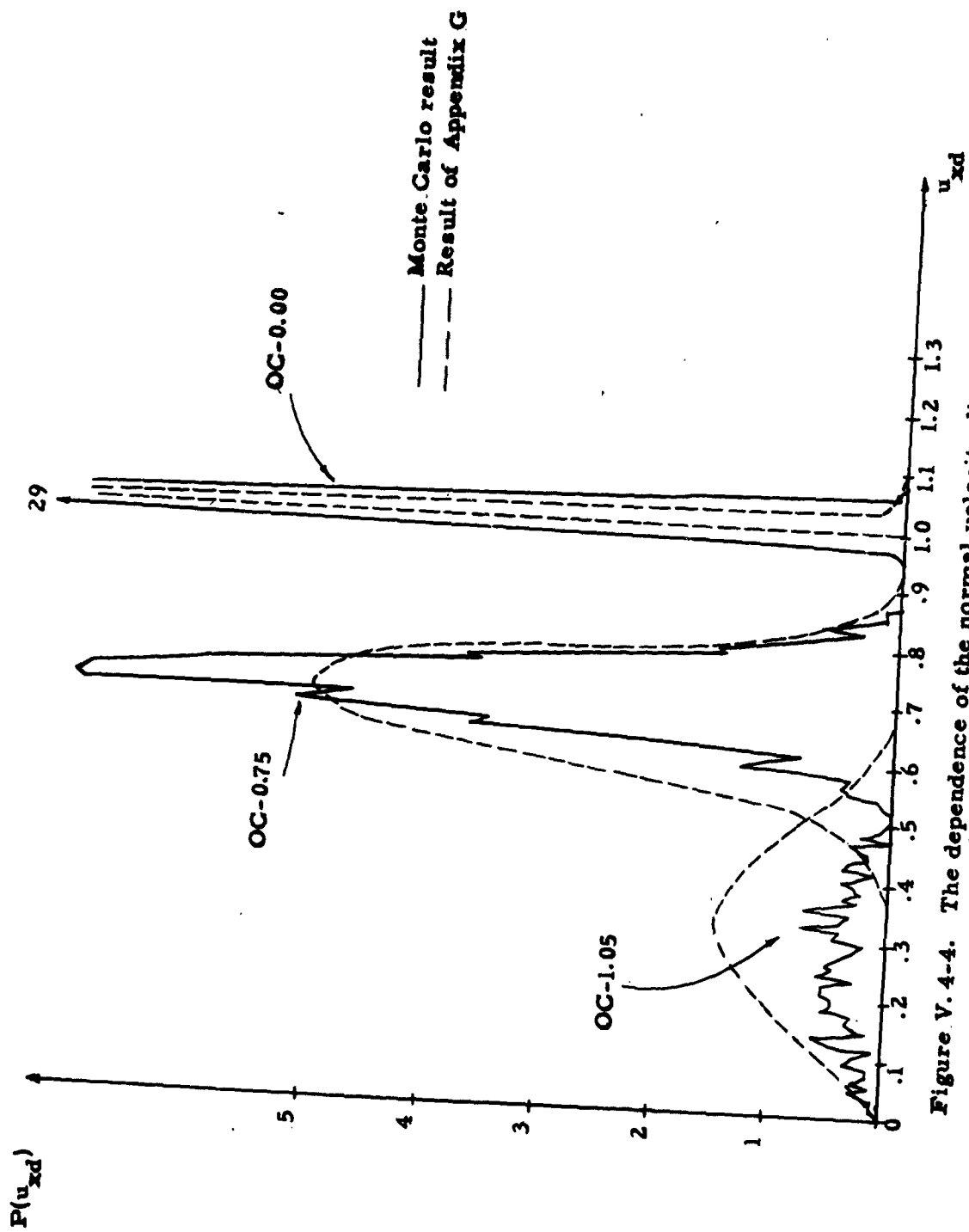


Figure V.4-4. The dependence of the normal velocity distribution at the anode on B/B_c in the open-circuited diode

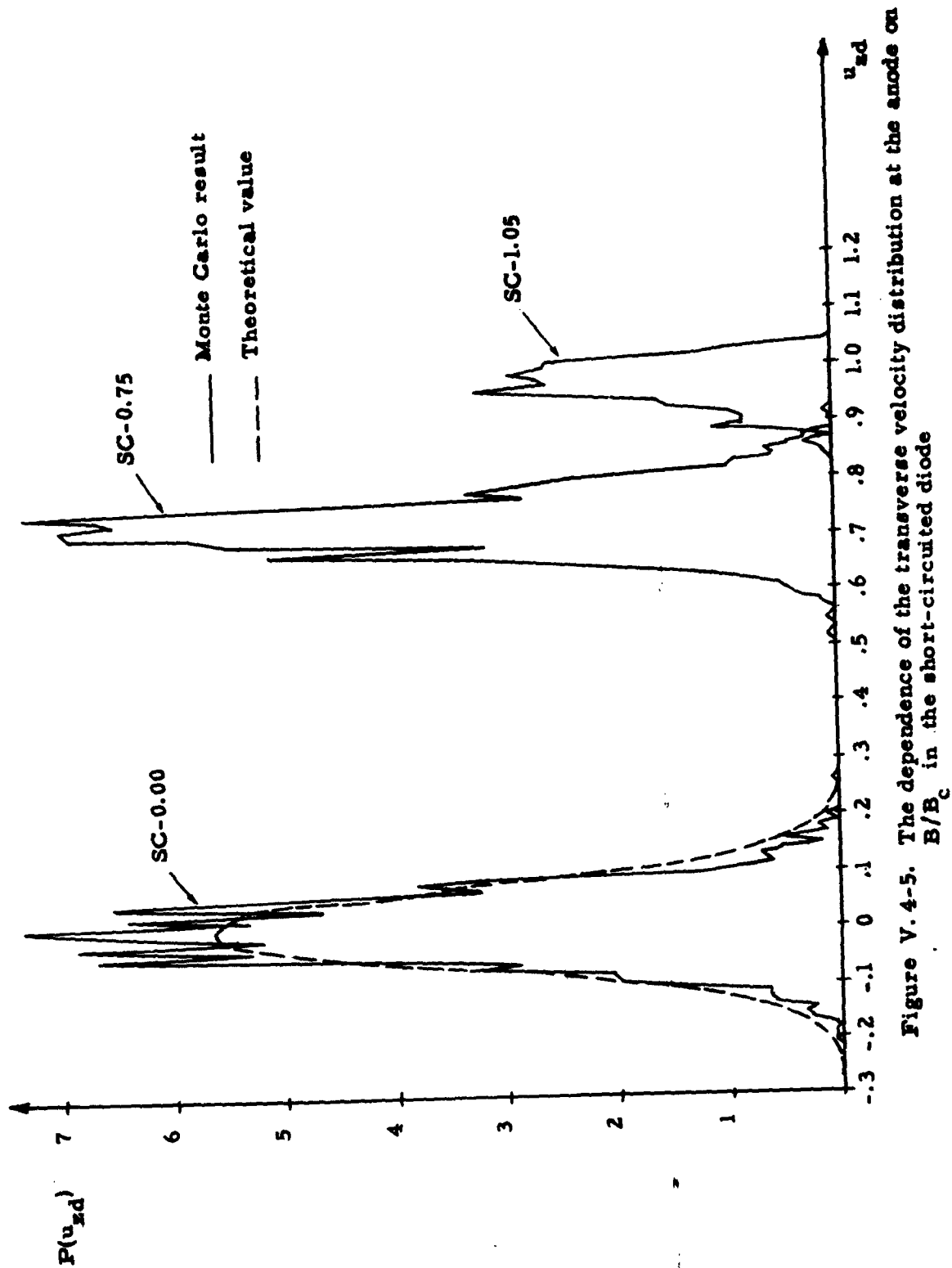


Figure V.4-5. The dependence of the transverse velocity distribution at the anode on B/B_c in the short-circuited diode

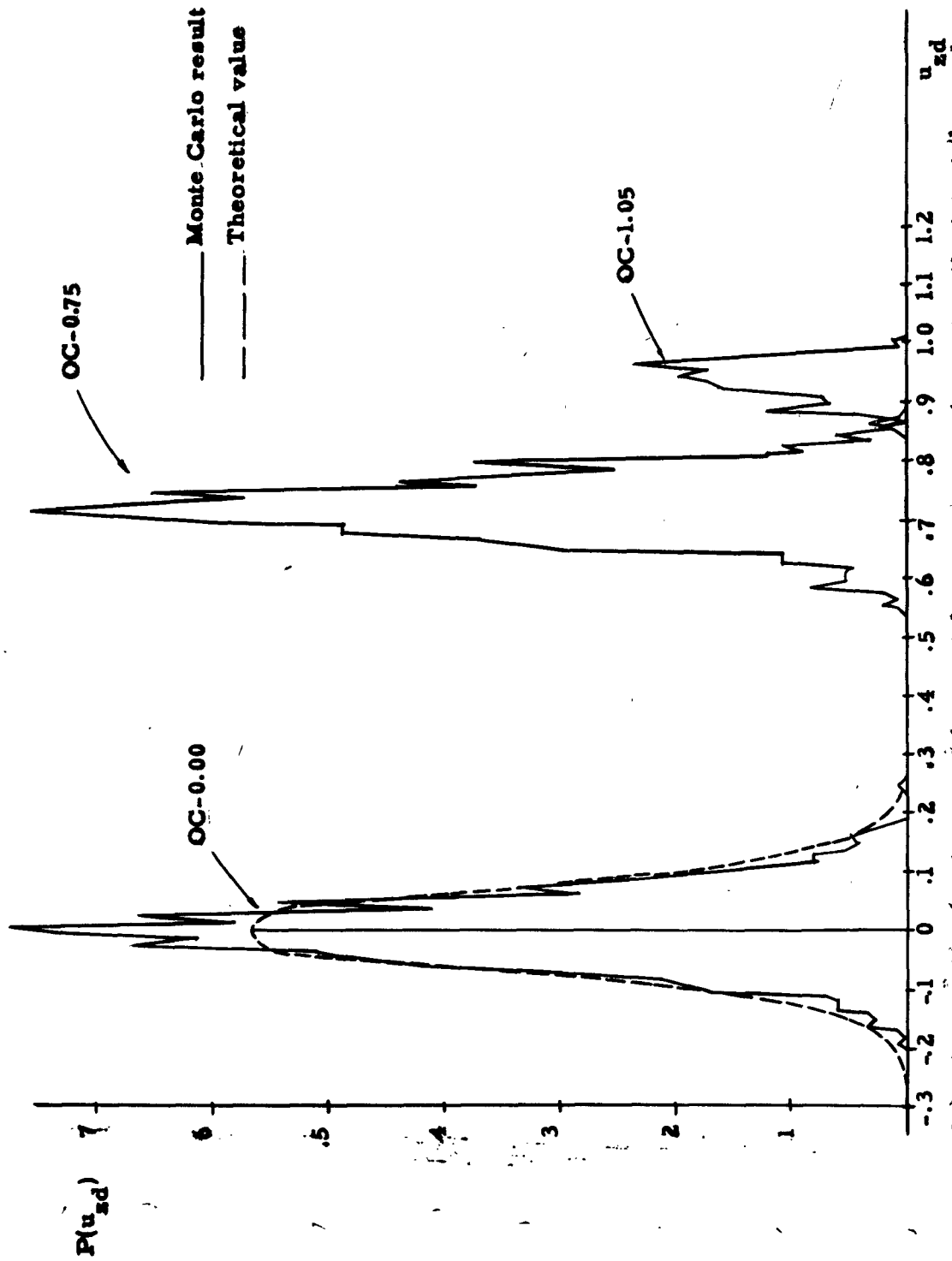


Figure V.4-4. The dependence of the transverse velocity distribution at the anode on B/B_c in the open-circuited diode

field, the spread in the distribution of x -directed velocities decreases as the stream moves from the potential minimum to the anode. The distribution of z -directed velocities remains unchanged at any point in the diode, since there is no z -directed force for zero magnetic field.

A most interesting result is that the spread in the distribution of x -directed velocities at the anode increases with magnetic field, while the spread in the corresponding distribution of z -directed velocities decreases. The spread of the distribution is a measure of the equivalent temperature of the stream. For $B/B_c = 1.05$, the temperature evaluated in the normal direction appears to have increased by a factor of 8 to 10 above its cathode value.

To determine how much of the increased spread was caused by rf effects and how much could be explained on the basis of the multi-velocity nature of the dc flow, a simple analytic model was examined. The model is the infinite planar diode with thermal velocity distributions at the cathode in both the x and z directions. An arbitrary amount of space-charge is permitted. However, the potential distribution is assumed to be such that any charge that would have a positive normal velocity at the anode would not be turned back between the cathode and anode. This restriction does not permit treatment of the space-charge-limited diode with potential minimum, but the results should be qualitatively similar. In Appendix G this restriction is discussed in detail, and the resulting distributions of x -directed velocity obtained.

The distributions obtained from the dc flow are compared with the Monte Carlo results in Figures V.4-3 and -4. The agreement between the corresponding distributions indicates that a large portion of the spread introduced by the magnetic field is directly due to average effects. The rf effects are masked out to a considerable degree. In the zero magnetic field velocity distributions there are electrons arriving at the anode with normalized velocities less than unity. These electrons have lost energy to the rf fields.

Measurements of equivalent temperature in an actual stream should show an increase of 8 to 10 times the cathode temperature, without rf gain or instabilities being considered. This is on the order of 10^4 degrees Kelvin. Measurements (e. g., Fulop, 1958), Van Duzer and Whinnery, 1961b) have shown that temperatures in the range between 10^4 and 10^6 degrees Kelvin exist in crossed-field streams. The lower temperatures appear to be explainable on the basis of the dc flow, but the higher ones do not. Appendix G shows that the spread in the distribution, hence temperature, increases with increasing anode voltage, at least for $B/B_c = 1$. In a more typical crossed-field device, with an anode voltage around 400 volts, the apparent temperature might be close to 10^5 degrees Kelvin. However, Fulop (1958) showed from measurements of anode current vs magnetic field that a cathode temperature of 10^5 degrees Kelvin would be necessary to account for his results on the basis of an analysis of the type given in Appendix G. The reasons for the higher measured temperatures are still not clear.

V. 5. Dependence of the Fluctuations on B/B_c

The current spectrum at the $X = 0.05$ reference plane for $B/B_c = 0$ is smoothed below $F = 0.375$ and fluctuates about full shot noise at higher frequencies, as described previously. In the following figures, the effect on all the spectra of the transverse field will be illustrated.

The x-directed current at $X = 0.05$ is seen to be relatively independent of B/B_c (Figure V. 5-1 and -2). At low frequencies, the smoothing decreases as B approaches B_c in the short-circuited diode. For $B = 1.05 B_c$, the minimum is beyond $X = 0.05$, so the noise current past the minimum was not determined. In the open-circuited diode, the convection current is forced to zero for all magnetic fields. The incomplete suppression observed in Figure V. 5-2 is attributable to the weighting of the spectrum.

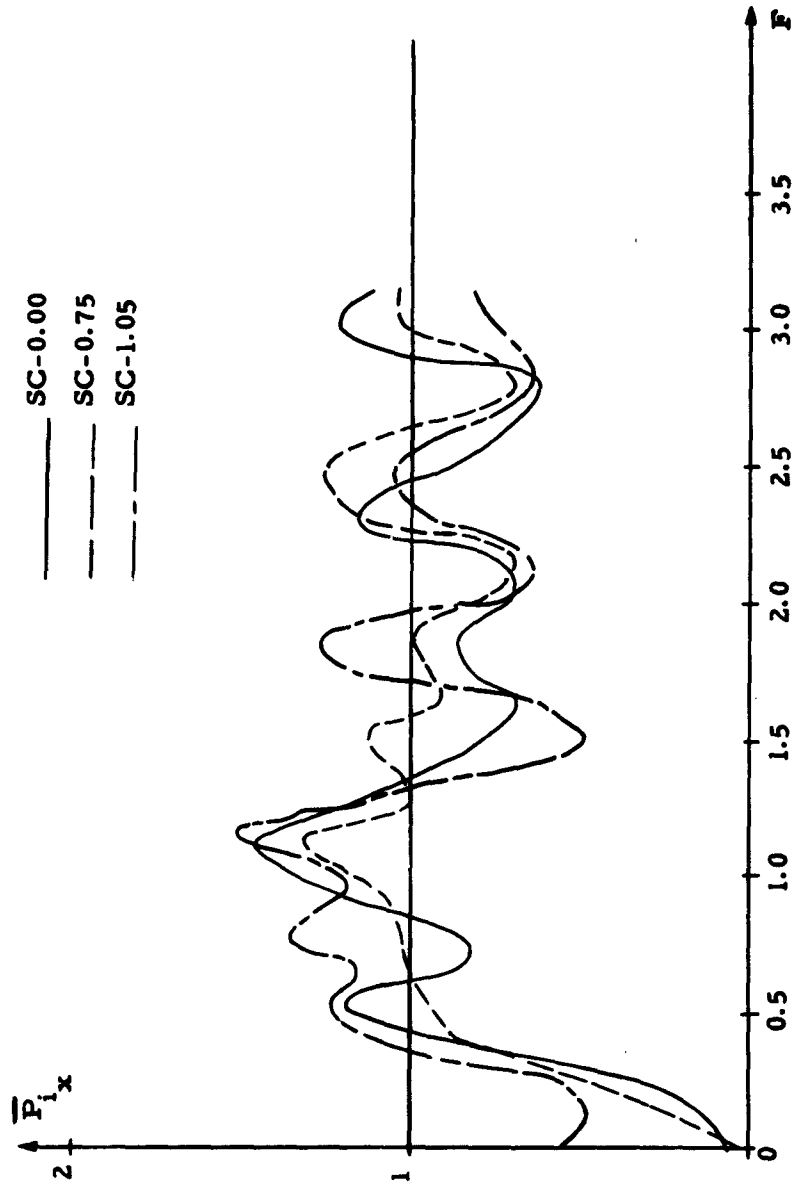


Figure V.5-1. x-directed current spectra at $X = 0.05$ in the short-circuited diode

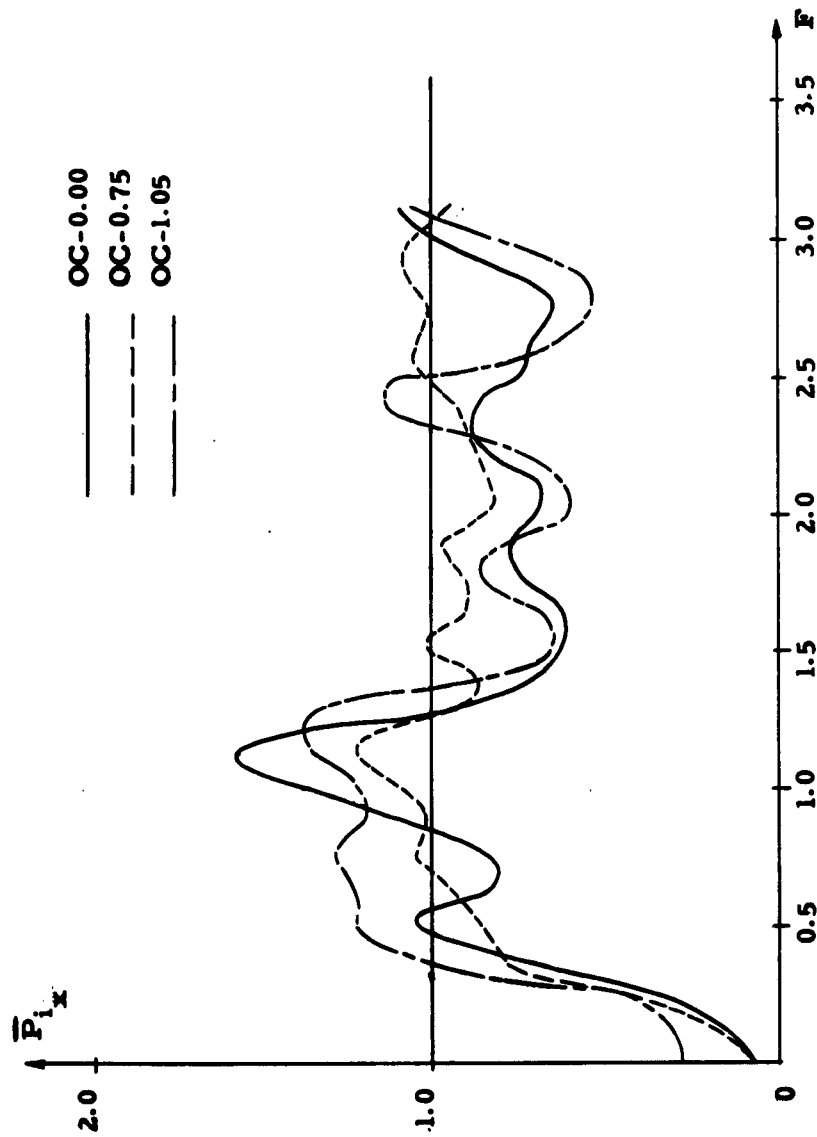


Figure V.5-2. x-directed current spectra at $X = 0.05$ in the open-circuited diode

It is apparent from Figures V. 5-3 and -4 that for all values of the magnetic field the x-directed velocity fluctuations propagate relatively unchanged in the cathode-potential minimum region. This constancy could be expected from the distributions shown in the last section. It can be argued at low frequencies for the "O" type beam since the average velocity of the stream remains constant in a retarding electric field, due to the Maxwellian nature of the velocity distribution. Dayem has shown this to be true at high frequencies in the ordinary diode, and this appears to be so in the crossed-field diode too. The discrepancy at low frequencies in the SC runs (Figure V. 5-3) is believed to be due to a small initial transient at the start of each run that was not permitted to damp out completely. The increase in the spectrum at $F = 3$ for SC-1.05 is not believed to be significant. The z-directed velocity fluctuations also appear to remain constant as they are propagated from the cathode to the potential minimum (Figure V. 5-5 and -6). The velocity spectra at $X = 0.05$ are not identical to the ones at the cathode (Figures V. 5-1 and -2) because they belong to different pieces of temporal data.

Not much could be determined about the correlation between the x-directed current and velocity at $X = 0.05$ from the cross-power spectra. For the runs made, both the real and imaginary parts of the cross-power spectra were within the range of variability around zero, much as they were at the cathode (Figure V. 2-3). The fractional correlation, defined as the ratio $(P_{i,v} / \sqrt{P_i P_v})$ was less than ± 0.15 over most of the spectra. More complete information about correlation at the minimum requires a much greater quantity of temporal data than was available here.

The effect of the transverse magnetic field on the spectra at the anode is much more pronounced than on the spectra at $X = 0.05$. For comparison with the results of Chapter III, the average potential minimum-anode transit angle must be determined. According to Tien and Moshman, an electron with average normal velocity

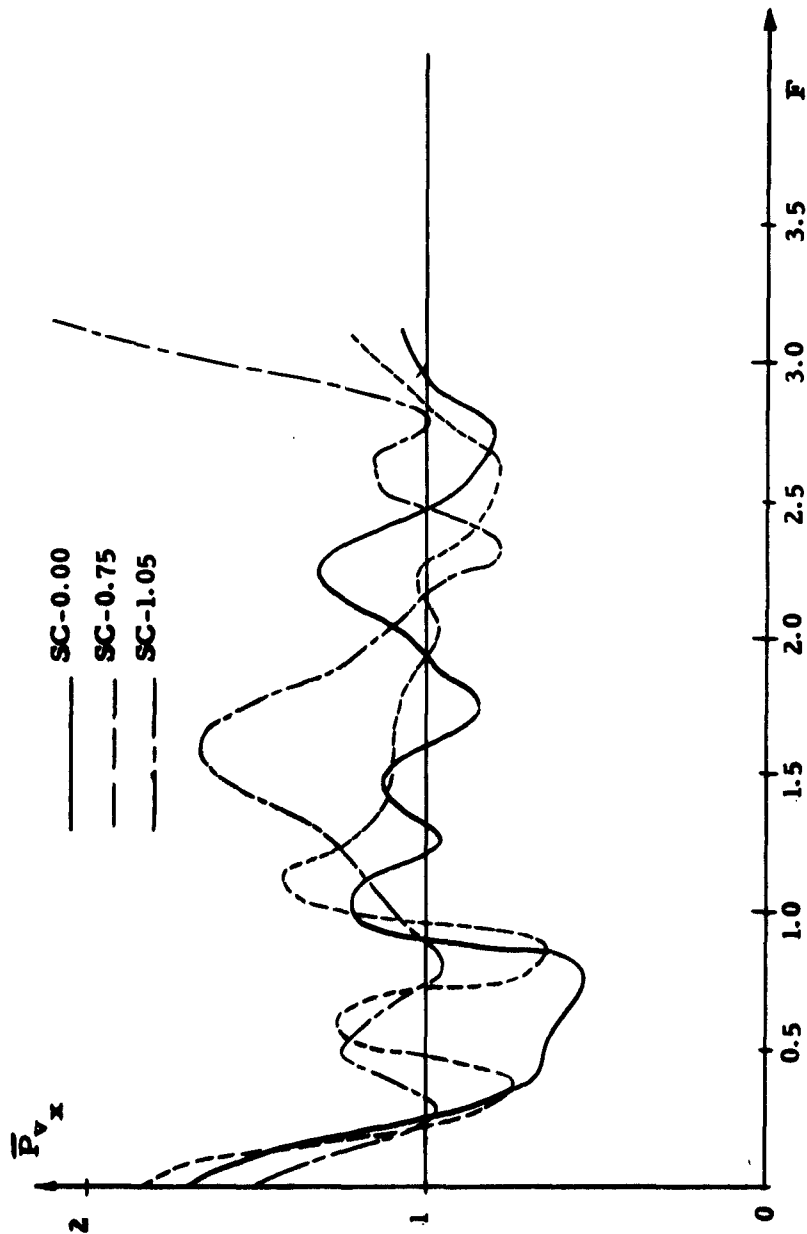


Figure V.5-3. x-directed velocity spectra at $X = 0.05$ in the short-circuited diode

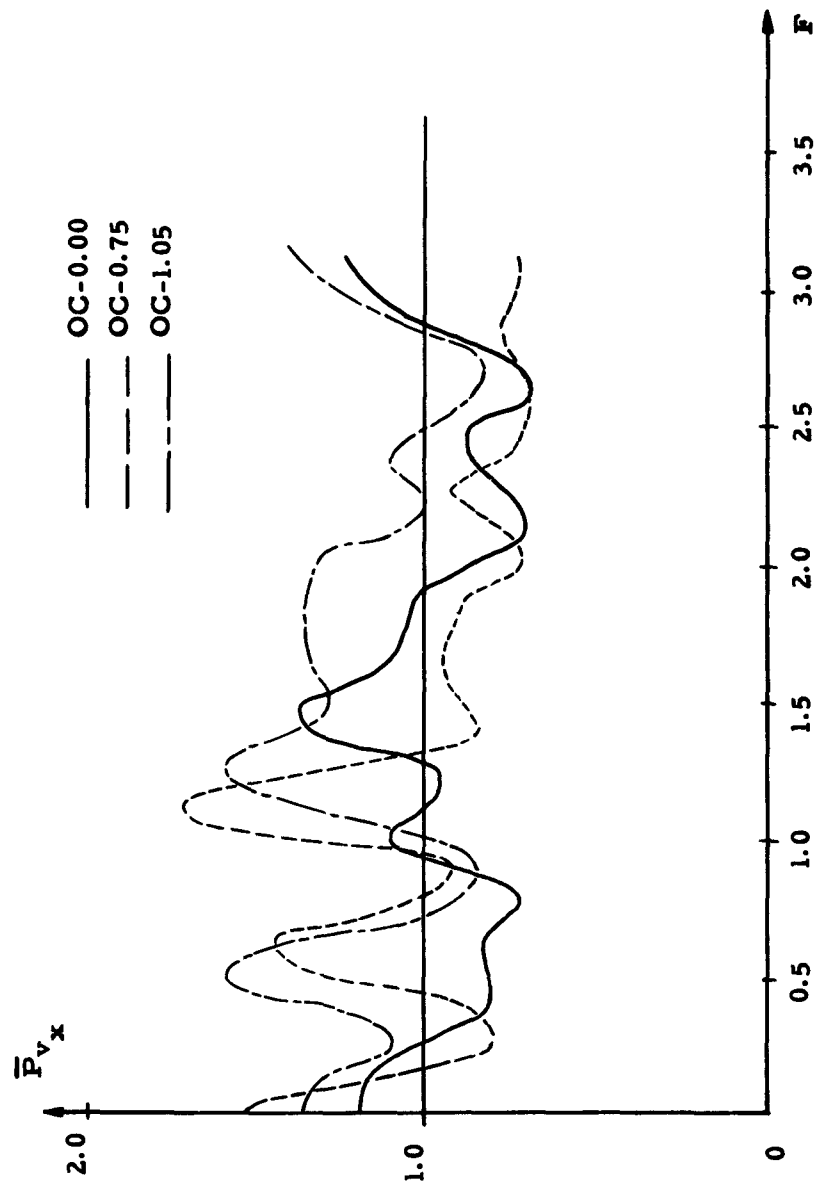


Figure V.5-4. x-directed velocity spectra at $X = 0.05$ in the open-circuited diode

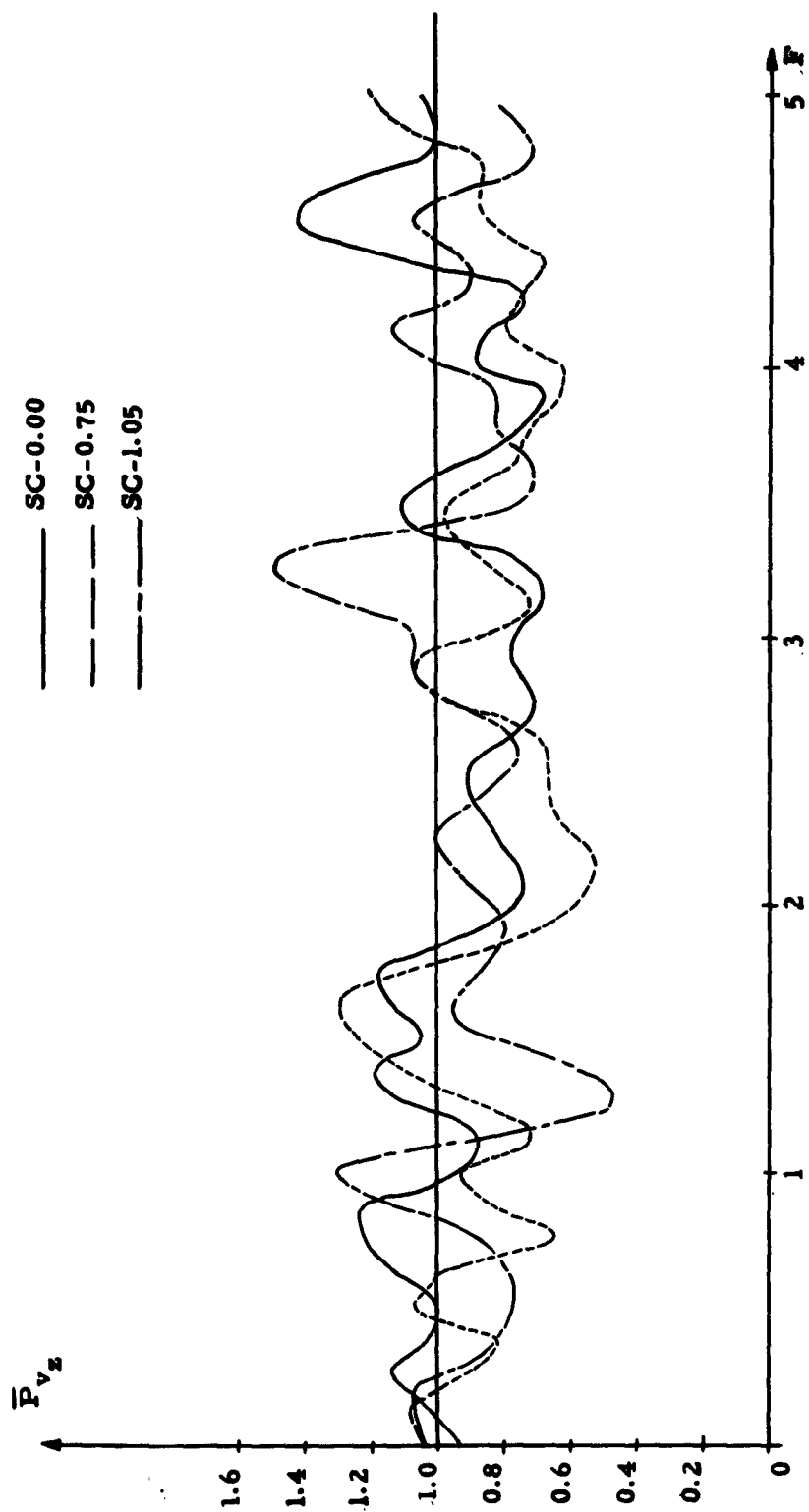


Figure V.5-5. z-directed velocity spectra at $X = 0.05$ in the short-circuited diode

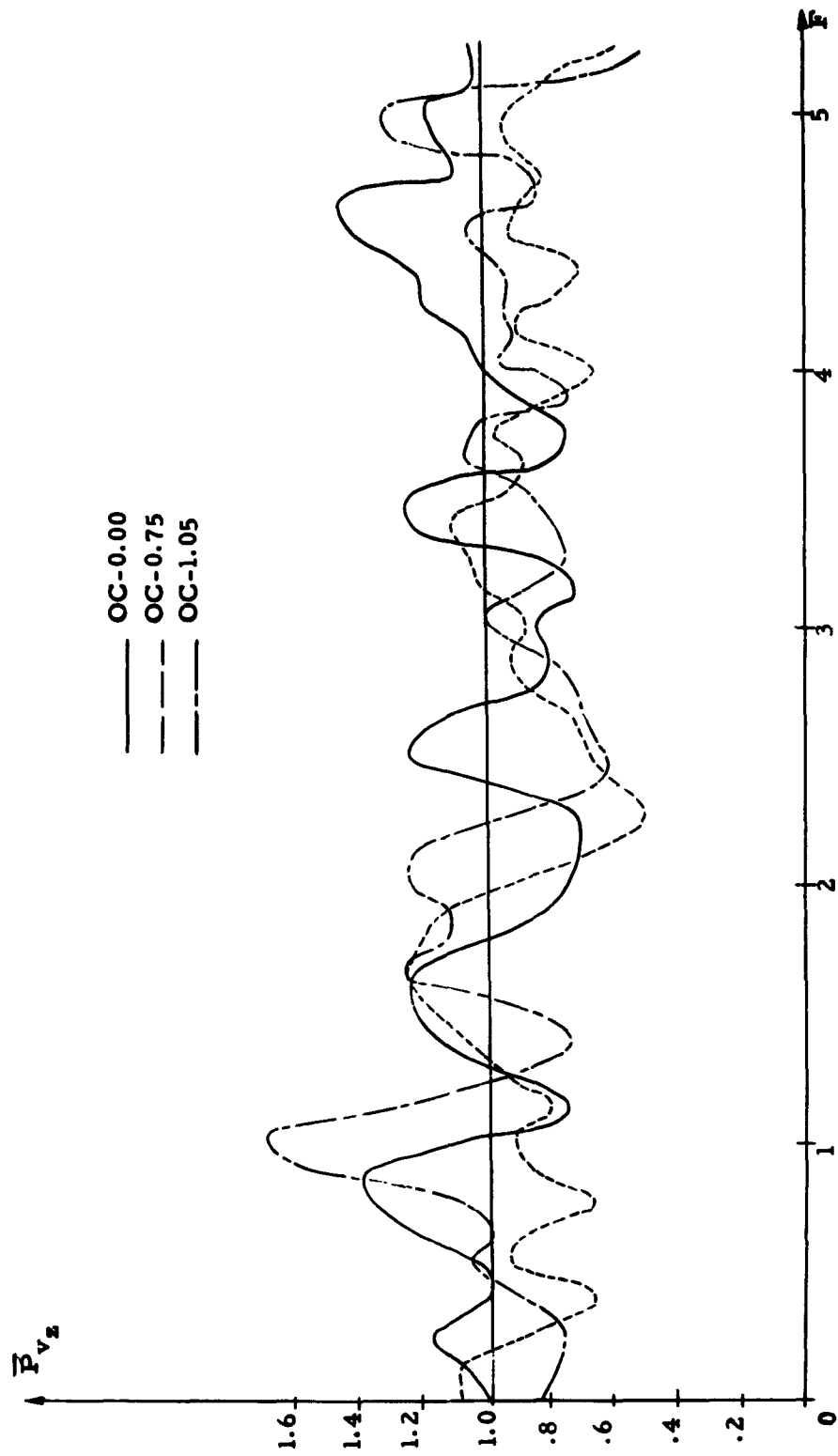


Figure V.5-6. z-directed velocity spectra at $X = 0.05$ in the open-circuited diode

at the potential minimum will take 122 time intervals to travel from there to the anode ($B/B_c = 0$). Since in their study m_Δ was equal to 50, we can determine that the average transit time T_{transit} equals 2.44. In the absence of the average velocity at the potential minimum, $T_{\text{transit}} = 3$.

Then

$$|\beta| = \omega \tau = 2\pi(2.44) F. \quad (1)$$

From III. 4(16), we can see that the transit angle increases with magnetic field. It is 1.13 times its zero magnetic field value at $B/B_c = 0.75$ and 2.09 times that value at $B/B_c = 1.00$. Therefore a normalized frequency of unity represents an average transit angle of nearly 5π for $B/B_c = 0$ and 0.75, and 10π for $B/B_c = 1.05$.

The anode current spectra agree fairly well with the results of the single velocity analysis (Figures V. 5-7 and -8). The noise currents rise from their low frequency smoothed values towards full shot noise. With increasing magnetic field, the low frequency limit in the short-circuited diode increases (although not evident in Figure V. 5-7), until for $B/B_c = 1.05$, full shot noise is present at all frequencies. In the open-circuited diode, this is modified at low frequencies where the convection current is again forced to zero by the model. In agreement with the discussion in Section III. 6, the noise currents start to increase as $|\beta|^2$, but then level off as they approach full shot noise. For $B/B_c = 0$, crossovers make the single-velocity analysis invalid when 21 % of shot noise is reached. This occurs at about $|\beta| = 3.5\pi$ (see Figure III. 6-9 and -11). This is in approximate agreement with the Monte Carlo results, where the leveling off occurs in the same region, near $F = 0.75$ to 1.0. Within the variability of the estimates, no currents greater than shot noise were observed.

The velocity spectra at the anode are far different from the ones obtained as results of the single-velocity analysis. In Figures V. 5-9 and -10, the x-directed velocity spectra increase with

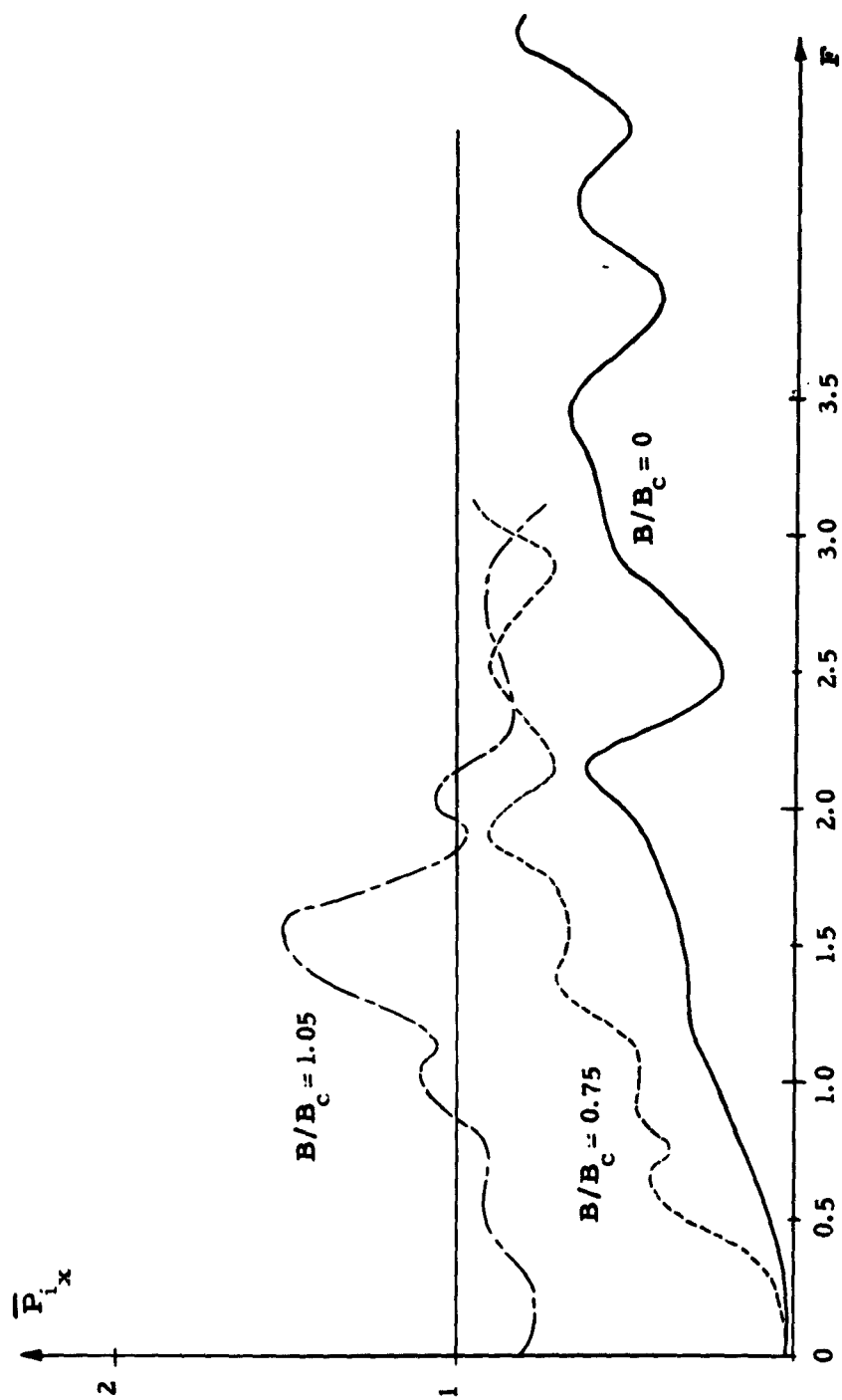


Figure V.5-7. x-directed current spectra at the anode in the short-circuited diode

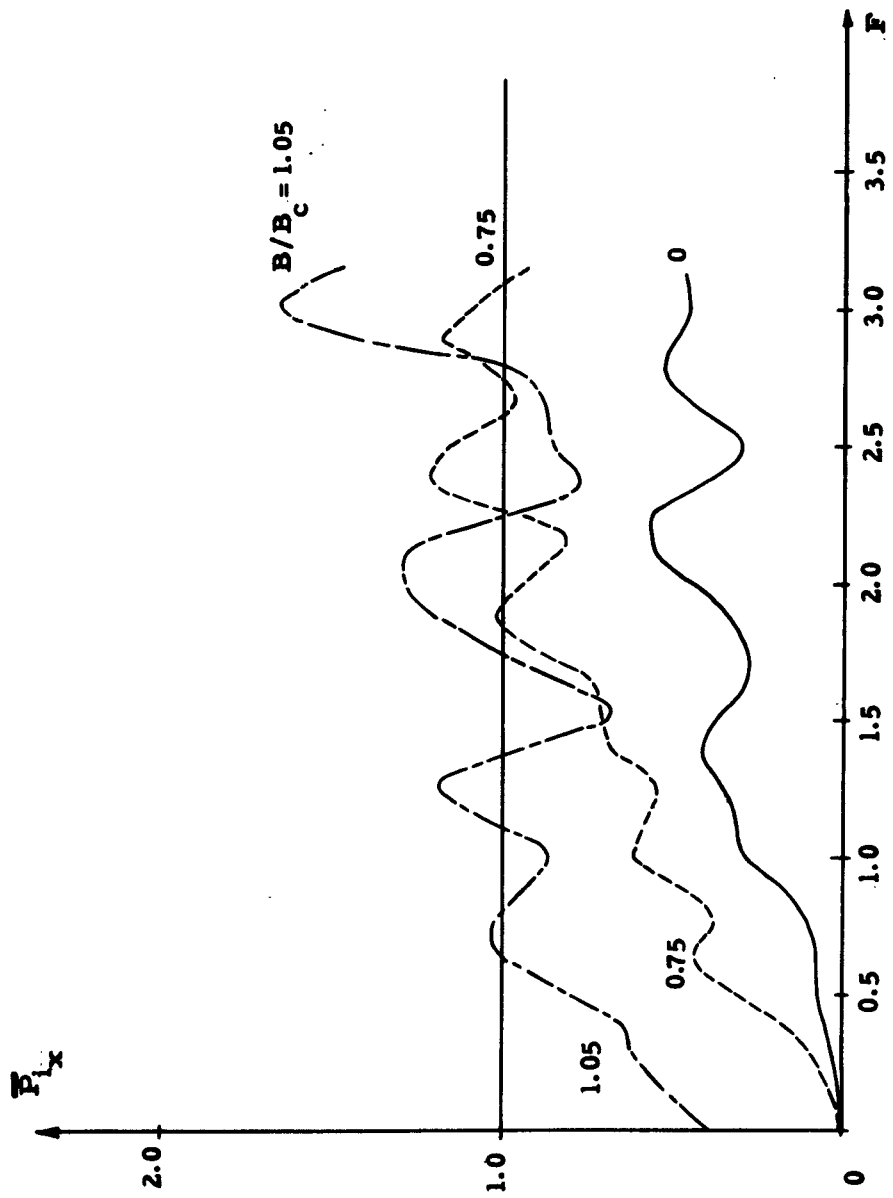


Figure V.5-8. x-directed current spectra at the anode in the open-circuited diode

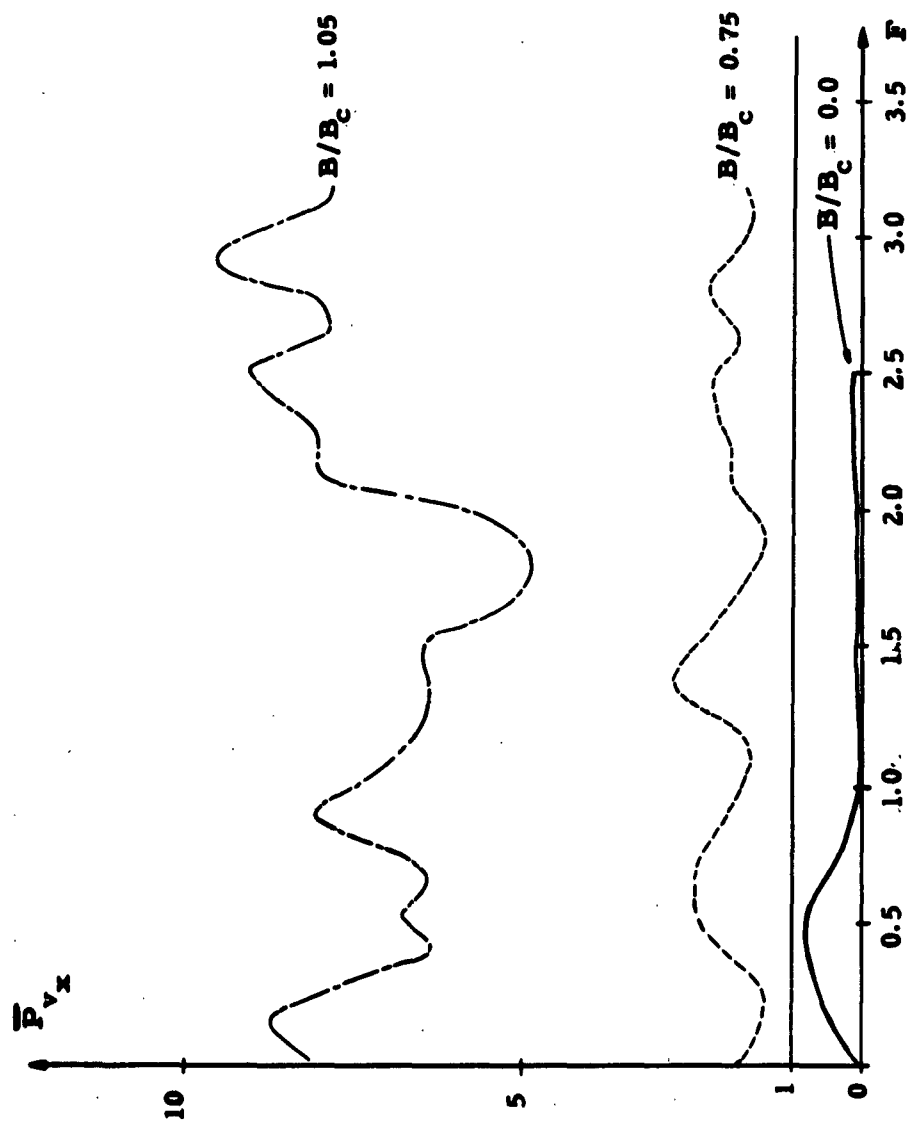


Figure V.5-9. x-directed velocity spectra at the anode in the short-circuited diode

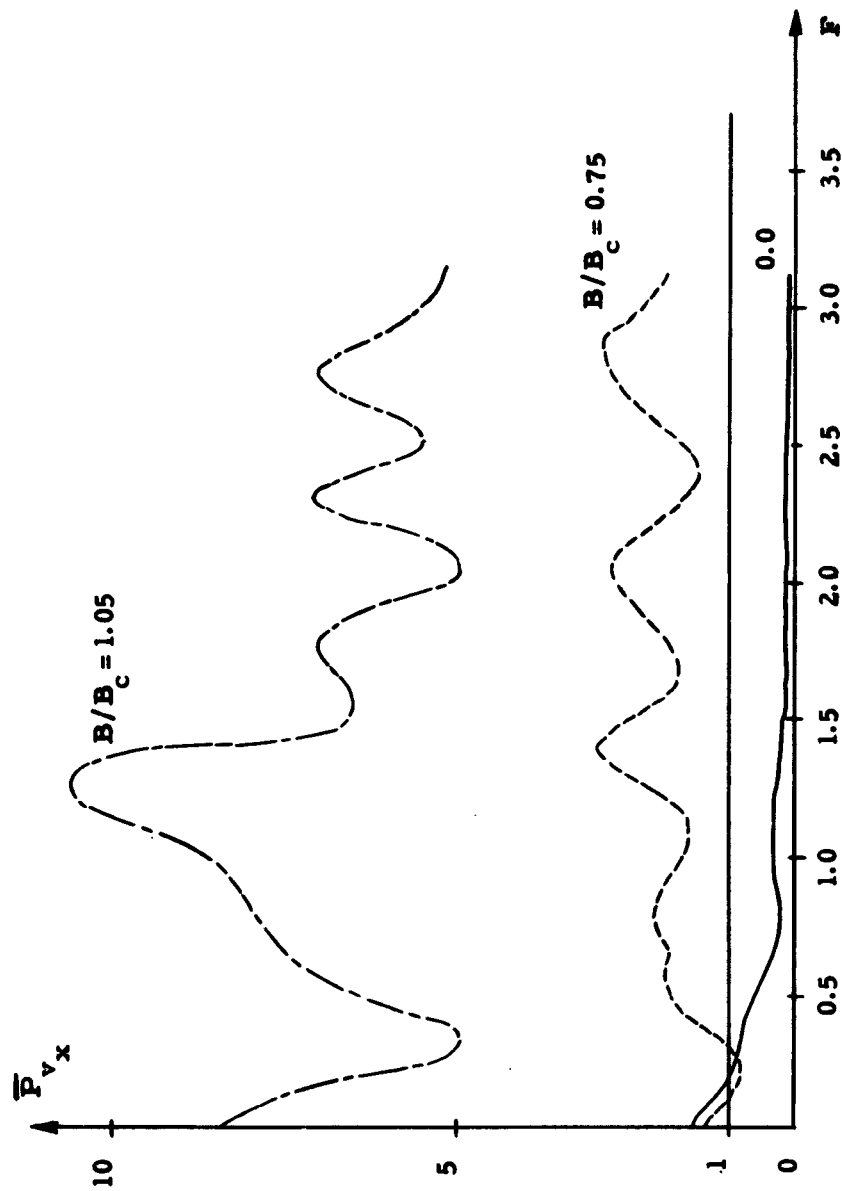


Figure V. 5-10. x-directed velocity spectra at the anode in the open-circuited diode

magnetic field in both the short- and open-circuited diodes. This result could have been anticipated from the velocity distributions of the last section. The spectra for zero magnetic field start off as predicted by the single-velocity theory. However, near $F = 0.4$ the velocity spectra start to decrease toward a very small value. It is likely that this effect is due to the relatively large velocity spread. A double precision calculation of this spectrum was carried out, and the same effect was obtained. The departure from the single-velocity theory again occurs in the range of frequencies where that theory is invalidated by crossovers.

The z-directed anode velocity spectra (Figure V.5-11 and -12) decrease with increasing magnetic field. This, too, is relatable to the decrease in the spread of the corresponding velocity distributions and is caused by the velocity sorting in the stream.

There is no apparent correlation between x-directed currents and velocities at the anode for non-zero magnetic fields. The fractional correlation is again less than ± 0.15 over most of the spectra, and this, too, can be attributed to the variability of the estimates. For zero-magnetic field, there is a fractional correlation of about 0.45 for both the short- and open-circuited diodes over much of the frequency range. This differs from the complete correlation predicted by the Llewellyn-Peterson equations primarily because of the velocity spread in the Monte Carlo model.

V. 6. Examination into the Validity of the Calculation

Although the parameters and normalization have been chosen to give adequately accurate spectra that are independent of the representation of the beam, these should be checked by actual computer runs. When it was discovered that the self-force term had been left out of the electric field equation for the SC_{ns} runs, it was decided to take this opportunity to check the effect of N_g in the computation. The fluid model is approximated by the sheet charge model when the change in electric field across a charge is

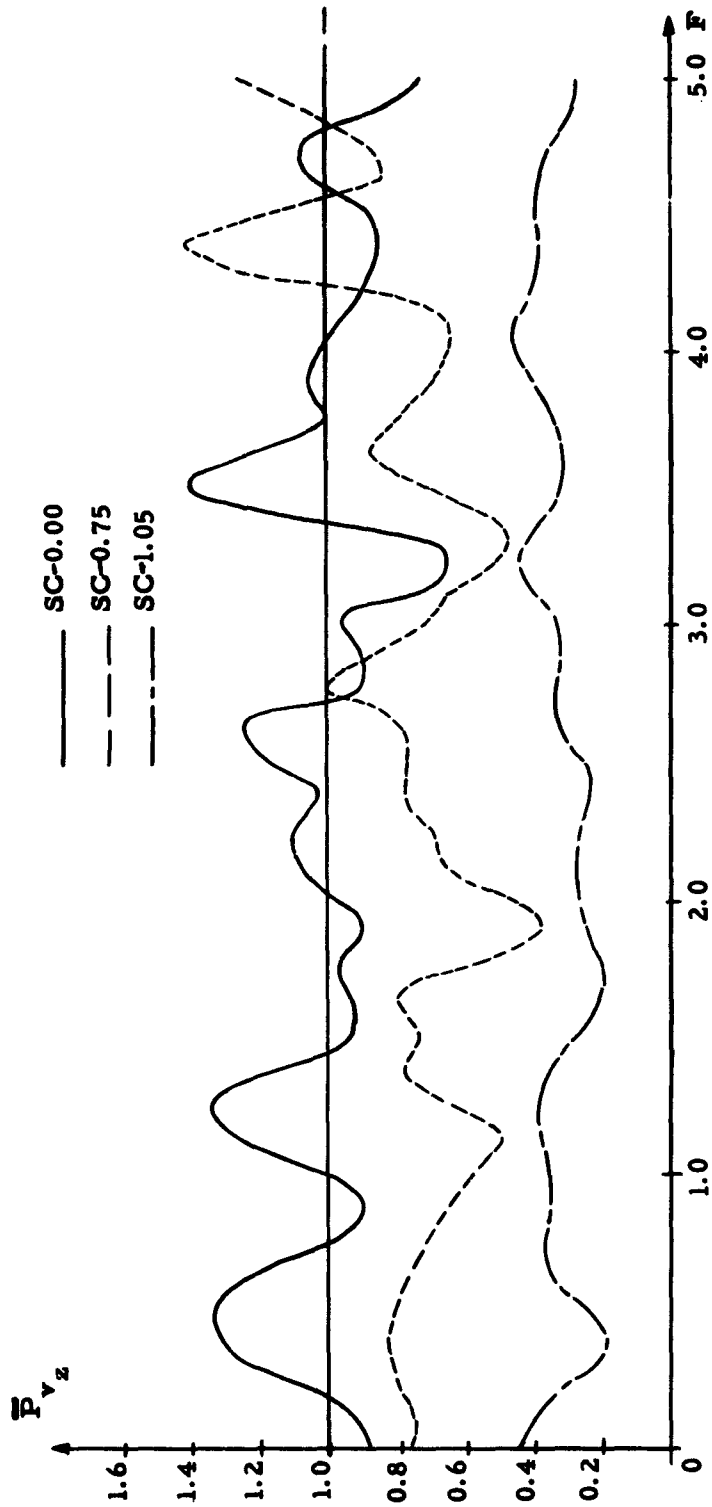


Figure V.5-11. z-directed velocity spectra at the anode in the short-circuited diode

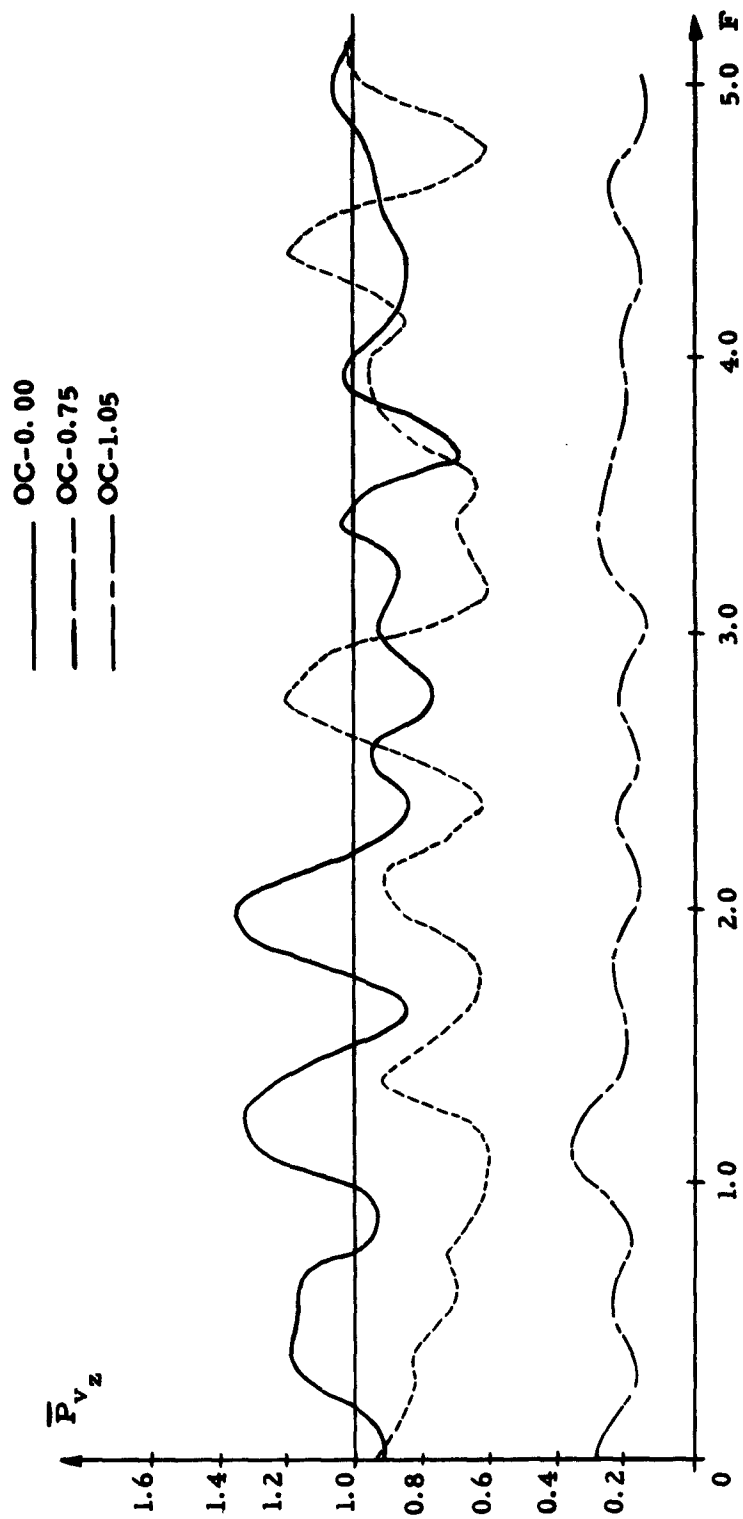


Figure V.5-12. z-directed velocity spectra at the anode in the open-circuited diode

small compared to the field at a point. This condition is met at the anode when (from IV.3(12)),

$$\frac{m \Delta n_{eo}}{4/9 \alpha} + \sum_k x^k \gg 1/2. \quad (1)$$

To determine when this is valid, we write (1) in the form

$$N_s \left[\frac{m \Delta n_{eo}}{4/9 \alpha N_s} + \bar{X} \right] \gg 1/2, \quad (2)$$

where \bar{X} is the summation of (1) divided by N_s . From Table V.2-3, the value of the first term of the bracket is between 0.3 and 0.35. The average position can be taken to be on the order of 0.1. Then for (1) to hold, $N_s \gg 1$. The present choice of parameters yields values of N_s greater than 100. Thus the electric field should be relatively independent of the self-force term.

This has been checked by rerunning the SC-1.05 calculation, including the self-force term. Here, in the cutoff region, the magnetic force nearly balances the electric force, and the effect of the missing term would be most important. The rerun SC-1.05 was started with initial conditions taken from the end of SC_{ns}-1.05. Within the range of expected variability, no major differences could be ascertained between the two sets of spectra. The difference in the spectra caused by the change of initial conditions did not appear to have any great effect on the spectra either.

With the self-force term known to have little effect on the spectra, a check was made on the direct effect of changing N_s , by reducing n_{eo} from 5 to 1. The SC-0.00 run was used for $n_{eo} = 5$, and a new B = 0 short-circuited diode run, including the self-force term was made with $n_{eo} = 1$. This comparison (Figure V.6-1) not only shows that the diode simulation and spectral analysis are essentially independent of N_s , but also that a reliable spectral analysis can be obtained with an average of only 0.2 charges

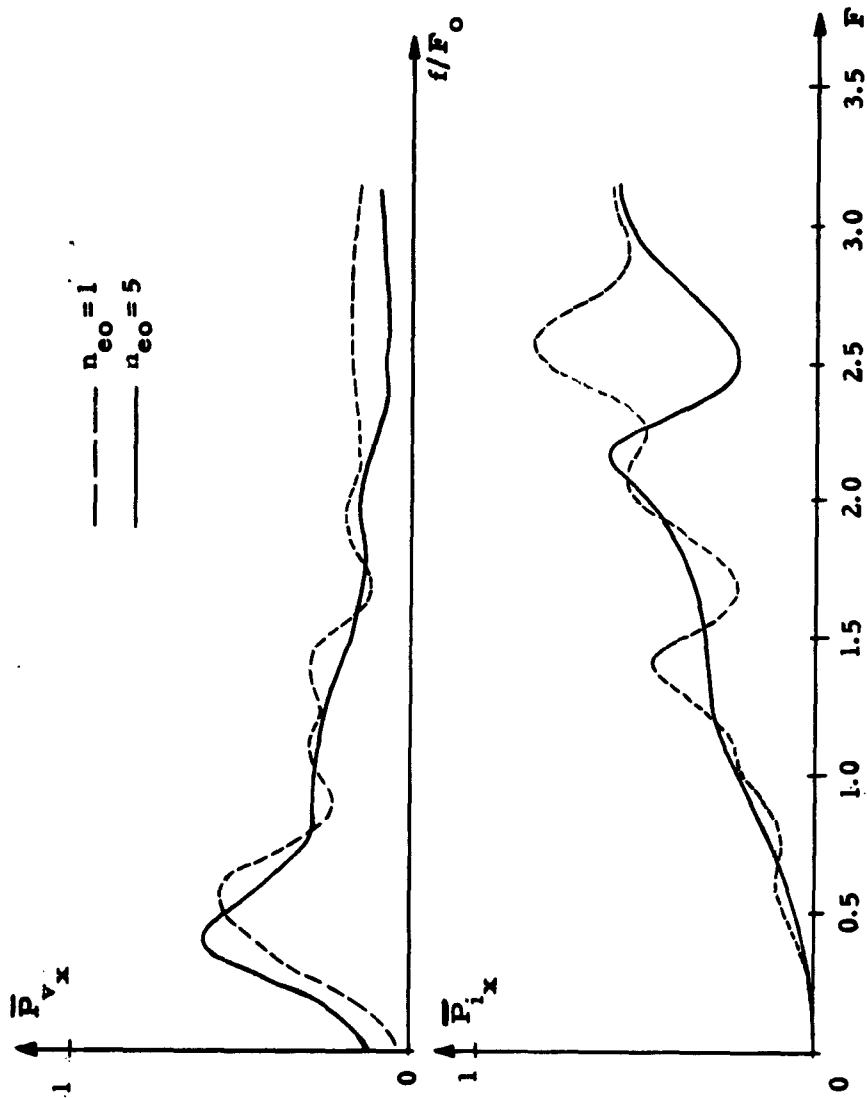


Figure V.6-1. Effect of N_g (or n_{eo}) on the spectra at the anode of the short-circuited diode

charges per step crossing the reference plane--in this case, the anode. The spectra at the minimum are also similar for both runs, although not as much so as at the anode. This separate run also gives further evidence for the existence of a decrease of the velocity spectral density beyond $F = 0.5$.

VI. EXPERIMENTAL VERIFICATION OF THE THEORIES

VI.1. Design of the Experimental Apparatus

Although the single- and multi-velocity theories of noise transport in the crossed-field diode disagree for some ranges of the parameters, there seems to be a general agreement with regard to the increase of both velocity and current fluctuations with magnetic field at small transit angles. As noted in the Introduction, there is much existing experimental evidence that demonstrates this increase with magnetic field. The purpose of further experimentation is then to provide information for a quantitative comparison with the theories. Because previous experimentation indicated the excess crossed-field noise to cover a wide range of frequencies, it was decided to perform an experiment at relatively low frequencies. Such an experiment can be considerably easier to conduct than one in the microwave range. In addition, it is possible to measure over a wider range of transit angles than could be obtained by using simple microwave techniques.

Therefore, a planar crossed-field triode was constructed to verify the small transit angle limit of the two theories. To obtain a measure of the noise convection current in the stream, a grid was placed at a small distance from the anode, acting as an effective anode for the equivalent diode. A grid-anode gap rather than a gridless gap or slit was used to permit a greater noise current to flow; smaller noise reduction factors could then be measured without more elaborate methods. The gridded gap has some disadvantages, which can be minimised by careful design.

When the grid is placed closer to the cathode than to the anode, the fields over a large part of the cathode-grid space are non-uniform. By placing the grid close to the anode, this effect is minimized, and electrons experience uniform fields over a large portion of their transit to the grid. A ratio of cathode-grid distance (d_{cg}) to grid-anode distance (d_{ga}) of three was chosen for this reason.

The grid structure, if allowed to collect current, would both overheat and add partition noise. Such heating would warp the grid structure materially, and the additional partition noise would be capable of masking the desired noise. The grid was therefore operated at or slightly below cathode potential, and grid currents less than 1/1000 of the anode current were measured. The amount of partition noise introduced was then a negligible part of the measured noise. Figure VI.1-1 diagrams the gun region of the triode. It contains actual dimensions measured by means of an optical comparator on the second version of the tube. The second version was modified from the first to correct a dc short circuit between beam-forming electrodes and the cathode and to add an appendage palladium leak and modified cathode end electrodes to permit beam observation. The spacings were made small to raise the perveance of the diode, thereby increasing the measurable noise at a fixed anode voltage. The cathode width was made larger than d_{cg} in order that the diode might come closer to resembling the infinite model.

The beam-forming electrodes to the left and right of the cathode were designed as somewhat arbitrary compromises between the Pierce (1940) and Kino (1960) configurations (Figure VI.1-2). Neither configuration would be adequate over the range of parameters to be studied. Since noise growth has been observed in a wide range of gun configurations, it would seem that the results would be rather insensitive to the shapes of these electrodes. They serve the purpose here of partially balancing the outward space-charge forces at the beam surface.

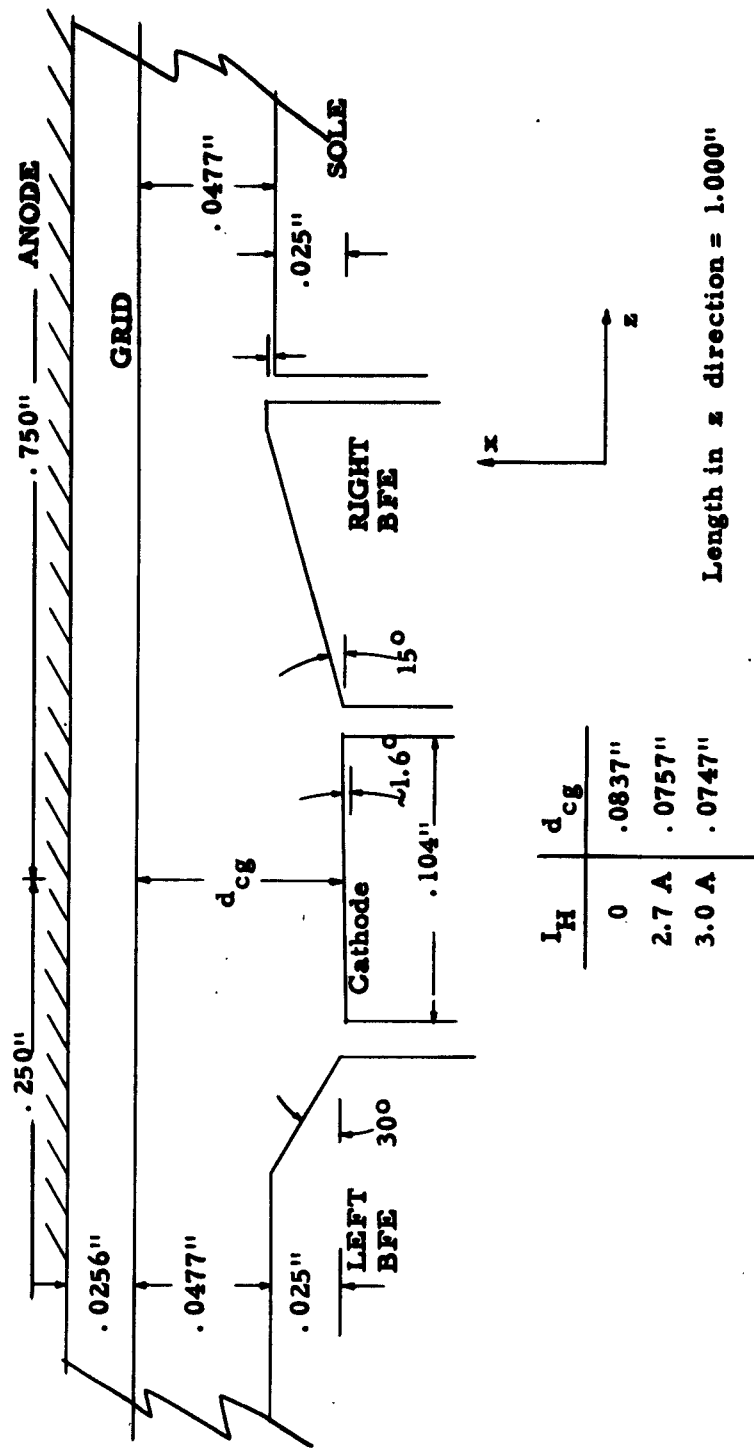


Figure VI.1-1. Detail of the gun region

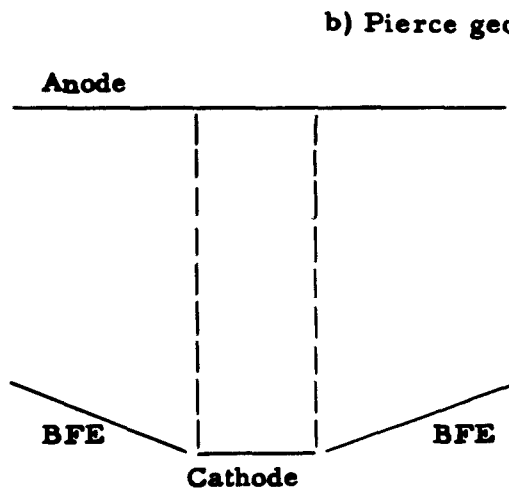
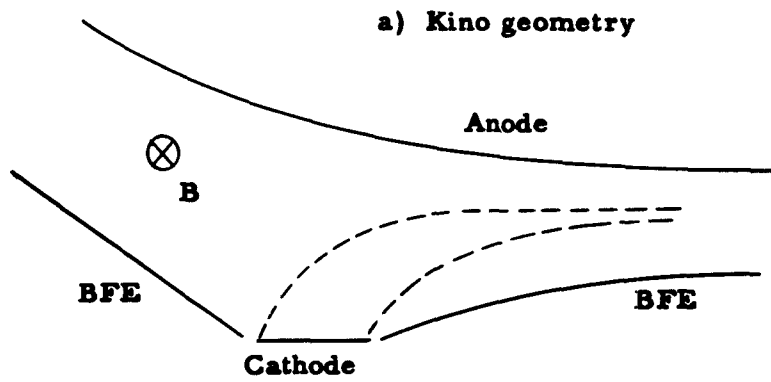


Figure VI.1-2. The a) Kino gun geometry and b) the Pierce gun geometry

The three beam-forming-electrodes, as well as the grid, were bypassed through capacitors with very short leads to the cathode. The capacitors were especially fabricated to permit operation within the vacuum envelope. They were constructed from commercial disc ceramic capacitors (.001 μ f) by first grinding down to the ceramic disc, then evaporating onto both sides of each disc a thin layer of gold on which copper was electrolytically deposited, with stainless steel leads imbedded. These capacitors withstood more than a half dozen "bakeouts" with no noticeable increase in leakage resistance.

The tube assembly (Figure VI.1-3) was fitted with an appendage Penning discharge ion pump/gauge and a pendulum-electrical contact ring arrangement for proper alignment in the magnetic field. The anode was fabricated from a solid copper block to provide good heat transfer to the outside, via external forced air cooling. Because of its large physical size, the anode was electrically connected to the copper box shielding the tube, thus avoiding the large unstable capacitances that would have resulted had it been isolated for rf. A tuned circuit was connected between grid and anode, and the noise voltage developed across it connected directly to a receiver through a coaxial cable terminated at the tuned circuit by a 330 Ω resistor. The elements at cathode rf potential were then isolated from the dc ground by means of rf chokes in each lead.

The single-velocity theory predicts that the noise voltage developed across the loaded gap is proportional to the x-directed convection current at the grid plane. We can show this by starting from the first of equations III. 3(1),

$$\tilde{V}_{\text{gap}} = a_{11} \tilde{J}_d + a_{12} \tilde{q}_{x \text{ grid}} + a_{13} \tilde{v}_{x \text{ grid}} + a_{14} \tilde{v}_{z \text{ grid}}. \quad (1)$$

In the grid-anode region, the space-charge parameter ξ is small, and the effect of the crossed magnetic field slight. Then it is reasonable to use the L-P equations with $\xi = 0$. If an external

0 1 2 3 4 5 6 7 8 9 10

SCALE (INCHES)

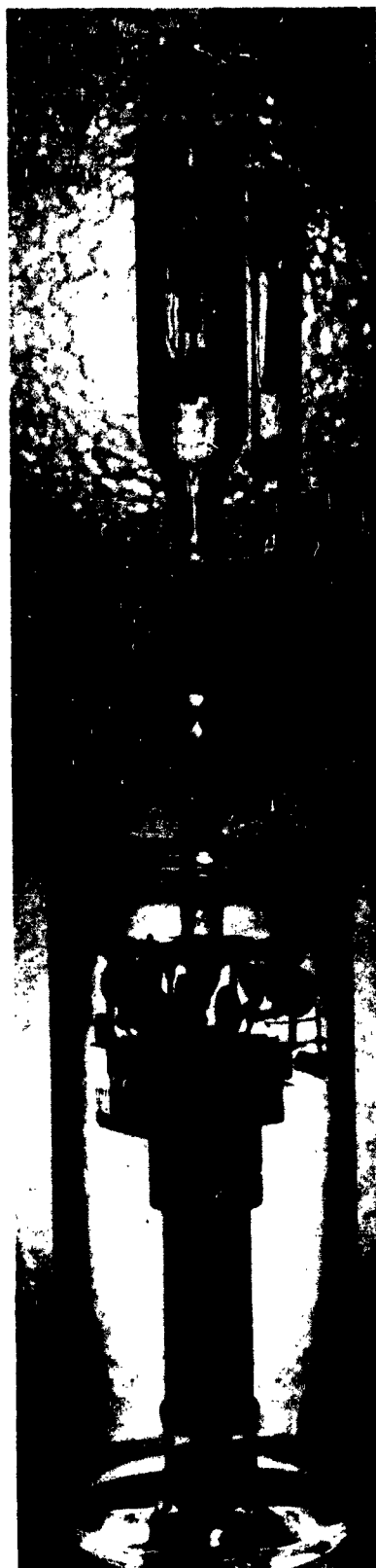


Figure VL.1-3. Experimental crossed-field triode

admittance per unit gap area Y_g is placed across the gap, these assumptions lead to the relation

$$V_{gap} = \frac{q_{x \text{ grid}}}{Y_g + 1/a_{11}} \quad (2)$$

For ξ exactly zero, a_{11} becomes the cold gap capacitive reactance per unit area. If ξ is given a non-zero value for the typical operating parameters, a high electronic parallel resistance results. This is entirely negligible compared with the external loading resistance. Thus the voltage is proportional to convection current at the triode grid plane. This same proportionality factor relates the voltage to the shot current produced by the temperature limited reference diode also connected across the tuned circuit (Figure VI.1-4). If the two noise sources are alternately activated and the reference diode current adjusted so that the noise signals are equal, then

$$R^2 = \frac{\langle i_{grid}^2 \rangle}{2eI_{triode}\Delta f} = \frac{I_{ref. diode}}{I_{triode}} \quad \left| \begin{array}{l} \text{equal} \\ \text{noise} \end{array} \right. \quad (3)$$

With this method of measurement, there are no errors introduced by nonlinearities in the receiver.

Measurements on the first version of the tube were conducted using an Airborne Instruments Laboratories 30 mc Precision Laboratory receiver having a noise figure near 2 db and a bandwidth of approximately 2 mc. A Communications Electronics type 901 receiver, covering 30 to 300 mc with a 0.3 mc bandwidth and 2.5 to 10 db noise figure was used with tube version number two.

The reference diode was of cylindrical geometry, with a directly heated tungsten filament. Figure VI.1-5 shows the dc characteristics of the diode. The diode was run with an anode voltage of 750 volts, ensuring temperature-limited operation well

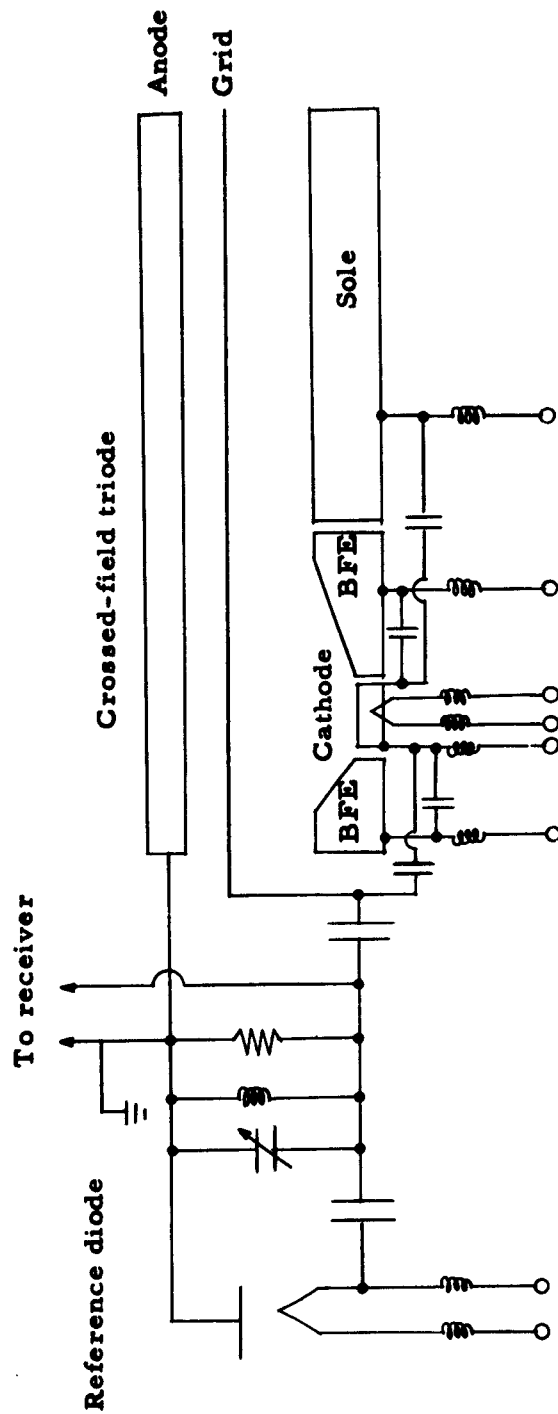


Figure VI.1-4. Schematic of noise measurement circuit

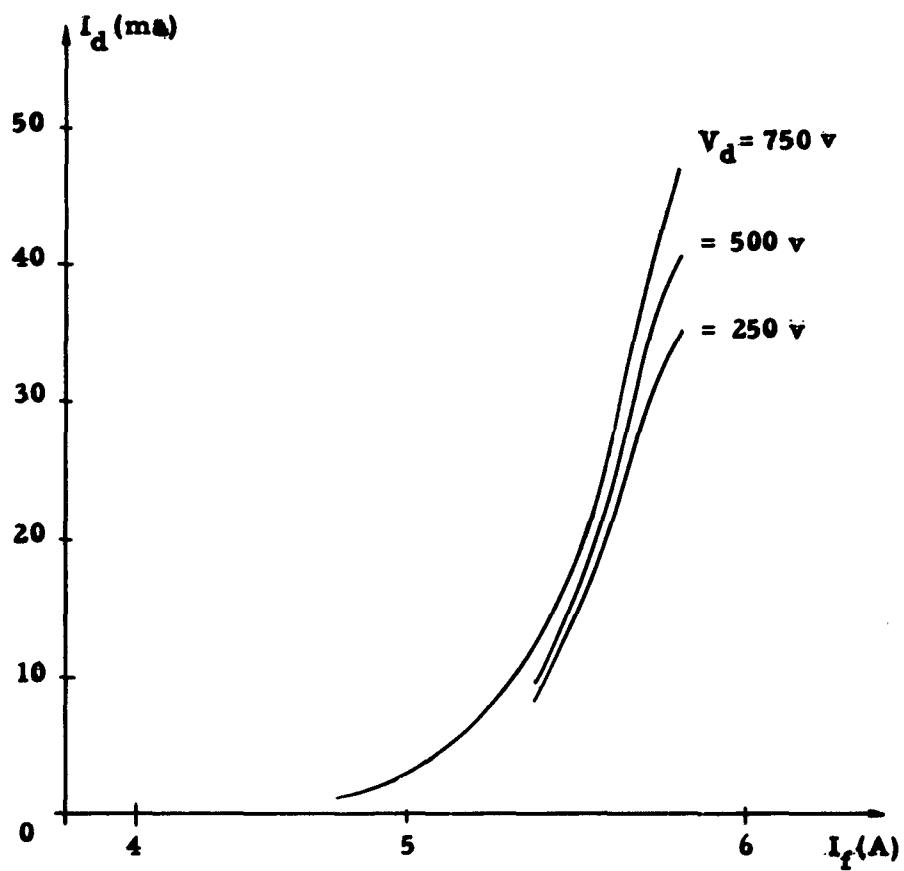


Figure VI.1-5. DC characteristics of temperature-limited reference diode

up to 50 ma. The diode current was found to be much less than this during most of the measurements.

VI.2. Space-Charge Limited Triode Behavior

Before describing the effects of the magnetic field, it is necessary to show how the cathode temperature and effective grid potential were obtained. The accurate comparison of the measurement with theory relies on the determination of these parameters. Since the grid was to be operated at cathode potential, the effective potential in the plane of the grid wires had to be determined. The anode current was used as a measure of this potential, V'_g .

Figure VI.2-1a shows the dc characteristics of the triode. For comparison with the theories, it is desirable to operate with a rather small value of V'_g . From the shape of the curves, the beam is space-charge-limited in this range of V'_g over a wide range of heater currents I_H . To maintain space-charge-limited conditions over a wider range of V'_g , a heater current of 3.0 amperes was used.

To evaluate the effective grid potential, the grid was first operated at a dc potential equal to $3/4$ of the anode potential. For a linear variation of potential from cathode to anode, this would place the grid plane potential at $3/4 V_d$. In the space-charge-limited diode, this plane is at a lower potential. However, the grid wires act to support the potential to a certain extent, and $V'_g \approx V_g = 3/4 V_d$. By then adjusting V_d to produce the same anode current with $V_g = 0$, the desired ratio

$$V_d / V'_g \Big|_{V_g = 0}$$

can be found (Figure VI.2-1b).

The cathode temperature, necessary for comparison of the experimental results with the theories, was estimated from the

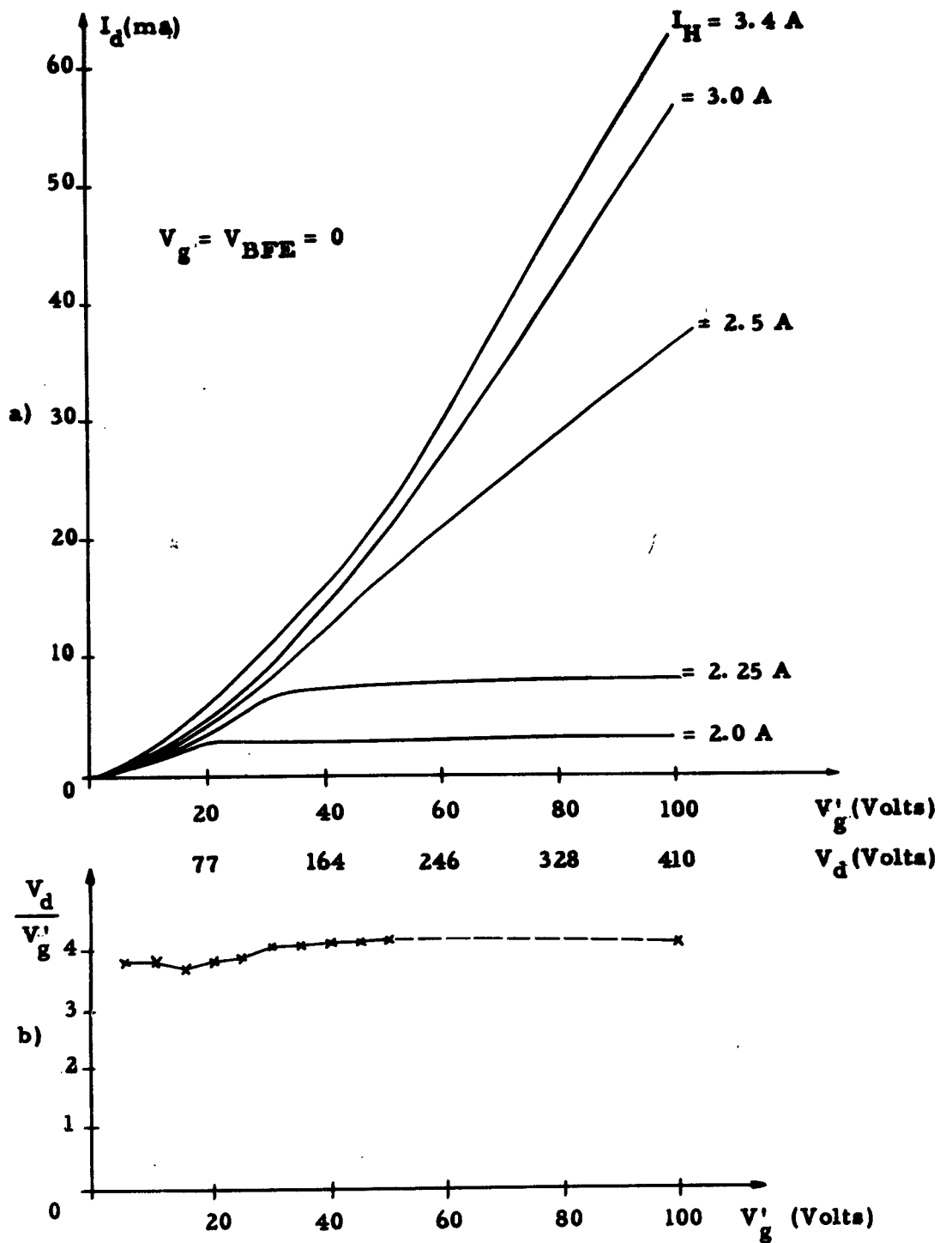


Figure VI. 2-1. DC characteristics of the experimental triode

brightness temperature of the bottom or base surface of the cathode. The cathode temperature was estimated to be 50°K below the base temperature (Figure VI. 2-2b). An error of 30°K is only about 2.5% at the temperatures of normal operation. By operating with $I_H = 3.0$ amperes, an estimated cathode temperature of 1160°K was obtained. This is equivalent to $kT_c/e = 0.1$ volts.

From III. 5(3) and (4), the noise current at low frequencies normalized to full shot current, is

$$R^2 = \frac{\langle i^2 \rangle}{2eI_d \Delta f} \bigg|_{\omega \tau \rightarrow 0} = 1.925 \frac{V_c}{V'_g} . \quad (1)$$

Figure VI. 2-2a shows the measured and theoretical values of R^2 as functions of T_c for V'_g equal to 5 and 10 volts. The theoretical curves rise with T_c , while the measured ones fall, and tend to level off toward the theoretical ones as T_c increases. This can be readily explained in terms of temperature-limited portions of the cathode. The approximation (1) is useful only when the entire emitting surface is space-charge limited. Although Figure VI. 2-1a shows that the current from the entire cathode is space-charge-limited for these operating conditions, there are still some small temperature-limited portions of the cathode surface, probably near the edges. As R^2 for the temperature-limited regions is unity, it is easy to see how, with $R^2 = 0.02$ in the space-charge-limited regions, only a 2% area of temperature-limitation can double the noise. This area decreases with increasing cathode temperatures, and the measured curves fall. For $V'_g = 10$ volts and $T_c = 1160^\circ$ ($U_0 = 0.01$), the reduction factor is about 0.01 more than it should be.

VI. 3. Effects of the Crossed Magnetic Field

From Figure III. 4-2 and Table V. 2-2 we can predict the variation of anode current with magnetic field from the single-

Figure VI. 2-2. a) Effect of cathode temperature on noise current with $B = 0$

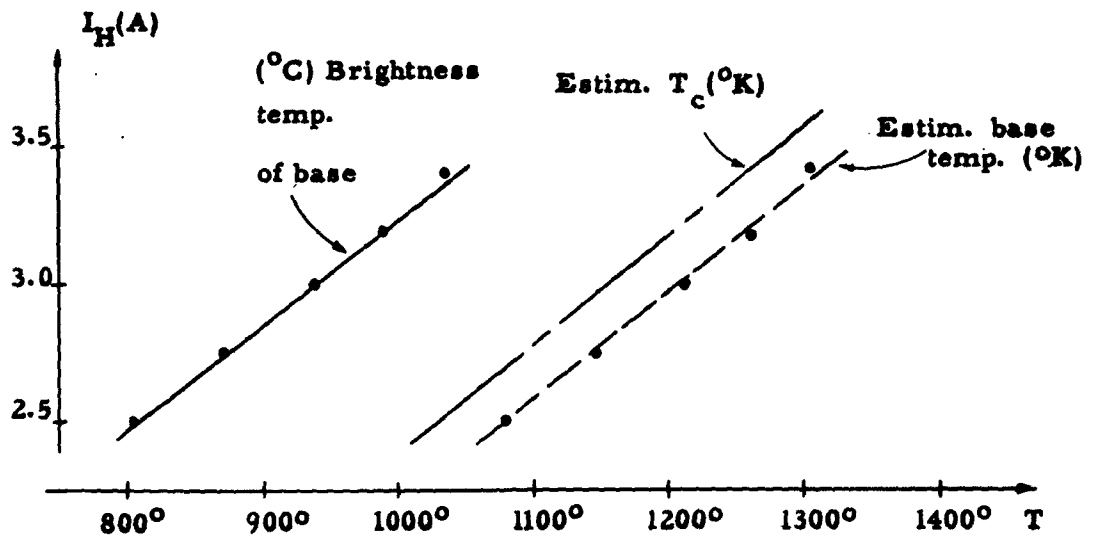
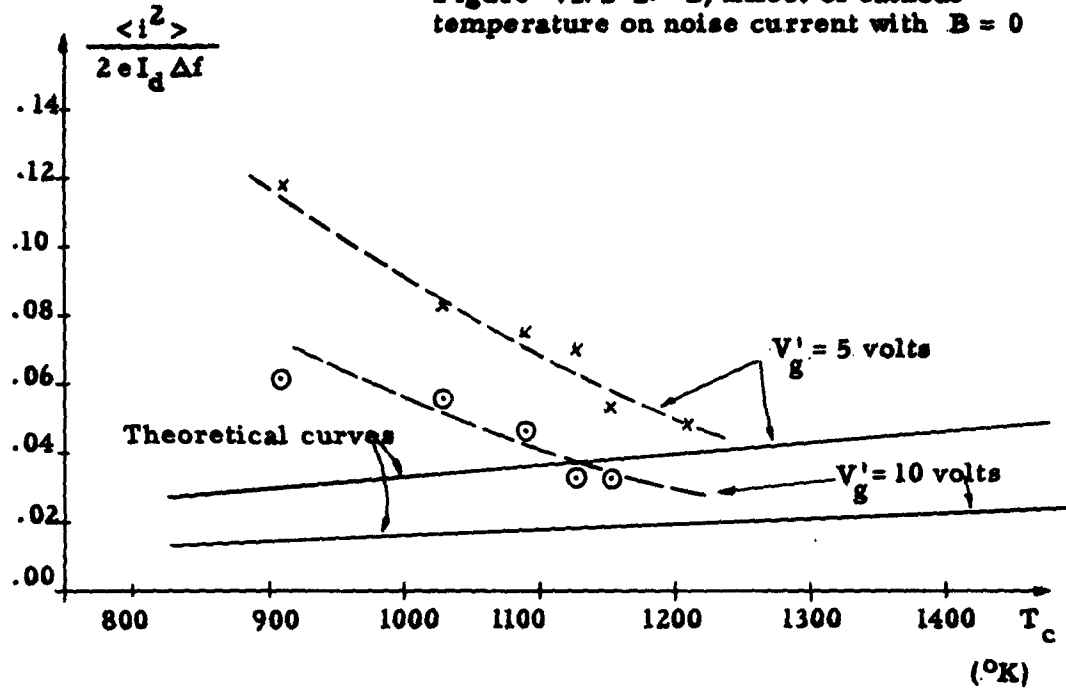


Figure VI. 2-2. b) Triode heater characteristics

velocity and Monte Carlo analyses, respectively. These curves are compared in Figure VI. 3-1 with experimental results for two values of equivalent grid voltage, $V'_g = 10$ and 20 volts. Several other values of V'_g were used, but the points all fell close to one curve, drawn solid in the figure to represent all data. The current is normalized to its zero magnetic field value, and the magnetic

field to $B_c = \sqrt{2V'_g / \eta d_{cg}^2}$. The dashed curve represents the results

of the single-velocity analysis, while the circled points were obtained from the Monte Carlo runs for the short-circuited diodes. There is good agreement between the two theories, but the measured currents are all larger near and beyond the critical magnetic field. The theories are fairly adequate for B/B_c less than 0.9, which is the same as θ less than π (from Figure III. 4-1).

The normalized noise current is shown in Figure VI. 3-2. At small magnetic fields, there is good agreement between both theories and the experimental results. As discussed in the last section, the measured noise currents are larger than the ones predicted by the single-velocity analysis in this range because of the existence of temperature-limited portions of the cathode. The circled points representing the Monte Carlo results are only results of a single spectral estimate. Because of this, it is surprising that they come as close as they do to the other curves. As the magnetic field is increased, both theory and experiment predict the same increase in noise. Beyond $B/B_c = 0.85$, the noise currents increase very rapidly, attaining values many times shot noise in the actual beam.

In order to investigate the shape and location of the beam, hydrogen gas was introduced into the tube through the palladium leak. By means of the excitation of the hydrogen by electron collisions, the beam could be observed visibly through a screened viewing window in the enclosure shielding the tube. Figures VI. 3-3 a) through f) show the beam as the magnetic field is increased from

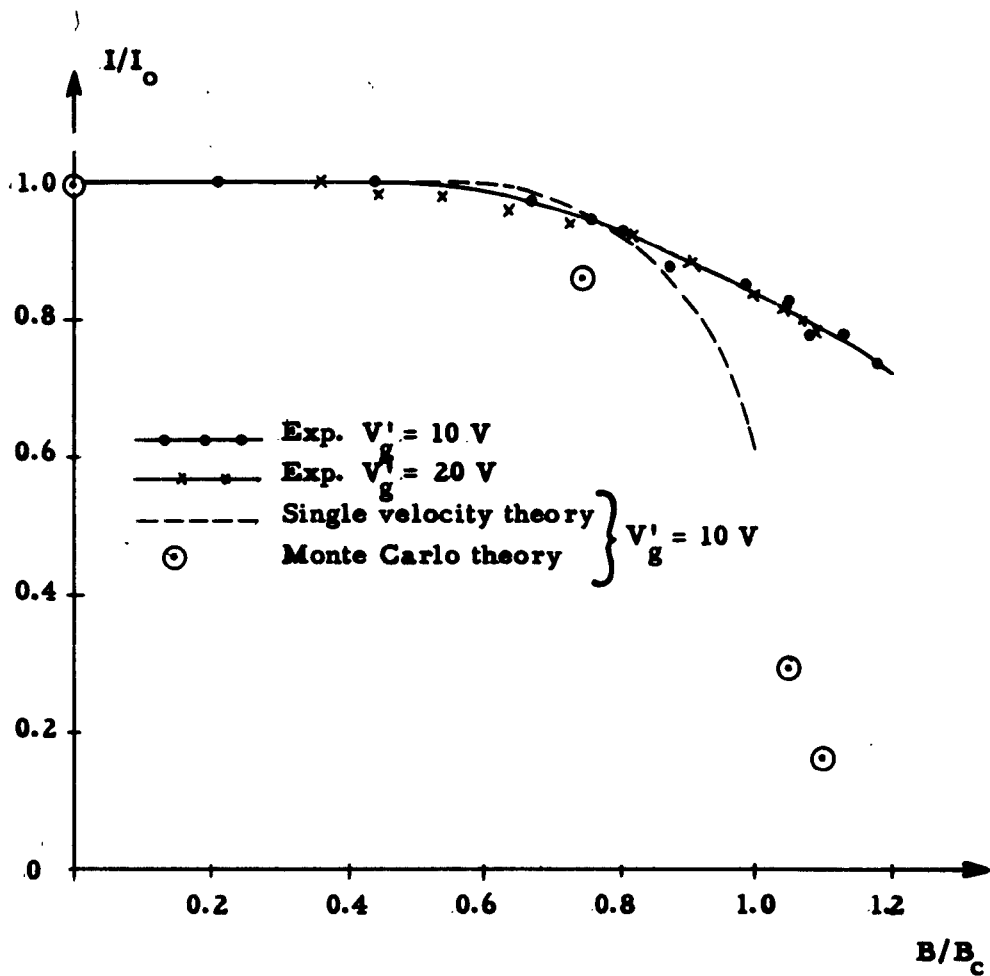


Figure VI. 3-1. Variation of average current with magnetic field

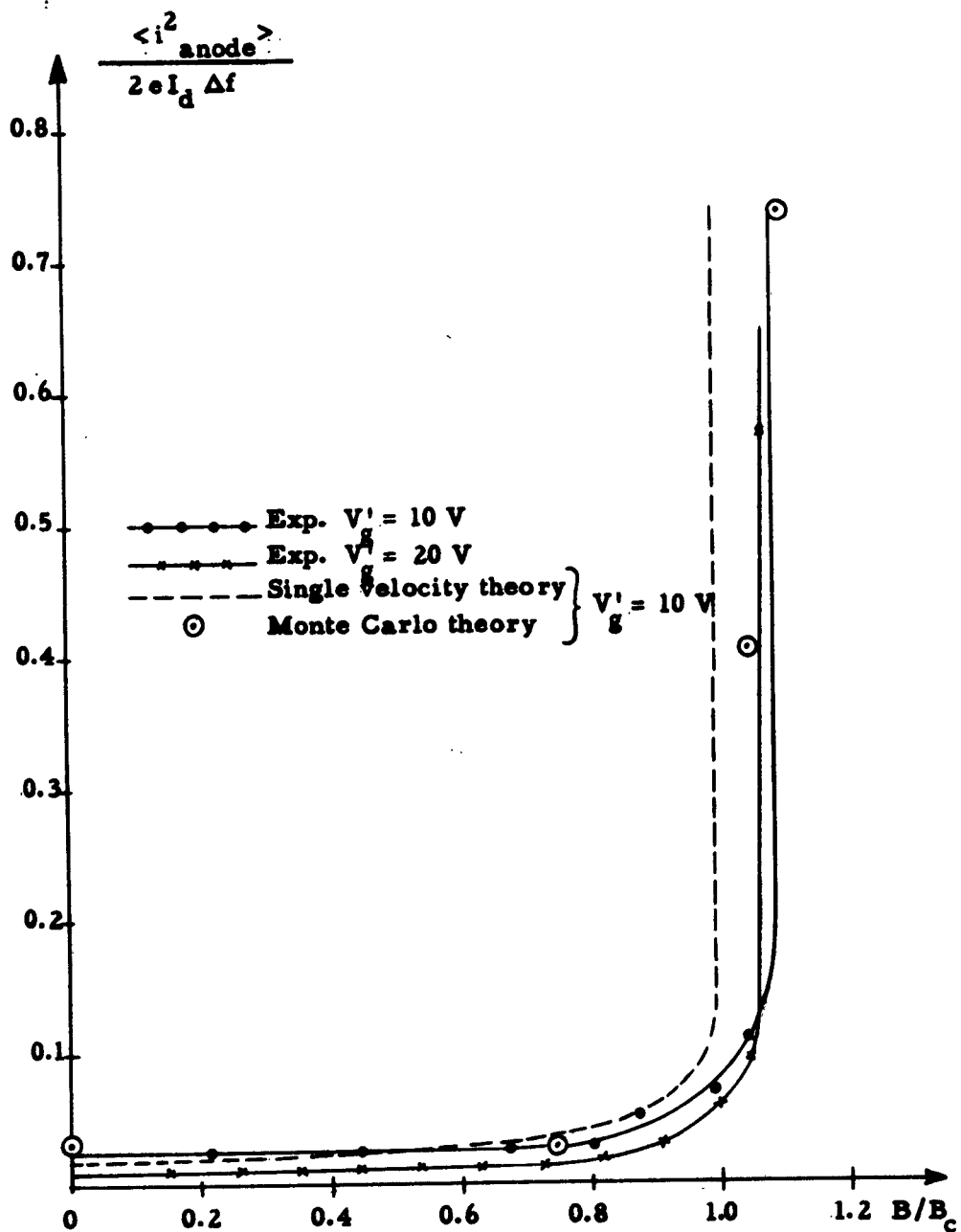


Figure VI. 3-2. Variation of anode noise current with magnetic field for the short-circuited diode at small transit angles

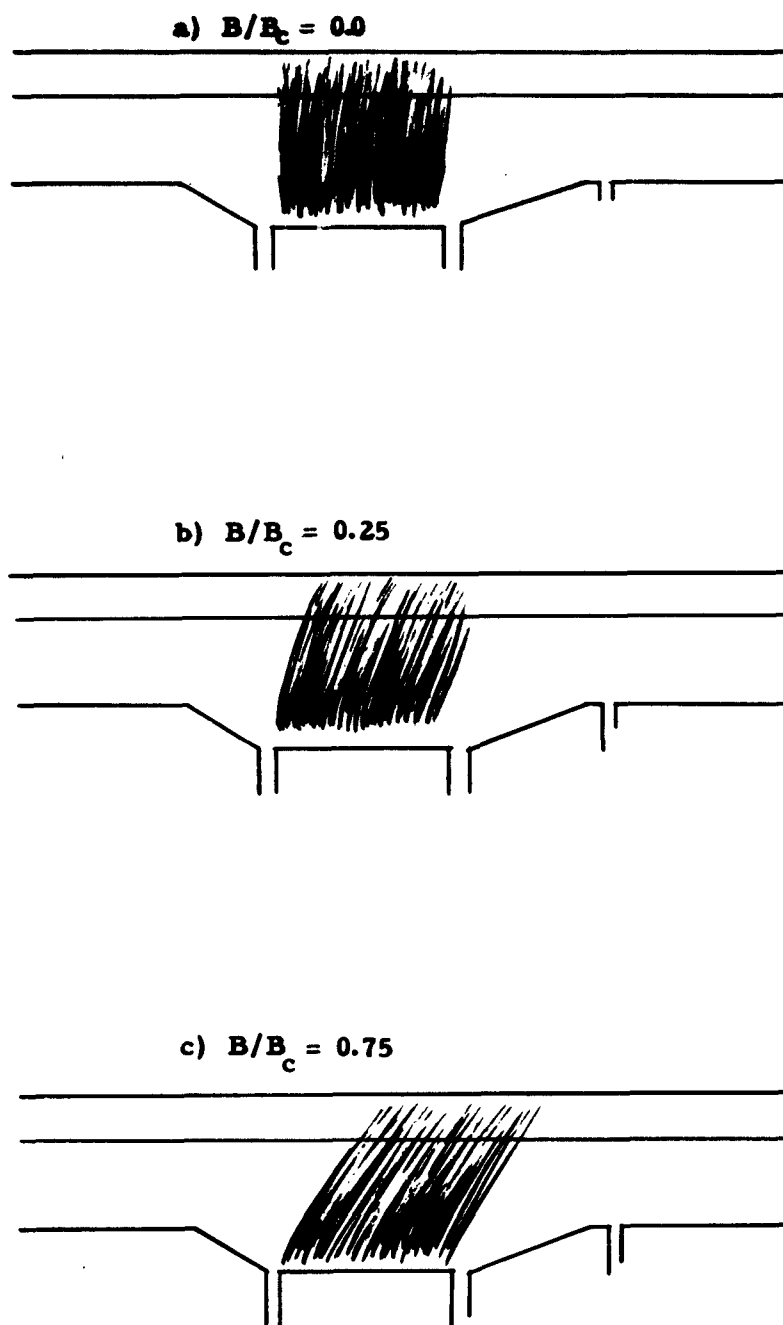
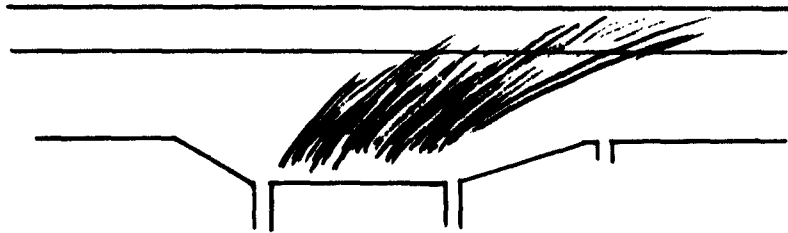
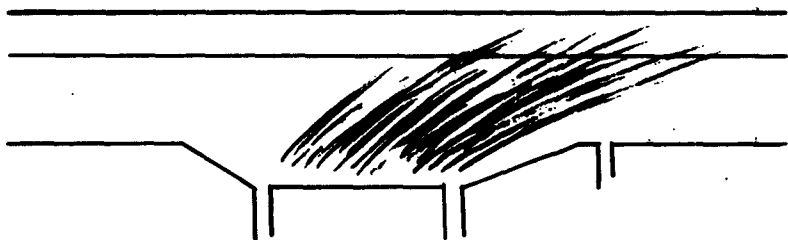


Figure VI. 3-3. Observations of the beam made by the introduction of H_2 gas into the tube

d) $B/B_c = 0.96$



e) $B/B_c = 1.0$



f) $B/B_c = 1.05$

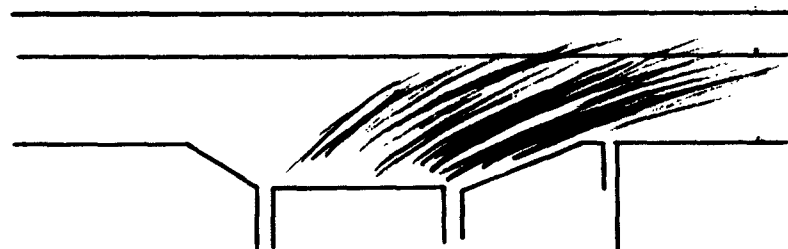


Figure VI. 3-3, Cont'd. Observations of the beam made by the introduction of H_2 gas into the tube

zero to a point just beyond B_c . The equivalent grid voltage V'_g was 100 volts, producing an anode current of nearly 60 ma with no magnetic field. Operation at lower currents did not produce a glow sufficiently bright for viewing.

The noise current varied with magnetic field in the same way as was observed at the lower effective grid voltages. Between $B/B_c = 0.75$ and 1.00 the beam was turned away from the anode considerably. At the same time, the noise current started to grow. At $B/B_c = 1.05$, the beam had turned until it grazed the grid plane. It was not possible to see along the entire length of the beam, because one of the supporting frames obstructed the view. As the beam grazed the grid plane, the noise rose sharply. The average anode current did not decrease appreciably at this point. It appears that the beam reached the anode at the end of the grid structure. This would not occur had an infinitely broad triode been constructed. This partly explains the lack of agreement between the measured and theoretical values of the average current (Figure VI.3-1) at the higher magnetic fields.

Introduction of the gas into the tube raised the noise current at magnetic fields below B_c . Nearer to the critical field, the noise rose more slowly with the gas in the tube. Average anode currents were higher, and grid currents became negative when the tube was operated under these conditions. The presence of positive ions in the beam accounts for the latter observations.

VI. 4. Related Experiments

An attempt was made to extend the noise current measurements to frequencies above 30 mc, where the measurements described in the previous section were made. The noise current "reduction factor" R^2 was found to peak at 65 mc, independently of the value of the magnetic field. A peak of $R^2 = 0.8$ was obtained with no magnetic field. This peak was not relatable to transit time effects. The average transit time increased by a factor of two when the magnetic field was increased from zero to the critical value, yet the peak

frequency remained constant. With no magnetic field, the transit angle was around unity at 65 mc for an equivalent grid voltage of 10 volts.

The peak was caused by a circuit effect. At 30 mc, the impedances across both the reference diode and the grid-anode gap were equal. However at 65 mc, there was a resonance in the circuit and the impedance across the grid-anode gap appeared to increase to a maximum. A resonance in the rf chokes, which isolate the cathode and beam-forming electrode structure from the rf ground, was the most likely cause of the problem. The measurements at 30 mc were well down on the resonance curve, and were not affected by this difficulty. Before further attempts to extend the experiment to higher frequencies are made, more work will have to be done to insure that similar circuit problems do not arise.

The beam-forming electrodes and the sole electrode (BFE's) were connected to one another and the cathode for all of the measurements that have already been discussed. In the course of the measurements it was found that the left BFE in the tube version number two sagged against the cathode when the latter was run at its normal temperature. By operating at a lower heater current of 2.7 amperes, the BFE could be isolated from the cathode. From Figure VI. 2-1a, it can be seen that the tube characteristics at the corresponding lower cathode temperature (1090°K) are not much different from the ones obtained at the usual operating point. The noise current was measured at 30 mc for two effective grid voltages, $V'_g = 10$ volts and $V'_g = 100$ volts. The BFE's were joined together and operated between zero and two volts more negative than the cathode.

At the lower value of V'_g , it was found that the noise current reduction factor R^2 decreased with more negative BFE voltage, when the magnetic field was held constant. This could be attributed to the fact that the beam moved closer to the anode when the BFE's became more negative. Effectively, the value of the critical

magnetic field in the BFE-grid region increased appreciably, since the two volts on the BFE were a large fraction of the 10 volt effective grid voltage.

To separate the effect of the BFE voltage on the overall beam shape and its more local effect on the immediate cathode region, the higher value of $V'_g = 100$ volts was used. Here the effects were in the same direction as with the lower value of V'_g , but the decreases of R^2 were by a much smaller amount. The noise current rose sharply near the same critical magnetic field for the complete range of BFE voltages used. The effect of the BFE voltage in this case was to change the potential along the edge of the beam, primarily in the lower-velocity region near the cathode. There was no evidence that this had any effect on the noise growth in the stream.

VII. CONCLUSIONS AND SUGGESTIONS FOR FURTHER WORK

VII.1. Conclusions

The single-velocity and Monte Carlo analyses, and the measurements on the crossed-field triode all show that there is a growth of noise in the crossed-field stream for magnetic fields near the critical field, B_c . In particular, these measurements and those by other workers indicate that there is an increase of the normal component of convection current fluctuations at the anode of a crossed-field diode above the fluctuations existing with no magnetic field. The noise current grows slowly with increasing magnetic field at first, and then increases rapidly near $B = B_c$. This rapid increase coincides with the conditions for the stream to just graze the anode, or the effective anode in the triode measurements reported here. Beyond $B = B_c$, noise currents greater than full shot noise by a couple of orders of magnitude have been observed in these and other experiments.

The single-velocity model predicts the same growth of noise current, over the frequency range for which it is valid. The more detailed Monte Carlo analysis also predicts this behavior. The single-velocity model is not valid for magnetic fields beyond B_c , for in that case the stream returns to the cathode. Although the Monte Carlo study can be carried beyond that point, it becomes less and less representative of a physical crossed-field gun. For magnetic fields less than B_c , both theories agree in detail with the noise current measurements.

Measurements by other workers have shown the existence of large electron velocity spreads at the anodes of crossed-field devices. The single-velocity analysis predicts the increase of velocity fluctuations at low frequencies in the short-circuited diode, but none at higher frequencies or in the open-circuited diode. The Monte Carlo analysis shows that the distribution of normal velocity at the anode does spread with increasing magnetic field. A simple dc model predicts the same magnitude of spread as the detailed Monte Carlo analysis. There is no increase in beam energy in the simple model; only the effects of the magnetic field and the initial velocities cause this "geometrical" spread. This phenomenon helps to explain the slow decrease of anode current with increasing magnetic field observed in crossed-field diodes. Lindsay (1962) too suggests this explanation on the basis of a similar dc model. However, it does not completely explain the slow fall-off of current (Fulop, 1958) nor some other measurements of high equivalent temperature.

Analyses of the one-dimensional model of the crossed-field diode agree quite well with experimental results for magnetic fields less than B_c . Yet the edge wave growth and potential minimum instability postulated by Van Duzer and Whinnery (1961b) do not appear in this model. Growth takes place in the body of the stream. These results do not rule out the possibility of another growth mechanism that would be more important for $B > B_c$.

Although no instabilities of the potential minimum were found, some new results were obtained for this region. In the one-dimensional model, the Monte Carlo analysis shows that there are few major differences between the crossed-field and ordinary minima, for $B \lesssim B_c$. The normal and transverse velocity distributions and spectra maintain their initial form as they propagate toward the minimum from the cathode.

The shot noise current at the cathode is transported to the potential minimum undiminished at frequencies above the plasma frequency at the minimum, f_{pm} . Below this frequency there is some smoothing of the shot current at small magnetic fields, but none at the higher fields near B_c . In the vicinity of the plasma frequency, the details of the spectra have been examined more closely. The current spectra, or shot noise reduction factors R^2 for $B = 0$ and $B = .75 B_c$ are very similar. This is in agreement with the results of a linearized approximate analysis of the crossed-field potential minimum in a one-dimensional stream (Van Duzer and Whinnery, 1961a).

The short-circuited diode with zero magnetic field has been treated both by the Monte Carlo method and by extending Whinnery's (1960) approximate analysis to more velocity classes. Both analyses show a peak in R^2 above unity near f_{pm} . The peak is more directly related to the transit time of electrons from the cathode to the minimum, as the approximate analysis shows. Its presence is predicted for the infinite diode by Whinnery and again by Siegman and Watkins (1957) using an open-circuited diode model. The "Tien" dip below f_{pm} was found in the unsmoothed Monte Carlo results for both the open- and short-circuited diodes. Whereas the approximate analysis does not show this dip, it may when the results are weighted over many velocity classes of critical charges. The Monte Carlo results for the open-circuited diode agree qualitatively with the approximate theories, but not with the similar Monte Carlo study of Dayem (1960). No reason for this discrepancy could be found.

Study of the spectral methods indicate that much care must be exercised before valid conclusions can be drawn about particular spectra. The variability of the spectra, for example, make the existence of correlation between current and velocity fluctuations at the potential minimum impossible to determine for the amount of data available from these runs. Longer runs would be needed to gain this information. The length of data used here is quite suitable, however, to determine the gross effects of the magnetic field on the noise transport process.

The range of validity of the single-velocity electronic theories (Llewellyn-Peterson, 1941, 1944; Van Duzer, 1961a) was investigated. It was found that input velocity fluctuations would cause charges to cross over one another when the frequency of the fluctuations was sufficiently high. This is not much of a problem at high average beam velocities, but it is an important factor when using the crossed-field transformation equations and when using the Llewellyn-Peterson equations for the space-charge-limited diode with low anode voltages. Use of the space charge parameter ξ was extended to the crossed-field diode equations. The approximation $\xi = 1$ for the space-charge-limited diode permits simplification of the various relations, but care must be taken to insure that erroneous effects do not result. At the low frequency limit the coefficients are not corrected for $\xi = 1$. At slightly higher frequencies, however, this approximation gives results that are very close to the exact results, especially for high anode voltages.

VII. 2. Suggestions for Further Work

Although the present work contributes to the understanding of some aspects of noise transport in crossed-field streams, there is much left to be done.

The transformation equation approach should prove useful in the future for the evaluation and reduction of amplifier noise figures, although the problem of velocity spread should be considered in more detail. Its extension to other models, perhaps two-dimensional ones, should be studied. The steady state flow in the crossed-field, space-charge limited diode could be determined for a wider range of

parameters. This would be an extension of the work of Yankina (1959) and Lindsay (1960).

The Monte Carlo study should be extended to values of magnetic field beyond B_c . Perhaps a two-dimensional model, as used by Wadhwa (1962), could be investigated further. Calculation over a wider range of anode voltages would be useful, too. These computations might be very time-consuming and expensive even on the newer digital computers, unless new techniques and simplifications could be found.

Measurements in the crossed-field triode or tubes of similar geometry should be extended to higher frequencies, to check the validity of the theories. Noise currents should also be carefully measured in other configurations.

The discrepancy between the zero-magnetic-field Monte Carlo results for the open-circuited diode reported here and those obtained by Dayem (1960) should be investigated further. More accurate calculation, using longer computer runs, should be used to check on this open-circuited diode problem. Longer runs would also make possible the determination of any correlation between velocity and current fluctuations at the potential minimum. The nature of the "Tien dip" could also be examined more thoroughly in this manner.

The potential minimum noise current reduction factor curves have never been verified experimentally in detail, and this difficult problem deserves renewed efforts. Vlaardingerbroek (1960, 1961) used the Llewellyn-Peterson equations to evaluate R^2 from noise measurements on a microwave triode. He obtained values for R^2 of 0.64 at 1400 mc and of 4 at 4000 mc. The latter was in the range of the plasma frequency at the potential minimum. These measurements are in qualitative agreement with the results of both the approximate analysis and the Monte Carlo study. This approach might be refined to permit more complete verification of the theories.

By using a low current density beam in a diode of large cathode area, Siegman (1957b) hoped to move the minimum away from the cathode to facilitate direct noise current measurements. His experiment was unsuccessful because of non-uniform emission and other factors. However, the idea of scaling distance and frequency may yet prove important. Experiments on noise amplification (Pollack and Whinnery, 1962) have shown the possibility of artificially producing velocity distributions with high equivalent temperatures in an electron stream. The scaling to lower frequencies and larger spacings that would be produced by introducing such a high temperature beam at the "cathode" of a suitable diode could make measurements of R^2 more practical.

APPENDIX A

DETAILS OF THE TIME DOMAIN ANALYSIS

We consider the case of " β " electrons, those with sufficient initial velocity to cross the potential minimum ($\eta_0 > 0$). To evaluate II. 5(3) and II. 5(4), we assume that $x_m \ll d$ so that the second part of the integral of II. 5(4) is negligible, and we further assume that for large values of ξ , ξ_2 and τ are related so that

$$\frac{\xi_2(\tau)}{\xi_d} = \left(\frac{\tau}{\tau_d} \right)^3 \quad (\text{A-1})$$

where τ_d is the transit time from the minimum to the anode. This approximate result is deduced from the 4/3 power law of voltage vs distance, for a diode with zero electron velocity at the potential minimum.

Figures A.1(a) and (b) show typical trajectories for $\eta_0 > \eta_1$ and $\eta_1 > \eta_0$, respectively. From the figures it is evident that

$$\frac{\xi_0(\tau_0)}{\xi_d} = \left(\frac{\tau_0 - \tau_{om}}{\tau_d} \right)^3 = \left(\frac{\tau}{\tau_d} \right)^3 \text{ for } \eta_0 > \eta_1$$

while (A-2)

$$\frac{\xi_0(\tau_0)}{\xi_d} = \left(\frac{\tau_0 - \tau_{om}}{\tau_d} \right)^3 = \left(\frac{\tau - \tau'_{om}}{\tau_d} \right)^3 \text{ for } \eta_1 > \eta_0,$$

where τ_{om} and τ_{lm} are the cathode to minimum transit times for perturbing and critical charges, respectively, and

$$\begin{aligned} \tau'_{om} &= \tau_{om} - \tau_{lm} & \eta_1 > \eta_0 \\ &= 0 & \eta_0 \geq \eta_1. \end{aligned} \quad (\text{A-3})$$

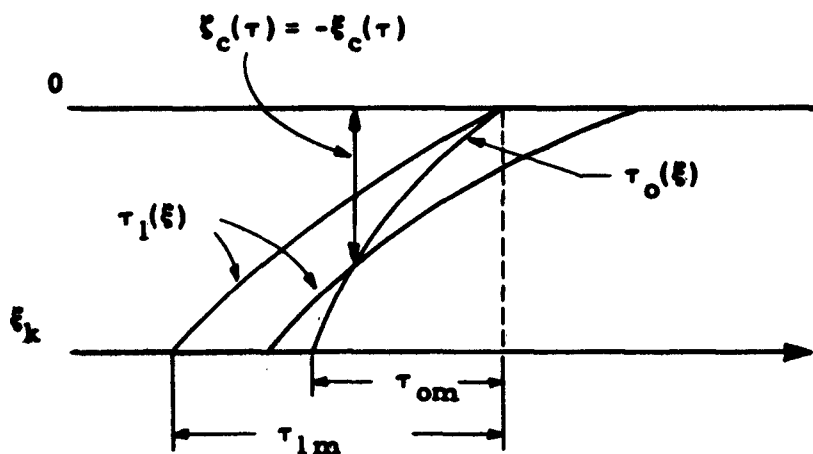


Figure A.1(a). Trajectories for $\eta_0 > \eta_1$

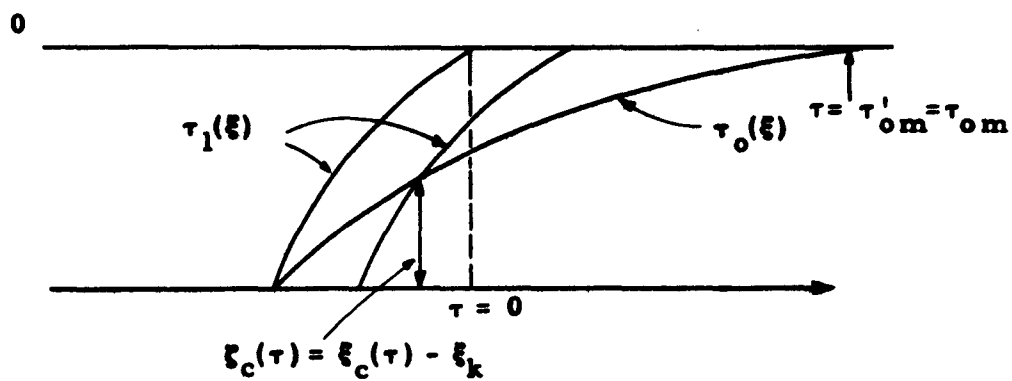


Figure A.1(b). Trajectories for $\eta_1 > \eta_0$

After integration of II.5(4),

$$h_1(\tau) = -\xi_1 \left(\frac{\tau}{2} \right) + f \left(\frac{\tau}{\tau_d} \right), \quad (\text{A-4})$$

$$f \left(\frac{\tau}{\tau_d} \right) = \xi_k \left(\frac{\tau}{\tau_d} \right)^3 + b_3 \left(\frac{\tau}{\tau_d} \right)^2 - c_3 \left(\frac{\tau}{\tau_d} \right) + d_3, \quad (\text{A-5})$$

with the following definitions of the constants:

$$\begin{aligned} b_3 &= \frac{3}{\tau_d} \int_{\xi_k}^0 \tau_1(\xi) d\xi \approx \frac{3}{\tau_d} \int_{\xi_1(\tau)}^0 \tau_1(\xi) d\xi \\ c_3 &= \frac{3}{2} \int_{\xi_k}^0 \tau_1^2(\xi) d\xi \approx \frac{3}{2} \int_{\xi_1(\tau)}^0 \tau_1^2(\xi) d\xi \quad (\text{A-6}) \\ d_3 &= \frac{1}{3} \int_{\xi_k}^0 \tau_1^3(\xi) d\xi \approx \frac{1}{3} \int_{\xi_1(\tau)}^0 \tau_1^3(\xi) d\xi. \end{aligned}$$

The integral equation II.5(2) can be transformed easily into the frequency domain in terms of the normalized frequency a . Since there is no effect on critical charges for $\tau > \tau_d$,

$$g_1(a) = \frac{1}{2\pi} \int_0^{\tau_d} h_1(\tau) e^{-ja\tau} d\tau. \quad (\text{A-7})$$

This integral can be expressed as an integral over all time, giving $g_{1\infty}(a)$ of the infinite diode, and a finite spacing correction factor.

$$g_1(a) = g_{1\infty}(a) - F(a\tau_d) \quad (\text{A-8})$$

$$F(a\tau_d) = -\frac{1}{2\pi} \int_0^{\tau_d} f\left(\frac{\tau}{\tau_d}\right) e^{-ja\tau} d\tau - \frac{\xi_k}{2\pi ja} e^{-ja\tau_d}. \quad (A-9)$$

Similarly, II. 5(3) can be transformed. For $\eta_0 > \eta_1$, using (2),

$$g_0(a) = \frac{1}{2\pi} \int_0^{\tau_d} h_0(\tau) e^{-ja\tau} d\tau = g_{0\infty}(a) - F(a\tau_d) \quad (A-10)$$

But for $\eta_1 > \eta_0$, the upper limit of the integral must be changed, since the perturbing charge does not reach the anode until $\tau = \tau_d + \tau'_{om}$. Thus for $\eta_1 > \eta_0$,

$$g_0(a) = \frac{1}{2\pi} \int_0^{\tau_d + \tau'_{om}} h_0(\tau) e^{-ja\tau} d\tau \quad (A-11)$$

or

$$g_0(a) = g_{0\infty} - F(a\tau_d) e^{-ja\tau'_{om}}, \quad (A-12)$$

as $f(\tau/\tau_d)$ becomes $f[(\tau - \tau'_{om})/\tau_d]$ in (A-4). Equation (12) is true in general, since τ'_{om} is defined to be zero for $\eta_0 \geq \eta_1$. Transforming $j(\tau)$ of II. 5(2) into $g(a)$, we obtain an expression analogous to II. 4(6). Adding the transform of the perturbation charge,

$$g_p(a) = -\frac{e^{-ja\tau'_{om}}}{2\pi}, \quad (A-13)$$

we arrive at the reduction factor for noise for a given η_1 and η_0 ,

$$\begin{aligned} |\tau_\beta|^2 &= \left| \frac{g_\beta(a) + g_p(a)}{g_p(a)} \right|^2 = \\ &= \left| 1 - \frac{\sqrt{\pi} g_0(a) e^{ja\tau'_{om}}}{1 + \sqrt{\pi} g_1(a)} \right|^2. \end{aligned} \quad (A-14)$$

Substituting (8) and (12) into (14), we obtain the final expression for the case of perturbing electrons flowing past the minimum ($\eta_0 > 0$), II. 5(5).

APPENDIX B

DETAILS OF THE FREQUENCY DOMAIN POTENTIAL MINIMUM ANALYSIS

We will only consider the case of the β electrons ($\eta_0 > 0$). By using Δq from II. 5(8) in II. 5(1) and integrating the resulting fields to obtain ΔV , the current $i_r(x_m)$ can be found. The details of the integrations can be found in Whinnery's analysis. Substituting into II. 5(9), we have for the normalized current reduction factor:

$$\begin{aligned} r_\beta = & \left[1 + \frac{b_0}{2\sqrt{\pi}ja} \int_{\xi_k}^0 e^{-ja\tau_1} d\xi + \frac{1}{2\sqrt{\pi}ja} \int_{\xi_k}^0 e^{-2ja\tau_1} d\xi + \right. \\ & \left. \frac{a_0}{2\sqrt{\pi}ja} \int_{\xi_k}^0 e^{-ja(\tau_1 - \tau_{om})} d\xi - \frac{1}{2\sqrt{\pi}ja} \int_{\xi_k}^0 e^{-ja[\tau_1 + \tau_0 - \tau_{om}]} d\xi \right] \\ & \sqrt{\left[1 + \frac{b_0}{2\sqrt{\pi}ja} \int_{\xi_k}^0 e^{-ja\tau_1} d\xi + \frac{1}{2\sqrt{\pi}ja} \int_{\xi_k}^0 e^{-2ja\tau_1} d\xi \right]} \quad (B-1) \end{aligned}$$

where

$$a_0 = ja \int_0^{\tau_{od}} \frac{\xi(\tau_0)}{\xi_d} e^{-ja\tau_{od}\tau_0} + e^{-ja\tau_{od}} \quad (B-2)$$

and

$$b_0 = -ja \int_{\tau_{1k}}^0 \frac{\xi(\tau_1)}{\xi_d} e^{-ja\tau_1} d\tau_1 - ja \int_0^{\tau_{2d}} \frac{\xi(\tau_2)}{\xi_d} e^{-ja\tau_2} d\tau_2 - e^{-ja\tau_{2d}} \quad (B-3)$$

By partial integration, it can be shown that

$$\frac{1}{2\sqrt{\pi}ja} \int_{\xi_k}^0 e^{-2ja\tau_1} d\xi = \frac{\sqrt{\pi}}{2\pi} \int_0^\infty -\xi_1\left(\frac{\tau}{2}\right) e^{-ja\tau} d\tau = \sqrt{\pi} g_1 \infty. \quad (B-4)$$

We further define

$$G_1 = \frac{1}{2\pi ja} \int_{\xi_k}^0 e^{-ja\tau_1} d\xi \quad (B-5)$$

The last integral, I_n , in the numerator of (B-1), can be evaluated by defining

$$\tau_o^*(\xi) = \int_{\xi}^0 \frac{d\xi}{\sqrt{\eta(\xi) + \eta_o}} = \tau_{om} - \tau_o(\xi) \quad (B-6)$$

so that

$$I_n = \frac{\sqrt{\pi}}{2\pi ja} \int_{\xi_k}^0 e^{ja(\tau_o^* - \tau_1)} d\xi. \quad (B-7)$$

The time function corresponding to (B-7) is

$$f_o(\tau) = \sqrt{\pi} \int_{-\infty}^{\infty} \int_{\xi_k}^0 \frac{e^{ja(\tau_o^* - \tau_1)}}{2\pi ja} e^{ja\tau} d\xi da = \sqrt{\pi} \int_{\xi_k}^0 H_s(\tau + \tau_o^* - \tau_1) d\xi, \quad (B-8)$$

H_s being the Heaviside step function. The integrand in (B-8) has a value only for $\tau \geq \tau_1 - \tau_o^*$, and Figures B.1(a) and (b) show the relation of $f_o(\tau)$ to $\xi_c(\tau)$. For $\eta_o > \eta_1$,

$$f_o(\tau) = \int_{\xi_c}^0 d\xi = -\xi_c(\tau) = \xi_c(\tau), \quad (B-9)$$

while for $\eta_1 > \eta_o$,

$$f_o(\tau) = \int_{\xi_k}^{\xi_c} d\xi = \xi_c - \xi_k. \quad (B-10)$$

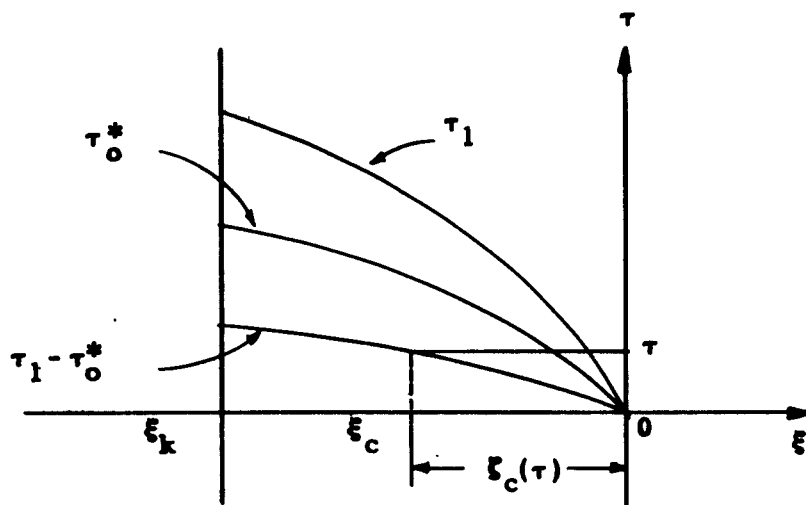


Figure B.1(a). Curve of $\tau_1 - \tau_0^*$ for $\eta_0 > \eta_1$

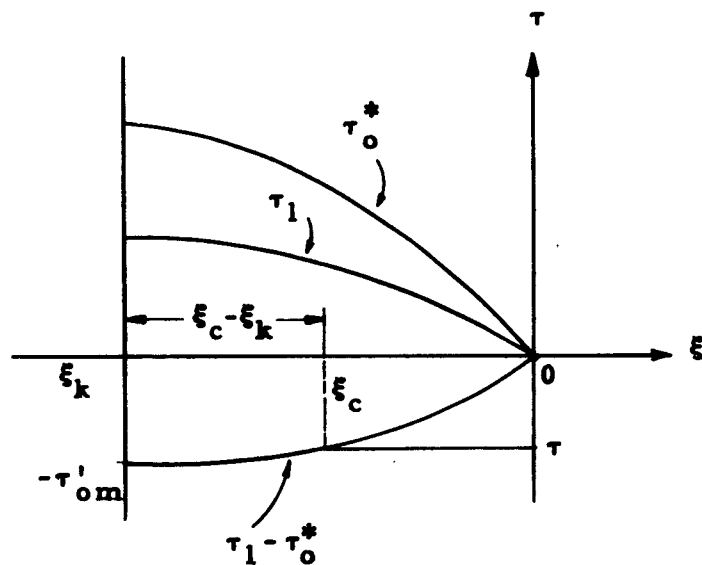


Figure B.1(b). Curve of $\tau_1 - \tau_0^*$ for $\eta_1 > \eta_0$

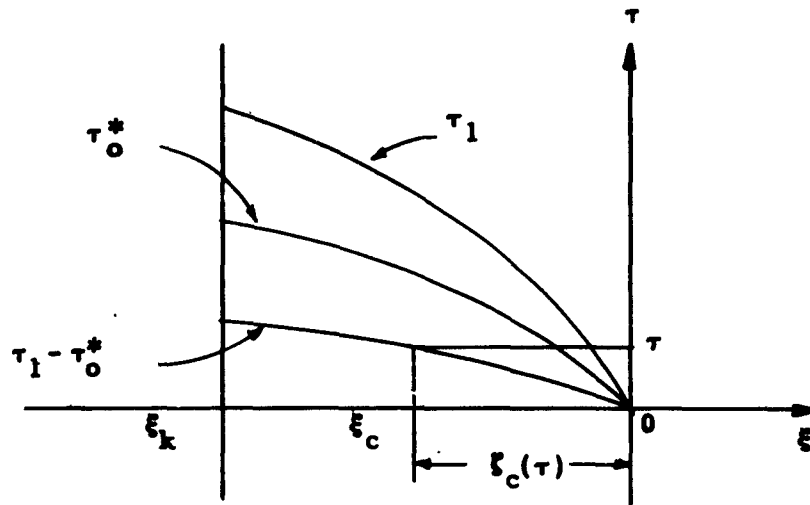


Figure B.1(a). Curve of $\tau_1 - \tau_0^*$ for $\eta_0 > \eta_1$

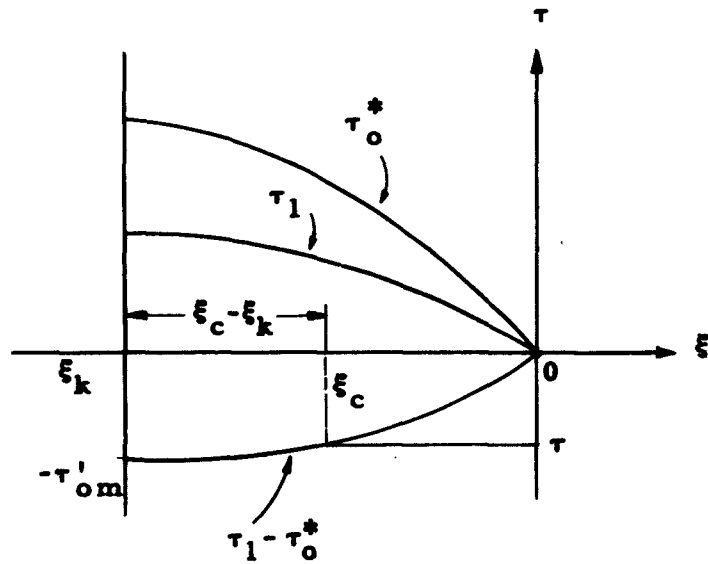


Figure B.1(b). Curve of $\tau_1 - \tau_0^*$ for $\eta_1 > \eta_0$

It should be noted, however, that the function $f_o(\tau)$ for $\eta_1 > \eta_o$ is displaced in time so that now

$$f_o(\tau) = \xi_c(\tau + \tau'_{om}); \quad \eta_1 > \eta_o. \quad (B-11)$$

Thus, the integral (21) is actually

$$I_n = \sqrt{\pi} g_{oco} e^{ja\tau'_{om}}; \quad (B-12)$$

b_o can be evaluated from (17) by again neglecting the integral in $\xi(\tau_1)$. Using the approximation (1) for $\xi(\tau_2)$ and retaining only terms up to second order in $1/a\tau_d$,

$$b_o = -e^{-ja\tau_d} \left[\frac{3j}{a\tau_d} + \frac{6}{(a\tau_d)^2} \right] \quad (B-13)$$

Similarly, using (2) and referring to Figure A.1,

$$a_o = -e^{-ja\tau_{om}} b_o. \quad (B-14)$$

Note that τ_{od} equals $\tau_d + \tau_{om}$ for both $\eta_o > \eta_1$ and $\eta_o < \eta_1$.

Substituting the above into (B-1), we obtain II. 5(10).

APPENDIX C NUMERICAL APPROXIMATIONS FOR THE POTENTIAL MINIMUM ANALYSIS

Evaluation of the noise reduction factor $|r|^2$ in the analysis of the potential minimum at high frequencies, Chapter II, requires the computation of the Fourier transforms of certain functions obtainable numerically from the trajectories of critical and perturbing charges. By fitting relatively simple analytic expressions to these functions, considerable simplification of the transforms results.

The trajectories are first evaluated from II.4(2). Then the crossover function for $\eta_0 > 0$, defined in II.4(3), and $\xi_1(\tau)$, the inverse of $\tau_1(\xi)$ are both found to have the general form shown in Figure C.1.

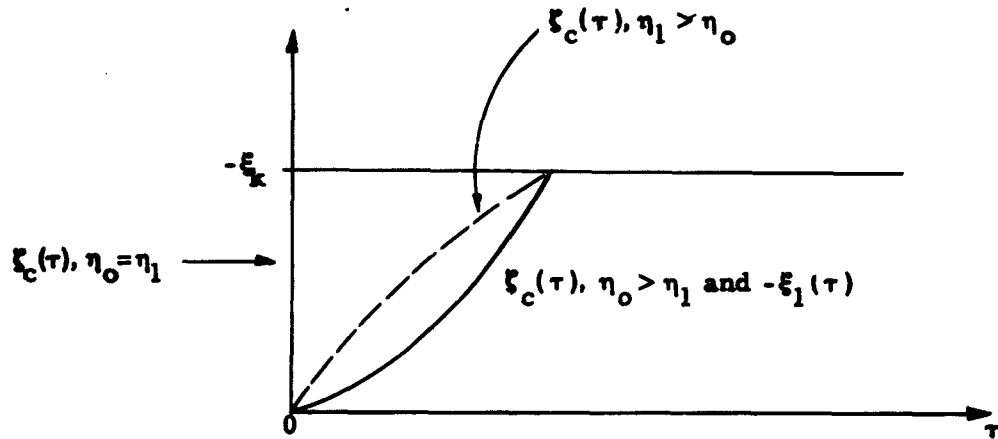


Figure C.1. Form of crossover function and critical charge trajectory

An exponential approximation up to a particular time seems appropriate. This time is τ_{1m} for $\xi_1(t)$ and $\tau_{10} = |\tau_{1m} - \tau_{om}|$ for $\xi_c(\tau)$. We may choose for the crossover function

$$\xi_c(\tau) \approx p(e^{q\tau} - 1), \quad 0 < \tau < \tau_{10} \quad (C-1)$$

$$= -\xi_k \quad \tau_{10} < \tau.$$

Then, noting that

$$p(e^{q\tau_{10}} - 1) = -\xi_k \quad (C-2)$$

after some manipulation II. 4(8) becomes

$$g_{\infty} \approx \frac{pq}{2\pi} \left[\frac{e^{(q-j a)\tau_{10}-1}}{a^2 + j a q} \right] \quad (C-3)$$

For $\eta_1 = \eta_0$, $\xi_c(\tau)$ becomes the step function $-\xi_k H_s(\tau)$ where $H_s(\tau)$ is the Heaviside unit step. By permitting q and τ_{10} to approach zero while $pq\tau_{10}$ approaches $-\xi_k$,

$$g_{\infty} = \frac{j\xi_k}{2\pi a}, \quad \eta_1 = \eta_0, \quad (C-4)$$

the same result obtained by Whinnery (1960).

Table C.2 gives the values of the parameters evaluated for various values of η_1 and η_0 . In all cases, a ratio of emission current to anode current of 5 was used, giving a value of $-\xi_k = 1.8845$ for use in the trajectory calculations.

In a similar manner, the trajectory $\xi_1(\tau)$ can be approximated by

$$\begin{aligned} -\xi_1(\tau) &= \beta (e^{\alpha\tau} - 1), & 0 < \tau < \tau_{1m} \\ &= -\xi_k, & \tau_{1m} < \tau. \end{aligned} \quad (C-5)$$

Then $g_{1\infty}$ (from II. 4(9)) becomes

$$g_{1\infty} = \frac{\alpha\beta}{4\pi} \left[\frac{e^{(\alpha-2ja)\tau_{1m}-1}}{a^2 + ja\alpha/2} \right] \quad (C-6)$$

This and the following approximations were obtained by Whinnery, and are repeated here for completeness. Table C-1 gives the parameters α , β , and τ_{1m} for the values of η_1 chosen.

The integral in II. 5(11) can be put into the same form as $g_{1\infty}$ after partial integration. We obtain

$$G_1 = \frac{\alpha \beta}{2\pi} \left[\frac{e^{(\alpha - ja)\tau_{lm} - 1}}{a^2 + ja\alpha} \right] \quad (C-7)$$

with the use of the exponential approximation.

For $\eta_0 < 0$, the case of the α electrons that are returned to the cathode, Figure C.2 shows typical curves of the crossover function.

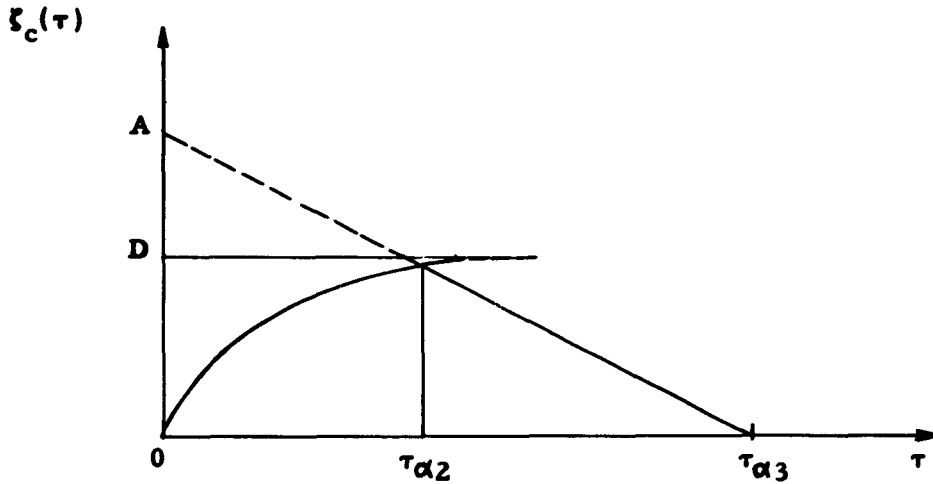


Figure C.2. Crossover function for α electrons

This can be approximated by

$$\begin{aligned} \xi_c(\tau) &= D(1 - e^{-C\tau}), & 0 < \tau < \tau_{\alpha 2} \\ &= A - B\tau, & \tau_{\alpha 2} < \tau < \tau_{\alpha 3} \\ &= 0, & \tau_{\alpha 3} < \tau. \end{aligned} \quad (C-8)$$

Substitution in II.4(8) gives, after some manipulation and elimination of A,

$$g_{\infty} = \frac{CD}{ja(C+ja)} + \frac{B}{a^2} (e^{-ja\tau_{\alpha 2}} - e^{-ja\tau_{\alpha 3}}) \quad (C-9)$$

Values of B, C, D, $\tau_{\alpha 2}$ and $\tau_{\alpha 3}$ are given in Table C.3.

η_1	τ_{1m}	α	β
0.01	5.58	0.925	0.0108
0.125	3.18	0.84	0.149
0.25	2.61	0.71	0.352
0.50	2.09	0.515	0.970
1.00	1.62	0.19	5.270

Table C-1. β -electron trajectory parameters

η_1	η_0	τ_{10}	q	p
.01	.01	—	—	—
	.125	2.40	3.31	0.0000673
	.25	2.97	2.37	0.00165
	.50	3.49	2.02	0.00161
	1.00	3.96	1.18	0.0176
.125	.01	2.40	-2.00	-1.90
	.125	—	—	—
	.25	0.554	6.44	0.055
	.50	1.090	2.16	0.198
	1.00	1.559	1.345	0.264
.25	.01	2.97	-1.62	-1.9
	.125	0.554	-4.50	-2.06
	.25	—	—	—
	.50	0.526	4.08	0.250
	1.00	0.995	1.52	0.531

Table C-2. β -electron crossover parameters (Cont'd. next page)

η_1	η_0	τ_{10}	q	p
.50	.01	3.49	-1.38	-1.89
	.125	1.090	-2.12	-2.09
	.25	0.526	-3.27	-2.30
	.50	—	—	—
	1.00	0.469	2.875	0.662
1.00	.01	3.96	-1.16	-1.90
	.125	1.559	-1.282	-2.17
	.25	0.995	-1.79	-2.27
	.50	0.469	-3.01	-2.50
	1.00	—	—	—

Table C.2. β -electron crossover parameters, (Cont'd.)

η_1	$-\eta_0$	B	C	D	τ_{d2}	τ_{d3}
0.01	0.1	0.301	16.50	1.302	0.5	4.820
	0.3	0.333	7.40	0.906	0.5	3.228
	0.5	0.359	7.22	0.667	0.4	2.259
	0.7	0.369	6.35	0.489	0.4	1.724
	0.9	0.389	8.30	0.347	0.4	1.294
	1.1	0.378	7.46	0.228	0.3	0.904
0.125	0.1	0.332	7.55	1.302	0.8	"
	0.3	0.345	7.14	0.906	0.6	
	0.5	0.379	7.22	0.667	0.5	
	0.7	0.399	6.66	0.489	0.5	
	0.9	0.388	7.90	0.347	0.4	
	1.1	0.378	9.50	0.228	0.3	
0.25	0.1	0.353	4.00	1.302	1.1	"
	0.3	0.373	6.16	0.906	0.8	
	0.5	0.402	6.11	0.667	0.6	
	0.7	0.399	6.29	0.489	0.5	
	0.9	0.389	6.92	0.347	0.4	
	1.1	0.378	7.50	0.228	0.3	

Table C.3. α -electron crossover parameters (Cont'd. next page)

η_1	$-\eta_0$	B	C	D	$\tau_{\alpha 2}$	$\tau_{\alpha 3}$
0.50	0.1	0.361	3.03	1.302	1.2	"
	0.3	0.374	4.40	0.906	0.8	
	0.5	0.402	5.54	0.667	0.6	
	0.7	0.399	5.93	0.489	0.5	
	0.9	0.388	8.30	0.347	0.4	
	1.1	0.378	7.46	0.228	0.3	
1.00	0.1	0.401	2.50	1.302	1.63	"
	0.3	0.408	3.44	0.906	1.0	
	0.5	0.457	4.57	0.667	0.8	
	0.7	0.434	5.36	0.489	0.6	
	0.9	0.438	5.44	0.347	0.5	
	1.1	0.452	6.82	0.228	0.4	

Table C-3. α -electron crossover parameters (Cont'd)

APPENDIX D THE FLUCTUATION TRANSFORMATION COEFFICIENTS

The single-velocity transformation equations can be written in matrix form as

$$\begin{bmatrix} \tilde{V}_d \\ \tilde{q}_{xb} \\ \tilde{v}_{xb} \\ \tilde{v}_{zb} \end{bmatrix} = \begin{bmatrix} a_{11} & a_{12} & a_{13} & a_{14} \\ a_{21} & a_{22} & a_{23} & a_{24} \\ a_{31} & a_{32} & a_{33} & a_{34} \\ a_{41} & a_{42} & a_{43} & a_{44} \end{bmatrix} \begin{bmatrix} \tilde{J}_{xd} \\ \tilde{q}_{xa} \\ \tilde{v}_{xa} \\ \tilde{v}_{za} \end{bmatrix} \quad (D-1)$$

where the symbols have been previously defined. This is convenient for the open-circuited diode where $\tilde{J}_{xd} = 0$. For the short-circuited diode, where $\tilde{V}_d = 0$, it is convenient to modify (1) so that \tilde{V}_d is an independent quantity. Then (1) can be written as

$$\begin{bmatrix} \tilde{j}_{xd} \\ \tilde{q}_{xb} \\ \tilde{v}_{xb} \\ \tilde{v}_{sb} \end{bmatrix} = \begin{bmatrix} b_{11} & b_{12} & b_{13} & b_{14} \\ b_{21} & b_{22} & b_{23} & b_{24} \\ b_{31} & b_{32} & b_{33} & b_{34} \\ b_{41} & b_{42} & b_{43} & b_{44} \end{bmatrix} \begin{bmatrix} \tilde{v}_d \\ \tilde{q}_{xa} \\ \tilde{v}_{xa} \\ \tilde{v}_{sa} \end{bmatrix} \quad (D-2)$$

The relations between the a_{ij} and b_{ij} coefficients are as follows:

$$\begin{aligned} b_{11} &= 1/a_{11} \\ b_{ij} &= -a_{ij}/a_{11} ; j \neq 1 \\ b_{i1} &= a_{i1}/a_{11} ; i \neq 1 \\ b_{ij} &= a_{ij} - a_{i1}a_{1j}/a_{11} ; i, j \neq 1. \end{aligned} \quad (D-3)$$

The crossed-field Van Duser coefficients were derived for the one-dimensional diode, so they must reduce to the Llewellyn-Peterson coefficients when the magnetic field, or $\theta = \omega_c \tau$, is reduced to zero. Table D.1 gives a complete list of both coefficients. The Van Duser coefficients have been put in terms of the space-charge factor ξ where convenient, for comparison with the corresponding L-P coefficients. Only a_{11} and a_{12} have been left in terms of an average quantity other than ξ or velocity. The average initial acceleration is conveniently left in these coefficients because it is set to zero as an assumption in the space-charge-limited diode. Since the s -directed velocity is simply given by

$$v_{sb} = v_{xa} + \omega_c x, \quad (D-4)$$

the fluctuations in v_{sb} are just proportional to the fluctuations in v_{xa} . Therefore

$$a_{41} = e^{-\beta} \quad (D-5)$$

and

$$a_{4j} = 0 ; j \neq 1.$$

Table D.1. The a_{ij} coefficients

Van Duzer Coefficients	Llewellyn-Peterson Coefficients
$\frac{\tau^2}{\epsilon_0 \beta} \left\{ \frac{v \sin \theta}{x_a \theta} + a_{xa} \tau \left(\frac{1 - \cos \theta}{\theta^2} \right) + \xi \left(\frac{v_{xb} + v_{xa}}{1 - \cos \theta} \right) \right\}$ $\left[\frac{(Q+P)\theta^2 \beta}{(\theta^2 + \beta^2)^2} - \frac{\sin \theta}{\theta} + \frac{\beta^2}{\beta^2 + \theta^2} \right] \left\{ \right\}$	$a_{11} \frac{\tau^2}{\epsilon_0 \beta} \left(\frac{v_{xb} + v_{xa}}{2} \right) \left\{ 1 - \frac{\xi}{3} \left[1 - 12 \frac{(2P - \beta Q)}{\beta^3} \right] \right\}$
$\frac{\tau^2}{\epsilon_0 \beta} \left[\frac{-v_{xa} \beta Q - a_{xa} \tau P}{(\theta^2 + \beta^2)} \right]$	$a_{12} \frac{\tau^2}{\epsilon_0 \beta} \left[\frac{-v_{xa} \beta Q - a_{xa} \tau P}{\beta^2} \right]$
$-\xi \frac{(v_{xb} + v_{xa})}{\eta} \left(\frac{P}{\theta^2 + \beta^2} \right) \left(\frac{\theta^2}{1 - \cos \theta} \right)$	$a_{13} - \xi \frac{(v_{xb} + v_{xa})}{\eta} - \frac{2P}{\beta^2}$
$-\xi \frac{(v_{xb} + v_{xa})}{\eta} \left(\frac{\theta^2}{1 - \cos \theta} \right) \left(\frac{1}{\theta^2 + \beta^2} \right) \left[\frac{\beta Q}{\theta} - \frac{(\theta^2 + \beta^2)(1 - e^{-\beta})}{\beta \theta} \right]$	$a_{14} 0$
$\xi \left(\frac{v_{xb} + v_{xa}}{v_{xb}} \right) \left(\frac{\theta^2}{1 - \cos \theta} \right) - \frac{P}{\theta^2 + \beta^2}$	$a_{21} \xi \left(\frac{v_{xb} + v_{xa}}{v_{xb}} \right) - \frac{2P}{\beta^2}$

Table D.1. The a_{ij} coefficients (Cont'd.)

Van Duzer Coefficients	Llewellyn-Peterson Coefficients
$\left[\frac{v_{xb} - \xi(v_{xb} + v_{xa})}{v_{xb}} \right] e^{-\beta}$	$a_{22} \left[\frac{v_{xb} - \xi(v_{xb} + v_{xa})}{v_{xb}} \right] e^{-\beta}$
$\xi \frac{\epsilon_0}{\eta \tau^2} \left(\frac{v_{xb} + v_{xa}}{v_{xb}} \right) \frac{\theta \sin \theta}{1 - \cos \theta} \beta e^{-\beta}$ $= \frac{J_{xd}}{v_{xb}} \beta e^{-\beta} \frac{\sin \theta}{\theta}$	$a_{23} \xi \frac{\epsilon_0}{\eta \tau^2} \left(\frac{v_{xb} + v_{xa}}{v_{xb}} \right) \beta e^{-\beta} = \frac{J_{xd}}{v_{xb}} \beta e^{-\beta}$
$-\xi \frac{\epsilon_0}{\eta \tau^2} \left(\frac{v_{xb} + v_{xa}}{v_{xb}} \right) \theta \beta e^{-\beta}$	$a_{24} 0$
$\frac{\eta \tau^2}{\epsilon_0 \beta} \left\{ \frac{\frac{\sin \theta}{v_{xb}} \beta - \left[\frac{v_{xb} \cos \theta - v_{xa} + \xi(v_{xb} + v_{xa})}{v_{xb}(\theta^2 + \beta^2)} \right] \frac{\sin \theta}{\theta}}{v_{xb}(\theta^2 + \beta^2)} + \frac{\sin \theta}{\theta} e^{-\beta} \right\}$	$a_{31} \frac{\eta \tau^2}{\epsilon_0 \beta} \left[\frac{v_{xb}(\beta Q - P) + v_{xa} P - \xi(v_{xb} + v_{xa}) P}{v_{xb} \beta^2} \right]$
$-\frac{\eta \tau^2}{\epsilon_0} (1 - \xi) \left(\frac{v_{xb} + v_{xa}}{v_{xb}} \right) \frac{(1 - \cos \theta)}{\theta \sin \theta} \beta e^{-\beta}$	$a_{32} -\frac{\eta \tau^2}{2 \epsilon_0} (1 - \xi) \left(\frac{v_{xb} + v_{xa}}{v_{xb}} \right) \frac{e^{-\beta}}{\beta}$

Table D.1. The a_{ij} coefficients (Cont'd.)

Van Duzer Coefficients		Llewellyn-Peterson Coefficients
$\left[\frac{v_{xa} - \xi(v_{xb} + v_{xa})}{v_{xb}} \right] e^{-\beta}$	a_{33}	$\left[\frac{v_{xa} - \xi(v_{xb} + v_{xa})}{v_{xb}} \right] e^{-\beta}$
$\left(\frac{v_{xb} + v_{xa}}{v_{xb}} \right) (\xi - 1) \left(\frac{1 - \cos \theta}{\sin \theta} \right) e^{-\beta}$	a_{34}	0
$1 - \left(\frac{\beta}{\theta} \sin \theta + \cos \theta \right) e^{-\beta}$	P	$1 - (1 + \beta) e^{-\beta}$
$1 + \left(\frac{\theta}{\beta} \sin \theta - \cos \theta \right) e^{-\beta}$	Q	$1 - e^{-\beta}$

APPENDIX E

THE VALIDITY OF THE SINGLE-VELOCITY THEORY IN TERMS OF CROSSOVERS

One of the assumptions of the Llewellyn-Peterson and Van Duzer electronic theories is that the fluctuations are small compared with the average values of all quantities. The coefficients are valid as long as this and the other assumptions are obeyed. In the space-charge-limited diode, however, it is not difficult to violate the small fluctuation assumption with regard to velocity.

We will consider this assumption to be violated when the trajectories of individual charges cross one another, for then the single-velocity nature of the beam becomes questionable. If an electron leaving the entrance plane at $t = t_a$ follows a trajectory $x(t, t_a)$, then crossovers occur when dx/dt_a is positive at a fixed value of t , as illustrated in Figure E-1. We therefore desire to find the point at which this condition occurs.

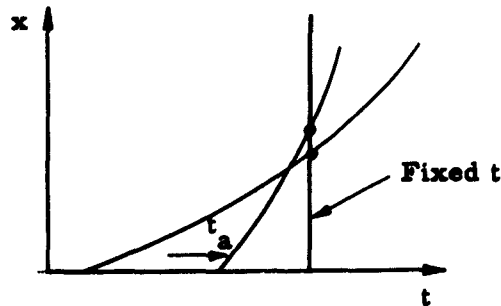


Figure E-1. The criterion for crossovers

The trajectory can be expressed (see Van Duzer) as:

$$\begin{aligned}
 x(t, t_a) = & \frac{\dot{x}(t_a)}{\omega_c} \sin \omega_c(t-t_a) + \frac{\ddot{x}(t_a)}{\omega_c^2} \left[1 - \cos \omega_c(t-t_a) \right] \\
 & + \frac{\eta J_{xd}}{\epsilon_0 \omega_c^3} \left[\omega_c(t-t_a) - \sin \omega_c(t-t_a) \right] + \frac{\eta J_x(\omega) e^{j\omega t}}{\epsilon_0 (\omega_c^2 - \omega^2)} \left\{ \frac{1 - e^{-j\omega(t-t_a)}}{j\omega} \right. \\
 & \left. - \frac{\sin \omega_c(t-t_a)}{\omega_c} e^{-j\omega(t-t_a)} - \frac{j\omega}{\omega_c^2} \left[1 - \cos \omega_c(t-t_a) \right] e^{-j\omega(t-t_a)} \right\}
 \end{aligned} \quad (E-1)$$

where $\omega_c = |e/m| B$, and

$$J_x = J_{xd} + \tilde{J}_x(\omega) e^{j\omega t} = J_{xd} + \tilde{J}_x(t) \quad (E-2)$$

is the total x-directed current density in the stream. The velocity and acceleration can be split into dc and ac parts,

$$\dot{x}(t_a) = v_{xa} + \tilde{v}_{xa}(t_a) = v_{xa} + \tilde{v}_{xa0} e^{j\omega t_a} \quad (E-3)$$

$$\ddot{x}(t_a) = a_{xa} + \tilde{a}_{xa}(t_a) = a_{xa} + \tilde{a}_{xa0} e^{j\omega t_a}. \quad (E-4)$$

With the form of the quantities as in (3) and (4)

$$\frac{d \left[\tilde{v}_{xa}(t_a) \right]}{dt_a} = j\omega \left[\tilde{v}_{xa}(t_a) \right], \text{ etc.} \quad (E-5)$$

From Van Duzer,

$$\tilde{a}_{xa}(t_a) = \frac{\eta}{j\omega \epsilon_0} \left[\tilde{J}_x(t_a) - \tilde{q}_{xa}(t_a) \right] - \omega_c \tilde{v}_{za}(t_a) \quad (E-6)$$

Differentiating (1) with respect to t_a , substituting the above equations into the result and collecting terms,

$$\frac{dx(t, t_a)}{dt_a} = -v_{xb} + \tilde{v}_{xa}(t_a) \left[j\omega\tau \frac{\sin\theta}{\theta} - \cos\theta \right] - \left[\frac{\eta\tau}{j\omega\epsilon_0} \tilde{q}_{xa}(t_a) + \theta \tilde{v}_{za}(t_a) \right] \left[j\omega\tau \left(\frac{1-\cos\theta}{\theta^2} \right) - \frac{\sin\theta}{\theta} \right] \quad (\text{E-7})$$

where v_{xb} is the average velocity at the "b" plane (see Equation III.4(1), and $\omega_c(t-t_a) = \omega_c\tau = \theta$.

From III.4(6),

$$\xi = \frac{\eta J_d \tau^2}{2 \epsilon_0 (v_{xb} + v_{xa})} \approx 2 \frac{(1-\cos\theta)}{\theta^2} \approx 1 \quad (\text{E-8})$$

for the space-charge-limited diode. Then the requirement for no crossovers reduces to

$$v_{xb} \left[1 + \xi \frac{\tilde{q}_{xa}(t_a)}{J_d} \left\{ 1 + \frac{j\theta \sin\theta}{\omega\tau(1-\cos\theta)} \right\} \right] > \tilde{v}_{xa}(t_a) \left[j\omega\tau \frac{\sin\theta}{\theta} - \cos\theta \right] - v_{za}(t_a) \left[j\omega\tau \left(\frac{1-\cos\theta}{\theta} \right) - \sin\theta \right] \quad (\text{E-9})$$

Since ξ is always less than unity and \tilde{q}_{xa} is very much less than J_{xd} , that term can be neglected. By assuming that there exist at the "a" plane independent velocity fluctuations such that

$$\frac{\tilde{v}_{za}^2(t_a)}{2\eta} = \frac{\tilde{v}_{xa}^2(t_a)}{2\eta} = V_e = kT_c/e, \quad (\text{E-10})$$

the condition becomes

$$\frac{v_{xb}^2}{2\eta V_e} > \left[1 + 2(\omega\tau)^2 \left(\frac{1-\cos\theta}{\theta^2} \right) \right]. \quad (\text{E-11})$$

This may be done because $(2\eta V_e)^{1/2}$ is the rms velocity at the potential minimum. The unity in the bracket can be ignored at large transit angles as long as θ is not near 2π . As $\theta \rightarrow 2\pi$, the relation relaxes considerably. From III.4(9) and (11),

$$\frac{v_{xb}^2}{2\eta} \approx V_d \left[\frac{(1 - \cos \theta)^2}{2\phi(\theta)} \right] \quad (\text{E-12})$$

where $\phi(\theta) = 1 - \cos \theta + \frac{\theta^2}{2} - \theta \sin \theta$. Then crossovers are prevented when

$$(\omega\tau)^2 < \frac{\theta^2(1 - \cos \theta)}{4\phi(\theta)} \frac{V_d}{V_e} \quad (\text{E-13})$$

For $(\omega\tau)^2$ greater than the quantity on the right of (13), the single-velocity analysis is no longer valid in the space-charge-limited diode.

APPENDIX F

ESTIMATION OF η_1 FROM THE MONTE CARLO ANALYSIS

The approximate analysis of the potential minimum (Chapter II) requires that the critical charges be given a finite energy on their arrival at that plane. This is so that the infinite transit time resulting when charges arrive in the quadratic potential region with zero energy can be avoided. Although the choice of a particular value of this energy, η_1 in normalized form, is somewhat arbitrary, we should obtain some estimate of a suitable value.

We can consider that an instantaneous decrease in the depth of the potential minimum is equivalent to an energy added to charges that would normally have arrived there with zero energy. Although we know that the average arrival velocity is independent of the depth of the minimum, the energy any particular charge has on arrival depends on that depth. As an approximation we can then let

$$\eta_1 = \sqrt{\tilde{V}_m^2(t)} / \frac{kT_c}{e}, \quad (\text{F-1})$$

where $\overline{\tilde{V}_m^2}(t)$ is the mean square value of the fluctuating part of the minimum potential.

If the spectral density of V_m is known, then $\overline{V_m^2}(t)$ can be obtained from it by means of statistical theory as

$$\overline{V_m^2}(t) = \int_0^{\infty} V_m^2(f) df, \quad (F-2)$$

where $V_m^2(f)$ is the spectrum considering positive frequencies only. The spectral density can be computed directly from the Monte Carlo data, and this is shown in Figure F.1. The spectrum for the short-circuited, zero magnetic field run is shown. It has been normalized to $2(kT_c)^2/eI_d$, where I_d is the average current passing the minimum.

If the spectral density of \tilde{V}_m is not known from the Monte Carlo data directly, an alternate method, suggested by the work of Pierce (1954) can be utilized. Full shot noise is produced by the randomness of electronic emission at the thermionic cathode. If the potential minimum did not fluctuate, this noise current would reach the anode, diminished in the same ratio as the average current. However, a noise current $R^2(f)$ times full shot noise ($2eI_d\Delta f$) is "observed" at the potential minimum, by a Monte Carlo calculation, for example.

Then the potential minimum spectrum must be

$$V_m^2(f)\Delta f = \left(\frac{\partial V_m}{\partial I_d} \right)^2 2eI_d\Delta f |R^2(f) - 1|. \quad (F-3)$$

Since the current passing the minimum is related to V_m and the emitted current I_e by

$$I_d = I_e \exp(-V_m / \frac{kT_c}{e}), \quad (F-4)$$

$$\text{then } V_m^2(f)\Delta f = \frac{2(kT_c)^2}{eI_d} \Delta f |R^2(f) - 1|. \quad (F-5)$$

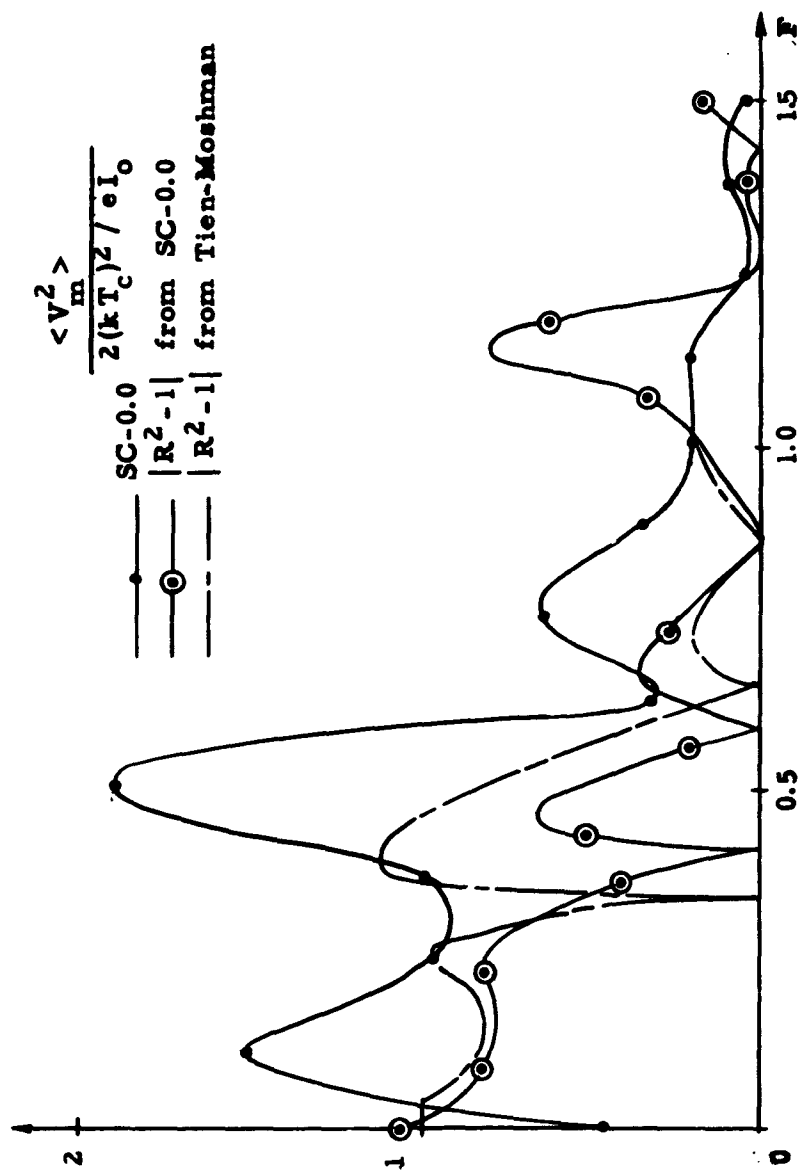


Figure F.1. Spectra of \tilde{V}_m for estimation of η_1

The factor $|R^2(f)-1|$ should be the equivalent of $V_m^2(f)$ normalized to $2(kT_c)^2/eI_d$. This is the same normalization used for the direct evaluation of the spectrum of V_m . Figure F.1 includes the curve $|R^2(f)-1|$ obtained from the SC-0.00 run and the same curve obtained from the Tien-Moshman Monte Carlo study. Agreement with the results of the direct spectral analysis of V_m is only good on a qualitative basis. However, the integral needed for (2) is roughly within a factor of two for the different methods.

Because the work on the approximate analysis was performed before the present Monte Carlo study was initiated, values for (5) were taken from the Tien-Moshman calculation. The quantity kT_c/e has a value of 0.1 volts, and I_d is equal to 0.131 micro-amperes. This small value of current was chosen by Tien and Moshman for a sample area of their infinite diode. It is not believed to be an otherwise significant quantity. The integral (2) was evaluated numerically over the lower part of the frequency range, and estimated from the smoothed spectral data at higher frequencies.

With this data, $\sqrt{V_m^2(t)} = 0.0125$ volts. Then, from (1), $\eta_1 = 0.125$. A more common value of current might be 100 or 1000 times the value used here. This would lead to a value for η_1 ranging from 0.004 to 0.01. For these reasons, two of the values used in the approximate analysis were $\eta_1 = 0.01$ and 0.125.

APPENDIX G

DISTRIBUTION OF THE NORMAL COMPONENT OF ANODE VELOCITY-- EXCLUDING AC EFFECTS

At a thermionic cathode in the y - z plane, the probability of emitting an electron per unit time (current probability) with normal velocity between v_{xa} and $v_{xa} + dv_{xa}$ and transverse velocity between v_{za} and $v_{za} + dv_{za}$ is

$$P(v_{xa}; v_{za}) dv_{xa} dv_{za} = \frac{2}{\sqrt{\pi}} \frac{v_{xa}}{(2kT_c/m)^{3/2}} e^{-\frac{1}{2} \frac{m(v_{xa}^2 + v_{za}^2)}{kT_c}} dv_{xa} dv_{za}. \quad (G-1)$$

The cathode plane is symbolized by "a" and the anode plane by "b".

Normalizing velocities to $v_d = \sqrt{2\eta V_d}$ and energies to eV_d , (1) can be written in terms of v_{xa} and v_{za} as

$$P(u_{xa}^2; u_{za}) du_{xa}^2 du_{za} = \frac{1}{\sqrt{\pi}} \frac{e^{-\frac{1}{2}(u_{xa}^2 + u_{za}^2)/U_e}}{U_e^{3/2}} du_{xa}^2 du_{za}. \quad (G-2)$$

In an ordinary (zero-crossed-magnetic-field) electron stream there is no coupling between x- and z-directed velocities so that excluding ac effects, the distribution of normal velocities at the anode may be written as

$$P(u_{xb}) du_{xb}^2 = \frac{e^{-\frac{1}{2}(u_{xb}^2 - 1)/U_e}}{U_e} du_{xb}^2, \quad (G-3)$$

where $u_{xb}^2 = 1 + u_{xa}^2$, since each electron gains a kinetic energy equal to eV_d . Now all electrons have velocities u_{xb} greater than unity. As is well known, the increase in average energy produces a decrease in the relative, as well as absolute "spread" in velocity about the mean velocity. Figure G.1 is a sketch of the normal velocity distributions at the cathode and anode for $U_e = 0.01 (kT_c/eV_d = 0.01)$.

It is interesting to see what effect the crossed-magnetic field has on the normal velocity distribution at the anode. Now there is a coupling of normal and transverse velocities, but by invoking the conservation of energy, we can write

$$u_x^2 + u_z^2 = U(X) + u_{xa}^2 + u_{za}^2. \quad (G-4)$$

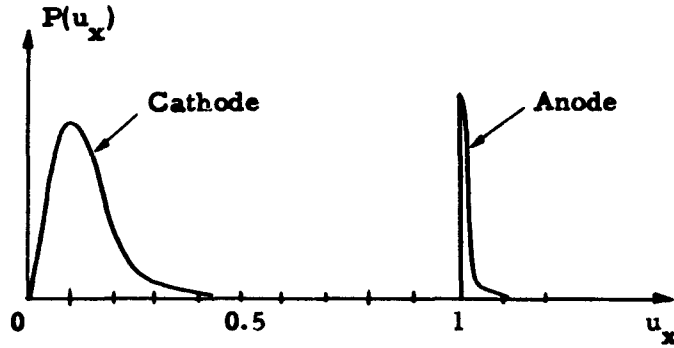


Figure G.1. Normal velocity distributions at cathode and anode in an ordinary electron stream

$U(X)$ is the normalized potential at $X = x/d$. The transverse velocity varies across the space linearly,

$$u_z = u_{za} + (B/B_c)X. \quad (G-5)$$

Equations (4) and (5) can be combined to give

$$u_x^2 = U(X) - 2(B/B_c)X u_{za} - (B/B_c)^2 X^2 + u_{xa}^2. \quad (G-6)$$

An electron will have a positive u_x at a plane X if

$$U(X) \geq (B/B_c)^2 X^2 + 2(B/B_c)X u_{za} - u_{xa}^2. \quad (G-7)$$

As long as the curve $U(X)$ lies above the right hand side of (7) for $u_{xa} = 0$, then the condition (7) is true anywhere if it is true at the anode, where

$$1 \geq (B/B_c)^2 + 2(B/B_c) u_{za} - u_{xa}^2. \quad (G-8)$$

Figure G.2 shows these relations.

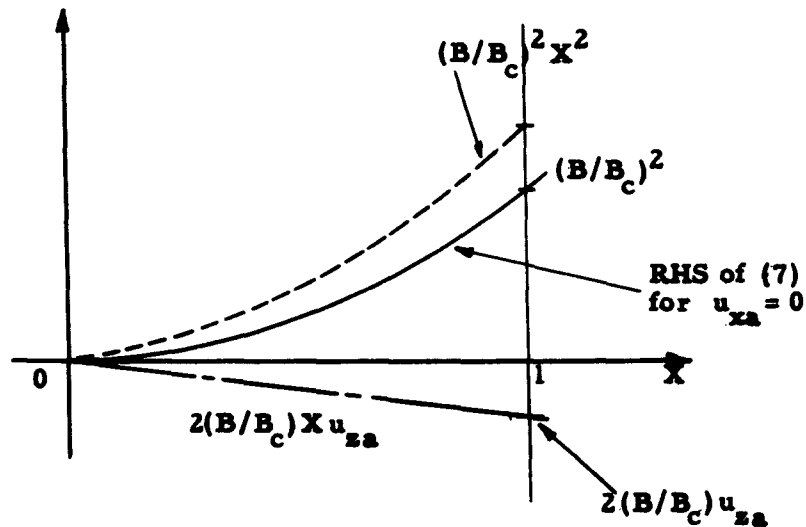


Figure G.2. Conditions on the potential distribution to determine trajectories

The condition (7) is not true everywhere in the space-charge-limited diode, because a negative minimum potential curve must intersect the right hand side of (7) at two points. Whenever (7) does hold, the resulting regime of operation is termed "magnetic-field-limited" by Lindsay (1960). We shall assume that (7) holds everywhere in the diode. Then the final destinations of charges are independent of $U(X)$ and the anode velocity distributions are considerably simpler to obtain. If this is not the case, the distributions become complicated functions of $U(X)$. Although the distributions obtained by making this simplifying assumption do not hold in the space-charge-limited diode, they should give some idea of the desired distributions.

The joint probability corresponding to (2) at the anode can be written by substituting (4) and observing that the Jacobian of the transformation is unity,

$$P(u_{xb}^2; u_{zb}) du_{xb}^2 du_{za} = \frac{1}{\sqrt{\pi}} \frac{e^{-((u_{xb}^2 + u_{zb}^2 - 1)/U_e)}}{U_e^{3/2}} du_{xb}^2 du_{zb} \quad (G-9)$$

To find the distribution of normal velocities, (9) must be integrated over all transverse velocities that an electron can have on arrival at the anode. Rewriting (6) at the anode,

$$u_{zb} = \frac{u_{xa}^2 + 1 + (B/B_c)^2 - u_{xb}^2}{2(B/B_c)} \quad (G-10)$$

All charges that reach the anode will have

$$u_{zbo} = \left[1 + (B/B_c)^2 - u_{xb}^2 \right] \leq u_{zb} < \infty \quad (G-11)$$

The integral over u_{zb} then becomes

$$\frac{1}{\sqrt{\pi}} \int_{\frac{u_{zbo}}{U_e^{1/2}}}^{\infty} e^{-u_{zb}^2/U_e} d\left(\frac{u_{zb}}{U_e^{1/2}}\right) = \frac{1}{2} \left[1 - \operatorname{erf} \left| \frac{u_{zbo}}{U_e^{1/2}} \right| \right] \quad (G-12)$$

where "erf" is the error function and the negative sign holds for u_{zbo} positive. The normal anode velocity distribution for u_{zbo} positive, after substituting (12) is:

$$P(u_{xb}) du_{xb} = \frac{u_{xb}}{U_e} e^{(1-u_{xb}^2)/U_e} \left[1 - \operatorname{erf} \frac{u_{zbo}}{U_e^{1/2}} \right] du_{xb} \quad (G-13)$$

Using the parameters of Chapter IV: $U_e = 0.01$ and $0 < B/B_c < 1$. Then $u_{zbo}/U_e^{1/2}$ is on the order of 5 or more for u_{xb} less than unity, and an approximation can be made for the

error function (Dwight, 1957),

$$\text{erf } t = 1 - \frac{e^{-t^2}}{\sqrt{\pi} t} \quad \text{for large } t. \quad (\text{G-14})$$

Substituting for u_{zbo} from (11), after some simplification, (13) becomes

$$P(u_{xb}) du_{xb} = \left\{ \frac{2(B/B_c)}{\sqrt{\pi} U_e^{1/2}} e^{-\frac{[1-(B/B_c)^2]^2}{4(B/B_c)^2 U_e^2} u_{xb}^2} \right\} \frac{u_{xb}}{1 + (B/B_c)^2 - u_{xb}^2}. \quad (\text{G-15})$$

$$e^{\frac{[1-(B/B_c)^2]^2 u_{xb}^2}{2(B/B_c)^2 U_e^2}} - \frac{u_{xb}^4}{4(B/B_c)^2 U_e^2} du_{xb}$$

Figure G.3 shows $P(u_{xb})$ for $U_e = 0.01$ and $B/B_c = 0, 0.75$ and 1.00 . The distributions spread from the cathode distribution with increasing magnetic field. This is in direct contrast with the results (Figure G.1) for $B/B_c = 0$, where the spread is reduced as the beam moves to the anode. Since total energy is conserved, the transverse velocity distribution should contract.

Let us compare the distribution of u_x^2 for $B/B_c = 1$. For this case,

$$P(u_{xb}^2) du_{xb}^2 = \frac{e^{-u_{xb}^4/4 U_e}}{\sqrt{\pi} U_e^{1/2} (1 - \frac{u_{xb}^2}{2})} du_{xb}^2 \quad (\text{G-16})$$

The probability density drops to $1/e$ of its initial value when $u_{xb}^2 \approx 2 U_e^{1/2}$. This contrasts with the distribution at the cathode, where the $1/e$ value is reached when $u_{xa}^2 = U_e$. As

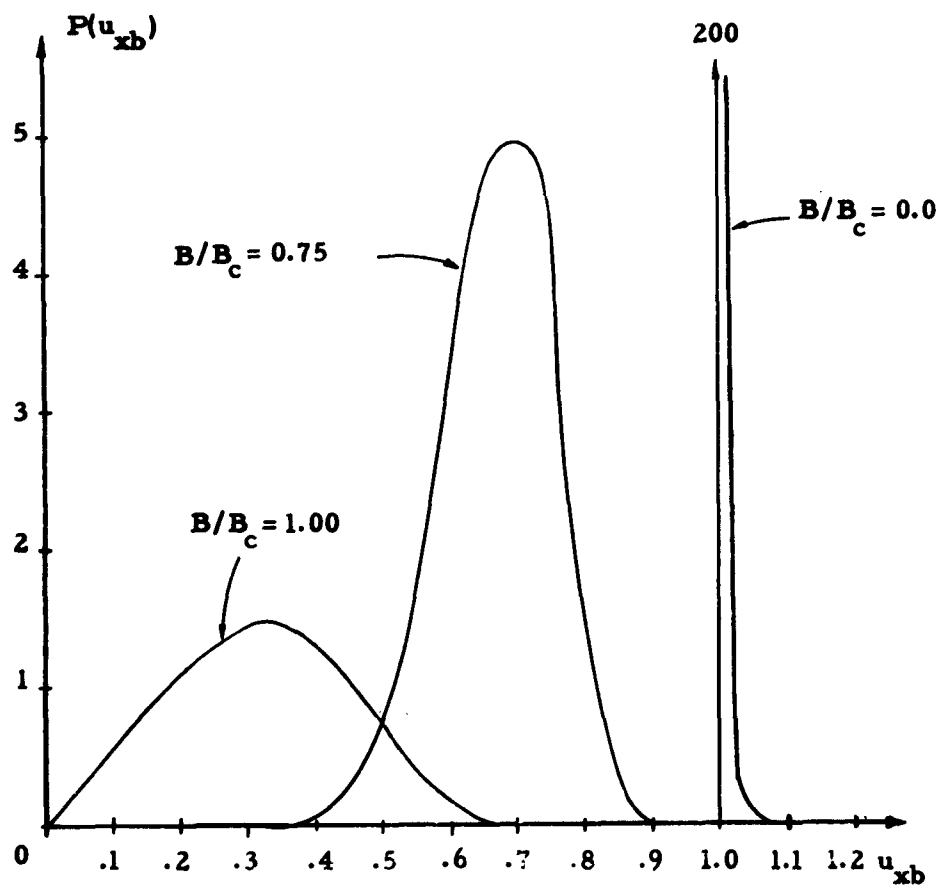


Figure G.3. The dependence of the normal anode velocity distribution on B/B_c

long as $U_e < 1/4$, the distribution at the anode has a larger energy spread than the distribution at the cathode (Figure G. 4).

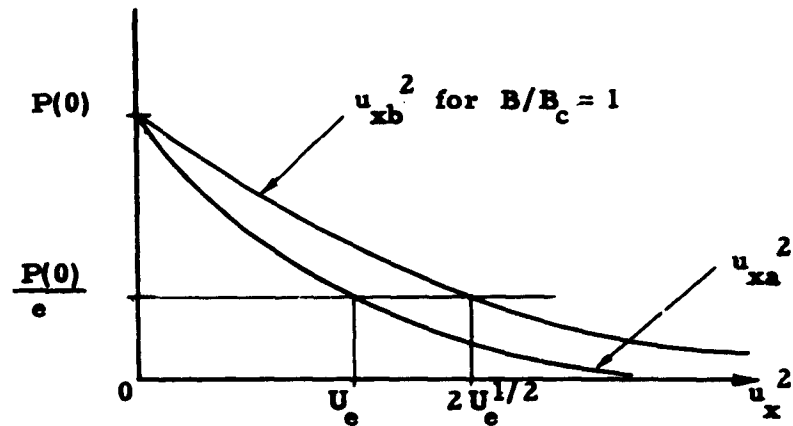


Figure G. 4. Distribution of u_x^2 as a function of U_e .

In the actual diode, as V_d increases, U_e decreases and the relative spread in the normal energy distribution increases. Since kT_c/e is a constant, the absolute energy spread must also increase.

REFERENCES

- Anderson, J. R., "Noise Measurements on an M-type Backward-Wave Amplifier," Proc. I.R.E., Vol. 48 (May 1960), p. 946.
- Blackman, R. B. and Tukey, J. W., The Measurement of Power Spectra, New York: Dover Publications, 1958.
- Caughran, J., "Pseudo-Random Number Generator," IBM SHARE PROGRAM No. G5 BC DEV, Computer Center, University of California, Berkeley, California, 1961.
- Cutler, C. C. and Quate, C. F., "Experimental Verification of Space-Charge and Transit-Time Reduction of Noise in Electron Beams," Phys. Rev., Vol. 80 (1950), p. 875.
- Dayem, A. H., private communication (work performed at the Bell Telephone Laboratories), 1960.
- Doehler, O., Proceeding of the Symposium on Microwave Devices, Polytechnic Institute of Brooklyn, New York, 1956.
- Dwight, H. B., Tables of Integrals and Other Mathematical Data, 3rd Edition, New York: The Macmillan Company, 1957.
- Fry, T. C., "The Thermionic Current Between Parallel Plane Electrodes: Velocities Distributed According to Maxwell's Law," Phys. Rev., Vol. 17 (April 1921), p. 441.
- Fulop, W., "The Cut-Off Characteristics of Magnetrons (Static Regime)," Jour. Electronics and Control, Vol. 5 (December 1958), pp. 531-548.
- Hess, R. L., "Large-Signal Traveling Wave Tube Operation: Concepts and Analysis," Aeronautical Systems Division Report, 61-15, U. S. Air Force (July 1961).
- Hull, W. A., "The Effect of a Magnetic Field on the Motion of Electrons Between Coaxial Cylinders," Phys. Rev., Vol. 18 (1921), p. 31.

Kino, G. S., "A Design Method for Crossed-Field Electron Guns,"
Trans. I. R. E., ED-7, No. 3 (1960), p. 170.

Langmuir, I., "The Effect of Space Charge and Initial Velocities
on the Potential Distribution and Thermionic Current
Between Plane Parallel Electrodes," Phys. Rev., Vol. 21
(April 1923), p. 419.

Lindsay, P. A., "General Steady-State Theory of Linear Magne-
trons (I)," Jour. of Electronics and Control, Vol. 8, No.
3 (March 1960), p. 177.

Lindsay, P. A., private communication, 1962.

Little, R. P., Ruppel, H. M. and Smith, S. T., "Beam Noise in
Crossed Electric and Magnetic Fields," Jour. Appl. Physics,
Vol. 29 (September 1958), p. 1376.

Llewellyn, F. B., Electron Inertia Effects, New York: Cambridge
University Press, 1941.

Llewellyn, F. B. and Peterson, L. C., "Vacuum Tube Networks,"
Proc. I. R. E., Vol. 32 (March 1944), pp. 144-166.

Pierce, J. R., "Rectilinear Electron Flow in Beams," J. Appl.
Phys., Vol. 11 (1940), pp. 548-554.

Pierce, J. R., "General Sources of Noise in Vacuum Tubes,"
Trans. I. R. E., ED-1, No. 4 (December 1954), pp. 135-167.

Rack, A. J., "Effect of Space Charge and Transit Time on Shot
Noise in Diodes," B. S. T. J., Vol. 17 (October 1938),
pp. 592-619.

Rando, J. F., "Noise Figure of Crossed-Field Amplifiers,"
Electronics Research Laboratory Report, Series No. 60,
Issue No. 383, University of California, Berkeley, California,
July 13, 1961.

Siegman, A. E., "Analysis of Multivelocitv Electron Streams by
the Density Function Method," Jour. Appl. Phys., Vol. 28,
No. 10. (October 1957 (a)), pp. 1132-1138.

- Siegman, A. E. , "Microwave Noise Fluctuations in the Potential-Minimum Region of an Electron Beam, " Stanford Electronics Laboratory Tech. Report, No. 401-1, Electron Tube Laboratory, Stanford University, April 22, 1957 (b).
- Siegman, A. E. and Watkins, D. A. , "Potential-Minimum Noise in the Microwave Diode," Trans. I. R. E. , Vol. ED-4 (January 1957), pp. 82-86.
- Siegman, A. E. , Watkins, D. A. and Hsieh, H. , "Density-Function Calculations of Noise Propagation on an Accelerated Multivelocitv Electron Beam, " Jour. Appl. Phys. , Vol. 28, No. 10, (October 1957), pp. 1138-1148.
- Thompson, B. J. , North, D. O. and Harris, W. A. "Fluctuation in Space-Charge-Limited Currents at Moderately High Frequencies," RCA Review, Vol. 4 (January 1940, et. seq.).
- Tien, P. K. and Moshman, J. , "Monte Carlo Calculation of Noise Near the Potential Minimum of a High-Frequency Diode, " Jour. Appl. Phys. , Vol. 27, No. 9 (September 1956), pp. 1067-1078.
- Van Duzer, T. , "Noise in Crossed-Field Electron Beams," Appendix V, Ph. D. Dissertation, University of California, Berkeley, California, August, 1960.
- Van Duzer, T. , "Transformation of Fluctuations Along Accelerating Crossed-Field Beams, " I. R. E. Trans. , ED-8, No. 1 (January 1961(a)), pp. 78-86.
- Van Duzer, T. private communication, 1961(b).
- Van Duzer, T. and Whinnery, J. R. , "High Frequency Behavior of the Crossed-Field Potential Minimum," I. R. E. Trans. , Vol. ED-8, No. 4 (July 1961(a)), pp. 331-341.
- Van Duzer, T. and Whinnery, J. R. , "Noise in Crossed-Field Electron Beams," Crossed-Field Microwave Devices, (ed. E. Okress), New York: Academic Press, 1961(b), pp. 327-357.

- Vivian, W. E., "Transport of Noise at Microwave Frequencies Through a Space-Charge-Limited Diode," J. Appl. Phys., Vol. 31, No. 6 (June 1960), pp. 957-962.
- Vlaardingerbroek, M. T., "Small-Signal Performance and Noise Properties of Microwave Triodes," Philips Research Reports, Vol. 15 (April 1960), pp. 124-221.
- Vlaardingerbroek, M. T., Private Communication, 1961.
- Wadhwa, R. P., et. al., "Research on Crossed-Field Electron Devices," Electron Physics Laboratory, Quarterly Progress Report, No. 8, et. seq., Department of Electrical Engineering, University of Michigan, Ann Arbor, Michigan, December 1, 1960, et. seq.
- Wadhwa, R. P., private communication, 1962.
- Watkins, D. A., "Noise at the Potential Minimum in the High-Frequency Diode," J. Appl. Phys., Vol. 26 (May 1955), pp. 622-624.
- Whinnery, J. R., "Noise Phenomena in the Region of the Potential Minimum," I.R.E. Trans., Vol. ED-1, No. 4 (December 1954), pp. 221-237.
- Whinnery, J. R., "Noise Phenomena in the Region of the Potential Minimum," Electronics Research Laboratory Report, Series No. 60, Issue No. 132, University of California, Berkeley, California, February 28, 1955, (for a more detailed version of the above).
- Whinnery, J. R., "High-Frequency Effects of the Potential Minimum on Noise," I.R.E. Trans. ED-7, No. 4 (October 1960), pp. 218-230.
- Yadavalli, S. V., "Tube Noise Under Large Transit Time Conditions," Institute of Engineering Research Interim Technical Report, Series No. 1, Issue No. 61, University of California, Berkeley, California, January 15, 1953.

Yankina, A. A., "Quantitative Solution of the Problem of the
Distribution of Potential in a Planar Magnetron,"
Radiofizika (U. S. S. R.), Vol. 2 (February 1959), pp. 255-
261.

DISTRIBUTION LIST
CONTRACT DA 36-039 SC-85278

ORGANIZATION	NO. COPIES	ORGANIZATION	NO. COPIES	ORGANIZATION	NO. COPIES
OASD (R & E) Room 3E1065 The Pentagon Washington 25, D.C. ATTN: Technical Library	1	Commanding Officer U.S. Army Electronics Command Fort Monmouth, New Jersey ATTN: AMSEL-RD	3	The European Office U.S. Army R&D Liaison Group APO 757 New York, New York (FOR RETRANSMITTAL TO CONTRACTOR, DA 91-591 EUC-1312)	1
Commander Armed Services Technical Information Agency Arlington Hall Station Arlington 12, Virginia ATTN: TISIA	10	Commanding Officer U.S. Army Electronics Materiel Support Agency Fort Monmouth, New Jersey ATTN: SELMS-ADJ	1	University of Michigan Electron Tube Laboratory Ann Arbor, Michigan ATTN: Professor J. F. Rowe	1
Advisory Group on Electron Devices 346 Broadway New York 13, New York	2	Corps of Engineers Liaison Office U.S. Army Electronics R&D Laboratory Fort Monmouth, New Jersey	1	Stanford University Electronic Research Laboratory Palo Alto, California ATTN: Professor D. A. Watkins	1
Director U.S. Naval Research Laboratory Washington 25, D.C. ATTN: Code 2027	1	Naval Corps Liaison Officer U.S. Army Electronics R&D Laboratory Fort Monmouth, New Jersey ATTN: SELRA/LNR	1	California Institute of Technology Electron Tube & Microwave Laboratory Pasadena, California ATTN: Professor R. Gould	1
Commanding Officer & Director U.S. Navy Electronics Laboratory San Diego 52, California	1	Commanding Officer U.S. Army Electronics R&D Laboratory Fort Monmouth, New Jersey ATTN: Director of Research	1	Massachusetts Institute of Technology Research Laboratory of Electronics Cambridge, Massachusetts ATTN: Professor L. Smullin	1
Chief, Bureau of Ships Department of the Navy Washington 25, D.C. ATTN: 681A-1	1	Commanding Officer U.S. Army Electronics R&D Laboratory Fort Monmouth, New Jersey ATTN: Technical Documents Center	1	Hughes Aircraft Company Culver City, California ATTN: Dr. Mendel, Microwave Tube Laboratory	1
Commander Aeronautical Systems Division Wright-Patterson AFB, Ohio ATTN: ASAPRL	1	Commanding Officer U.S. Army Electronics R&D Laboratory Fort Monmouth, New Jersey ATTN: Technical Information Division (FOR RETRANSMITTAL TO ACCREDITED BRITISH AND CANADIAN GOVERNMENT REPRESENTATIVES)	3	Raytheon Manufacturing Company Microwave & Power Tube Operations Waltham 54, Massachusetts ATTN: W. C. Brown	1
Commander Air Force Cambridge Research Laboratories L. G. Hanscom Field Bedford, Massachusetts ATTN: CCR CCSD CRZC	1	Commanding Officer U.S. Army Electronics R&D Laboratory Fort Monmouth, New Jersey ATTN: SELRA/PR (Mr. Garoff) SELRA/PR (Mr. Hanley) SELRA/PRG (Mr. Zinn) SELRA/PRT (Mr. Kaplan)	1 1 1 1	General Electric Research Laboratory Electron Tube Division, The Knolls Schenectady, New York ATTN: E. D. MacArthur	1
Commander Air Force Cambridge Research Laboratory L. G. Hanscom Field Bedford, Massachusetts ATTN: CRXL-R, Research Library	1	Commanding Officer U.S. Army Electronics R&D Laboratory Fort Monmouth, New Jersey ATTN: Logistics Division (For: SELRA/PRM, Project Engineer)	1	Radio Corporation of America Laboratories Princeton, New Jersey ATTN: Dr. L. S. Nergaard	1
Commander Rome Air Development Center Griffiss Air Force Base, New York ATTN: RAALD	1	Commanding Officer U.S. Army Electronics R&D Laboratory Fort Monmouth, New Jersey ATTN: SELRA/PRM, Record File Copy	1	Bell Telephone Laboratories Murray Hill, New Jersey ATTN: Dr. W. Kluver	1
AFSC Scientific/Technical Liaison Office U.S. Naval Air Development Center Johnstown, Pennsylvania	1	Commanding General U.S. Army Materiel Command Washington 25, D.C. ATTN: R&D Directorate	1	Sylvania Electric Products Physics Laboratory Bayside, L. I., New York ATTN: L. R. Bloom	1
Chief of Research and Development Department of the Army Washington 25, D.C.	1	Commanding General U.S. Army Materiel Command Washington 25, D.C. ATTN: R&D Directorate	1	Westinghouse Electric Corporation Research Laboratory Beulah Road, Churchill Boro Pittsburgh 35, Pennsylvania	1
Chief, U.S. Army Security Agency Arlington Hall Station Arlington 12, Virginia	2	Commanding General U.S. Army Combat Developments Command Fort Belvoir, Virginia ATTN: CDCMR-E	1	Research Division Library Raytheon Company 28 Seyon Street Waltham 54, Massachusetts	1
Deputy President U.S. Army Security Agency Board Arlington Hall Station Arlington 12, Virginia	1	Commanding Officer U.S. Army Communication & Electronics Combat Development Agency Fort Huachuca, Arizona	1	Watkins-Johnson Company 3333 Hillview Avenue Palo Alto, California	1
Commanding Officer U.S. Army Electronics Research Unit P. O. Box 205 Mountain View, California	1	Headquarters, Electronic Systems Division L. G. Hanscom Field Bedford, Massachusetts ATTN: ESAT	1	S. F. D. Laboratories, Inc. 800 Rahway Avenue Union, New Jersey	1
Commanding Officer Diamond Ordnance-Fuze Laboratory Washington 25, D.C. ATTN: Library Room 211, Building 72	1	Director, Fort Monmouth Office U.S. Army Communication & Electronics Combat Development Agency Fort Monmouth, New Jersey	1	Commanding Officer U.S. Army Research Office (Durham) Box CM, Duke Station Durham, No. Carolina ATTN: CRD-AA-IP, Mr. Uleh	3
Commander U.S. Army Missile Command Redstone Arsenal, Alabama ATTN: Technical Library	1	AFSC Scientific/Technical Liaison Office U.S. Army Electronics R&D Laboratory Fort Monmouth, New Jersey	1	University of Connecticut Storrs, Connecticut ATTN: George E. Dombrowski, Dept. of Electrical Engineering	1
Sylvania Electronic Systems 100 First Avenue Waltham 54, Massachusetts ATTN: Mr. Ernest E. Hollis	1	Commanding General White Sands Missile Range New Mexico ATTN: Technical Library-169	1	Varian Associates 611 Hanover Way Palo Alto, California ATTN: Technical Library	1